UNIVERSITY OF SOUTHAMPTON

SYNTHESIS, STRUCTURE AND ELECTROCHEMISTRY OF POSITIVE INSERTION MATERIALS FOR RECHARGEABLE LITHIUM BATTERIES

A thesis submitted for the degree of Doctor of Philosophy

by

Emmanuelle Angeline Raekelboom

DEPARTMENT OF CHEMISTRY

FACULTY OF SCIENCES

February 2002

UNIVERSITY OF SOUTHAMPTON

ABSTRACT

FACULTY OF SCIENCES

DEPARTMENT OF CHEMISTRY

Doctor of Philosophy

SYNTHESIS, STRUCTURE AND ELECTROCHEMISTRY OF POSITIVE INSERTION MATERIALS IN RECHARGEABLE LITHIUM BATTERIES

By Emmanuelle Angeline Raekelboom

Lithium copper oxides $Li_xCu_2O_4$ (x = 2,3,4) have been synthesised for lithium battery application using solid state and solution reactions under various conditions. Li_2CuO_2 (*Immm*) has been prepared in air at 800 °C for 10-15 h from a stoichiometric mixture of copper oxide and lithium hydroxide. Synthesis using high pressure oxygen (250 bar, 4 h, 700 °C) and hydrothermal (1.5 kbar, 10 h, 600 °C) was used for the formation of mixed-valence cuprate $Li_3Cu_2O_4$ (C2/*m*) and the isostructural $Li_2NaCu_2O_4$ (250 bar in O_2, 4 h, 700 °C) from simple oxides. The latter has been characterised using powder neutron diffraction and crystallises in the space group C2/*m* (a = 10.2733(2), b = 2.80324 (3), c = 7.58532(9) Å and β = 119.6903 (8)°). The lithium ions occupy the tetrahedral positions whereas the sodium ions are found to be exclusively in octahedral environment. $LiCuO_2$ can not be obtained directly; it was synthesised by chemical lithium extraction of the lithium rich oxide, $Li_3Cu_2O_4$ using Br_2 in CH_3CN. The latter, was found to crystallise in the space group C2/*m*. The structures of all the lithium copper oxides prepared are composed of one dimensional infinite chains of edge-sharing CuO_4 square planes coordinated to lithium in tetrahedral (Li_2CuO_2, $Li_3Cu_2O_4$) and octahedral ($LiCuO_2$, $Li_3Cu_2O_4$)positions.

Electrochemical testing was carried out in a two-electrode cell using composite electrodes containing the oxide materials, carbon black to enhance the electronic conductivity and polytetrafluoroethylene as Teflon® binder. Lithium foil has been used as reference and counter electrode and 1 M LiPF6 in EC-DMC as the electrolyte. The slow galvanostatic charging of Li_2CuO_2 until 4.5 V yields charge specific capacity of 320 $mAhg^{-1}$ (theoretical capacity of 490 $mAhg^{-1}$) at a cycling rate of 11 mAg^{-1} which is followed by a large specific discharge capacity of 250 $mAhg^{-1}$(0.8 Li^+) distributed mostly between 2 and 3 V. Application as additive material with the positive electrode $LiMn_2O_4$ was found to be successful as it compensates the initial loss of specific charge capacity due to the formation of the passivation on the negative electrode. The slow galvanostatic cycling of $Li_3Cu_2O_4$ (theoretical capacity of 380 $mAhg^{-1}$) between 1.6 and 4.5 V yields a charge density of 160 $mAhg^{-1}$ (0.6 Li^+) at a cycling rate of 10 mAg^{-1}. The results for $Li_2NaCu_2O_4$ indicates the presence of sodium that may disrupt the lithium ion pathway. $LiCuO_2$ (theoretical capacity of 263 $mAhg^{-1}$) provides between 1 and 4.3 V a specific capacity of 500 $mAhg^{-1}$ with an average voltage of 2.5 V. The discharge is thought to involve the formation of Cu^I or Cu^0 in this material.

The discharges for the oxides are accompanied by a high hysterisis of 1 V due to slow ion transport in the electrode material that limits the electrode reaction. The diffusion coefficient $D_{Li+} = 10^{-12}$-10^{-13} cm^2s^{-1}, was estimated by current pulse methods for $Li_3Cu_2O_4$. The electron charge transport is not limiting as both $Li_3Cu_2O_4$ and Li_2CuO_2 are semiconductors (E_a~0.1eV), showing high electronic conductivies of 10^{-2} and 10^{-3} Scm^{-1}, respectively. A study of phase transitions in the electrode by *ex* and *in-situ* X-ray diffraction confirmed the transitions between Li_2CuO_2 (*Immm*), $Li_3Cu_2O_4$ (C/2*m*) and $LiCuO_2$ (C/2*m*). Decomposition to CuO and loss of crystallinity when the cell charged above 4 V was also observed.

Lithium ion exchange of $Na_2Mn^{IV}{}_3O_7$ was performed using reflux of LiBr at different temperatures in ethanol (70 °C) and hexanol (125 °C). This has lead in both cases to undistorted layered manganese oxides $Li_{2-x}Mn_3O_7$ (space group: $R\bar{3}m$), having high oxidation states of 3.95 and 3.60 respectively, with different cationic arrangement within and between the manganese oxide layers. Cationic disorder in the structure was found to increase for the compound exchanged in hexanol. The electrochemistry was carried out using composite electrodes prepared by a dry method. The galvanostatic charging (theoretical capacities of ~ 320 $mAhg^{-1}$) until 4.5 V yields charge densities of 150 and 125 $mAhg^{-1}$ at a cycling rate of 17 and 37 mAg^{-1} for the ethanol and hexanol compounds respectively. Both showed a conversion to a spinel phase upon cycling. A better capacity retention was obtained for the compound exchanged in ethanol at 70 °C. Transport measurements (D_{Li+}~10^{-14} cm^2s^{-1}) were carried out by FITT and ac impedance. Porous insertion electrode $Li_{2-x}Mn_3O_7$ was modelled for purposes of ac impedance and shows a possible formation of the surface layer on the positive electrode upon cycling.

Table of contents

Chapter five – Synthesis and structure of layered sodium and lithium Mn(IV) oxides, $A_2Mn_3O_7$

Chapter six – Electrochemical properties of the lithium Mn(IV) oxides, $Li_{2-x}Mn_3O_7$

Acknowledgements

I would like to thank my supervisors Dr John Owen and Prof. Mark Weller for their help and guidance throughout my PhD and for allowing me to attend international conferences in Italy (10^{th} IMLB) and Corsica (7^{th} Euroconference of Ionics), the EPSRC for funding the three years work and the REES (Research Experience for European Student) for allowing me to go in Japan.

A number of people from the inorganic and electrochemistry departments have given me support, advice, encouragement and friendship to which I am very grateful including, in chronological order, Andrew Hector, Christopher Knee, Adam Whitehead, Emmanuel Eweka, Susanna SilvaMartinez, Johan Elliot, Yaser Abu-Lebeh, Lucianna Pitta, Phil Nelson, Girts Vitins and Thierry Le Gall.

I would also like to thank all the members past and present of the Owen and Weller groups and those who have collected data at Rutherford Labs in my absence.

The use of equipment in the inorganic teaching, electrochemistry and SOC laboratories has been appreciated with the help of A. Blayden, Alistair Clark for the SEM instrument.

Finally, I would like to say a 'merci beaucoup' to all my family and friends in France who have always been there for help and support. And a special thank you also to Stephen for his patience and advice.

Abbreviations

XRD	X-ray Diffraction
PXD	Powder X-ray Diffraction
PND	Powder Neutron Diffraction
HRPD	High Resolution Powder Diffraction
T. o. f.	Time Of flight
e. s. d.	Estimated Standard Deviation
SEM	Scanning Electron Microscopy
EDX	Energy Dispersive X-ray spectroscopy
UV/VIS	Ultra-violet/Visible
MAS NMR	Magic Angle Spinning Nuclear Magnetic Resonance Spectroscopy
OCV	Open Circuit Voltage
GITT	Galvanostatic Intermittent Titration Technique
FITT	Faradaic Intermittent Titration Technique

''C'est en terme d'obstacle
qu'il faut poser le problème de la
connaissance scientifique''

Gaston Bachelard
(1884 -1962)

Chapter 1

Introduction

1.1 Energy storage in batteries

Since electricity cannot always be stored directly, it is necessary to utilise an indirect form of storage. Possibilities include the conversion of electrical energy into potential energy (pumped-hydro schemes), kinetic energy (flywheels), thermal energy (night storage heaters) or chemical energy. One form of chemical energy is hydrogen, generated by electrolysis, which may be stored and subsequently converted back into electricity in a fuel cell. Another form is the energy of the electrons and ions in certain inorganic compounds, which are able to intercalate species (e.g. Li^+) without any major structural changes. Batteries that use these materials can then chemically store and convert by an electrochemical process, the energy.

Since the invention of the first "pile" (alternate silver and zinc discs) by Alessandro Volta 200 years ago, many significant steps in the development of the batteries have been made. The invention of the Daniell cell, which gave for the first time a continuous current of useful magnitude, allowed for example, the expansion of the telegraphic systems in the 1850s. The first effective demonstration of a secondary (rechargeable) battery, a lead-acid battery, was given by Gaston Planté in 1881. The technology of the lead-acid battery was thus established.

Later, at the beginning of the 20^{th} century, the discoveries of the first alkaline batteries (nickel-cadmium and nickel-iron batteries) by Waldemar Jungner and Thomas Edison launched the basis of the modern battery industry. Advances in battery science and technology allowed the development of the primary alkaline zinc battery (Leclanché) and the improvement of the lead-acid battery. Entirely new secondary batteries have been developed and commercialised, the nickel-metal-hydride and the lithium batteries are examples.

In the actual spectrum of the conversion and storage of electrochemical energy, three main regions related to different energy ranges use various battery systems:

(1) In the domain of portable electronics (energy < 10^2 Wh), research has focused on aqueous alkaline batteries such as the zinc primary batteries (zinc-manganese oxide, zinc-silver-oxide, zinc-mercury-oxide) and the rechargeable nickel-metal-hydride batteries and over the last two decades on non-aqueous lithium batteries.

(2) In the domain of remote power supply batteries and electric vehicles (energy between 10^2 Wh and 10^5 Wh), traditional systems such as lead-acid or nickel- cadmium batteries have benefited from physical design improvements to enhance energy and power density but due to the toxicity and consequent price of the heavy metals lead and cadmium,

these systems are slowly being replaced by more advanced power sources such as the lithium-ion, nickel-metal-hydride batteries and the fuel cell technology.

(3) The latter is dominant in the higher energy domain (energy > 10^5 Wh) of heavy electric vehicles, nuclear power, space or defence.

Table 1.1 summarises the characteristics reactions of secondary battery systems cited.

1.2 Lithium rechargeable batteries

The majority of the electrical technologies previously cited require rechargeable batteries. After the introduction by Sony in 1990 of the first commercial rechargeable lithium battery, 60 % of the value of the world battery market was supplied by secondary batteries. Of all the possible systems, the rechargeable lithium battery has stood a forerunner and market leader with 280 millions units sold in the world.

A comparison with the traditional battery systems is shown in the Ragone plot (Figure 1.1). The Figure 1.2 shows that the lithium batteries in fact offer, compared to conventional systems, double specific energy (Wh kg^{-1}). This is due to the high average potential (~3.6 V, three times that of nickel-cadmium) and specific capacity ($mAhg^{-1}$) offered by the lithium battery due to the low molar mass of lithium (7 $gmol^{-1}$).

The principles of the lithium batteries have been outlined with the schematic description of the first $LiCoO_2$ battery followed by the actual developments in the lithium rechargeable batteries.

Table 1.1 Characteristic reactions of secondary batteries systems.

Battery System	Cathode/ Anode	Electrolyte used and reaction	Nominal Voltage (V)
Lead acid	PbO_2/ Pb	H_2SO_4 as aqueous solution $Pb + SO_4^{2-} \leftrightarrow PbSO_4 + 2e^-$ (anode on discharge) $PbO_2 + 4H^+ + SO_4^{2-} + 2e^- \leftrightarrow PbSO_4 + 2H_2O$ (cathode on discharge) $PbO_2 + 2\ H_2SO_4 + Pb \leftrightarrow 2\ PbSO_4 + 2\ H_2O$ (total reaction)	2
Ni-Cd	NiOOH/ Cd	KOH as aqueous electrolyte $Cd + 2OH^- \leftrightarrow Cd(OH)_2 + 2e^-$ (anode on discharge) $2NiOOH + 2H_2O + 2e^- \leftrightarrow 2Ni(OH)_2 + 2OH^-$ (cathode on discharge) $2NiOOH + Cd + 2H_2O \leftrightarrow Ni(OH)_2 + Cd(OH)_2$ (total reaction)	1.2
Ni-MH	NiOOH/ Hydrogen adsorbed alloy	KOH as aqueous solution $H_2 + 2OH- \leftrightarrow 2H_2O + 2e^-$ (anode on discharge) $2NiOOH + 2H_2O + 2e^- \leftrightarrow 2Ni(OH)_2 + 2OH^-$ (cathode on discharge) $2NiOOH + H_2 \leftrightarrow 2Ni(OH)_2$ (total reaction)	1.2
Lithium ion	$LixCoO_2$/ Li + C	Organic electrolyte + Li salt $Li(C) \leftrightarrow Li^+ + e^-$ (anode on discharge) $Li^+ + e^- + Li_xCoO_2 \leftrightarrow LiCoO_2$ (cathode on discharge) $Li(C) + Li_xCoO_2 \leftrightarrow LiCoO_2$ (total reaction)	3.7

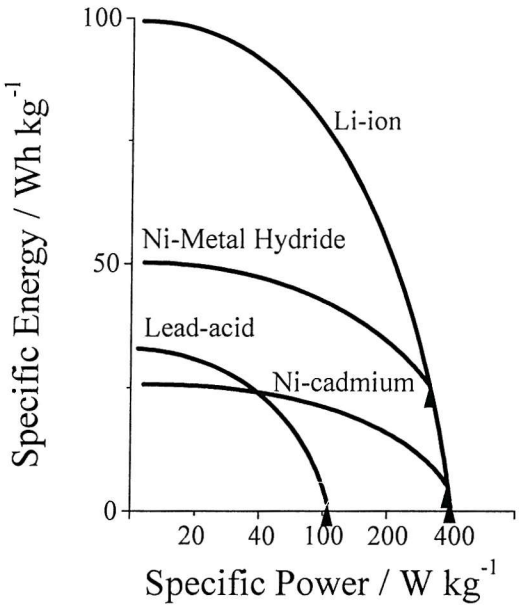

Figure 1.1 A Ragone plot of energy and power density for various battery systems, showing the deterioration of energy density with increasing power demand.

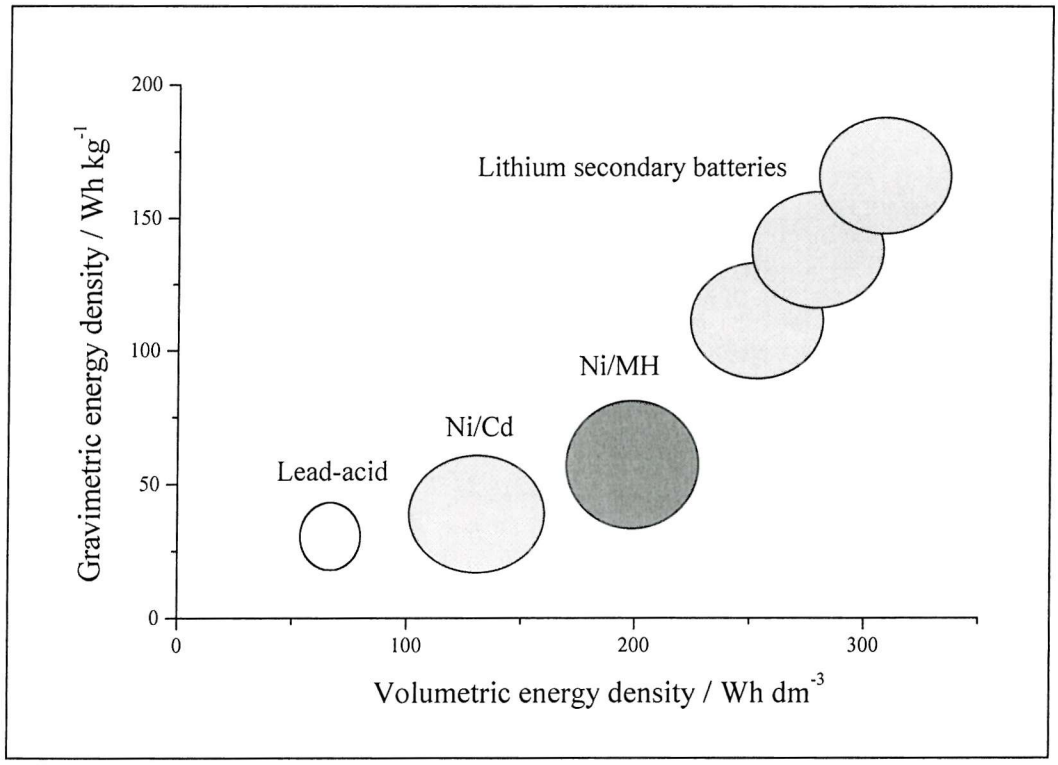

Figure 1.2 Comparative plot of energy density of secondary batteries.

1.2.1 Principle of lithium battery- The Sony cell

The elements of the "rocking chair" Sony cell are shown schematically in Figure 1.3b. The cell is also called a spring or LION cell to distinguish it from the lithium metal design in Figure 1.3 a.

The cell consists of a positive electrode composed of a thin layer of powdered $LiCoO_2$ mounted on an aluminium foil and a negative electrode formed from a thin layer of a powdered graphite, or other carbons, mounted on a copper foil. The two electrodes are separated by a porous plastic film soaked in an electrolyte ($LiPF_6$ dissolved in a mixture of dimethyl carbonate and ethylene carbonate). The cell is constructed in the discharged state and charging the cell involves diffusion of lithium ions within the $LiCoO_2$ particles towards their interfaces with the electrolyte, the lithium ions then cross the electrolyte and are intercalated between the carbon layers in the graphite electrode in the case of the lithium ion battery. Compared with some aqueous systems, the electrolyte takes no part in the reaction except for conveying the electroactive lithium ions between the two electrodes.

Charge balance requires that the equivalent number of electrons must pass around the external circuit. Discharge reverses the process moving the electrons out of the graphite and reforming $LiCoO_2$. In an earlier design, lithium metal was employed rather than graphite as negative electrode but the reactivity of lithium with the electrolyte and formation of lithium dendrites has resulted in concerns over safety for this design.

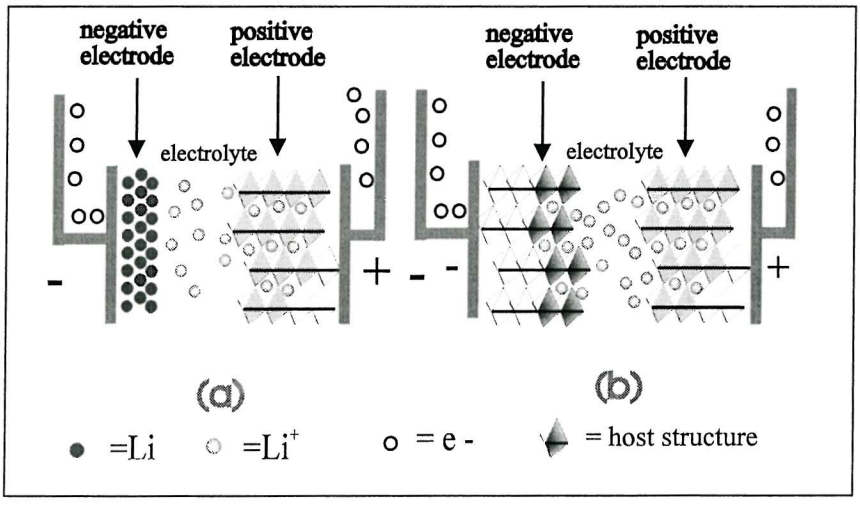

Figure 1.3 Schematic diagram of a lithium cell with lithium metal as the negative electrode (a) and a lithium ion with an insertion negative electrode e.g. carbon (b) (with the permission of Dr J. Owen [2]).

1.2.2 Development of the lithium ion rechargeable battery

A review of positive electrode materials for rechargeable batteries will be presented in paragraph 1.4. The review of negative electrode and electrolyte materials are highlighted here.

1.2.2.1 Negative electrode materials

In the lithium rechargeable battery, carbon instead of lithium metal, is used as the anode-active material. Carbon exists in various forms ranging from a crystalline state to an almost amorphous state, and the raw materials used to produce anodes include natural graphite, oil pitch, coal tar, hydrocarbon gas, benzene, various resins, etc. These anodes are categorized into three groups (1) graphite, (2) non-graphitized glass-like carbon (hard carbon) which does not graphitize even if it is treated at high temperature and (3) soft carbon, easily changeable with heat treatment. Generally graphite and hard carbon are used as anodes. In practice, at room temperature, graphite accepts sufficient lithium to form LiC_6 which on delithiation can deliver 372 $mAhg^{-1}$[3-6]. The graphite anode (mesocarbon micro beads (MCMB) [7]) sintered at 3000 °C has a capacity of 400 $mAhg^{-1}$ during charging, while on discharge delivers a capacity as low as 290 $mAhg^{-1}$. This is based on the irreversible retention when a thin, lithium ion conductive film (solid electrolyte interface, SEI [8]) is formed on the surface of the graphite during the first charge. In the hard carbon prepared from polycondensation of oil pitch, lithium is taken in, not only between the carbon layers but also in the crevices between crystal particles (doping place) and as a result, hard carbon accepts more lithium than the given formula LiC_6 and becomes a high capacity anode. However, the irreversibility of the first cycle as well as the potential change is considerable compared with graphite.

The search for newer and higher performance electrode materials leads to the development of alloy anodes based on Sn [9-12] and Si [13,14]. Though the lithium intercalated into Li_4M-$Li_{4.4}M$ (M: metal) showed a high capacity of about 800-3000 $mAhg^{-1}$, a stable cycling performance was not obtained as the associated volume change was more than four times during lithium insertion. The use of oxide anodes was also proposed such as tin oxides [15], $FeVO_4$ and $InVO_4$ [16] and MnV_2O_6 (Brannerite-type) [17]. Almost all of these oxides change their form from crystalline to amorphous during lithium intercalation.

Large capacity fade on cycling limits their use and stabilisation of the structures of these oxide materials may be possible by selective partial substitution of the transition metals with other elements.

1.2.2.2 Electrolyte materials

In lithium rechargeable batteries, an aqueous electrolyte cannot be used, as lithium would react. Hence, inorganic salts (like $LiClO_4$) dissolved in organic liquids with a large stability window have been considered as possible electrolytes. To be a good electrolyte, such a non-protonic electrolyte must have good ionic conductivity and high chemical stability. Also to operate between –20 and +60 °C, the solvents must have a low melting point, a high boiling point and low vapour pressure.

Cyclic carbonic acid esters like propylene carbonate (PC) and ethylene carbonate (EC) have high dielectric constants reducing the coulombic interactions. However they show high viscosity values due to the interaction between molecules. Lower viscosity is more desirable for easier movement of the lithium ion. In chain-like esters such as dimethyl carbonate (DMC) and diethyl carbonate (DEC), lower viscosity and dielectric constants values allow a movement between the molecules. It is common practice to mix two or more solvents so as to obtain a desired set of properties which is suitable for high performance batteries. Since the electrolyte based on PC is reported to decompose in contact with graphitized carbon anodes, a suitable solvent mixture (EC/DMC) or (EC/DEC) has been used [18]. The molar conductivities of electrolytes consisting of 1M of $LiPF_6$ in EC/DMC and EC/DEC (1:1), are 11.2 and 7.8 S cm^{-1} respectively.

More recently the replacement of the liquid electrolyte by a solid polymer has led to all-solid-state rechargeable lithium batteries [19]. In the polymer lithium ion battery (PLI), the membrane acts both as the electrolyte and the separator. They are more compact and lighter than the liquid electrolyte batteries. Polyethylene oxides (PEO) complexed with sodium and lithium salts have been studied [20,21] and the conduction mechanism consists of a segmental motion of the polymer chain in the amorphous state [22]. High ionic conductivity of $10^{-4}/10^{-3}$ S cm^{-1} has been obtained by bridging PEO chains [23], introduction of side chains [24] and the improvement of supporting lithium salt.

Finally, different to the dry solid state electrolyte, the gel-type solid polymer electrolyte (polyacrylonitrile PAN or PMMA polymer) [25] contains, in fact, an organic liquid known as plasticizer and shows up to 10^{-3} S cm^{-1} at room temperature.

Even if polymer has lower conductivity than liquid electrolytes in general, they have excellent points such as ease of battery fabrication in various shapes and better safety.

1.3 Solid-state chemistry of insertion compounds

The success of lithium batteries would not have been possible without advances in the solid-state chemistry of insertion solids [26]. A review of known insertion compounds is presented. In the following paragraph, attention will be focussed on those insertion compounds that are useful in rechargeable batteries (anode and cathode materials).

1.3.1 Review of insertion compounds

A classification of insertion compounds by chemical composition of their host lattice is proposed.

1.3.1.1 Metals

Ions can be inserted in metals and form alloys. For example, the spontaneous electrochemical alloying of lithium with various metals such as Sn, Pb, Al, Au, Pt, Zn, Cd, Ag, Mg, Ti, Cu, and Ni were carried out by A. Dey *et al* [27]. X-ray diffraction patterns indicated the presence of intermetallic compounds. These binary lithium alloys have been considered as replacement for metallic lithium in rechargeable lithium cells.

1.3.1.2 Carbon

Molecules, anions or cations (NH_3, AsF_6^-, Li^+...) can be intercalated into carbon. In fact, graphite is built of ABAB layers, which are held together by van der Waals forces, each layer containing sp^2 bonds. If lithium ions intercalate into these layers, the layer arrangement changes to AAA. The host structure offered is resilient enough to provide reversibility. With Li^+, Li_xC_6 ($0 < x < 1$, 372 $mAhg^{-1}$) has found application as anode materials in lithium ion rechargeable batteries.

1.3.1.3 Organic Compounds

Conjugated organic polymers are found to have electronic conductivity. Compounds like polyacetylene, polyaniline and polypyrrole [28-30] are another class of intercalation compounds.

1.3.1.4 Transition metal chalcogenides

TiS_2 was the first inorganic layer compound used as intercalation material for Li^+ [31]. Since then many other layered materials using the electrochemical lithium insertion have been obtained such as other sulphides Li_xMoS_2 and Li_xNiPS_3 [30] and the oxohalides Li_xFeOCl [32]. $Li_xMo_6Se_8$ results in lithium insertion in the three dimensional structure of the Chevrel compound Mo_6Se_8. It offers a three-dimensional lattices of sites [33].

Other molecules or cations (NH_3, Na^+) can also be intercalated in these compounds. They have in general good metallic character. The intercalation is often accompanied by expansion of the structure, structural and electronic property modification.

1.3.1.5 Transition metal oxides

Transition metal oxides present a variety of host structures with different dimensionalities: from the 1D structures in chains in $Li_xCu_2O_4$ (x = 2, 3, 4) [34] (see Chapter 3) to the 2D layered $Li_xV_2O_5$ [35-37], $Li_xV_3O_8$ [38], $LiMO_2$ (M= Fe [39], Co, Ni [40-42], Mn [43,44]) and 3D LiM_2O_4 (M = Ti [45], Mn [47,49]), $Li_xV_6O_{13}$ [46].

It should be noted the change in optical properties as intercalation takes place in several transition oxides. The altered electronic structure may shift the absorption or reflection energy. This electrochromic effect can be found in oxides of Nb, Mo, Ta when used as a cathodes or in Cr, Ni, Rh, and Ir oxides when used as an anode [50,51]. The most studied material is the defect perovskite-type WO_3. It starts to absorb light (max at 1.3 eV; 900 nm) when electron $5d^1$ (t_{2g}) is introduced after the reduction of W^{+6} to W^{5+}.

1.3.2 Relating solid-state chemistry to positive insertion electrodes

In this section will be reviewed the properties that an insertion solid should possess to be a positive insertion material for lithium rechargeable batteries and how this relates to the structure and composition of the solid.

1.3.2.1 Structure/properties relationship

Insertion solids may be defined as hosts into which atoms (ions and electrons) may be inserted or removed without a major disruption of the structure [52-54]. Intercalation will be used specifically for insertion into a layered material.

The key structure/property relationships for an insertion solid are listed in Table 1.2 [26].

Table1.2 Criteria for insertion compounds as positive electrodes.

1 Must be an insertion host for lithium
2 Low Fermi level and Li+ site energy to allow high open-circuit voltage
3 Little variation of potential with Li content or state of charge
4 Accommodate large quantity of Li per formula unit to allow large capacity
5 Low formula mass and molar volume for high specific and volumetric capacity
6 Sustain high rate of Li insertion and deinsertion
7 Good reversibility through the cycles
8 Avoid co-intercalation of solvent
9 Stable in contact with electrolyte
10 High electronic conductivity
11 Low cost and non toxic
12 Easily fabricated into electrode

1.3.2.2 The cell potential

The criteria are numerous and some are, indeed, essential. The voltage of the cell is one of them and this should be large. The voltage between the two electrodes is related to the work the cell can deliver on transferring electrons around an external circuit and to the free energy change on transferring lithium from one intercalation electrode to the other. The free energy change ΔG associated with the transfer of one mole of lithium between the two electrodes is equivalent to the difference in the chemical potential of lithium in the two electrodes. From the Gibbs equation, the potential V equals to:

$$V = -\frac{(\mu_{Li}^{cathode} - \mu_{Li}^{anode})}{nF} \qquad (1.1)$$

where V is the open circuit voltage of the cell, $\mu^{cathode}{}_{Li}$ and $\mu^{anode}{}_{Li}$ the chemical potentials of lithium in the positive insertion electrode and graphite electrode ($\mu^{anode}{}_{Li} = 0$ for lithium metal) respectively, $n = 1$ since one e^- is transferred for each lithium and F is the Faraday's constant (96485 $Cmol^{-1}$).

On discharge , lithium is transferred from a state of high energy $\mu^{anode}{}_{Li}$ in the one of low energy $\mu^{cathode}{}_{Li}$ in the positive electrode.

The voltages against Li^+/Li of intercalated compounds are shown below.

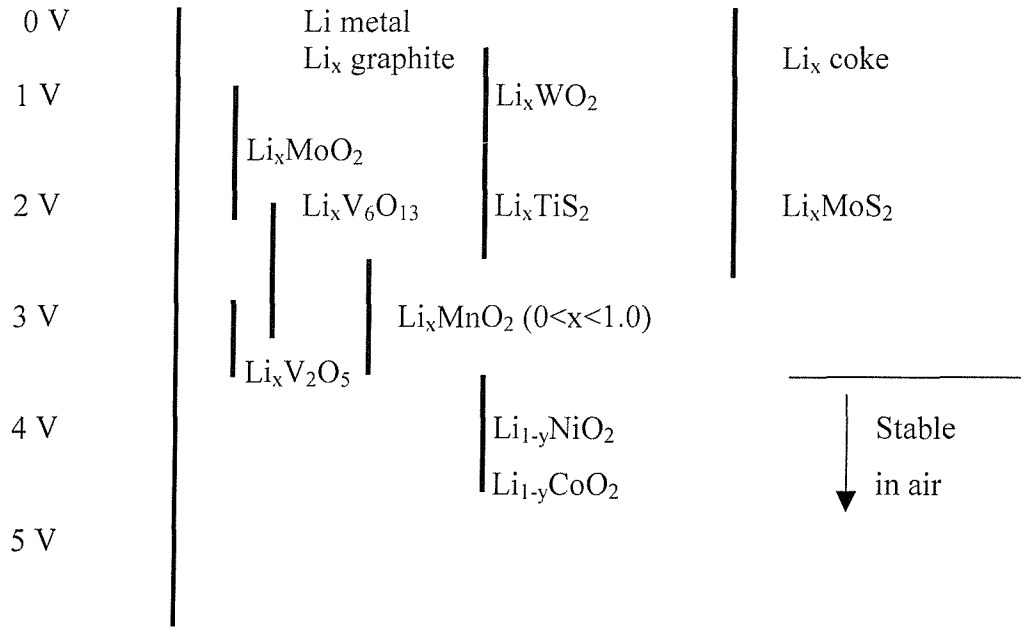

The chemical potential changes with the lithium content in the electrode and the potential of a positive electrode is usually measured against lithium metal which has an invariant μ_{Li}. If the energy to put an isolated ion and its electron into the lattice is denoted ε, then the chemical potential for a fraction x of inserted ions is as follows:

(1.2) $$\mu(x) = \varepsilon + kT \ln \frac{x}{1-x} + Ux$$

or

(1.3) $$E(x) = E^0 + \frac{RT}{F} \ln \frac{1-x}{x} + E_{\text{int}}(x)$$

E^0 is the standard potential due to the guest-host interaction whereas Ux and $E_{int}(x)$ terms include the interaction of all guest ions with each other (mean field interaction) in case of a random ion arrangement. R ln (1-x)/x is related to the entropy of the inserted ions.

The electrode potential *vs.* x takes a s-shaped curve. Equations 1.2 and 1.3 describe a a single phase reaction that occurs during the intercalation of guest ions forming a continuous range of solid solutions. When a two-phase reaction occurs (first order transition), the thermodynamics is simpler since the electrode potential is constant.

1.3.2.3 The Fermi level

From equation 1.1, in order to ensure a large voltage, a positive insertion electrode that possesses a low $\mu^{\text{cathode}}_{\text{Li}}$, is desirable. Lithium is rarely in the form of Li atoms in the

insertion compounds but instead exists as Li^+ ions along with their charge-compensating electrons, the latter located in the d levels of the transition-metal ions. As a result, the chemical potential of lithium can be separated such as $\mu_{LI} = \mu_{Li+} + \mu_{e-}$.

The potential of a positive insertion and hence the voltage of the cell will depend on the energy of the electrons and the Li^+ ions in the host (see section 1.3.2 .4).

After insertion of electrons into a host, the Fermi level will be equal to $E_F = \mu_{e-}$. Maximising the positive electrode potential will consist of (1) reducing the Fermi level and (2) increasing the stability (low energy) for Li^+ in its sites in the compound. The energy of the lithium site will be discussed in the next paragraph.

The lowest Fermi level which can be achieved for an insertion compound is determined by the energy corresponding to the top of the valence band (Figure 1.4). In oxides the valence band is largely of oxygen 2p parentage and lies significantly below the top of the 3p valence band in the corresponding sulphides. Fermi levels in oxides can be more than 2 eV lower, resulting in potentials of between 4 and 5 V *vs.* Li. The focus is thereby on oxides rather than on chalcogenides. However the replacement of oxygen by a polyanion (XO_4^{3-}) like sulphate, phosphate, or arsenate lowers the Fermi level of the redox couple of the transition metal and thereby increases the cell potential.

For a transition metal oxide, the Fermi level is set by the position of the cation d levels. The lowest d levels are associated with those ions from the centre or right of the first transition series, *i.e.* Cr, Fe, Mn, Co, Ni. They all exhibit the +4 oxidation state corresponding to d levels that lie close to the top of the oxygen valence band. For example, $Li_{1-x}Cr_2O_4$ gives an open circuit potential of 5 V *vs.* Li. associated with the $Cr^{4+/3+}$ mixed- valence state [55]. Even further away on the first transition series, the Fermi level of Cu^{3+}, isoelectronic with Ni^{2+} is only several hundred meV higher than in Li_xNiO_2 and should give rather high voltage. However the $Cu^{2+/3+}$ mixed valence state in $Li_3Cu_2O_4$ (see Chapter 3) shows lower potentials on discharge due to a polarisation effect.

The sites for the electrons in an octahedral oxygen environment around the transition metal of a host material are represented on the band structure picture in Figure 1.4.

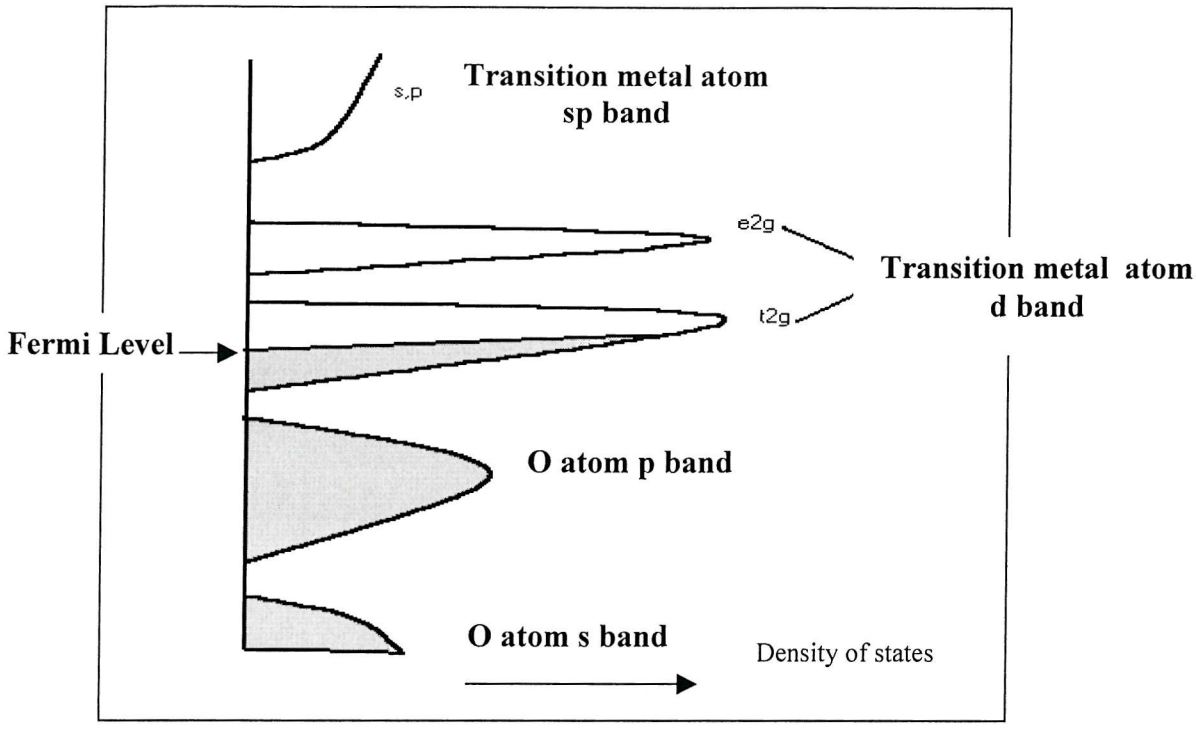

Figure 1.4 Band structure of a transition metal oxide from the GroupVB nd^3 $(n+1)s^2$. The p orbitals of the anions (O^{2-}) overlap with the s,p and d orbitals of the metal to produce bonding and antibonding orbitals. The lattice periodicity transforms these levels into bands.

1.3.2.4 The site energy of lithium

Since Li^+ has a filled outer core of electrons (unlike the transition metals ions), the geometry of the site is not important as long as the anions are distributed evenly around the site. Thus Li^+ would prefer two types of site: the octahedral and tetrahedral sites. In insertion lithium transition metal oxides, the voltage of the redox couple M located in octahedral sites depends on the site energy of lithium ions. The voltage increases when the site energy of the lithium ions decreases which occurs when they occupy tetrahedral sites. Because of a more uniform distribution of atoms, the lithium is more stable in a tetrahedral than in octahedral oxygen environment. The high voltage given by an insertion material is then based on the destabilisation energy of the host structure.

This is illustrated by the high electrode voltage delivered by $LiMn_2O_4$ (4.1 V) which stems from lithium in a tight tetrahedral coordination whereas an insertion in octahedral sites and formation of $Li_2Mn_2O_4$ yield voltage of 3 V. This is also at the origin of the different voltages obtained from the spinel $LiCoMnO_4$ (5.0 V) and $LiCoO_2$ (3.7 V) that operate by means of the $Co^{3+/4+}$ couple in both cases. The voltage increase in $LiCoMnO_4$ originates from

the site energy of Li^+ which occupies octahedral sites in $LiCoO_2$ but is distributed over tetrahedral interstices in $LiCoMnO_4$.

1.4 Insertion materials used as positive electrode in lithium rechargeable batteries- Description, comparison and performance

Whittingham [31] first proposed the feasibility of using an inorganic, TiS_2 for non aqueous secondary batteries of high specific and power density during the mid-70s. This compound has a good metallic character and undergoes lithium reversible intercalation over the compositional range $0 \leq x \leq 1$ in Li_xTiS_2. Despite its discharge voltage above 2 V with current densities of 1-10 mA cm^{-2}, the difficulties with practical nonaqueous batteries and reversible deposition over lithium negative electrode has restricted the use of the Li_xTiS_2/Li cells to "button-size" units.

In 1980, Mizushima *et al.* [40] prepared the layered $LiCoO_2$ (α-$NaFeO_2$ structure) at high temperature and the charged material by low-temperature electrochemical extraction of the lithium. The measured open potential of the Li_xCoO_2/Li cell was approximately twice that of Li_xTiS_2 giving a theoretical energy density of 1.1 $kWhkg^{-1}$. It took around 10 years to put $LiCoO_2$ to commercial use. This oxide is structurally more stable than TiS_2.

Meanwhile, many insertion compounds have been explored in the chalcogenides, oxyhalides (see section 1.3.1) and other transition metal oxides having the same stoichiometry than $LiCoO_2$, i.e. $LiMO_2$ with M = Fe and Ni. $LiMnO_2$ with the $LiCoO_2$ structure has been recently synthesised and studied.

The use of $LiMn_2O_4$ spinels as positive electrode was first reported in 1983 [47] and its attractive features led in 1996 to the first commercial $LiMn_2O_4$ rechargeable lithium battery [56].

Before a summary of the characteristics of the existing cathode materials, a review of the rock salt structure of $LiMO_2$ (M = transition metal) and the spinel phases will be given as introduction.

1.4.1 The rock salt structure of the ABO_2 phases

The rock salt or NaCl-type structure is one of the most common and well known structure types adopted by compounds of composition AX. The cation, A, is often an alkali metal, alkaline earth, or transition series cation and X is most commonly an oxide, sulfide or halide. The cations are octahedrally coordinated by anions as are the anions by cations; in term of a polyhedral structure description, both sets of counter-ions are distributed in a three-dimensional network of edge-sharing octahedra.

Several types of superstructures are formed when two cations A and B, occupy the octahedral sites in a non-random manner. In ternary rock salt oxide systems, a monovalent A and trivalent B combination for which the local electroneutrality (Pauling's rule) around oxygen is preserved is in the ABO_2 formula. This states that the sum of electrovalencies, *z/n* (*z* charge, *n* coordination number) of the nearest neighbour cations should equal the charge, *x*, of the anion, *i.e.* $\sum z/n = x$. Other formulae that contain tetra- and heptavalent B cation also adopt rock salt structures, i.e. A_2BO_3, A_5BO_6 but they will not be developed.

Almost all rock salt compounds of formula ABO_2 are isostructural with α-$LiFeO_2$, β-$LiFeO_2$, α-$NaFeO_2$, α-$NaMnO_2$ or β-$NaMnO_2$. The structure adopted is a function of the corresponding trivalent to monovalent cation radius ratio (r_B/r_A). If A and B cations have similar sizes, this will give disordered structures.

In order to compare the structure types, the A-B cation order is discussed, with reference to the cubic or pseudo-cubic rock salt subcell of each. In the NaCl unit cell, the cations lie in rows parallel to <110> at heights of z =0 and 0.5. Different ordering sequences occur within these rows in the previous type-structures and will be described in the preferred direction together with the arrangements in layers between the close-packed (cp) anions layers, i.e. parallel to (111) [57].

1.4.1.1 α-$LiFeO_2$ [58]

In this type structure obtained at 500 °C from β-$LiFeO_2$, the order adopted by the cations A and B parallel to both [110] and [-110] of the rock salt subcell, is in the sequence ABAB, to give a tetragonal body-centered unit cell, space group $I4_1/amd$, with a *c*-parameter doubled that of NaCl subcell. (Figure 1.6 a). This superstructure is adopted by a large family of phases, including the compounds $LiMO_2$ (M = Sc, In), $NaMO_2$ (M = Gd, Eu, Sm, Nd, Pr,

La) and Li_2MXO_4 (M = Mg,Mn, Co, Zn; X= Zr, Hf). The anatase (TiO_2) structure is also related to this structure except that the Li sites is unoccupied.

1.4.1.2 β-$LiFeO_2$ [58]

Related to the previous phase, this metastable phase is obtained at 450 °C as a precursor to the formation of stable α-$LiFeO_2$ (disordered structure of γ-$LiFeO_2$). The A and B cations order in the sequence ABBAAB parallel to [110] but ABAB parallel to [-110], as is the case for γ-$LiFeO_2$ (Figure 1.6 b). This gives rise to a monoclinic unit cell, space group C2/*c*.

1.4.1.3 α-$NaFeO_2$ [59]

In this structure, cations order into alternate layers perpendicular to [111]. The ordering is now bidimensional. Rows of like cations run parallel to [110] at heights of z = 0,0.5, but alternate ABAB parallel to [-110]. The ordering along [111] introduces a slight distortion of the lattice to hexagonal symmetry, space group $R\bar{3}m$ (Figure 1.7).

This structure is closely related to that of $CdCl_2$, in which layers of Cd and cation vacancies alternate perpendicular to [111]. However the cubic close-packed arrangement of anions in α-$NaFeO_2$ is different than in the $LiTiS_2$ structure (CdI_2 type-structure with hexagonal array of oxygen anions) (Figure 1.5).

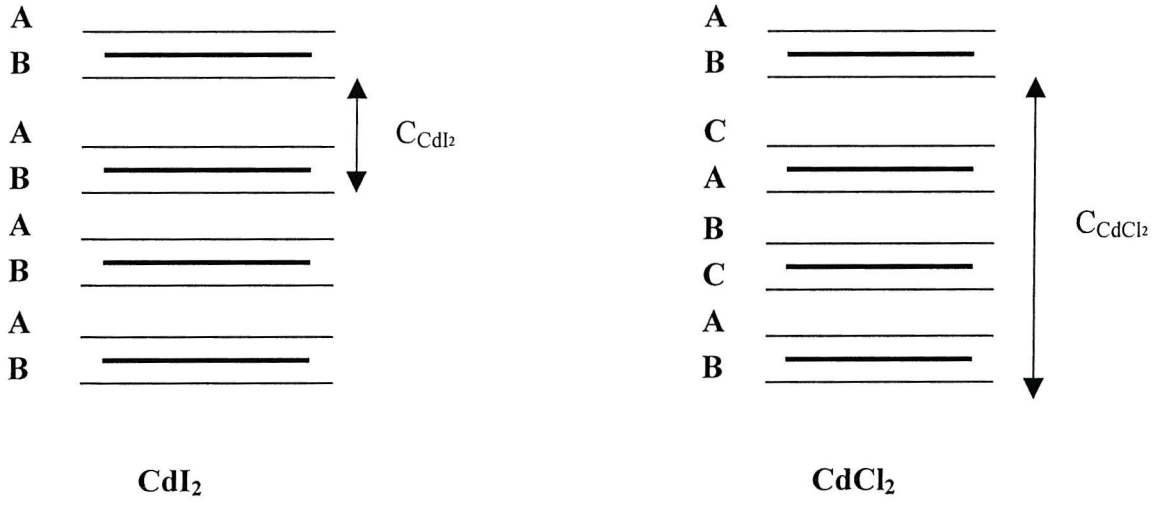

Figure 1.5 Stacking of MO_2 layers in $LiTiS_2$ (CdI_2 type) and $LiMO_2$ ($CdCl_2$ type). Close-packed oxygen layers are shown as A, B or C. Metal cations are situated in the middle bold layers. The a_{fc} parameter is doubled in $CdCl_2$ in order to match the sequences of the plan B.

The layered nature of this structure allows facile cation intercalation and isostructural transition metal lithium oxides $LiMO_2$ (M = V [60], Cr [61], Co [62], Ni [63]) and $LiFeO_2$ [56] obtained by low-temperature exchange of the sodium phase, crystallise in this layered α-$NaFeO_2$-type structure. More recently, layered $LiMnO_2$ [44] was synthesised using an ion-exchange technique and shows a monoclinic distortion (β-$NaMnO_2$ phase), space group C2/*c*.

1.4.1.4 α- **and** β-**$NaMnO_2$** [64]

These rock salt structures do not satisfy Pauling' s rule of electroneutrality around the oxygen because of the presence of Jahn- Teller active cations (see 1.4.2) that cause distortion of the octahedral cation environment. The low-temperature form of $NaMnO_2$, α-$NaMnO_2$ is a monoclinic distortion of α-$NaFeO_2$ structure in which Mn forms four short and two long bonds around the oxygen. β-$NaMnO_2$, however is orthorhombic and the octahedral distortion is alleviated in comparison with the α polymorph. The Na and Mn order in double rows staggered between consecutive layers in a zigzag formation. Two types of cation environment are displayed around the oxygen 4Na/2Mn and 2Na/4Mn.

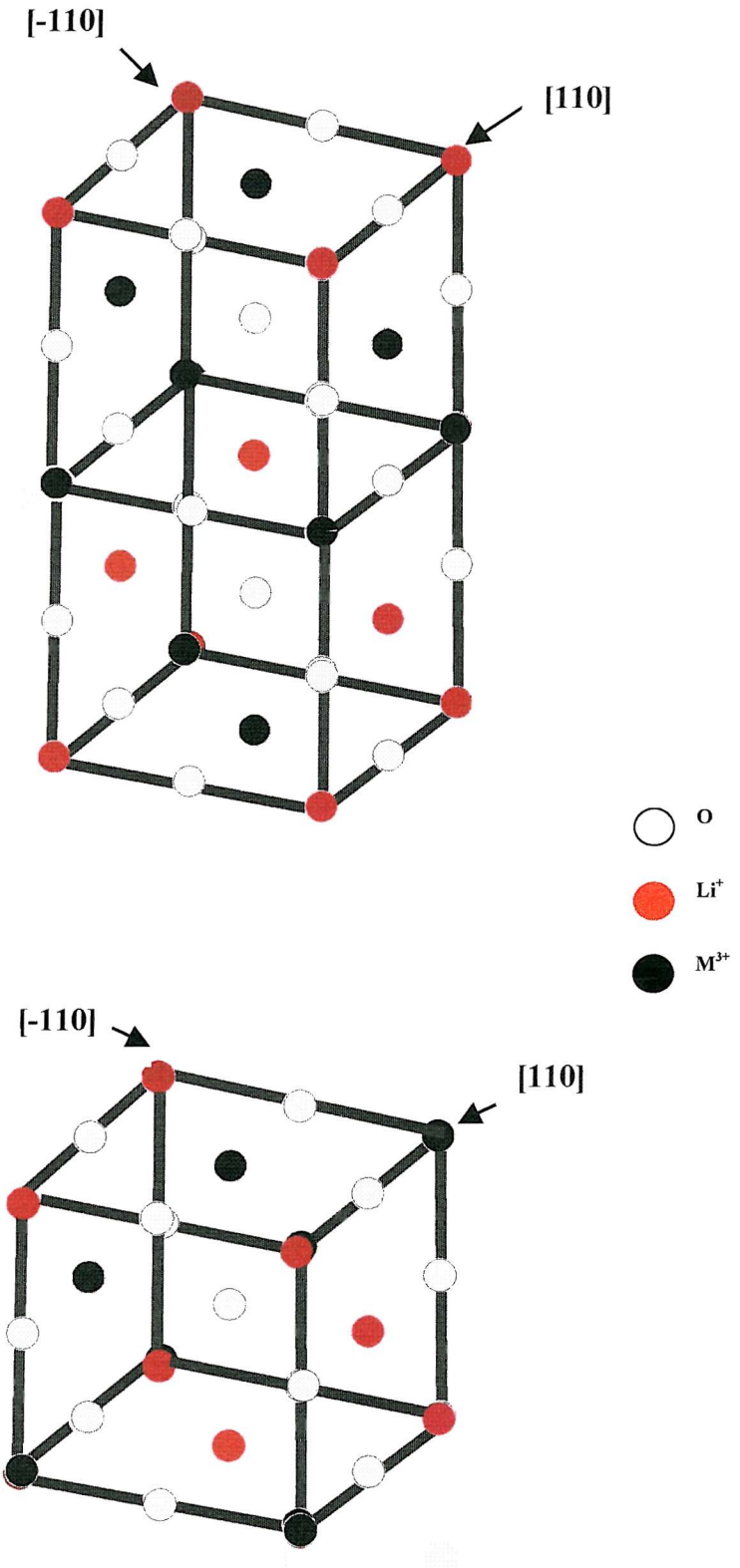

Figure 1.6 Crystal structures of γ-$LiFeO_2$ (a: top) and β-$LiFeO_2$ (b: bottom) with NaCl subcells outlined.

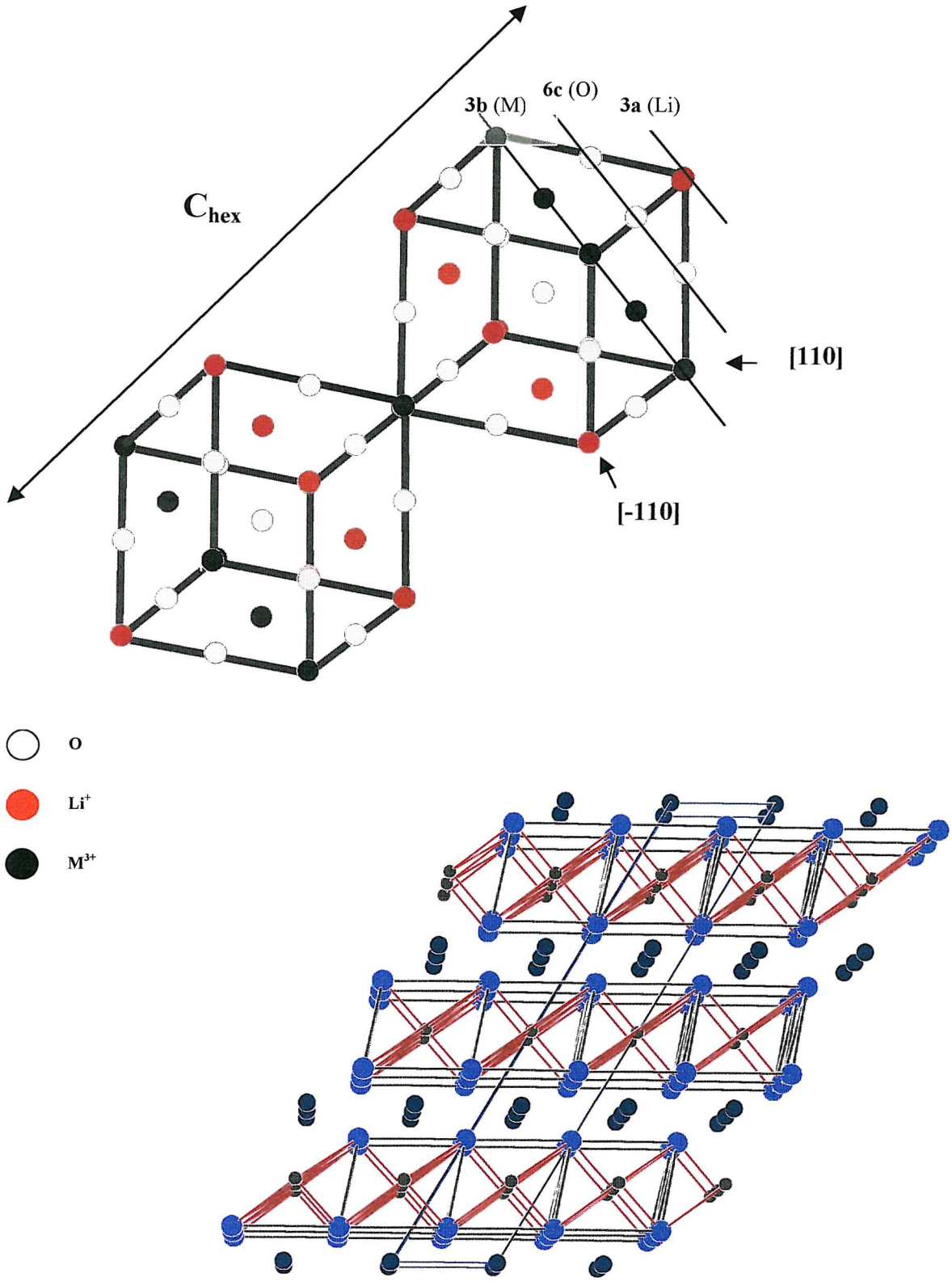

Figure 1.7 Top left: Formation of the layered structure by cation ordering along the (111) direction within the rocksalt structure of α-$NaFeO_2$. Bottom Right: Hexagonal unit ($R\bar{3}m$) cell of the layered structure (Li: dark blue, O: light blue, Mn: black circles).

1.4.2 The Jahn-Teller effect

The Jahn-Teller effect predicts that for degenerate electronic states a distortion that will lower the symmetry of the system must occur so as to split the degeneracy. In an octahedral environment, a tetragonal distortion corresponding to the extension along the z axis and a compression along the x and y axes, removes the degeneracy of the t_{2g} and e_g orbitals by stabilising the ones along the z axis due to less repulsion with the ligand, i.e. d_{xz}, d_{yz} and d_z^2 (Figure 1.8). Further distortion towards square planar geometry can occur when the extension along the *z*-axis reaches a maximum corresponding with the larger split between the $d_{x^2-y^2}$ and the d_z^2 orbital.

This is of particular importance for the structural chemistry of the first row transition metal ions with configurations of $3d^n$, which possess degenerate electronic states in octahedral geometry. The table 1.2 give examples of the Jahn-Teller active ions.

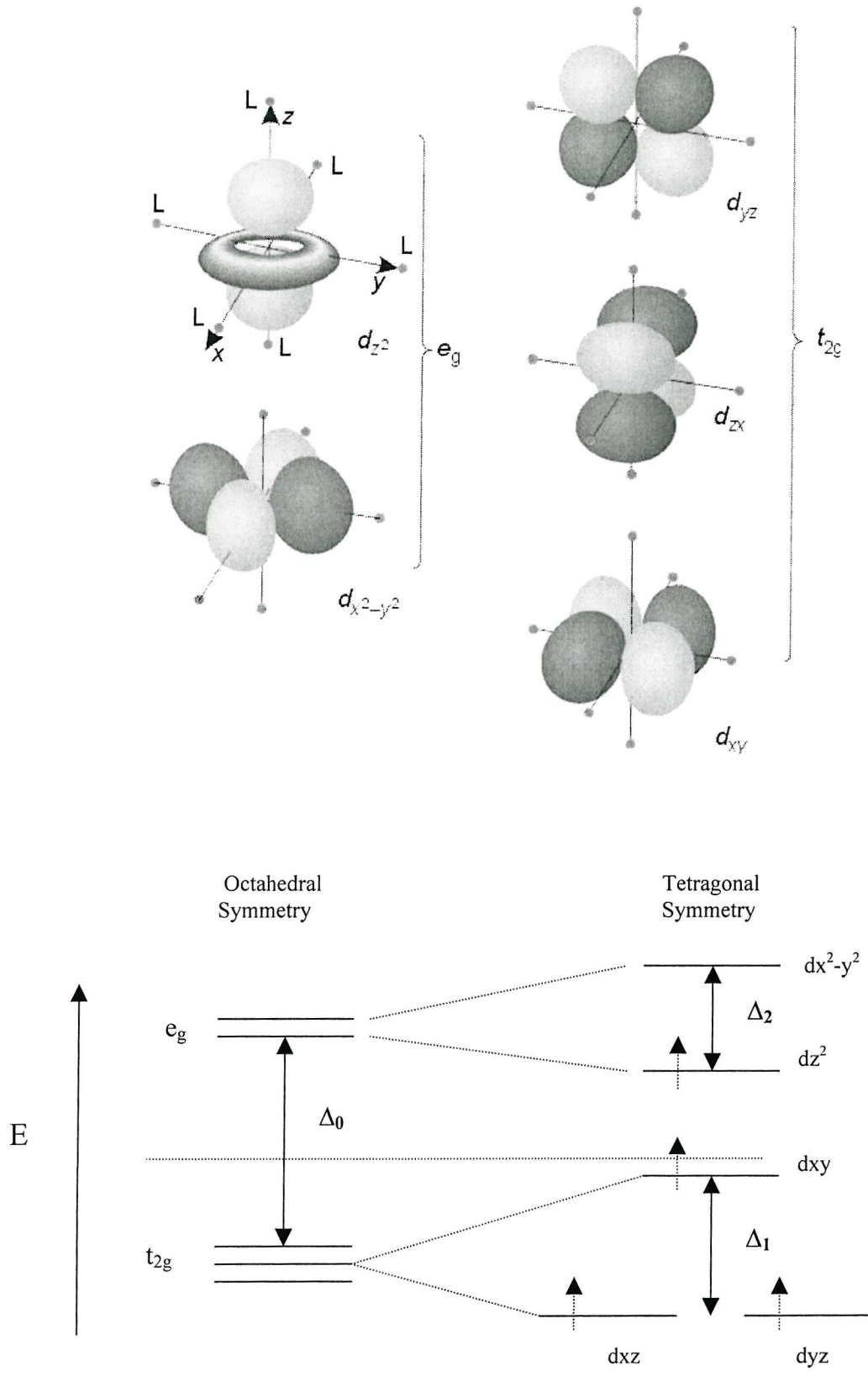

Figure 1.8 Top: The five d orbitals in an octahedral field showing their orientations with respect of the ligands L.
Bottom: Energy level diagram showing tetragonal distortion for a d^4 complex such as Mn^{3+}.

Table 1.2 Jahn-Teller active first row transition metal ions. The low (LS) and high (HS) spin electronic configurations are considered from d^4 to d^7 ions. Configurations on LS are more stable (from crystal field stabilisation energy of M. J. Winter, Ed. Oxford Chemistry Primers, *d*-Block Chemistry).

Configuration [Ne] $3d^n$	Type	Examples	Jahn-Teller effect
d^1	$(t_{2g})^1 (e_g)^0$	Ti^{3+}, V^{4+}	Y
d^2	$(t_{2g})^2 (e_g)^0$	V^{3+}, Cr^{4+}	Y
d^3	$(t_{2g})^3 (e_g)^0$	V^{2+}, Cr^{3+}, Mn^{4+}	N
d^4	HS $(t_{2g})^3 (e_g)^1$ LS $(t_{2g})^4 (e_g)^0$	Mn^{3+}, Cr^{2+}	Y Y
d^5	HS $(t_{2g})^3 (e_g)^2$ LS $(t_{2g})^5 (e_g)^0$	Mn^{2+}, Fe^{3+} Co^{IV}	N Y
d^6	HS $(t_{2g})^4 (e_g)^2$ LS $(t_{2g})^6 (e_g)^0$	 Co^{III}, Ni^{IV}	Y N
d^7	HS $(t_{2g})^5 (e_g)^2$ LS $(t_{2g})^6 (e_g)^1$	 Co^{II}, Ni^{III}	Y Y
d^8	$(t_{2g})^6 (e_g)^2$	Cu^{3+}, Ni^{2+}	N
d^9	$(t_{2g})^6 (e_g)^3$	Cu^{2+}	Y

1.4.3 Characteristics of $LiCoO_2$ as cathode material in lithium rechargeable battery

Easy to prepare, $LiCoO_2$ (a = 2.82, c = 14.08 Å) is mainly used for the cathode in present rechargeable lithium ion batteries. The lithium ions (de)intercalate into the van de Waals gap between CoO_2 layers in the 3a sites (Figure 1.7). Structural changes take place during lithium (de)intercalation and this process does not correspond to a simple continuous solid solution [65]. The reaction in fact proceeds in a topotactic manner, *i.e.*, two-phase reactions and single-phase reactions.

Within the composition range $0.9 < x < 1$ in Li_xCoO_2, a single hexagonal phase exists, whereas within $0.78 < x < 0.9$, two hexagonal phases coexist giving way to a region, $0.51 < x < 0.78$ within which the second hexagonal phase exists alone. On further removal of lithium a monoclinic distortion of this second phase is observed for compositions in the narrow range $0.46 < x < 0.51$. Below $x = 0.46$ an hexagonal phase is present until the composition $Li_{0.22}CoO_2$ is reached whereupon a second monoclinic phase appears coexisting with the hexagonal phase until the composition $Li_{0.18}CoO_2$ is obtained, at which point the monoclinic phase exists alone. Below $x = 0.15$ another hexagonal phase appears corresponding to the fully delithiated and stable CoO_2. This last layered cobalt dioxide is found isostructural to TiS_2 (CdI_2 structure). Since new phase in $Li_{1-x}CO_2$ appears near $x = 0.5$, cycling is performed usually for *x*-values $0 < x < 0.5$. During these structural changes, the a parameter changes little, but the c-axis changes from 14.1 to 14.6 Å with lithium deintercalation.

In the early stages of this work, the conventional materials of $LiCoO_2$, $LiNi_{0.7}Al_{0.3}O_2$ and $LiMn_2O_4$ were synthesised and cycled in order to verify the method of preparation of the positive electrodes. The conditions of their synthesis together with the first charge and discharge curves of Li/Li_xCoO_2, $Li/Li_xNi_{0.7}Al_{0.3}O_2$, $Li/Li_xMn_2O_4$ at current density of 0.3 $mAcm^{-2}$ between 3 and 4.25 V are reported at Figure 1.9. The lithium (de)insertion in these three compounds takes place at potential around 4 V.

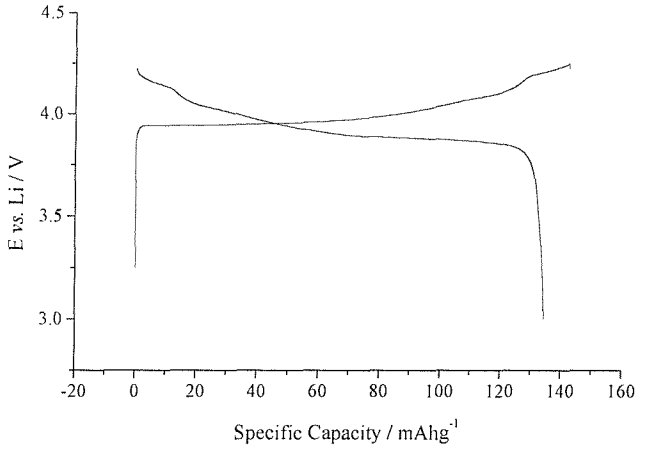

Solid state synthesis in air of $LiCoO_2$ from Li_2CoO_3 and Co_3O_4 for 5 hours at 650° C then sintered at 900 °C

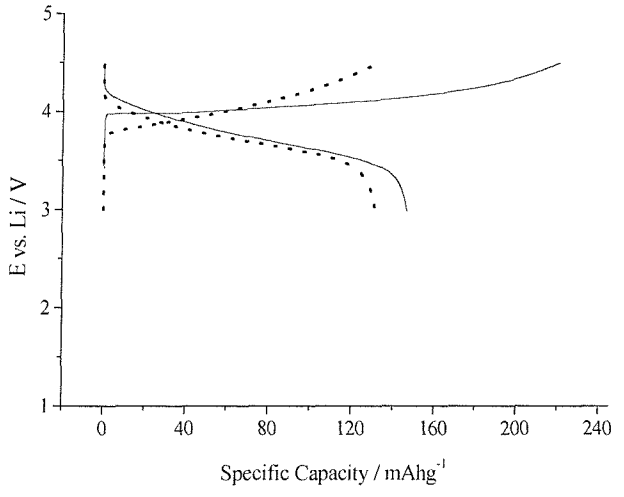

Synthesis in oxygen of $LiNi_{0.7}Al_{0.3}O_2$ from Li_2O_2,NiO and Al_2O_3 at 700° C. The dash curve represents the 5^{th} cycle

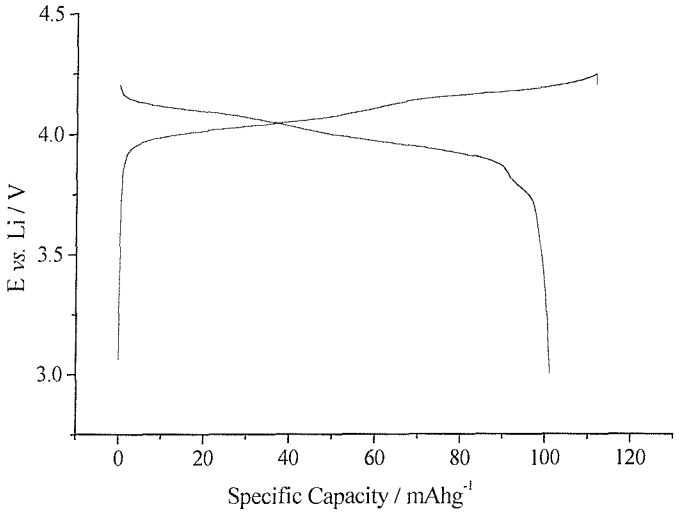

Solid state reaction in air of $Li_{1.03}Mn_2O_4$ from Li_2CO_3 and MnO_2 at 750° C

Figure 1.9 First charge-discharge curves of Li/Li_xCoO_2, Li/$Li_xNi_{0.7}Al_{0.3}O_2$, Li/$Li_{1.03}Mn_2O_4$ cells at current density of 0.3 $mAcm^{-2}$ between 3 and 4.25 V. Electrolyte 1 M $LiPF_6$ in EC/DMC (1:1 volume ratio).

The charge-discharge curve of $LiCoO_2$ shows a good specific discharge capacity of 135 $mAhg^{-1}$ (theoretical 274 $mAhg^{-1}$) and small initial capacity loss. $Co^{4+/3+}$ gives rise to a high potential >4 V vs. Li^+/Li couple. As seen in section 1.3.2.3, the electronic structure of $LiCoO_2$ has an influence on the voltage its provides. In this structure, the Fermi level is very low since Co^{3+} ($3d^6$) adopts a low-spin configuration (t_{2g}^6 eg^o) in an octahedral oxygen environment [66]. This leads to an increase of the voltage against lithium. The extraction of lithium from between the layers is facile with a lithium chemical diffusion coefficient of 5×10^{-8} cm^2 s^{-1} for $Li_{0.65}CoO_2$ [67].

1.4.4 Characteristics of $LiNiO_2$ as cathode material in lithium rechargeable battery

The structure of $LiNiO_2$ is identical to $LiCoO_2$ (Figure 1.7). In contrast to $LiCoO_2$, it can not be prepared as a stoichiometric material but instead formula like $Li_{1-x}Ni_{1+y}O_2$ are obtained (Li_2O_2 + NiO in oxygen at 700 °C), the best electrochemical performance being obtained from materials close to the stoichiometric composition.

The Jahn-Teller distortion arises now from Ni^{3+} (low spin d^7 configuration) and is a factor of instability. In fact the removal of lithium results in three single-phase reactions and a two-phase reaction; the formation of rhombohedral solid solutions within the composition ranges $0.85 < x < 1$, $0.32 < x < 0.43$ and between $x = 0.50$ and $x = 0.75$ a single monoclinic phase is observed. $Li_{0.5}NiO_2$ transforms on heating to a cubic spinel $Li[Ni_2]O_4$ which has for effect to reduce the Li^+ ion mobility and the conductivity. Over the range x = 0-0.32 a mixture of two rhombohedral phase exists, one of then being NiO_2 ($CdCl_2$ structure type) [68-70].

The low-spin configuration d^7 leads to fully occupied t_{2g} levels and one electron in the e_g orbital. The location of the Fermi level in the higher energy e_g orbital, compared with the lower energy t_{2g} of the cobalt compound, results in an average voltage several hundred meV lower for Li_xNiO_2. Specific capacity of 150-160 $mAhg^{-1}$ depending on the rate of charge/discharge is obtained over the range $0.3 < x < 0.9$. Although structural changes exist, the chemical diffusion for Li deintercalation is very high, equal to 10^{-7} cm^2 s^{-1} [71].

The $Li_xNi_{0.7}Al_{0.3}O_2$ material was found to have similar electrochemical characteristics than $LiNiO_2$ (figure 1.9). The initial discharge capacity is found however to decrease with the Al dopant (180 mAg^{-1} for $LiNiO_2$). The loss due to irreversible capacity at the first cycle is

found to be smaller for $LiCoO_2$ and maximum for $LiNi_{0.7}Al_{0.3}O_2$ due the instability of the electrolyte in contact of $LiNi_{0.7}Al_{0.3}O_2$ material at high voltage. The polarisation is also found bigger for $LiNi_{0.7}Al_{0.3}O_2$.

In order to improve on the properties of $LiNiO_2$ or take the advantages of the lower cost of this material, substitution of nickel by other ions has been developed such as the solid solutions of $Li(Ni_{1-x}Co_xO_2)$ [72], cheaper than $LiCoO_2$ with many of its advantages. $LiNi_{0.85}Co_{0.25}O_2$ (provided by Matsushita) has been cycled and its capacity increases to about 185 $mAhg^{-1}$ (130 $mAhg^{-1}$ for $LiCoO_2$) and is developed to form the next-generation cathode, after $LiCoO_2$ (Figure 1.10).

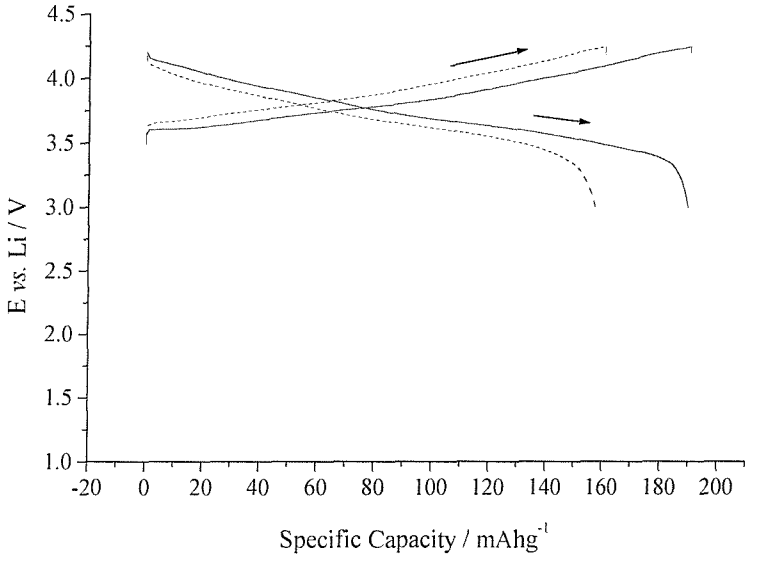

Figure 1.10 Charge-discharge curves (first and fifth) of $Li/Li_xNi_{0.85}Co_{0.25}O_2$ (Matsushita) cell at current density of 0.3 $mAcm^{-2}$ between 3 and 4.25 V. Reaction between $Ni(OH)_2$, $Co(OH)_2$ and LiOH. Electrolyte 1 M $LiPF_6$ in EC/DMC (1:1 volume ratio).

1.4.5 Structural stability of lithium manganese oxides

Manganese oxides exist in a large variety of structures (Table 1.3) that display tunnel and layered frameworks consisting of MnO_6 octahedral units shared by corners and/or edges. As an example, mineralogical manganese oxides exist in different forms: the tetragonal rutile-type pyrolusite β-MnO_6 (in which MnO_6^{8-} share two edges), the orthorhombic ramsdellite (in which MnO_6^{8-} share four edges), psilomelane and the monoclinic romanechite , etc. Synthetic manganese dioxides prepared by either electrolytic (EMD) or chemical (CMD) method belong to the nsutite (γ-MnO_2) group.

Manganese dioxides were originally developed in Leclanché cell and then as positive electrode materials for primary cells. They showed interesting properties as cathodic materials for rechargeable lithium batteries [73]. Since then, lithium insertion into various forms of MnO_2 have been carried out (e. g. γ-MnO_2 [74], spinel $LiMnO_4$ [75]).

Lithium insertion reactions in MnO_2 exhibit voltage of ~3 V corresponding to the energy of lithium on octahedral sites. Also the insertion feature at 4 V in λ-MnO_2 reflects the energy of the tetrahedral sites [76]. They show in general reversible capacities of 120-150 $mAhg^{-1}$ depending on the preparation route with the best performance for α-MnO_2 (150 $mAhg^{-1}$ after 120 cycles).

All MnO_2 structures can be described as a distribution of cations Mn^{4+} (having a small ionic radius of 0.53 Å) in the interstices of a more or less close-packed network of oxygen atoms. The manganese dioxides can be classified according to the nature of the polymerisation of MnO_6 octahedra chains between two basal layers to form (n×m) tunnels openings [77]. The various structures of the lithium manganese oxides are also listed in Table 1.3 [78].

Table 1.3 Crystallographic data of some Mn-O compounds.

Compounds	Mineral	Crystal Symmetry	Lattice parameters	Features
MnO	manganosite	cubic (F*m3m*)	a = 4.44	rock-salt
α-MnO_2	hollandite (cryptomelane)	tetragonal (I*4/m*)	a =9.81, c = 2.85	(1×1)/(2×2) tunnels
R-MnO_2	ramsdellite	orthorhombic (P*bnm*)	a = 4.53, c = 9.27 c =2.87	(1×2) tunnels
β-MnO_2	rutile (pyrolusite)	tetragonal (P*4/mnm*)	a= 2.39, c =2.87	(1×1)tunnels
γ-MnO_2 (ε-MnO_2)	nsutite	rutile and ramsdellite domains	a = 9.65, c = 4.43	(1×1)/ (1×2)tunnels randomly dispersed
δ-MnO_2	vernadite	hexagonal	a = 2.86, c = 4.7	(1×∞)layers
λ-MnO_2	spinel	cubic (F*d3m*)	a = 8.04	(1×3)tunnels
MnO_x-H_2O	birnessite	hexagonal	a = 2.84, c = 14.64	(1×∞)layers
$LiMn_2O_4$	spinel	cubic (F*d3m*)	a = 8.25	(1×3)tunnels
	spinel related	tetragonal ($I4_1/amd$)	*a =5.44, c=2.81	
$Li_2Mn_2O_4$ (T-$LiMnO_2$)	spinel related	tetragonal ($I4_1/amd$)	a =5.64, c=9.31	(1×3)tunnels
C-$LiMnO_2$	spinel related	cubic	a = 4.16	
α-$LiMnO_2$ (M-$LiMnO_2$)		monoclinic(C*2m*)	a =5.44, b =2.81 c =5.39, β= 116.0	layers
β-$LiMnO_2$ (O-$LiMnO_2$)		orthorhombic (P*mnm*)	a = 2.81, b = 6.31	corrugated layers
MnO(OH)	manganite	monoclinic (B $2_1/d$)	a = 8.86, b = 5.24 c =5.70, β= 90.0	
α-Mn_2O_3	bixbyite	cubic (I*a3*)	a = 9.41	C-type
Mn_3O_4	hausmannite	tetragonal ($I4_1/amd$)	a = 9.81, c= 2.85	spinel

1.4.5.1 Characteristics of $LiMnO_2$ as cathode material in lithium rechargeable battery

Li-Mn-O compositions do not readily form layered $LiCoO_2$-type structure due to the Mn^{3+} ($3d^4$ high spin) Jahn-Teller active cations causing distortion of the MnO_6 octahedron and reducing the symmetry. As mentioned in the previous classification, $LiMnO_2$ exists under four polymorph phases: orthorhombic [79], monoclinic [80], low temperature and high temperature tetragonal phases [81,82].

1.4.5.1.1 Orthorhombic $LiMnO_2$ (O-$LiMnO_2$)

The structure consists of corrugated layers as in β-$NaMnO_2$ (see 1.4.1.4). O-$LiMnO_2$ exists both in a low-temperature modification with an initial charge capacity close to 230 $mAhg^{-1}$ [83] and in a high temperature modification with an initial charge capacity of 150 $mAhg^{-1}$ [84]. Upon cycling, the material is unstable towards lithium extraction and transform into spinel-like materials [85].

1.4.5.1.2 Layered monoclinic $LiMnO_2$ (M-$LiMnO_2$)

This material, reported by Armstrong and Bruce [80], is isostructural with $LiCoO_2$ and is not thermodynamically stable at temperatures above 300 °C. However it can be prepared by ion exchange from isostructural α-$NaMnO_2$ in *n*-hexanol at 150 °C [80] or in ethanol at 64 °C [86].

Electrochemical tests of M-$LiMnO_2$ showed initial capacities up to 250 $mAhg^{-1}$ for lithium extraction in the first charge to 4.7 V *vs* Li. Lithium extraction and reinsertion into the layered M-$LiMnO_2$ was not found to be reversible. Further cycling in this range is accompanied by a rapid deterioration of the capacity, a collapsing of the layer structure followed by a gradual transformation into a spinel-like material [87] without reaching the capacity of the pure spinel material.

More recently solid solutions of $LiMn_{1-x}Co_xO_2$ with hexagonal symmetry ($R\bar{3}m$) were obtained using ion-exchange route [88,89]. Substituting as little as 2.5% suppresses the distortion and yields a capacity of 200 $mAhg^{-1}$ with good capacity retention and conversion to a nanostructured spinel-like phase.

1.4.5.1.3 Tetragonal $Li_2Mn_2O_4$ (T-$LiMnO_2$)

Low temperature T-$LiMnO_2$ is the phase resulting from lithium intercalation into the lithium manganese spinel. It can be prepared from $LiMn_2O_4$ by electrochemical and chemical lithiation in molten LiI at 460 °C [90] or with *n*-butyl lithium [91] or LiI [92] in CH_3CN at temperature below 100 °C. They show ordered rock salt structure with both manganese and lithium ions occupying octahedral sites.

The electrochemical properties for the material prepared at 100 °C shows capacity of 260 $mAhg^{-1}$ on initial extraction, with however a fast loss of capacity due to the deterioration of the electrode material upon cycling [85].

High temperature T-$LiMnO_2$, prepared by reaction of O-$LiMnO_2$ with Li_2CO_3 at 1000 °C [93] shows similar charge capacity. The deterioration of the electronic contact between the electrode particles is causing a fast loss of capacity during the cycling.

1.4.5.2 Characteristics of $LiMn_2O_4$ as cathode material in lithium rechargeable battery

1.4.5.2.1 Spinel ($MgAl_2O_4$) related structures

The spinel-type structure will form, with appropriate ion size and valence of the transition metal, in the cubic space group F*d3m*, where oxygen ions in *32e* take cubic oxygen packing and cations can reside in tetrahedral *8a*, and octahedral *16c* and *16d* sites (Figure 1.11). The chemical formula of such structures can be written as $A[B_2]O_4$ where A is the ion on the tetrahedral position and *B* is the ion on the octahedral position, denoted by square brackets. If *A* is a divalent and *B* is a trivalent cation, two extreme distributions of cations among the variable sites are possible: the normal $A[B_2]O_4$ and the inverse $B[BA]O_4$ distribution. The cation distribution is determined by composition, ionic charge, ionic radius, crystal and ligand field effects and anion polarization [94]. For example, the ferrites of general formula MFe_2O_4 ($Fe^{3+}[M^{2+}Fe^{3+}]O_4$) are inverse spinel whereas Mn_3O_4 ($Mn^{2+}[Mn^{3+}]_2O_4$), $MnCo_2O_4$ have a direct spinel structure due to the indifferent d^5 electronic structure of Mn^{2+} which is also stable in an tetrahedral environment.

In the lithium manganese oxide system, the cations with valence 1-4 may form a direct spinel structure $LiMn_2O_4$ since the lithium ions take preference for the tetrahedral sites.

The spinel-like manganese oxides and their characteristics are summarised at Table 1.4.

Table 1.4 Electrode characteristics of lithium manganese oxide spinel-type compounds. *The indice in subscript for the capacities represents the cycle number.

Compound	Insertion range	Electrode voltage *vs.* Li/V	Calculated Capacity/mAhg^{-1}	*Observed Capacity/ mAhg^{-1}
$Li_{2+x}Mn_4O_9$ x = 0	x = 0-3	3 and 4	202 at x = 3	175_1, 170_{10}
$Li_{4+x}Mn_5O_{12}$ x = 0	x = 0-3	3	156 at x = 3	145_1, 150_{10}
$Li_xMn_2O_4$ x = 1	x = 0-1 x = 1-2 x = 2-2.5	4 3 1.5	148 at x = 1 143 at x = 2	140_1, 110_{100} 130_1, 86_{30} 74_1, 50_5
$Li_xMn_2O_{4.14}$ x = 1.04	x<1	4	148	112_1, 110_{100}
$Li_xMn_2O_4$ x = 1.03	x <1	4	148	134_1, 128_{90}
$Li_xMn_2O_4$ x = 0	x = 0-1.5	1-3	114 at x = 1	171

The lithium manganese oxides possess average oxidation states in range from +4 to +2.66. Mn (IV) is present in the first oxides $Li_2Mn_4O_9$ ($Li_{0.89}Mn_{1.78}O_4$) and $Li_4Mn_5O_{12}$ ($Li[Li_{0.16}\ Mn_{0.84}]_2O_4$) prepared at 400°C in air and at 500-700 °C in oxygen, respectively. Insertion of ~0.75 Li/Mn is possible and the materials exhibit voltages in the 3 V region as octahedral 16*c* sites are entered. The elevated oxidation state of Mn provides minimised lattice volume expansion as Jahn-Teller distortion is suppressed in both lithiated compounds [95]. Due to the difficulty of preparing homogeneous materials, their application in 3 V lithium is limited.

The normal spinel $LiMn_2O_4$ has been the most attractive material offering high voltage and rather good capacity retention. A description of its structure and electrochemical properties is presented in the following paragraph.

1.4.5.2.2 $LiMn_2O_4$

As described previously, $LiMn_2O_4$ [47-49] is a three-dimensional host with a spinel-like structure (space group Fd3m) consisting of cubic close-packed oxide ions with Mn in one half of the octahedral sites and Li^+ in one eighth of the tetrahedral sites within the cubic close-packed oxide array. Tunnels formed by the face-sharing of tetrahedral lithium (8a) and empty octahedral (16c) sites intersect in three dimensions and support rapid lithium diffusion (Figure 1.11). Half of the octahedrally coordinated manganese ions are Mn^{3+} (high spin $3d^4$, $t_{2g}^3e_g^1$) and half Mn^{4+}. Mn^{3+} being Jahn-Teller active (section 1.4.1), causes distortion of the structure during the cycling.

On inserting lithium into octahedral (16c) sites of $Li_xMn_2O_4$ at 3 V, the Mn^{4+} is reduced to Mn^{3+} which promotes a cooperative Jahn-Teller distortion of the octahedral sites to tetragonal symmetry (12% expansion along the *c*-axis) and the nucleation of a second phase of $Li_2Mn_2O_4$. Until x = 2, the cubic and tetragonal spinels coexist, the former phase converting to the latter. This transition causes a deterioration in the cyclability due mainly to the accumulation of unintercalated $LiMn_2O_4$ at the end of the discharge [26].

In the 4 V regime within which lithium is extracted from the 8a sites in $Li_{1-x}Mn_2O_4$, a continuous range of solid solutions for $0 < x < 0.5$ occurs [47,48] followed by the coexistence of two spinel phases of composition x = 0.5 and x = 1. This corresponds to two plateaux separated by ~0.1 V observed in the charge-discharge curve at 4 V (Figure 1.9 p 24).

The loss of capacity in the 4 V region is now due to poor particle contact in the $0.5 < x < 1$ range [96], electrolyte decomposition at high voltage [97] and Mn^{2+} dissolution in the electrolyte [98,99].

In Figure 1.9 is shown the charge-discharge curve of $Li_{1.03}Mn_2O_4$ obtained from the *Matsushita* company (Japan) in which the manganese is replaced by lithium on the 16 d octahedral sites. The cycling shows less than 6% loss of capacity during the first charge.

Replacement of the manganese by a non Jahn-Teller element, e.g. Cr [100], Fe [101], Co [102,103], Ni [104], Cu [105] shows also improved performance by limiting the presence of two phases during the delithiation in the 3 V region. This however happen at the expense of the discharge capacity.

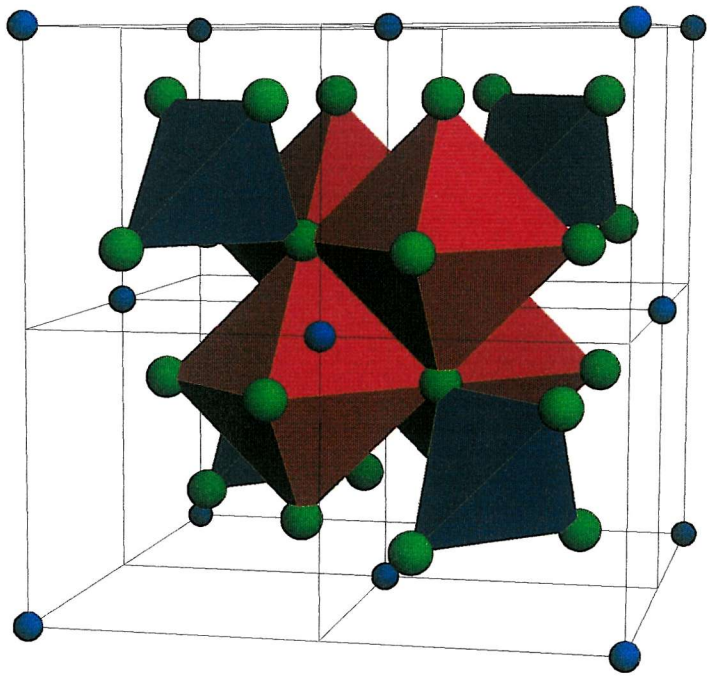

Figure 1.11 Spinel structure showing the octahedral sites (in red) and tetrahedral (in blue) occupied by manganese and lithium respectively . The oxygens are shown in green and the lithiums in blue.

1.5 Scope of this work

There has been a significant amount of work published concerning the electrochemistry (anode materials, electrolyte, electrodes...) of the rechargeable lithium battery. Advances in solid-state chemistry were crucial for the achievement of the success they had in lightweight and portable sources of electricity. The structures of the 2-D layered $LiCoO_2$ and the 3-D spinel $LiMn_2O_4$ have attracted most of the attention since they offer good properties as insertion cathode materials. So far the optimisation of the cathode performances was often based on the design of new compounds having similar structures (*e.g.* $LiNiO_2$, $LiMnO_2$) or resulting from substitution by other transition metals (*e.g.* $LiMn_{1-x}Co_xO_2$, $LiMn_{2-x}M_xO_4$ M =Cr, Fe, Co, Ni, Cu).

In this work, the intention is to investigate in the less studied system Li-Cu-O, the properties of the couple Cu(II)/Cu(III). The work in chapters three and four centres on the preparation and electrochemical characterisation of the lithium copper oxides.

The second area of interest was the syntheses by lithium ion exchange of lithium manganese oxides containing high oxidation state of manganese which could lead to improved electrochemistry towards lithium. Chapters five and six cover the influence of syntheses on the composition, structure and thus electrochemical properties of the resulting lithium manganese oxides.

1.6 References

[1] *CRC Handbook of Solid State Electrochemistry*. Eds. P. J. Gellings and H. J. M. Boumesster, CRC Press. Inc., USA, (1997).

[2] J. R. Owen, *Chem. Soc. Rev.*, **26** (1997) 259.

[3] Z. X. Shu, R. C. McMillan, J. J Murry, *J. Electrochem. Soc.*,**140** (1993) 922.

[4] J. M. Tarascon, D. Guyomard, *Electrochim. Acta*, **38** (1993) 1221.

[5] T. Ohzuku, Y. Ywakoshi, K. Swai, *J. Electrochem. Soc.*, **140** (1993) 2490.

[6] Recent Advances in Rechargeable Li Batteries, *Solid Sate Ionics*, **69** (1994) 4.

[7] *Battery handbbook,* Eds. M. N. Takami and T. Takamura, Asakura Shoten, Tokyo, (1996) 787.

[8] E. Peled, D. Golodnitsky, G. Arfel, *J. Solid State Chem.*, **3** (1993) 229.

[9] J. O. Besenhard, J. Yang, M. Winter, *J. Power Sources*, **68** (1997) 87.

[10] J. Yang, Y. Takeda, N. Imanishi, T. Ichikawa, O. Yamamoto, *Extented Abstracts, SSI-12*, Halkidiki, Greece, A-31 (1999) 88.

[11] N. Nagayama, T. Morita, H. Ikuta, M. Wakihara, M. Takano, S. Kawasaki, *Solid State Ionics*, **106** (1998) 33.

[12] A. Whitehead, J. M. Elliot, J. R. Owen, *J. Power Sources*, **81** (1999) 33.

[13] M. Wakihara, T Morita, A. Modeki, H. Ikuta, *Extended Abstracts, SSI-12*, Halkidiki, Greece, A-34 (1999) 92.

[14] H. Kim, Y. J. Kim, D. G. Kim, H. J. Sohn, T. Kand, B. Park, *Extended Abstracts*, Como Italy, (200) 78.

[15] P. A. Connor, F. Belliard, M. Behn, J. T. S Irvin, *Extented Abstract, SSI-12*, Halkidiki, Greece, A-29 (1999) 85.

[16] S. Denis, E. Baudrin, F. Orsini, G. Ouvrard, M. Touboul, J. M. Tarascon, *J. Power Sources*, **81/82** (1999) 79.

[17] S. S. Kim, H Ikuta, M. Wakihara, *Solid State Ionics*, **139** (2001) 57.

[18] M. Arakawa, J. Yamaki, *J. Electroanal. Chem.*,**219** (197) 273.

[19] P. G. Bruce, *Philos. Trans. R. Soc. London A*, **354** (1996) 415.

[20] P. V. Wright, *Br. Polymer. J.*, **7** (1987) 273.

[21] M. B. Armand, J. M. Chabano, M. J. Duclot in: *Fast Ions Transport in Solids*, North Holland, New York, (1979) 131.

[22] D. F. Shriver, G. C. Farrington, *Chem. Eng. News*, **20** (1985) 42.

[23] J. F. Le Nest, S. Callens, A. Gandini, M. B. Armand, *Electrochim. Acta*, **37** (1992) 1585.

[24] A. Nishimoto, M. Watanabe, Y. Ikeda, S. Kohjiya, *Electrochim. Acta*, **43** (1998) 1177.

[25] G. Feuillard, P. Perche, *J. Appl. Electrochem.*, **5** (1975) 63.

[26] P. G. Bruce, *Chem Comm.*, (1997) 1817.

[27] A. N. Dey, *J. Electrochem.* Soc., **18** (1971) 1547.

[28] *Handbook of Batteries*, 2nd ed., Ed. D. Linden, New York (1995).

[29] P. Poks, M. Grzesczuckzuk, *Polish J. Chem.*, **71** (1997) 1140.

[30] K. Naoi, K. Ueyama, T. Osaka, W. H. Smyrl, *J. Electrochem.* Soc., **137** (1990) 494.

[31] M. S. Whittingham, *Prog. Solid State Chem.*, **12** (1978) 41.

[32] M. S. Whittingham, *Prog. Solid. State Chem.*, **12** (1976) 315.

[33] W. R. Mc Kinnon in : *Solid State Electrochem.*, Ed. P. G. Bruce, Cambridge University Press, (1995) 173.

[34] H. Arai, S. Okada, Y. Sakurai, J. Yamaki, *Solid State Ionics*, **106** (1998) 45.

[35] A. N. Dey, B.P. Sullivan, US. Pat. 3,655,585, (1972).

[36] R. J Cava, A. Santoro, D. W. Murphy, S. M. Zahurak, R. M. Fleming, P. Marsh, R. S. Roth, *J. Solid State Chem.*, **65** (1996) 63.

[37] K. West, B. Zachau-Christiansen, T. Jacobsen, S. Skaarup, *Electrochim. Acta*, 38 (1993) 1215.

[38] K. West, B. Zachau-Christiansen, M. J. L. Ostergård, T. Jacobsen, *J. Power Sources*, **20** (1987) 165.

[39] R. Kanno, T. Shirane, Y. Kawamoto, Y. Takeda, M. Takano, M. Ohashi, Y. Yamaguchi, *J. Electrochem. Soc.*, **143** (1996) 2435.

[40] K. Mizushima, P. C. Jones, P. J. Weiseman, J. B. Goodenough, *Mater. Res. Bull.*, **15** (1980) 783.

[41] J. B. Goodenough, K. Mizushima, T. Takeda, *Proceedings of the 4th Int. Conference on Ternary and Multinary Compounds*, Tokyo, (1980).

[42] Ohzuku, H. Komori, M. Nagayama, K. Sawai, T. Hirai, *J. Ceram. Soc. Jap.*, **100 (3)**, (1992) 346.

[43] L. Croguennec, P. Deniard, R. Brec, *J. Electrochem. Soc.*,**144** (1997) 3323.

[44] A. R. Armstrong, P. G. Bruce, *Nature*, **381** (1996) 499.

[45] N. Koshiba, K. Takata, M. Nakanishi, E. Asaka, Z. Takehara, *Denki Kagaku*, **62** (1994) 870.

[46] K. West, B. Z. B. Zachau-Christiansen, T. Jacobsen, S. Atlung, *J. Power Sources*, **14** (1985) 231.

[47] M. M. Thackeray, W. I. F. David, P. G. Bruce, J. B. Goodenough, *Mat. Res. Bull.*, **18** 1983) 461.

[48] M. M. Thackeray, J. P. Johnson, L. A. de Picciotto, W. I. F. David, P. G. Bruce, J. B. Goodenough, *Mat. Res. Bull.*, **19** (1984) 179.

[49] J. B. Goodenough, M. M. Thackeray, W. I. F. David, P. G. Bruce, *Rev. Chim. Miner.*, **21** (1984) 435.

[50] *Handbook of Inorganic Electrochromic Materials*, Ed. C. Granqvist, Elsevier Sciences, Amsterdam, (1995).

[51] C. Bohnke, O Bonhke , *J. Aplied Electrochem.*, **18** (1988) 715.

[52] *Solid State Electrochemistry*, Ed. P. G. Bruce, Cambridge University Press, Cambridge, (1995).

[53] *Intercalation chemistry*, Ed. A. J. Jacobson and M. S. Whittingham, Academic Press, New York, (1982).

[54] A. M. Chippindale, P. G. Dickens and A. V. Powell, *Prog. Solid. State Chem.*, **21** (1991) 133.

[55] C. Sigala, D. Guyomard, A. Verbaere, Y. Piffard and T. Tournoux, *Solid State Ionics*, **81** (1995) 167.

[56] Japan Electronics, March 6th, 1996

[57] G. C. Mather, C. Dussarrat, J. Etourneau, A. R. West, *J. Mat. Chem.*,**10** (2000) 2219

[58] J. C. Anderson, M. Schreiber, *J. Phys. Chem. Solids*, **25** (1969) 961.

[59] R. Hope, B. Shepers, *Z. Anorg. Allg. Chem.*, **295** (1958).

[60] K. Kobayashi, K. Kosuge, S. Kachi, *Mater. Res. Bull.*, **4** (1969) 95.

[61] W. Rudorff, H. Becker, *Z. Naturforsch*, **9** (1954) 614.

[62] W. D. Johnston, R. R Heikes, D. Sestrich, *J. Phys. Chem. Solids*, **7** (1958) 1.

[63] J. B. Goodenough, D. G Wickham, W. J. Croft, *J. Appl. Phys.*, **29** (1958) 382.

[64] C. Fouassier, P. Hagenmuller, *J. Solid State Chem.*, **3** (1971) 1.

[65] G. G. Amatucci, J. M. Tarascon, L. C. Klein, *J. Electrochem. Soc.*, **143** (1996) 1114.

[66] M. Shibuya, T. Nishima, T. Matsue, I. Uchida, *J. Electrochem. Soc.*, **143** (1996) 3157.

[67] M. G. R. S Thomas, P. G. Bruce, J. B. Goodenough, *Solid State Ionics*, **17** (1985) 13.

[68] W.Li, J. N. Reimers, J. R. Dahn, *Solid State Ionics*, **67** (1993)123.

[69] T. Ohzuku, A. Ueda, N. Nagayama,, *J. Electrochem. Soc.*, **140** (1993) 1862.

[70] M. M. Tackeray, *J. Electrochem. Soc.*, **142** (1995) 2558.

[71] P. G. Bruce, A. Lisowka-Olelsial, M. Y. Saisi, C. A. Vincent, *Solid Sate Ionics*, **57** (1992) 353.

[72] C. Sodoune, C. Delmas, *Solid State Ionics*, **53-56** (1992) 370.

[73] L. Li, G. Pistoia, *Solid State Ionics*, **47** (1991) 231.

[74] S. Sarciasux, A. Le Gal La Salle, A. Verbaere, Y. Piffard, G. Guyomard, *Mat. Res. Soc. Symp. Proc.*, **548** (1999) 251.

[75] J. M. Tarascon, G. Guyomard, *J. Electrochem. Soc.*, **138** (1991) 2864.

[76] B. Zachau-Christiansen, K. West, T. Jacobsen, S. Atlung, *Solid State Ionics*, **40-41** (1990) 580.

[77] S. Turner, P. R. Buseck, *Sciences*, **212** (1981) 1024.

[78] C. Julien, M. Massot, , *Conference on New trends in Intercalation Compounds for Energy Storage*, NATO-ASI, Bulgaria, Sept (2001).

[79] R.Hoppe , G. Brachtel , M. Jansen, *Z Anorg. Allg. Chemie,* **1** (1975) 417.

[80] A. R. Armstrong, P. G Bruce., *Nature,* **381** (1996) 499.

[81] M. M. Thackeray, W. I. F David, P. G. Bruce., Goodenough, J.B., *Mat. Res. Bull.*, **18** (1993) 461.

[82] Reimers J. N., Falkner T., Bonakdarpour A.B., in : *Abstract in the Electrochemical Society Meeting*, **95 (2)** (1995) N° 95.

[83] J. N. Reimers, E. W. Fuller, E. Rossen, J. R. Dahn, *J. Electrochem. Soc.*, **140** (1993) 3396.

[84] I. J. Davidson, R. S. Mc Millan, J. J. Murray, J. E. Greedan, *J. Power Sources*, **54** (1995) 3396.

[85] G. Vitins, Chem. Thesis Proposal, University of Riga, Latvia, (1999).

[86] F. Capitaine, P. Gravereau, C. Delmas, *Solid State Ionics*, **89** (1996) 197.

[87] G. Vitins, K. West, *J. Electrochem. Soc.*, **144** (1997) 2587.

[88] A. R. Armstrong, A. D. Robertson, R. Gitzendanner.; P. G. Bruce, *J. Solid State Chem.*, **145** (1999) 549.

[89] A. D. Robertson, A. R. Armstrong , A.J. Fowkes, P. G. Bruce, *J. Mater. Chem.*, **11** (2001) 113.

[90] B. Fuchs, S. Kemmler-Stack, *Solid State Ionics*, **68** (1994) 279.

[91] A. Mosbah, A. Verbaere, M. Tornoux, *Mat. Res. Bull.*, **18** (1983) 1375.

[92] J. M. Tarascon, D. Guyomard, *J. Electrochem. Soc.*, **138** (1991) 2864.

[94] P. Porta, F. S Stoue, R. G. Turner, *J. Solid State Chem.*, **11** (1974) 135.

[95] A. de Kock, M. H. Rossouw, A. de Picciotto, M. M. Thackeray, W. I. F David, R. M. Ibberson, *Mat. Res. Bull.*, **25** (1990) 657.

[96] Y. Xia, M. Yoshio, *J. Electrochem. Soc.*,**143** (1996) 825.

[97] G. Pistoia, A. Antoni, R. Rosati, D. Zane, *Electrochim. Acta*, **41** (1996) 2683.

[98] J. M. Tarascon, W. R . McKinnon, F. Coowar, T. N. Bowmer, G. Amatucci, D. Guyomard, *J. Electrochem. Soc.*,**141** (1994) 1421.

[99] R. J. Gummow, A. de Kock, M. M. Thackeray, *Solid State Ionics*, **69** (1994) 59.

[100] C. Sigala, D. Guyomard, A. Verbaere, Y. Piffard, M. Tournoux, *Solid State Ionics*, **81** (1995) 167.

[101] H. Kawai, M. Nagata, M. Tabuchi, H. Tukamoto, A. R West, *Chem Mater.*, **10** (1998) 3266.

[102] H. Kawai, M. Nagata, H. Tukamoto, A. R. West, *J. Mater. Chem*, **8** (1998) 837.

[103] H. Kawai, M. Nagata, H. Tukamoto, A. West, *J. Power Sources*, **81-82** (1999) 67.

[104] Q. Zhong, A. Bonakdarpour, M. Zhang, Y. Gao, J. R. Dahn, *J. Electrochem. Soc.*, **144** (1997) 205.

[105] Y. Ein-Eli, W. F. Howards, *J. Electrochem. Soc.*,**144** (1997) L205.

Chapter 2

Experimental Techniques

2.1 Introduction

Several synthetic methods were used for the preparation of the ternary lithium and sodium transition metal oxides. These can be divided into three main categories under various conditions; the ceramic (in air and under high pressure oxygen of 250 bar at 700 °C), ion exchange from sodium precursor (in solution at 70 °C <T<130 °C) and hydrothermal synthesis (1.5 kbar at T=500 °C). These techniques will be described in this chapter with examples of their use in the work.

The previous methods yields crystalline products and the initial characterisation of the solids synthesised in this work, was carried out using the laboratory powder x-ray diffractometer. Typical data sets were collected over 30 minutes, allowing the products to be identified with reference to the previous work and searches through the JCPDS (Joint committee of Powder Diffraction Studies) data base. Phase purity and cell parameters were also examined in these initial experiments. Materials of more interest were studied in greater details using the full profile Rietveld refinement of PXD data collected over 15 hours. For several samples, where more detailed structural refinement was needed, or information regarding the lighter element (*e.g.* lithium) was required, powder neutron diffraction was carried out.

A variety of other complementary techniques have also been used throughout the work for the chemical characterisation and will be also described. ^{7}Li MASNMR was used to establish the lithium site population within the framework of the lithium copper oxides. The chemical composition of the lithium manganese oxides was determined by flame emission and UV-visible spectroscopy. Scanning electron microscopy has been used to study the morphology of the materials.

The oxides synthesised will be formed into positive composite electrodes according to a dry technique. The cell will be constructed with lithium metal as anode. Electrodes characterisation will involve the measurement of the potential/composition curves by galvanostatic cycling from which, incremental capacity plots (cyclic voltammetry) will be derived. *In-situ* x-ray analysis of the electrode will be performed to reveal any structural changes due to ion insertion. Lithium mass transport will be measured by Intermittent Titration Techniques (GITT and FITT) and the complex impedance techniques will be used to monitor electronic conductivity and to examine the interfacial charge transfer resistance. All these techniques used for the preparation of the cell, constant current cycling, *in-situ* x-ray

analysis, diffusion coefficient measurement, electronic conductivity and ac impedance will be described at the end of this chapter.

2.2 Synthetic methods

2.2.1 Standard ceramic synthesis

The preparation of the material in the solid state by the direct reaction of a mixture of solid starting materials is probably the most widely used method for the preparation of polycrystalline solids in the solid state. Generally the stoichiometric amount of the relevant component metal oxides are combined. Where the oxides are hygroscopic, the carbonate or another oxo-salt which decomposes to the oxide on heating is often used to allow accurate weighting. For example, in the preparation of $LiCoO_2$ (Chapter 1, 1.4.3), stoichiometric amounts of Li_2CO_3 and Co_3O_4 were ground to an intimate mixture with a pestle and mortar, transferred to a crucible and fired in a furnace at 650 °C for 5 hours then sintered at 900 °C.

The reaction process occurs by ion diffusion at particles interface and in reactions between oxides the most mobile ions are normally the cations, as these are usually smaller than the oxide ions. It is these ions that diffuse through the oxides and between reactant blocks. As the rate of diffusion of the reactants is typically very slow, long reaction times are required, however, the rate can be increased by raising the reaction temperature. Enhancement of the reaction rate between solids is also achieved by maximising the number of interfaces at which the reaction can occur. This can be achieved by frequent and thorough grinding of the material to decrease particle size and pelletising the material. The grinding process also aids homogeneity and thus improves the formation of a single phase product.

Where a particular oxidation state or reaction stoichiometry is required, the reaction environment may be controlled using furnace where a particular gas, *e.g.* oxygen/nitrogen is passed over the reaction mixture during heating like in the synthesis of $LiNiO_2$ (Chapter 1, 1.4.4), where the oxygen stream allows the stabilisation of the Ni^{3+}. In the case where components are volatile, the reaction mixture can be sealed in an evacuated quartz tube. In the case of $Li_3Cu_2O_4$, a high pressure oxygen (250 atm) is needed for a pure phase (Chapter 3, 3.3.3.1) at 700 °C. The high pressure rig (Figure 2.1) [1] uses a double vessel system with an inner alumina tube containing a small volume of oxygen surrounded by a s steel vessel containing nitrogen under high pressure. The oxygen pressure, delivered by a compressor is

set at a value slightly higher than that of the surrounded nitrogen allowing a continuous flow of oxygen over the sample.

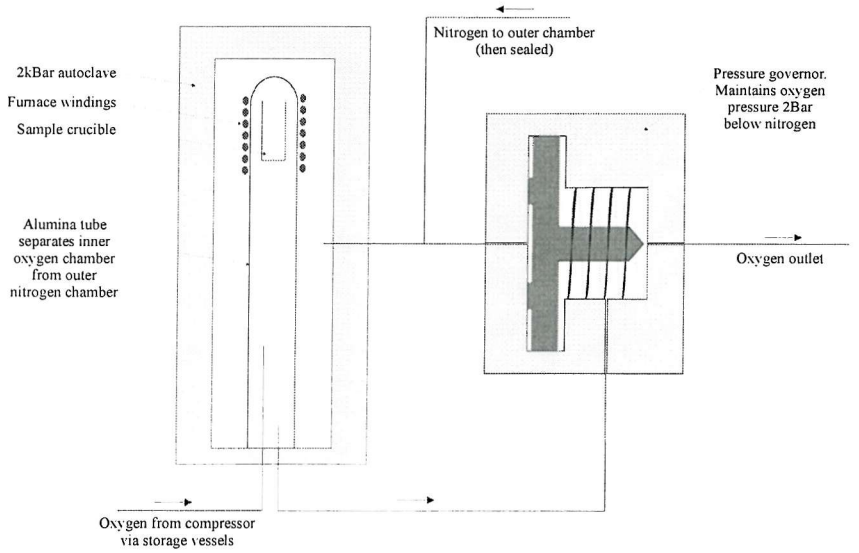

Figure 2.1 Apparatus for annealing samples under high pressure, flowing oxygen.

2.2.2 Lithium ion exchange reaction

This synthesis using Na^+ template for the formation of a layered structure and then the replacement of Na by Li was used at Chapter 5 (5.3.1) for the layered $Na_2Mn_3O_7$. This reaction has been used previously for the preparation of the layered $LiMnO_2$ that was ion exchanged for lithium [2]. The ion exchange conditions were kept the same in both cases and consist of refluxing the sodium compound in a solution of dry lithium bromide in a non-aqueous solvent such as *n*-hexanol (*b.p.* 150 °C) or ethanol (*b.p.* 70 °C) at temperatures close to their boiling points (*b.p.*). The product, a dark brown slurry, was separated and washed with methanol, the best solvent for NaBr. The LiBr salt was found to be well suited for this purpose since it is highly soluble in both solvents *n*-hexanol and ethanol, whereas the NaBr formed in the reaction, is poorly soluble in *n*-hexanol and ethanol but dissolved in methanol. The cage 15-crown-5 ether was sometimes used to facilitate the extraction of NaBr into the solution.

Ion exchange can also be achieved via nitrate melt reactions in which the material is mixed with an excess of the lithium nitrate for instance and heated to a temperature greater than the melting point, typically 240-370 °C, but lower that the boiling or decomposition temperature of the latter material. These reactions were not studied in this work.

2.2.3 Hydrothermal synthesis

Hydrothermal reactions have been carried out using an hydrothermal bomb apparatus pictured at Figure 2.2 [1]. High temperatures, up to 800 °C and pressure up to 1.5 kbar, were achieved. Samples were loaded into a gold capsule and sealed. The capsules were placed into high pressure vessels and a filler rod was added at the top to reduce the bomb volume. The furnace was lowered over the bomb which was opened to the line via a three way offset cross valve which allows the pressure in the bomb to be monitored constantly via a gauge. The reservoir was then opened and the furnace switched on. Once the furnace reached its operating temperature, the pump was used to pomp up the pressure hydrothermally after the reservoir had been closed. The three way valve was then closed and the experiment could proceed for several days.

For the synthesis of $Li_3Cu_2O_4$ (Chapter 3, 3.3.3.1) from the stoichiometric mixture of Li_2O_2, Li_2O and CuO, the temperature was kept at 600 °C and 1.5 kbar.

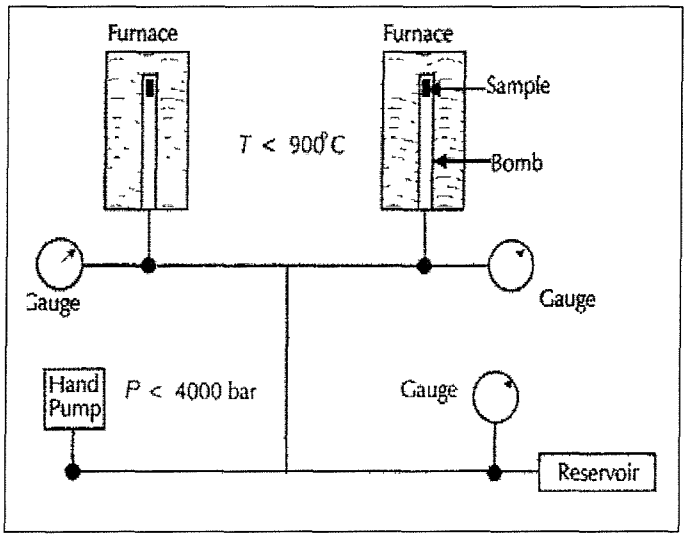

Figure 2.2 Schematic diagram of the hydrothermal apparatus.

2.3 The theory of diffraction

In 1913, shortly after X-rays had been discovered by Wilhelm Röntgen, Max Von Laue suggested that they might be diffracted when passed through a crystal, for their wavelengths are comparable to the separation of lattice planes. The earliest approach to the analysis of diffraction patterns produced by crystals was to regard a lattice plane as a semi-transparent mirror, and to model a crystal as stacks of reflecting lattice planes of separation *d*. Some of the incident radiation is diffracted, while the remainder passes through with the potential of being diffracted by neighbouring planes. This model (Figure 2.3) makes it easy to calculate the angle the crystal must make to the incoming beam of X-rays for constructive interference to occur. The path-length difference of the two adjacent rays shown is AB+BC=$2d\sin\theta$.

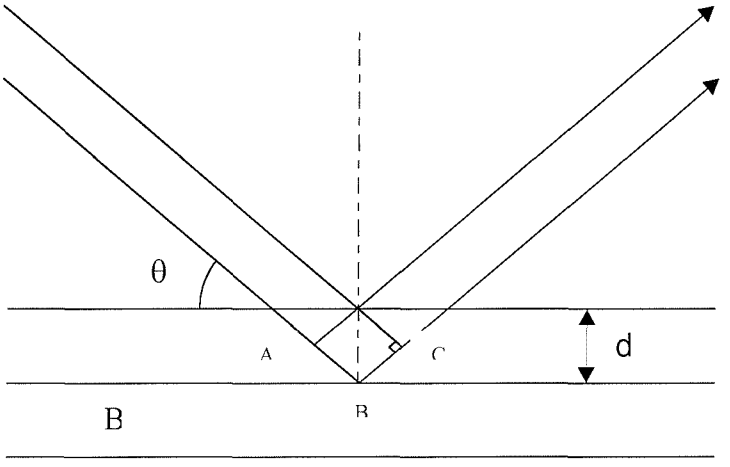

Figure 2.3 Diffraction from parallel planes of point scatterers.

A bright reflection is observed when the glancing angle or Bragg angle satisfies the Bragg Law:

$$n\lambda=2d\sin\theta$$

At angles of incidence other than the Bragg angle, diffracted beams are out of phases and thus destructive interference occurs. Not all the calculated diffraction maxima are seen due to the existence of reflection conditions or systematic absences. In addition to absences, which arise from a non primitive lattice, there are others caused by some symmetry elements such as screw axes and glide planes.

The interplanar separations in the crystal are calculated by measuring the diffraction maxima and generally first order diffraction only is considered (n = 1 in the Bragg Law). The crystal system is derived from these *d* values or *d*-spacing, by identification of the planes involved. Planes are defined by their Miller indices, *hkl*, the reciprocal values of the positions where the plane cut the *a*, *b* and *c* axes respectively. In two dimensions simple trigonometry may be used to derive the relationship between the Miller indices and *d*-spacing. For orthorhombic systems the relationship between the Miller indices and *d*-spacing is thus given by :

$$\frac{1}{d^2} = \frac{h^2}{a^2} + \frac{k^2}{b^2} + \frac{l^2}{c^2}$$

2.4 Powder x-ray diffraction

The most widely used analytical technique for characterisation in the area of solid state chemistry is x-ray diffraction (XRD). This is due to its non-destructive nature and versatility. The advent of modern diffractometer and computer package has made the acquisition of such data a routine exercise. All of the compounds synthesised in this work are polycrystalline solids, so PXD was used as an initial means of characterisation in all cases.

2.4.1 Instrumentation

All PXD data in this work were collected on a Siemens D5000 diffractometer. This is a conventional θ -2θ diffractometer (Figure 2.4), which employs copper radiation passed through a single crystal monochromator to give only $K\alpha_1$ (λ = 1.5406 Å) radiation. The x-rays are collimated through an aperture diaphragm and directed onto the sample, which is mounted in a recessed plastic or aluminium sample holder. The sample rotates in a stepwise process, increasing the angle θ. The detector is correspondingly moved around the sample at twice the rate, increasing the diffraction angle (2θ) between preset values. The diffracted x-rays are collected by a standard scintillation counter. The recorded data is passed constantly to a computer where a real time display can be viewed. Data are collected by a Siemens Diffrac^{plus} software, when collection is complete, the data can be analysed using Siemens Diffrac^{plus} evaluation program (Eva). This allows recorded data to be compared with previous samples, or diffraction patterns stored on the JCPDS data base [3]. Typical data collection parameters for an initial scan were over the 10-60° 2θ range, with a step size of

0.02° over 30 minutes. More detailed data were collected for Rietveld refinement (2.5.4) over the 2θ range of 10-60°, step size 0.02° and collection time of 12 hours.

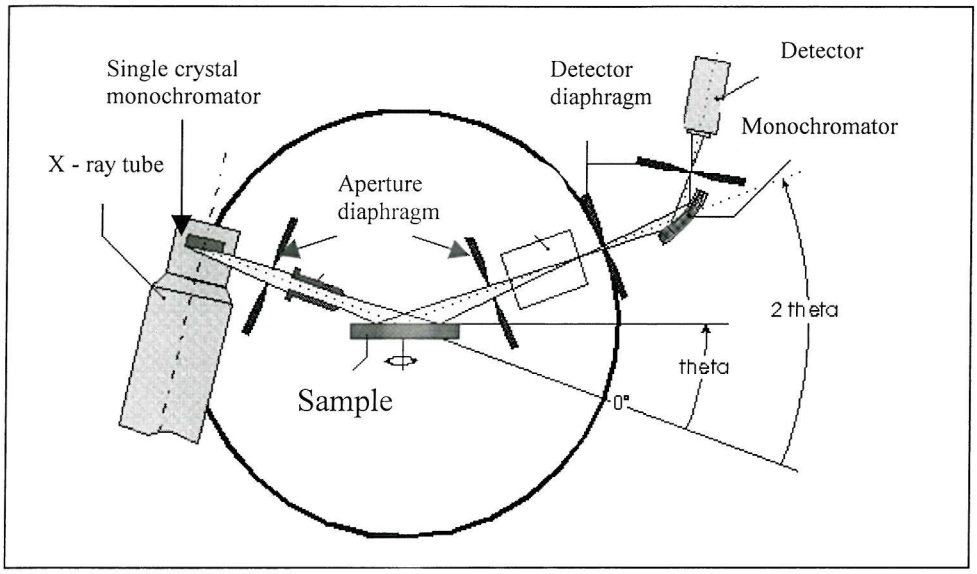

Figure 2.4 Schematic representation of the Siemens D5000 diffractometer.

2.4.2 Analysis of the PXD data

Initial analysis was carried out by comparison of the observed data with the JSPDS pattern where possible. When a phase was not included on the data base, an indexation of the XRD pattern was carried out using TREOR that allows a search over all the possible

symmetries [4]. The lattice parameters could now be calculated by inserting the information into the Cell program [5]. This software minimises the following equation:

$$M = \Sigma_n W_n (\sin^2 \theta_n^{Obs} - \sin^2 \theta_n{}^{calc})^2$$

using an iterative least square procedure, where W_n is a weighting factor proportional to $\tan\theta$. The resulting cell parameters, with estimated standard deviations (e.s.d' s) only reflect the goodness of fit between the observed positions and those calculated and therefore provide no indication of any systematic experimental errors or sample impurities.

2.5 Powder neutron diffraction

Powder neutron diffraction is a very powerful technique used in this work to study ternary transition metal oxides of light alkali metals and has a number of advantages over PXD. The main difference between the two diffractive techniques lies in the method by which the radiation is scattered.

In PXD, the x-rays are scattered by the electrons of the atoms and the scattering power is a function of atomic number. Unlike X-rays, neutrons interact with the nucleus itself. This means that the neutron scattering power of an atom is not directly related to the atomic number but is instead a combination of two factors, potential and resonance scattering. Potential scattering depends on the size and number of particles in the nucleus, while resonance scattering is a consequence of a 'bound' state which the neutron forms temporarily with the nucleus.

This means that lithium and oxygen can be located in the presence of much heavier atoms, and atoms with similar x-rays scattering lengths can sometimes be distinguished allowing occupancy of shared sites to be calculated. The nuclear dependence also allows isotopes of the same element to have substantially different scattering lengths to neutrons, thus allowing isotopic substitution to be used in structural studies.

A further consequence of the interaction with the nucleus rather than the electrons on atoms is the absence of the interference effect that causes the x-ray scattering to diminish with $\sin\theta/\lambda$, so the scattering intensity shows no angular dependence. This allows the collection of larger data sets with respectable intensity at small d-spacings which allows accurate determination of structural details.

Neutrons have no charge, which allows them to penetrate the surface of the materials. This makes possible to investigate the bulk of a sample. It also makes it possible to construct equipment around a neutron diffraction sample allowing routine experiment to be carried out at low temperature in a cryostat and at high temperature in a furnace.

These factors make neutron diffraction a very powerful technique in the structural analysis of transition metal oxides. The main problem in this area is the presence of light alkali metal cations, *e.g.* lithium, and the similarity of the x-ray scattering lengths of transition metal cations (Mn, Fe, Co, Ni) over mixed sites. All of these problems can be alleviated by

the use of the neutrons. The problems remain the cost and the low flux associated with neutrons which leads to lengthy experiment times.

2.5.1 Time-of-flight (t.o.f) PND

During the course of this work, two different instruments have been used to collect PND data; the medium resolution instrument Polaris and HRDP (High Resolution Powder Diffractometer), both of the ISIS facility at the Rutherford Appleton Laboratory (RAL). This facility uses a pulsed neutron spallation source. The neutrons are produced by bombarding a heavy metal target with highly energetic particles.

The pulses of neutrons radiation produced are separated according to their time of flight and hence their wavelength over a fixed distance. From the Bragg equation of a conventional diffraction experiment λ is fixed with d and θ as variables. Here for a t.o.f. experiment, λ and d are variables θ at fixed, and diffracted neutrons are detected accurately by fixed angle detectors according to their energy and hence velocity (time of flight).

Diffractometer utilising a pulsed neutron source operate in a fundamentally different way to a conventional reactor-based system/constant wavelength diffractometer. Both Polaris and HRPD measure the Bragg reflections at fixed scattering angles and monitor the time of arrival of a neutron after the initial burst produced by the target. Conventional diffractometers measure the Bragg reflections by scanning a detector over a range of angles from low to high 2θ. The relationship between t.o.f. and d-spacing is linear and is derived from de Broglie's relationship and Bragg's law as shown:

$$\lambda = \frac{h}{p} = \frac{h}{m_n v_n} = 2d\sin\theta$$

Where λ is in Å, the neutron mass m is 1.675×10^{-27} kg, h the Planck's constant equal to $6.62\ 10^{-34}$ Js^{-1} and the neutron velocity calculated from T, the time of flight and L, the flight path to give:

$$\lambda = \frac{0.3955}{v} = \frac{0.003955T}{L}$$

With v in ms^{-1}, T is in μs and L is in m. This shows that the neutron wavelength is proportional to the time of flight and therefore the wavelengths can be discriminated by their

arrival time to the detector. This allows the measurement of a range of d-spacings using a fixed scattering angle. Bragg's law can therefore be written as:

$$\lambda_{hkl} = 2d_{hkl} \sin\theta_0$$

The combinaison of the above equations gives the relationship in convenient units of time in μs and *d*-spacing in Å.

$$t_{hkl} = 505.55685 L d_{hkl} \sin\theta_0$$

From this, we can see that for a 10 m and 100 m instrument, a 1Å *d*-spacing will be detected in backscattering to have a time of flight of approximately 5000 μs and 50000 μs respectively.

In both diffractometers Polaris and HRPD, the time of flight can be converted to d-spacing by dividing by $505.55685 L \sin\theta$ for the particular diffractometer. After normalisation, Lsinθ for the backscattering detectors equal 12.190 m for Polaris and 95.452 m for HRPD. Therfore t_{hkl} (msec) = 6.163 d_{hkl} (Å) for Polaris and t_{hkl} (msec) = 48.256 d_{hkl} (Å) for HRPD.

2.5.2 POLARIS

The Polaris instrument is a high intensity, medium resolution diffractometer (Figure 2.5), with the intense neutron flux and large detector bank providing a high counting rate. This makes it ideal for the rapid collection of good quality data from simple structures or small samples (<500 mg). It receives a polychromatic, 'white', beam of neutrons from an ambient temperature water moderator. The sample position is 12 m from the moderator, and the incident and transmitted neutron flux is monitored by two glass scintillator detectors, positioned 4 m before the sample and 2.5 m after it. The beam dimension can be altered using two motor driven collimators in the incident beam. This allows the size of the beam to be reduced from the standard 40 mm high × 20 mm wide to match the sample size, or to reduce the background from sample environment equipment.

Samples are located in vanadium samples cans within an evacuated sample chamber and the scattered neutrons detected by a complex array of detectors shown at Figure 2.5. The different detectors are summarised at Table 2.1. The backscattering (C) bank yields the

highest resolution over d-spacing range 0.2-3.2 Å and for this reason was used in most refinements. When cell dimensions and space group information had to be obtained from the data, the 90 degrees (E) and the low angle (A) banks were also used to give higher d-spacing reflections. Data were not routinely collected from the long d-spacing (B) bank, however this could have been obtained if required at the expense of some of the backscattering detectors.

2.5.3 HRPD

HRPD is a high resolution powder neutron diffractometer. Its resolution is quoted as $\Delta d/d$ = 4-5 × 10^{-4} in backscattering mode. In this mode, a complicated array of ZnS scintillator detectors are fixed at scattering angles of $160 < 2\theta < 176$ °.

This leads to the highest available resolution n the d-spacing range of ~ 0.6 – 4.6 Å. HRPD has a path length of 95 m which gives long times of flight and high resolution, however the beam line only takes one in five pulses generated by the sources, leading to long collection times in the range 8-12 hours.

HRPD was designed to handle cell volumes with up to 400 structural parameters. This makes a superb instrument for the study of complicated structures, for example the low symmetry $Na_2Mn_3O_7$ studied in this work. In this case, high resolution data were needed to study the manganese distribution within the layers.

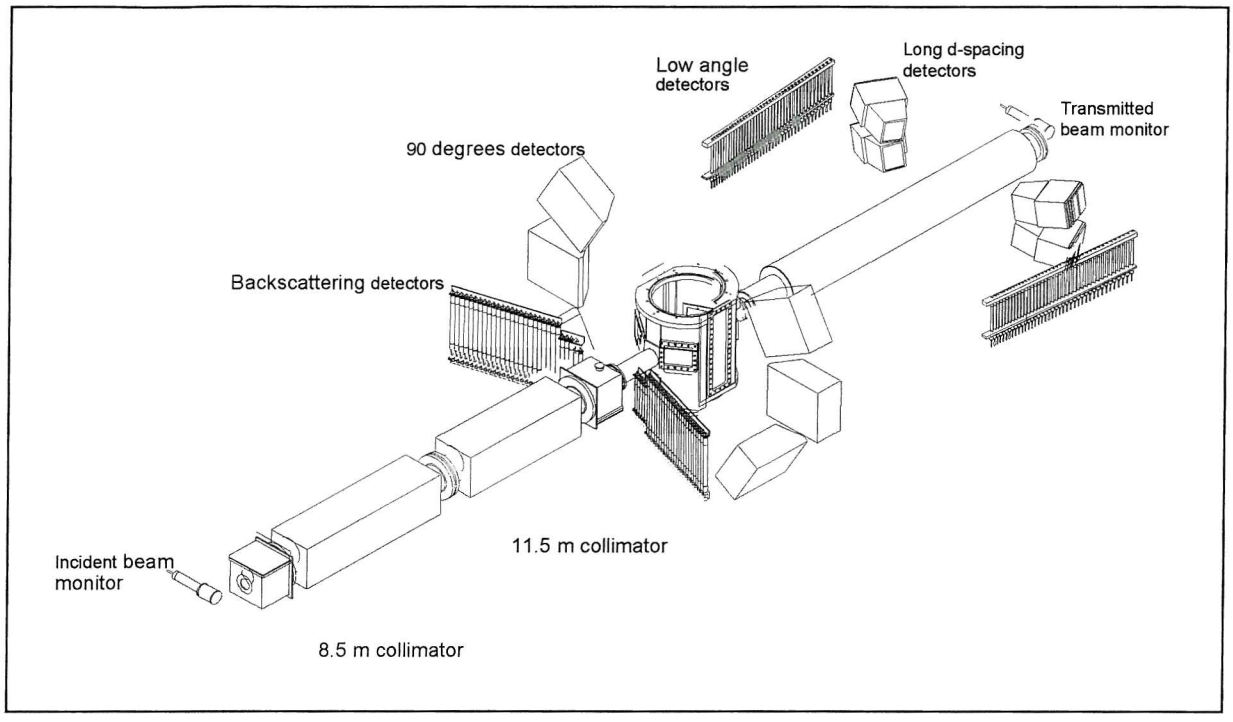

Figure 2.5 Schematic representation of the Polaris.

Table 2.1 Polaris detector configuration.

	Low angle (A)	Long d-spacing (B)	Backscattering (C)	90 Degrees (E)
Detector Type	^{3}He	ZnS	^{3}He	ZnS
2θ range <97°	28°<2θ <42°	13°<2θ <15°	130°<2θ <160°	83°<2θ
$\Delta d/d$	~1×10^{-2}	~3×10^{-2}	~5×10^{-3}	~7×10^{-3}
d-range (Å)	0.5 - 8.3	0.5 - 21.6	0.2 - 3.2	0.2 - 4.0

2.5.4 The Rietveld technique

Early techniques used in the analysis of powder diffraction data were based on those developed for the structural refinement of single crystals. These involved a least square refinement using F values based on structure factors extracted from the pattern. This was possible as each *hkl* reflection led to a single point whose intensity could be routinely measured. In fact, for a unit cell, the structure factor F_{hkl}, is the sum of the contributions of the scattering amplitudes f_j, and the phases shifts in this direction ϕ_j, of each atom j at a point (x_j, y_j, z_j), leading to the expression:

$$F_{hkl} = \sum_{j=1}^{N} f_j \exp[2\pi i(hx_j + ky_j + lz_j)$$

where h, k and l are the the Miller indices that define the plane from which the reflection takes place. For small crystal, it may be shown that the intensity of the scattered beam is proportional to the square of the structure factor:

$$I_{hkl} = kL^2|F_{hkl}|^2$$

where k is the scaling constant, L the Lorentz factor, a geometric function of the method of data collection and hence the instrument used. The scattered intensity is modified in reality by imperfection in the lattice structure. Defects and substitutional disorder cause local structural irregularities, particularly in non stoichiometric materials. In addition, thermal motion causes a reduction in scattered intensity as a result of time dependent vibrations of the atoms about their mean positions: the atoms in a plane *hkl* are displaced randomly from their ideal in-plane positions, disrupting the in-plane behaviour of their combined scattering. The correction to a structure factor reflected by a plane *hkl* takes the form :

$$T_{hkl} = \exp[-B_{hkl}\frac{\sin^2\vartheta}{\lambda^2}]$$

so that for a unit cell, the structure factor becomes:

$$F_{hkl} = \sum_{j=1}^{N} f_j n_j \exp[-B_{hkl}\frac{\sin^2\vartheta}{\lambda^2}]\exp[2\pi i(hx_j + ky_j + lz_j)$$

where n_j is the occupation factor of the j^{th} atom. The anisotropy of thermal motion can be described in the form of an ellipsoid, replacing the equation above with :

$$T_{hkl} = \exp[-1/4(B_{11}h^2a^{*2} + B_{22}k^2b^{*2} + B_{33}l^2c^{*2} + 2B_{12}hka^*b^* + 2B_{23}klb^*c^* + 2B_{13}hla^*c^*)]$$

This form will be used to describe the anisotropic temperature factors in this work.

In the powder diffraction experiment, small crystallites are randomly arranged leading to diffraction circles, with the diffraction pattern being a one dimensional cross section of the circles. This made the approach highly problematic due to the vast amount of information masked by overlapping peaks. In this situation, structure factor extraction was difficult if not impossible.

In 1967, H. M. Rietveld [6,7] developed the idea of a direct fitting of the entire diffraction pattern, again by least square minimisation, alleviating the need for structure factor extraction. This method took advantages of all the information contained in often very complicated patterns and led to much greater accuracy in structural refinement. Initial work centred on constant wave length PND due to its intrinsic near perfect Gaussian peak shape, however the development of more complex peak shape functions has allowed the Rietveld technique to be extended to PXD and time of flight PND. Today most experiments carried out to yield structural information from powder samples exploit the Rietveld method.

In a typical refinement an appropriate starting model is chosen from previously refined structures obtained from literature or data base searches. The scale factor and background parameters are then varied followed by the zero correction and displacement of the sample and the lattice parameter to allow the accurate positioning of the Bragg reflections, some initial refinement of the peak profile coefficient may also be attempted at this stage. The atoms positions can then be allowed to vary to fit the peak intensities, followed by the temperature factors on well positioned atoms to define their thermal motion. Finally the peak shape parameters can be refined along with additional background coefficient, this can account for any asymmetry or sample broadening effects. In some cases it may also be possible to vary the anisotropic temperature factors.

During the refinement the best squares fit to the many thousands of observables, Y_i's, is sought. The quantity to minimise in the least square refinement is the residual, S_y, given by:

$$S_y = \sum_i W_i [Y_i^{obs} - Y_i^{calc}]^2$$

where Wi = a weighting factor given by $1/Y^{obs}$

Y_i^{obs} = the observed intensity at the i^{th} step.

Y_i^{cal} = the calculated intensity at the i^{th} step.

A powder diffraction pattern can be thought of as being made up of a collection of individual reflection profiles, each having a peak height, position, width, decay tails and an integrated area proportional to the Bragg intensity, I_k. I_k is proportional to the square of the absolute structure factor, $|F_k|^2$. In all powder patterns where the Rietveld method is used, these profiles are not all resolved but overlap partially. A feature of the method is that no attempt is made to assign observed intensity to a particular Bragg reflection or to resolve overlapping reflections in advance. Consequently a reasonably good starting model is required.

Typically, many Bragg reflections contribute to the intensity, y_i, observed at an arbitrarily chosen point i, in the pattern. The calculated intensities are determined from the $|F_k|^2$ values calculated from the structural model by summing of the calculated contributions from neighbouring Bragg reflections plus a background.

$$y_i = s \sum_K L_K |F_k|^2 \phi(2\theta_i - 2\theta_K) P_K A + y_{bi}$$

where s is a scale factor, K represents the Miller indices, h, k, l, for a Bragg reflection, L_k contains the Lorentz, polarisation and multiplicity factors, ϕ the reflection profile function, P_k is the preferred orientation function, A is an absorption factor, F_k is the structure factor for the K^{th} Bragg reflection and y_{bi} is the background at the i^{th} step.

Preferred orientation arises when there is a stronger tendency for the crystallites to be ordered in one way and is defined by:

$$P_k = [G_2 + (1 - G_2)\exp(-G_1\alpha_k{}^2)]$$

where G_1 and G_2 are refinable parameters and α_k the angle between the preferred and the presumed orientations.

The starting model must be close to the correct model or the least squares procedure will not lead to a global minimum. Instead, the process will diverge or lead to a false minimum. This may be overcome by the use of multiple data sets or by the use of constraints. Multiple phases may be refined simultaneously and comparative analysis of the overall scale factors for the phases offers a method for quantitative phase analysis.

The background intensity at the i^{th} step, y_{bi}, can be obtained in several ways, typically it is modelled using one of a set of functions supplied with the program. The type of data being refined determines the choice of background.

The reflection profile function ϕ, approximates the effect of instrumental features and specimen features such as absorption. The model should adequately describe the instrumental resolution function over a wide range of 2θ and also incorporate sample broadening effects such as particle size, strain and stacking disorder. Peak shape is generally dictated by the instrument; for a SiemensD5000, the peak is psuedo-Voight, and described by the function:

$$\eta L + (1-\eta)G$$

where L and G are the Lorentzian and Gaussian contributions to the peak shape and η is the mixing parameter which can be refined as a linear function of 2θ.

$$\eta = N_a + N_b(2\theta)$$

where N_a and N_b are refineable parameters.

The Gaussian and Lorentzian contributions to the peak shape are represented by the equations:

$$G = \frac{(4\ln 2)^{1/2}}{H_k\sqrt{\pi}}\exp(-4\ln 2(2\theta_i - 2\theta_k)^2 / H_k{}^2)$$

where $2\theta_k$ is the calculated position for the k^{th} Bragg peak corrected of the zero point

$$H = \frac{2}{\pi H_k} \frac{1}{[1+4\frac{(2\theta_i - 2\theta_k)^2}{H_k^{\ 2}}]}$$

and H_k, the full width at half maximum (FWHM) of the k^{th} Bragg reflection.

For angle dispersive data, the dependence of the width of the reflection profiles measured as the full width at half maximum (FWHM) is typically modelled using the method of Caglioti *et al* [8] as:

$$H^2 = U\tan^2\theta + V\tan\theta + W$$

where U, V, W are refinable parameters. There are many other types of functions available to describe the reflection profile, as x-ray sources are generally neither Gaussian or symmetric. The sample broadening effects are modelled by a Lorentzian expression:

$$H = X\tan\theta + Y/\cos\theta$$

where the first term is associated with microscopic strain broadening and the second accounts for particle size broadening.

At low scattering angles the peak shape shows marked asymmetry due to finite beam slit width and sample heights. This results in the peak maximum shifting to slightly lower angle while the integrated intensity remains unchanged. This can be corrected by the use of a semi-empirical correction factor

$$1 - \frac{sP(2\theta_i - 2\theta_k)^2}{\tan\theta_k}$$

where P is the asymmetry parameter and equal to -1, 0, 1 when $(2\theta_i - 2\theta_k)$ is positive, zero or negative.

The refinable east square parameters fall into two distinct groups. The first one defines the position and shape of the peaks and consists of the unit cell parameters, the counter zero offset, and the asymmetry factor. The second group, the structural and thermal parameters, defines the contents of the unit cell. These consist of the profile scale factor, and the co-ordinated, occupation and temperature factor of each atom. In order to make a

quantitative assessment of he agreement between observed and calculated profiles, a number of reliability indices are defined as follows:

$$R_{profile} = R_p = \frac{\left[\sum_i Y_i^{obs} - Y_i^{calc}\right]}{\left[\sum_i Y_i^{obs}\right]} \times 100\%$$

This may be compared with the reliability index $R_{expected}$ derived purely from statistical considerations:

$$R_{expected} = R_e = \frac{[N-P+C]^{1/2}}{\left[\sum_i W_i (Y_i^{obs})^2\right]} \times 100\%$$

where N = number of observables, P = number of refinable parameters and C = number of constraints.

In addition, R_{wp} may be defined as:

$$R^2_{weightedprofile} = R^2_{wp} = \frac{\left[\sum_i W_i \left|Y_i^{obs} - Y_i^{calc}\right|^2\right]}{\left[\sum_i W_i (Y_i^{obs})^2\right]}$$

Finally the chi-squared parameter may be defined as:

$$\chi^2 = \frac{1}{N-P+C} \sum_i W_i \left|Y_i^{obs} - Y_i^{calc}\right|^2 = \left[\frac{R_{wp}}{R_e}\right]^2$$

which is the natural measure of the fit, and is normally minimised in the refinement. Thus for a good fit the weighted profile R-factor should approach the statistical expected R-factor value and thus χ^2 approach the unity. The goodness of fit can also be measured by examining a plot of the profile fit: for a good fit, the difference line between calculated and observed should be as flat s possible with fluctuation consistent with noise.

Powder x-ray diffraction data and powder neutron diffraction data were refined using the GSAS package of Larson and Von Dreele [9] on a PC computer.

2.6 ^{7}Li MAS NMR

NMR has always been one of the most powerful analytical tools for liquids and solution phase chemistry, but until recently it could not be applied to solids as the result was broad featureless peaks containing little information. In the liquid state, molecular tumbling is rapid and random and the direct nuclear field fluctuate significantly in both direction and intensity, conveniently averaging to zero. In the solid sate this not the case, resulting in considerable peak broadening.

This peak broadening is due to three characteristics of solids. Firstly the dipole coupling do not average to zero by the molecular tumbling previously described, while long range coupling is also important due to the crystalline nature of the materials. Secondly, the chemical shift of a nucleus is dependent on its local environment and its orientation to the magnetic field. In a solid, unlike a liquid, this clearly does not average to zero, leading to chemical shift anisotropy. Finally, long relaxation times are common and therefore multipulse techniques are less efficient. These factors make it much less straightforward to perform an NMR experiment on a solid sample.

These broad resonances can be significantly reduced using magic angle spinning (MAS). Dipole-dipole interactions and chemical shift anisotropy are both dependent on an orientation term proportional to $(3\cos^2\theta - 1)$ where θ is the angle between the applied magnetic field B_0 and the line joining the two nuclei in question. This term becomes zero, and hence no line broadening is seen, at the magic angle, $\theta = 54.73\ °$. So a powder can behave as a liquid by making all the internuclear vectors behave as if they had the magic angle. This is achieved by placing the sample in a small air driven turbine mounted at the magic angle to the external field and rotating the sample at several kHz (Figure 2.6). Experiments were carried out using a Bruker MSL-400 spectrometer at UMIST (University of Manchester). A spinning rate of 14.8 kHz was used. ^{7}Li NMR was carried out on samples and referenced to a 1M aqueous LiCl solution.

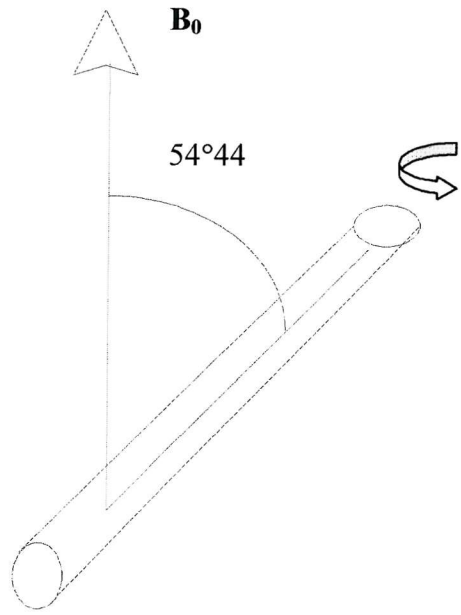

Figure 2.6 The mounting of a solid sample in a MAS NMR machine.

2.7 Flame photometry

Many elements such as lithium and sodium exhibit colours in a flame with an intensity that is concentration dependent. Flame photometry is concerned with the quantitative analysis of this emitted radiation.

A small amount of the solution is drawn through a nebuliser and mixed with oxygen and a combustible gaz. The mixture is then introduced to a flame at a controlled flow rate. Some of the electrons in the metal are excited by the thermal energy and light of characteristic wavelength emitted on returning to the ground state according to the Bohr condition:

$$hc/\lambda = E_1\text{-}E_2$$

An appropriate screen allows only the required radiation to be transmitted and measured using a photoelectric detector.

Lithium and sodium containing samples were measured for the degree of exchange using Corning 400 Flame photometer. The photometer was calibrated using standard solutions in the range 0-100 and 0-1000 ppm for the lithium and sodium respectively. Sample (~0.1 g) was added to water, dilute hydrochloric acid and hydrogen peroxide to reduce the manganese. The solution was then made up to 100 ml in a volumetric flask. The preparation of the standard solutions and samples is developed in more details at Chapter 5 (5.3.2.1).

2.8 Ultraviolet-visible (UV/VIS) spectroscopy

UV/VIS were recorded on a Perkin Elmer Lambda 19 spectrometer set up for absorbance spectroscopy with tungsten and deuterium lamps at the selected wavelength of 545 nm. UV/VIS was used in this work for the determination of the manganese concentration in the sample after its oxidation with potassium periodate to the strongly coloured permanganate ion MnO_4^-. A calibration curve of absorbance against concentration of permanganate ion enables the unknown concentration to be determined. Details on the preparation of the standard solutions figure at Chapter 5 (5.3.2.2).

2.9 Electron microscopy and analysis

Electron microscopy can be used in many different experiments, including electron diffraction and imaging. In this work, the technique was used to assess the quality and morphology of the samples synthesised using scanning electron microscopy (SEM) and their composition using energy dispersive x-ray spectroscopy (EDAX).

The electron microscope generates electron by thermoionic emission, which are then monochromatic by acceleration through a potential V. The voltage used for this acceleration determines the wavelength of the electrons as follows:

$$\lambda = \left(\frac{1.5}{V + 10^{-6} V^2} \right)^{1/2} nm$$

A typical accelerating voltage would be 100 keV, generating a wavelenth of 0.037 Å. The electrons are scattered by the atomic potentials in the same way as neutrons or x-rays. As with x-rays, there is a sharp fall of scattering power with $(\sin\theta / \lambda)$. The scattering factor generally increases with atomic number. Unlike x-rays and neutrons, electrons are scattered very strongly by matter allowing electron diffraction experiments to be carried out on gaseous samples. Electrons can be scattered in a variety of ways, see at Figure 2.7.

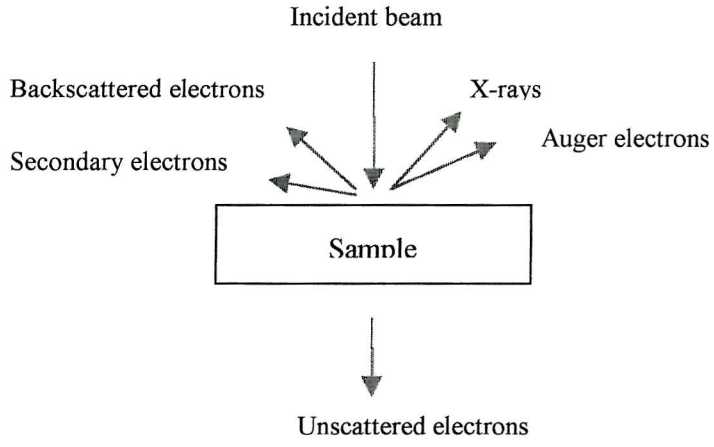

Figure 2.7 Schematic diagram of possible scattering in a SEM experiment.

Electron microscopy was carried out on a Philips XL 30 analytical scanning microscope at the Southampton Electrochemistry Department.

2.9.1 Scanning electron microscopy (SEM)

SEM has been used to study the morphology of materials. The microscope gives a magnified, high resolution image of the sample, by illumination with an electron beam rather than visible light.

A schematic representation of the SEM is shown in Figure 2.8. The electron beam is focused through a series of electromagnetic lenses, giving rise to a spot of beam on the sample of only a few nanometers. The spot scans the specimen, while the detector monitors a particular emission. In most cases, this is secondary electrons. Secondary electrons only leave the specimen if they are generated within 50 nm of the surface, so the image produced gives surface information and depth characteristic as a normally viewed image.

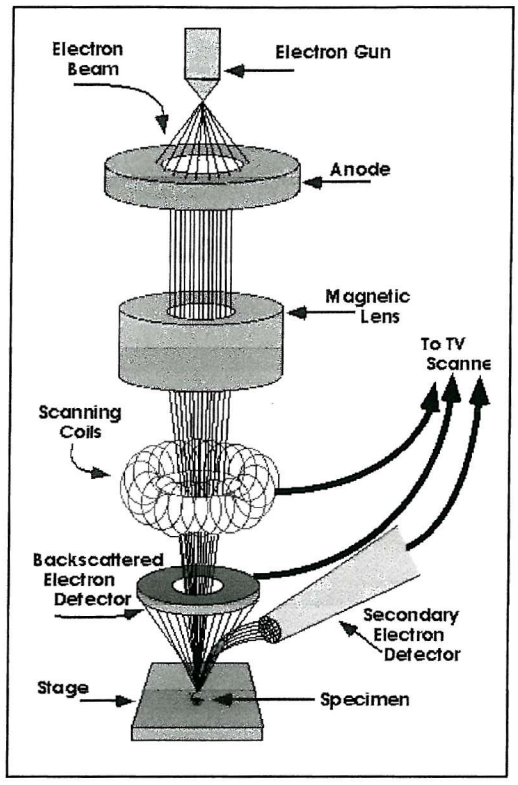

Figure 2.8 A schematic view of the SEM microscope.

2.9.2 Energy dispersive x-ray spectroscopy (EDX)

A relatively simple extension to SEM, using the same instrumentation and sample is energy dispersive x-ray analysis (EDX). This involves the detection of x-rays, which are emitted when inner shell electrons are removed from the sample and outer shell electrons drop to lower energy shells to fill the holes. The energy of these x-rays are obviously characteristic of the element from which they originated. A plot of x-ray energy against intensity can be used to give qualitative and quantitative information on the composition of the sample. Errors are often large for the lighter elements. In this work, EDX was found useful to estimate and compare the sodium left after the lithium ion exchange reactions.

2.10 BET

The surface area of the carbon black and materials synthesised in this work were determined by the BET (Brunauer, Emmett and Teller) method [10]. The method consists of forming a complete adsorbed layer of one molecule (*i.e.* n_a molecules) thick over the surface of known amount of material. The surface area (s) of the material can then be calculated from the equation $s = n_a\sigma$, where σ is the area of surface occupied by one molecule.

To determine the surface area of solids, known quantities of gas are emitted into a chamber containing a solid sample. By measuring the pressure and volume at equilibrium and comparing it to the initial values, the fractional surface coverage can be determined.

The BET measurement was carried out using a Gemini 2375.

2.11 Electrochemical techniques

2.11.1 Preparation of electrode and construction of the cell

For the galvanostatic cycling test, the electrodes were made using a dry method consisting of mixing polytetrafluoroethylene (PTFE) as a binder. This method is called dry method as opposed to the wet method, in which a slurry composed of the carbon black and Kynar Flex 2801 (binder) in THF solvent is coated on an aluminium foil using the doctor blade technique.

In this work, the composition of the electrodes was typically of 60-75 % active material, 20-35 % fine carbon (Monarch 1400, Acetylene Black, Shawinigan Black) and 5 % Teflon powder. The following Table 2.2 contains the data of the surface area of the different carbons black. Cycling tests were carried out in this work between 3.2 and 4.6 V using $LiMn_2O_4$ and the different carbons black. No marked influences on the capacities delivered by the spinel nor on their cyclability have been shown. The only difference is that an increase in the surface area of the black carbon would lead, at high voltage, to a slight increase of the parasitic charge capacity due to the irreversible electrolyte oxidation [11].

Table 2.2 Surface areas measured by BET of the carbon black used.

Carbon Black	Surface area (BET Measurement m^2g^{-1})
Monarch 1400 (Elftex)	450
Acetylene Black (Strem Chemicals)	74
Shawinigan Black	75

The electrodes were made by manual kneading of the components followed by a rolling procedure, using a Durston Minimill, with a gradual reduction of the thickness to 100-150 μm. All electrodes were cut into discs of surface area 0.95 cm^2, weighted and dried in a high vacuum at 120 °C in a Büchi TO-50. The content of active material in the electrode was found to be in the range of 11-19 mg.

The electrodes were cycled in a spring loaded and coin-type cell for the *in-situ* experiments. The latter was modified to allow its use in reflection-mode XRD measurement. A beryllium window was constructed on the cathode side. A good seal was obtained under prolonged measurements. The silver paste was used to improve the contact between the window and the rest of the stainless steel case. Both cells are shown at Figure 2.9. In both cases, a disc of lithium foil served as a reference and counter electrode. A known amount of electrolyte was absorbed in porous polypropylene discs or in glass fibber membranes as separator. The electrolyte used was the conventional 1 M LiPF6 in a 1:1 mixture of ethylene carbonate (EC) and dimethylcarbonate (DMC). The stability of the last electrolyte has been distinguished [11]. Its shows very low oxidation currents on $LiMn_2O_4$ (with 10% Super S carbon black) electrode up to 5.1 V *vs.* Li. during an extremely slow anodic sweep resulting in a total parasitic charge capacity of only 1.8 %.

In the light of these results, potential windows on the range 1-4.5 V can be used with 1 M LiPF6 in EC:DMC (1:1) and the different carbon blacks listed above. The electrolyte handling and cell preparation were carried out inside an argon filled glove box (Unilab, MBraun).

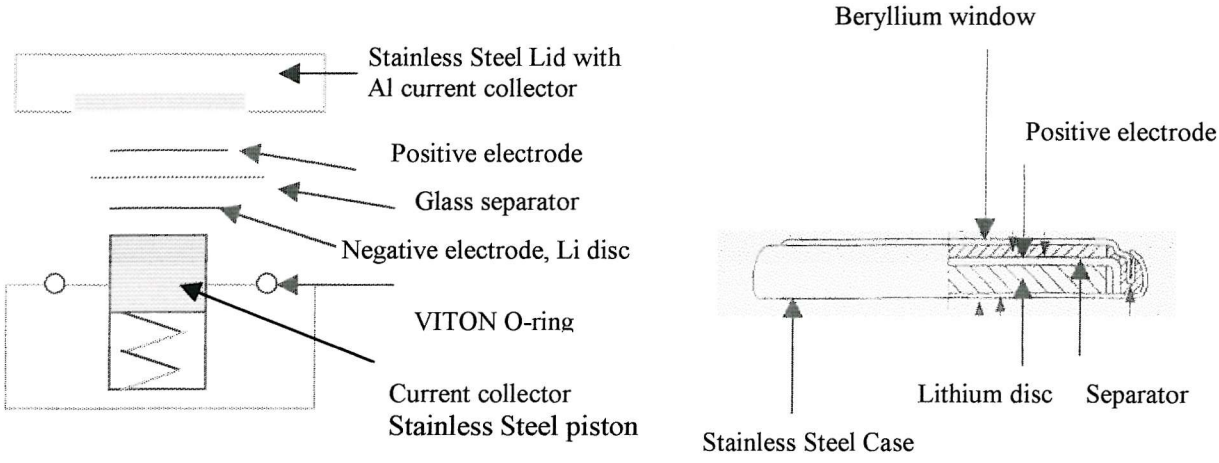

Figure 2.9 Schemas of the electrochemical cells used for long cycling (a left) and in-situ experiment (b right).]

2.11.2 Galvanostatic cycling

The galvanostatic cycling was performed on a home made galvanostat controlled by a program developed at the Southampton University by Dr. A. Whitehead.

The system allows simultaneous cycling of up to 6 long term (typically 1-2 months for 50 cycles) cells. In the experiments, galvanostatic discharge and charge to fixed voltage limits in the range of 1-4.4 V was used.

The composition of the electrode was calculated using Faraday's law:

$$Q = I\,t = \mathrm{n}x\mathrm{F}$$

Where Q is the charge (C), I the current (A), n the number of moles of active material (mol), x the lithium composition (number of ion) and F the Faraday constant (96485 C mol^{-1}).

The characteristic charge/discharge curves or composition curves (E *vs.* composition x) together with differential capacity curves (dx/dE *vs.* x) will be presented in order to analyse the performances of the materials.

2.11.3 Kinetic measurement by Intermittent Titration Techniques

Two electrochemical techniques were used to determine the chemical diffusion coefficient in the mixed-conducting electrode, the galvanostatic intermittent titration technique (GITT) and the Faradaic intermittent titration technique (FITT). They are represented schematically in Figure 2.10.

The diffusion process within the sample is assumed to obey Fick's second law of diffusion. The design of these methods and the analysis of the data obtained are based upon the analytical solution of the diffusion equations under various relevant initial and boundary conditions. These methods are discussed in detail elsewhere [13,14].

Both GITT and FITT are based on current pulse and this approach eliminates the problem of interference due to resistance polarisation in the use of potensiostatic techniques. The GITT technique combines transient and steady-state voltage measurements whereas the FITT concentrates on the relaxation after the pulse.

The time dependence of the potential after a current step can be expressed for the GITT and FITT respectively, at time $t < L^2/D_{Li+}$, as:

$$\frac{d(\Delta E)}{d(t^{1/2})} = \frac{2(dE/dx)V_M i_0}{FA\sqrt{\pi D}}$$

$$\frac{d(\Delta E)}{d(t^{-1/2})} = \frac{(dE/dx)V_M Q}{FA\sqrt{\pi D}}$$

where dE/dx- the slope of the voltage versus composition curve ($Vmol^{-1}$),

V_M- the molar volume (cm^3),

Q- the charge sent through the cell equal to the time pulse by the current pulse (C),

i_0- the constant current (A),

A- the apparent surface of the active material (cm^2),

F- the Faraday constant 96 485C mol^{-1},

D_{Li+} - the diffusion coefficient of Li ions ($cm^2\ s^{-1}$),

L- the characteristic diffusion length of the material (cm).

In this work, the lithium diffusivity in the material was measured using a spring cell (Figure 2.9) in which ceramic pellet was used as a cathode, lithium disc as an anode and a

glass filter soaked with 1 M LiPF6 in EC:DMC (1:1) as a separator and electrolyte. A Solartron 1287 Electrochemical Interface (Galvanostatic mode) was used to generate the constant current pulses and record the voltage. The experiment was conducted at room temperature. The parameters of the experiments are developed at Chapter (4.5) and 6 (6.7)

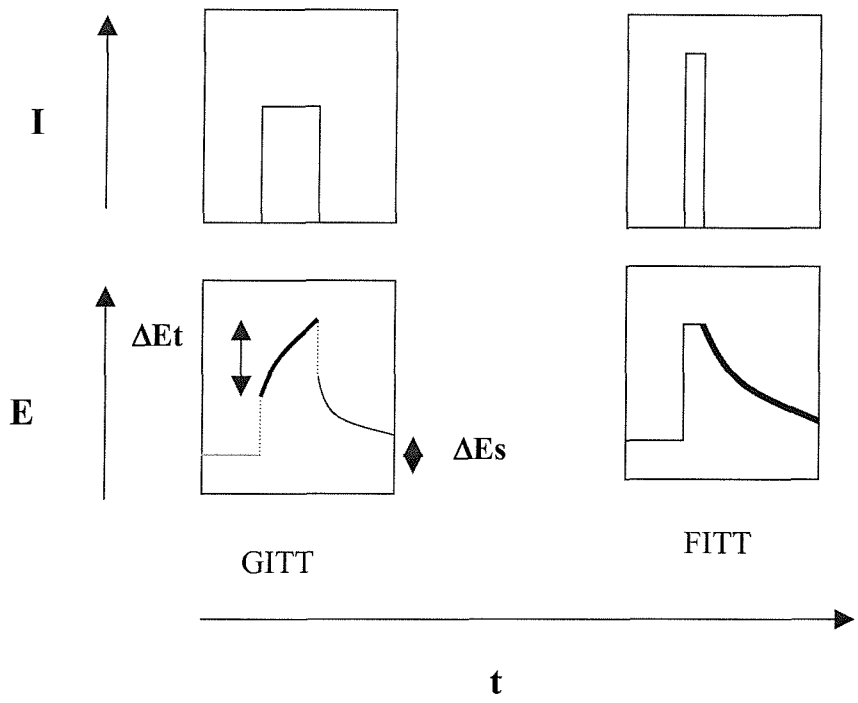

Figure 2.10 Schematic representation of both experimental GITT and FITT methods.

2.11.4 Analysis by ac impedance spectroscopy

2.11.4.1 The ac impedance spectroscopy

Electrical measurements by alternating current (ac) method were used to investigate the conductivities and interfacial properties [15,16].

Many electrical measurements, such as the ones mentioned above, involve changing the potential difference between two points. In an ac experiment, the potential difference is changed in a sinusoidal manner with time with an amplitude <10 mV (i.e. $\Delta E = \Delta E_0 \sin(\omega t)$). In this case the current response is also sinusoidal, but in general is out of phase with the exciting potential by an angle θ so that $\Delta i = \Delta i_0 \sin(\omega t + \theta)$. This response is expressed as an impedance (Z) which is a vector quantity, the magnitude of which is the ratio of the amplitude of the potential to the current, i.e. $|Z| = \Delta E_0 / \Delta i_0$, whilst the two components of the vector Z are $Z' = |Z| \cos\theta$ and $Z'' = |Z| \sin\theta$. Impedance diagrams are produced by representing in

the complex plane a series of Z values (points where Z' is plotted against Z'') corresponding to a range of frequencies (Nyquist plot).

The conductivity and interfacial measurements were performed on a Solartron 1287 Electrochemical Interface that was, in turn, connected to a Solartron 1260 Gain-Phase Analyser. The combined system potentiostatically controls the cell voltage and supplies a 10 mV ac perturbation sweeping the frequency range 10^{7}-10^{-4} *Hz*. The data were analysed with the ZView program that allows interactive specification of equivalent circuit models and their components values. The program generates as output the refined component values, the observed and calculated impedance responses and their percentage difference with also a reliability factor. Optimised component values for a wide variety of different equivalent-circuit models could be rapidly evaluated.

2.11.4.2 Conductivity measurement by ac impedance spectroscopy

The conductivity measurement was performed on a Solartron 1260 Gain-Phase Analyser in the frequency range from 5 Hz to 13 MHz. The measurements, using a conductivity cell were carried out between 18 and 100 °C in air. The pressed-powder electrodes were sintered at 400 °C and covered on both sides by evaporated gold or Ag paste. Both sides are blocking interfaces since there is no equilibration of charged species across the interfaces Au(or Ag)/$LiCu_2O_4$ (x = 3, 4).

In the general case of a polycrystalline material, the grains and the grain boundary (space) are at the origin of two semicircles in the impedance spectrum. The processes have in fact different relaxation times (RC). The first circle at high frequency is related to the bulk properties (R_b , C_b in parallel) of the material, whereas the second semicircle (R_{gb} , C_{gb} in parallel) observed at lower frequencies, corresponds to the grain boundary. Low capacities of 10^{-11}-10^{-12} Fcm^{-1} determine the fast relaxation of the bulk processes. Thin grain boundary area causes C_{gb} of 10^{-9}-10^{-10} Fcm^{-1}, placing it at low frequencies [17-19]. Often, the grain boundary impedance is observed to be less apparent in dense (about 100 %) and very pure ceramics.

A surface layer can also be formed in air at the surface of alkali metal oxide. The thin layer is often an alkali metal hydroxide. Confusion can arise with the semicircle of R_{ct} and C_{dl} in parallel at the interface. In this work, the passivating layer was removed by polishing the surface.

In this work, the total bulk resistance called Z_0 $(R_b + R_{gb})$ is deduced from the complex impedance diagrams (Nyquist plots) at the intercept on the real axis at the highest frequency. The electronic conductivity σ is obtained by means of the relation $\sigma = (1/ Z_0)(e/s)$ where (e/s) is the sample geometrical ratio, e and s being the thickness and surface of the pellet). The temperature dependence is of an Arrhenius-type *i.e.* $\sigma = \sigma_0 \exp(-\Delta E/kT)$ or $\sigma T = \sigma_0 \exp(-\Delta E/kT)$.

2.11.4.3 Interfacial electrochemistry

In the case of an electrochemical cell, the ac impedance was used to interpret the interface between the insertion electrode and the liquid electrolyte that penetrate the pores. The measurements was performed in the frequency range from 0.01 Hz to 100 kHz. A model of the electrode/electrolyte interface is shown at Figure 2.11.

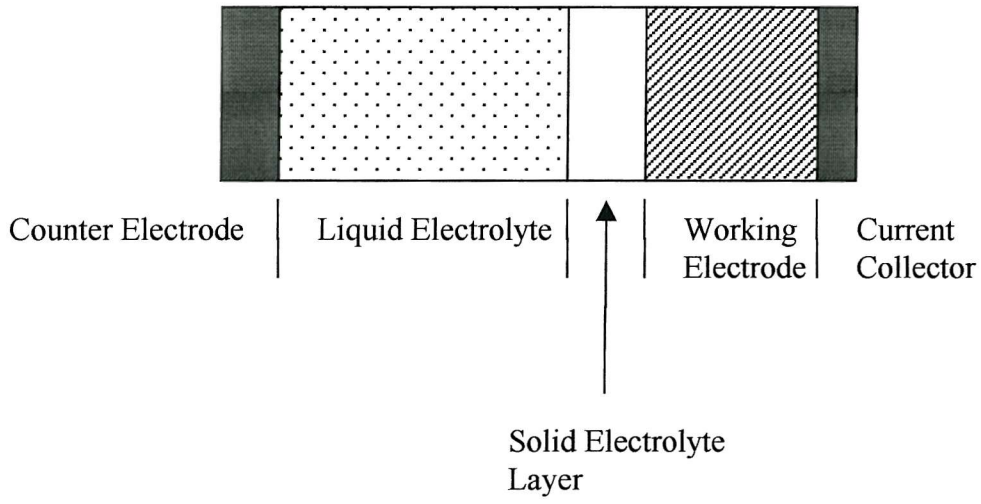

Figure 2.11 Electrode/electrolyte interface including the formation of a surface layer

In this model, three segments can be observed corresponding to three regions on the Nyquist plot (figure 2.13): the bulk electrolyte, the interface region and the bulk electrode. The bulk electrode resistance consists of a very low electronic resistance (R_b) in parallel with a higher insertion-ion resistance. The interface includes the region across which insertion-ion transfer (R_{ct}) and double-layer (C_{dl}) charging occur, and regions on either sides of the interface where these processes introduce insertion-ion concentration gradients in the electrolyte and electrode. Two types of currents through the interface must, therefore, be

distinguished: that due to insertion-ion and electron migration (faradaic process) and the displacement current due to charge polarisation (non faradaic process). These two currents flow in parallel branches of the modified Randles equivalent circuit at Figure 2.12 [20].

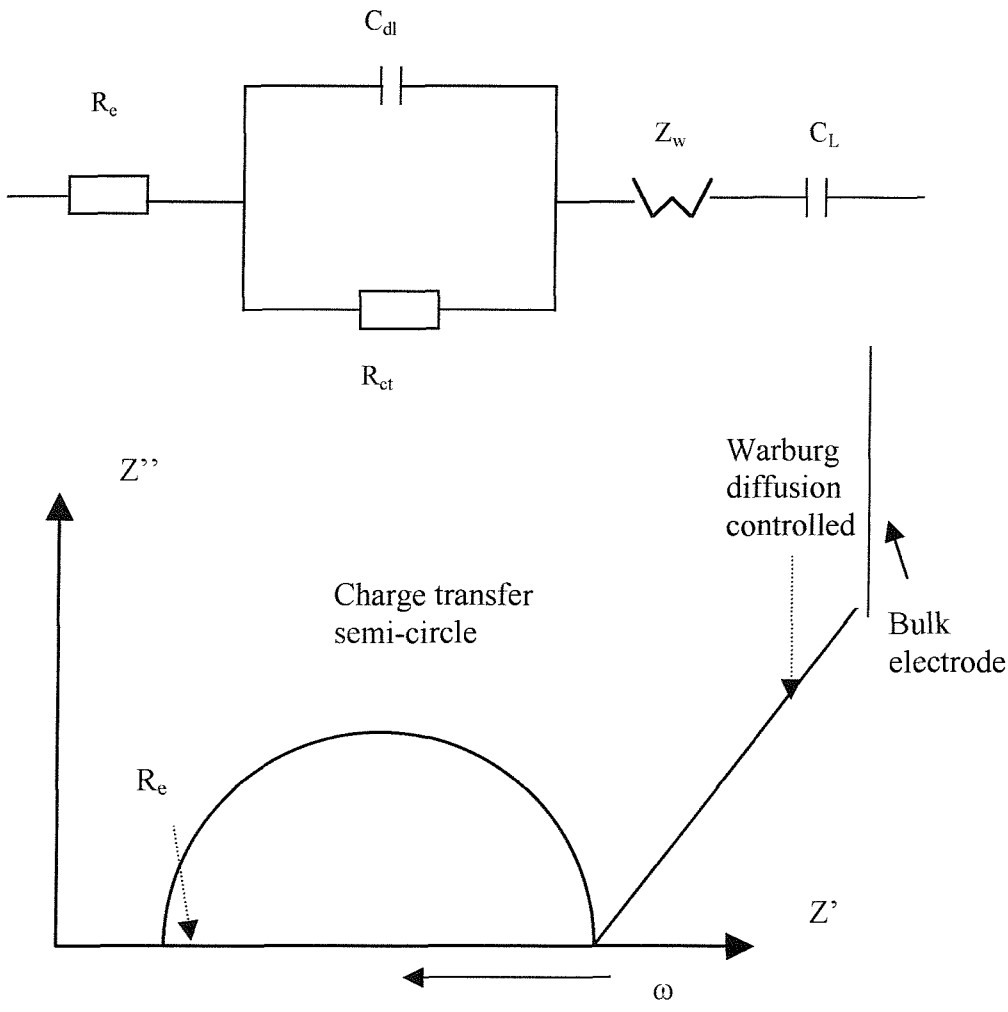

Figure 2.12 Modified Randles equivalent circuit(top) and schematic Nyquist plot.

In some case, a surface-layer electrolyte having a smaller insertion-ion conductivity than the liquid electrolyte modifies the double-layer capacitance. Across the surface layer, the ion transport may be represented by the insertion-ion resistance R_{sl} and polarisation of the surface-layer electrolyte by a capacitance $C_{sl} << C_{dl}$ in parallel. The new equivalent circuit with the surface-layer segment in series with the interfacial-region is shown in Figure 2.13.

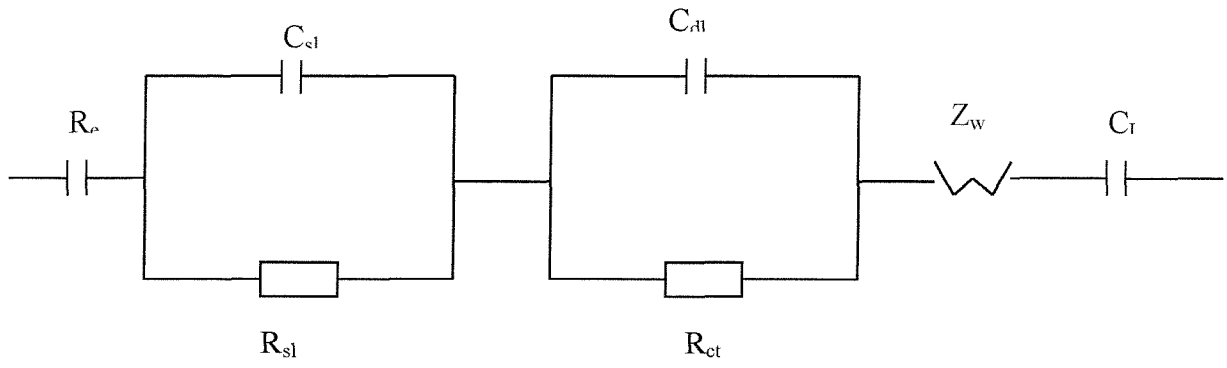

Figure 2.13 Equivalent circuit including a surface-layer segment in series with the interfacial-region.

A Warburg impedance arises from a slow diffusion of the species crossing the interface [21] and is at the origin of the inclined spike (45°) on the low frequency side of the semi-circle (R_{ct}, C_{dl}). It has the characteristic that $Z' = Z'' = A_w / \omega^{1/2}$ with A_w, the Warburg coefficient equal to:

$$Aw = \frac{Vm}{AnF(2D)^{1/2}} \frac{\partial V}{\partial c}$$

where V_m is the molar volume and $\partial V/\partial c$ is the slope of an the open-circuit *vs.* the concentration c.

2.12 References

[1] M. T. Weller, S. E. Dann, P. F. Henry, D. B. Currie, *J. Mat. Chem.*, **9** (1999) 283.

[2] A. R. Armstrong, P. B. Bruce, *Nature*, **381** (1996) 499.

[3] International Centre for Diffraction Data, 12 Campus Boulevard, Newton Square Pennsylvannia, 19073-3273, USA, (1995).

[4] P. E. Werner, L. Erikson, M. Westdahl, TREOR, (Powder indexing program), *J. Appl. Cryst.*, **18** (1985) 367.

[5] CELL (Program to calculate the cell parameters from indexed powder data), University of Oxford.

[6] H. M. Rietveld, *Acta Crytallogr.*, **22** (1967) 151.

[7] H. M. Rietveld, *J. Appl. Crystallogr.*, **2** (1969) 65.

[8] G. Caglioti, A. Paoletti, F. P. Ricci, *Nucl. Instrum. Methods*, **35** (1958) 223.

[9] A. C. Larson, R. B. Von Dreele, *Generalised Structure Analysis System*, MS-H805, Los Alamos, MS-8745 (1990).

[10] P. W. Atkins, *Physical Chemistry*, 6th Edition, OUP, Oxford, (1988) 861.

[11] D. Guyomard, J. M. Tarascon, *J. Power Sources*, **54** (1995) 52.

[12] G. Vitins, Chem. Thesis Proposal, Riga (1999).

[13] W. Weppner, R. A. Huggins, Electrochemical methods for determining kinetics properties of solids, Annual Review of Materials Science, (1978) 269.

[14] W. Weppner, R. A. Huggins, *J. Electrochem. Soc.*, **124** (1977) 1569.

[15] *Impedance Spectroscopy*, Ed. J. R. Macdonald (Wiley, New York, 1987).

[16] *A Guide to Measurement Technology and Techniques*, Ed. M. Honda (Yokogawa-Hewlett-Packard Ldt., 1989).

[17] F.T. Ciacchi, K. M Crane, S. P. S Badwal, *Solid. State Ionics*, **73** (1994) 49.

[18] M. L Baygard, G. G. Barna, *J. Electroanal. Chem.*, **91** (1978) 201.

[19] U. von Alpen, M. F. Bell, H. H. Hofer, *Solid State Ionics*, **7** (1982) 345.

[20] M. G. S. R. Thomas, P. G. Bruce, J. B. Goodenough, *J. Electrochem. Soc.*, **132** (1985) 1521.

[21] C. Ho, I. D. Raistrick, R. A. Huggins, *J. Electrochem. Soc.*, **127** (1980) 343.

Chapter 3

Structural review of the ternary copper oxides

Synthesis in the Li-Cu-O system, Li_xCuO_2 (x = 2, 1) and $LiACu_2O_4$ (A = Li,Na)

3.1 Introduction

While vanadium, cobalt, nickel and manganese oxides have attracted most of the recent attention as cathode materials for rechargeable lithium batteries, a copper-based system would represent an ideal alternative. Copper is after all one of the most abundant metals. Such a metal as copper tends to be cheap and relatively harmless. So far, in the Li-Cu-O/S systems, lithium insertion has been investigated for several copper-containing compounds such as CuS [1], CuO [2], Li_2CuO_2 and $LiCuO_2$ [3].

Cupric oxide CuO was the first copper oxide studied as a cathode material in primary lithium batteries by Gabano *et al.* [2] in the seventies and later by Broussely *et al* and Takashi *et al* [4]. The overall cell reaction can be written as 2Li (s) + CuO (s) $\rightarrow$ Li_2O (s) + Cu (s) delivering a specific power density of 1.29 kWh kg^{-1} (Faradaic capacity of 573 mAh/g) based on the Gibbs free energy change of the previous reaction. The working discharge voltage of the lithium cupric (OCV of 3.3 V) was found to be lowered to 1.5 V due to electrochemical and chemical reductions involving Li_2O_2 and Cu_2O [4]. The Li/CuO cells, like Li/CuS, were produced on an industrial scale as replacement of conventional "1.5 V" primary batteries (MnO_2/Zn, HgO/Zn). More recently Tarascon *et al* [5], reported, as a part of the study on the 3d transition metal oxides MO_2 (M = Co, Ni, Cu, Fe) as negative electrode for the Li-ion batteries, the effect of the micrometer particle size of Cu_2O and CuO on their electrochemical properties toward lithium.

Li_2CuO_2 and $LiCuO_2$ were studied as eventual candidates for positive insertion materials by Arai *et al* [3]. The Cu^{3+}/Cu^{2+} redox couple in Li_2CuO_2 was shown to be active in the potential range of 2.5-3.7 V versus lithium. During the first cycle, 0.7 Li ions could be electrochemically extracted at 3.5 V and 0.5 Li ions inserted of at 2.5 V. The lithium extraction from $LiCuO_2$, synthesised chemically from Li_2CuO_2, was found to decompose at high potential into CuO and O_2.

There has been no electrochemical study to date that has been carried out directly on the lithium cuprates containing mixed valence Cu^{II}/Cu^{III}. In the present work, in order to investigate their electrochemical properties toward lithium (see Chapter 4), the syntheses of Li_2CuO_2, $Li_3Cu_2O_4$ and $LiCuO_2$ were carried out, each of them under different conditions.

In this chapter, after a structural review of the existing Cu(II) and Cu(III/IV)-based compounds, the characterisation using X-ray diffraction will be presented together with the structure of the new sodium substituted mixed-valence lithium cuprate $Li_2NaCu_2O_4$ by powder neutron diffraction.

3.2 Structural copper chemistry

The copper valencies exhibited in its common compounds are, copper 1 and 2. In addition, it may be oxidised to the states Cu^{III} and Cu^{IV}.

The relative stability of copper in the +II, +III and +IV state are of interest in this work and will be discussed individually in the following paragraphs with reference to the environment of the ions in the crystal. Emphasis will be given for the structure and coordination of the lithium copper oxides.

3.2.1 Structural chemistry of divalent copper

Divalency is the most important oxidation state for copper as it is the most commonly observed. In this state copper can be found in an extremely large number of compounds in widely varying coordination geometries. This gives divalent copper an extensive structural chemistry.

As a consequence of the d^9 electronic configuration observed for divalent copper, the Jahn Teller effect has a profound influence on the structural chemistry of copper in this oxidation state. The characteristic arrangement of electronegative ligands around the Cu^{II} is the distorted (4+2) octahedral one or less frequently a distorted tetrahedral arrangement. This arrangement may have one or two weaker orthogonal interactions. The geometries thus observed are generally referred to as "4", "4 + 1" and "4+2" (Figure 3.1). Due to this extensive structural chemistry of copper in the dipositive state, the respective geometries of the differing coordination number will subsequently be dealt with individual.

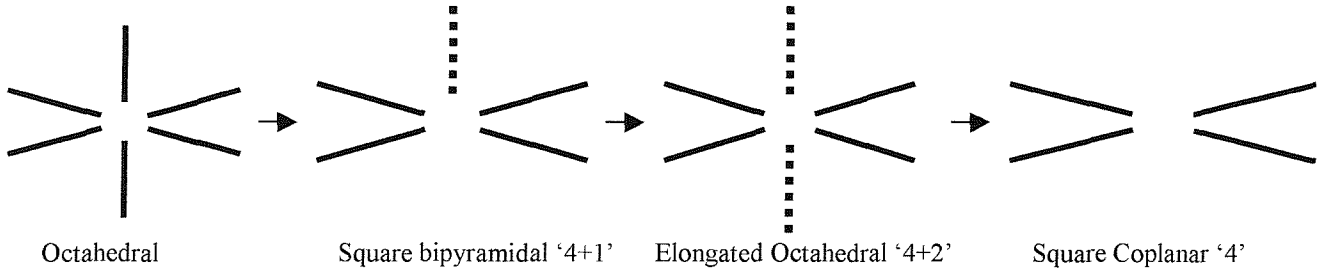

Figure 3.1 Regular and distorted structures for the copper (II) ion.

3.2.1.1 Divalent copper in 4-coordinate geometry

The formation of four coplanar bonds may be regarded as the limit of the extension of an octahedron along a 4-fold axis or a limit of compression of a tetrahedron along a 2-fold axis (normal to an edge).

Interactions with four coplanar oxygens are widely observed coordination geometry for divalent copper. The crystal field splitting for a square planar geometry is shown at Figure 3.2. The energies of the different orbitals are affected by the removal of the ligands. Among the e_g orbitals, since there is less repulsion between the ligand and the d_{z2} orbital, the energy of d_{z2} orbital drops. In the t_{2g} set, the effects are less marked since the orbitals do not point towards the ligands (Chapter 1 Figure 1.8). The result of the complete removal of the ligands is shown at Figure 3.2.

For example, divalent copper in Sr_2CuO_3 [6] or Li_2CuO_2 [7,8] tend to contain CuO_4 squares linked, either by edge or corner-sharing, to form infinite chains or sheets as shown at Figure 3.3 for Li_2CuO_2. For CuO_4 planes, the copper oxygen bond lengths vary typically between limits of 1.9 and 2 Å, most normally assuming bond lengths of 1.95 Å [8]. This type of geometry is regularly seen in many superconducting materials. Also, discrete square planes are known, for example in $Bi_2Cu_2O_4$ [9], but are much less commonly observed (Figure 3.4).

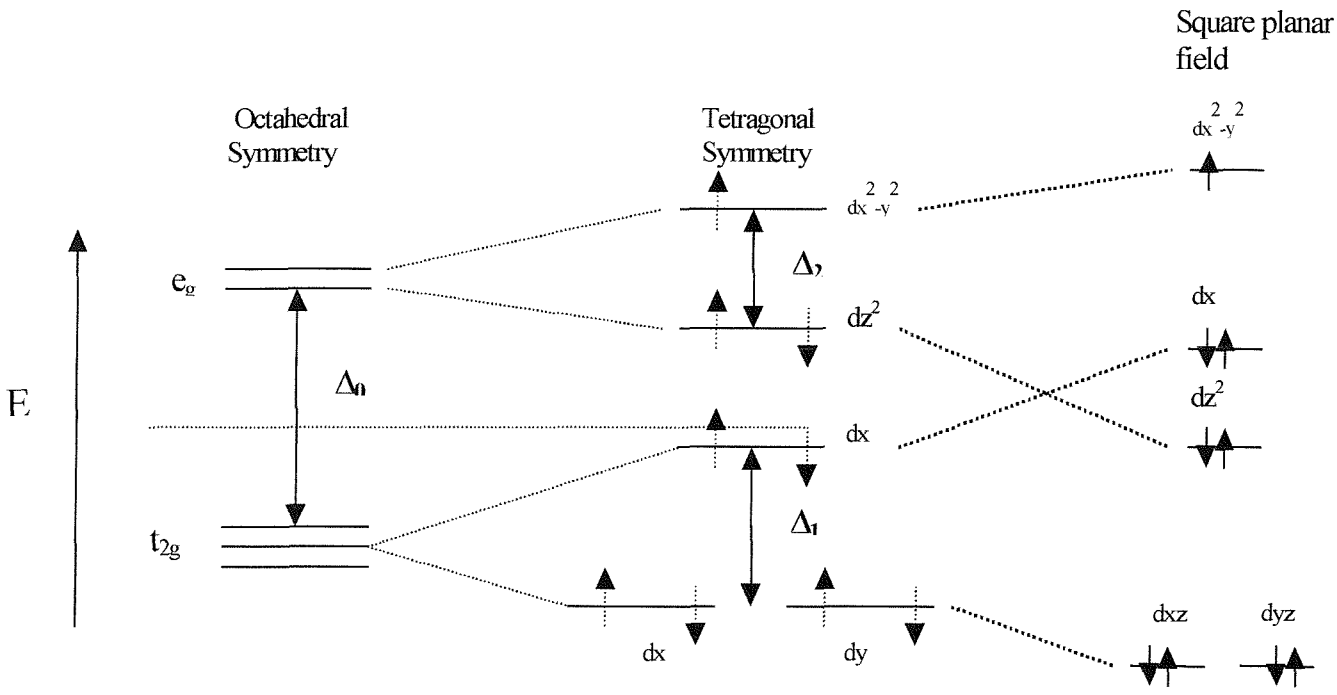

Figure 3.2 Energy level diagram of the square planar symmetry for a d^9 complex such as Cu^{II}.

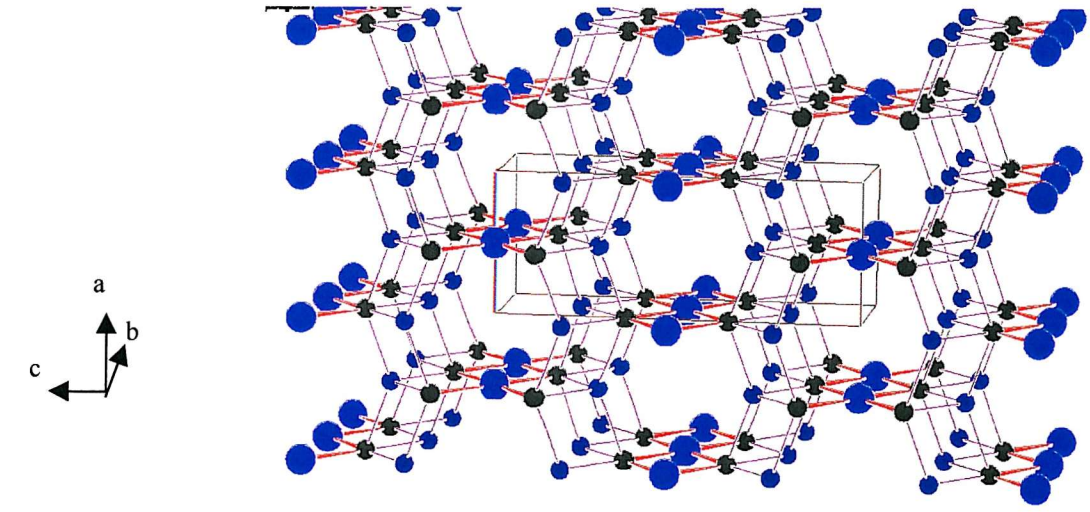

Figure 3.3 Corrugated chains of square-planar CuO_4 parallel to the ***b*** direction in the crystal structures of Li_2CuO_2. Black and light blue circles indicate oxygen and copper respectively. Lithium are shown as dark blue circles and occupy the centre of the tetrahedral ion cavities in Li_2CuO_2.

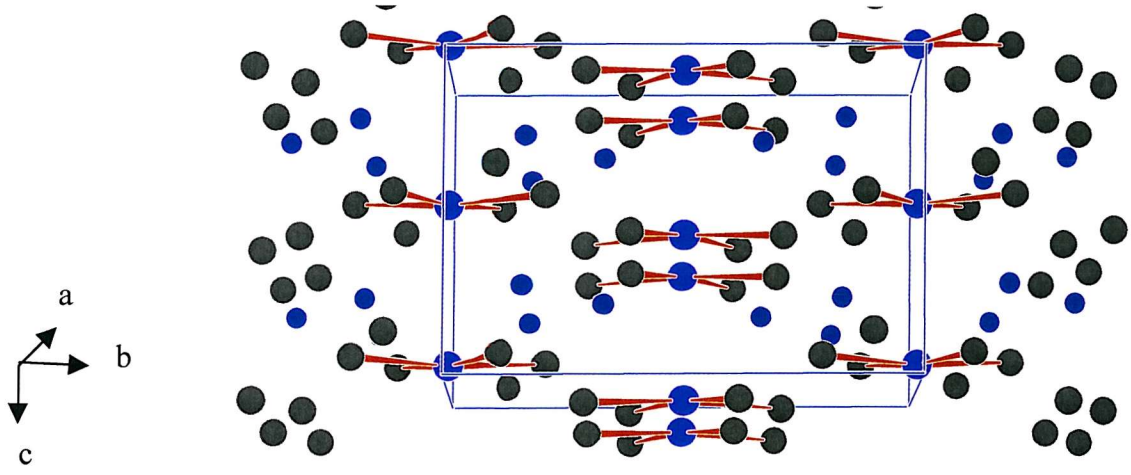

Figure 3.4 Structure of $Bi_2Cu_2O_4$ consisting of discrete CuO_4 square planes parallel to the *b* direction. Black and light blue circles indicate oxygen and copper respectively. Strontium are shown as dark blue circles.

3.2.1.2 Divalent copper in 5-coordination geometry

Divalent copper is regularly observed in 5-coordinate geometries. The geometries seen for such a coordination number are commonly trigonal pyramidal, and distorted square based pyramidal. Intermediate geometries to these two are also observed for copper in the divalent state.

The geometry predominantly observed for a coordination number of five is an elongated square based pyramid (Figure 3.1). In this structure, denoted as "4+1", the actual bond length is slightly longer than the values of 1.95 Å observed in square planar. The fifth interaction that forms the apex of the square is considerably weaker, resulting in bond lengths generally greater than 2.2 Å. As in the case of purely square planar structures, the linking of square planes either by edge or corner sharing to infinite chains and sheets, is regularly observed for "4+1" type geometries. Included among such structure are many of the superconducting materials. For example, in the widely $YBa_2Cu_3O_7$ superconductor, copper exists in two different coordination environments, square planar and square pyramidal.

Further distortions of the square based pyramids, in addition to those already described, are also observed. These are usually seen when the longer apical interaction is shorter relative to corresponding bonds in other structures. Under these circumstances one of the two ideal bond angles of 180° in the equatorial plane decreases whilst the other remains essentially unchanged. This distortion can be represented as a shift toward trigonal bipyramidal geometry.

For oxides containing copper in a trigonal bipyramidal geometry, the copper to oxygen bond lengths are generally observed between limits of 1.9 and 2.1 Å. In these bipyramids the five bonds lengths observed are frequently substantially different from one another. This specifically takes the form of the apical bonds being somewhat shorter than the corresponding equatorial bonds. In addition one of the five bonds, usually that of an equatorial interaction, is often observed to be longer than the remaining four bond lengths. As a result the trigonal bipyramids observed for divalent copper are often distorted. This distortion can be interpreted in terms of a shift of geometry toward the square based pyramidal geometry described previously.

Distortions for each of the two geometries examined above have been observed. Both of these distortions represent a shift toward a geometry that can be considered to be

intermediate geometry relative to those of trigonal bipyramidal and square based pyramidal. Such an intermediate geometry has been both observed and studied [10,11].

3.2.1.3 Divalent copper in 6-coordinate geometry

The structural chemistry of the 6-coordinate divalent copper is dominated by distorted octahedral geometry. The d^9 electronic configuration of the divalent ion means that the Jahn Teller effect has a significant influence and divalent copper is never observed in ideal octahedral geometry. As mentioned previously the Jahn Teller effect is a tetragonal distortion that takes the form of an elongation of the two trans bonds resulting in a material that can be classified as a "4+2" structure. This structure can be then considered to be a tightly bonded equatorial square plane with two additional weaker orthogonal interactions.

Many oxides contain divalent copper with such a geometry, including many of the superconducting oxides. In such materials, as has been previously observed in purely square planar or squared based pyramidal geometries, the linking of square by edge or corner sharing to form infinite chains or sheets is a common features.

The shorter equatorial bond length in "4+2" geometries are usually observed to be of comparable magnitude as those in "4"and "4+1" structures, generally falling between 1.95 and 2 Å The weaker axial bonds tend to be considerably longer, normally not falling below 2.2 Å. It can be as long as 2.6 Å and in such circumstances it becomes difficult to specify whether such interactions are significant and thus whether the structure should be classified as "4" or "4+2" type geometries. It is worth noting that the distortion from ideal geometry is not always as uniform as outlined above. Some octahedra distort to form what is denoted as a "4+1+1" geometry. In these configurations the axial bonds are, as before, longer than the corresponding equatorial ones but, individually, they have significantly different bond lengths. Such configurations are not unusual, occurring in many divalent copper compounds. Four bond lengths around copper in $PbCu_2(SeO_3)_3$ are reported as being between 1.9 and 2 Å with two additional orthogonal interactions at 2.32 and 2.59 Å. This example illustrates clearly such a "4+1+1" structure.

The tetragonal distortion outlined above is not the only possible consequence of the Jahn Teller effect. An elongation of the equatorial bonds leading to a "2+4" structure is equally as probable as a "4+2" geometry according to theoretical considerations of the Jahn Teller effect. This configuration, however, is rarely observed in practice. K_2CuF_4 is reported to have distorted octahedral coordination of fluorine around copper with two relatively short and four longer interactions of 1.95 and 2.05 Å respectively.

3.2.2 Structural chemistry of trivalent copper

Trivalency is, relative to the other oxidation states already considered an unfavoured oxidation state for copper. As a consequence the experimental conditions required in the synthesis of trivalent copper are necessarily severe *e.g.* under high pressure or in highly oxidising conditions. This constraint has limited the number of purely trivalent copper compounds known, relative to the large number of monovalent and divalent compounds. The known examples of trivalent copper tend to be composed of copper in combination with highly electronegative anions such as oxides and fluorides (*e.g.* Cs_3CuF_6) that are capable of stabilising the high oxidation state of the copper sites.

Trivalent copper differs from divalent copper in that the d^8 configuration of the trivalent ion means that it is not subject to Jahn Teller distortion. This electronic configuration is the same as Ni^{2+} ion. As a result the structural chemistry of trivalent copper has much in common with that observed for the divalent nickel ion. The favoured geometry of the d^8 configuration is square since in such geometry the strongly antibonding $d_{x^2-y^2}$ is elevated to high energy and left unpopulated (Figure 3.2). Thus purely square geometry is the most commonly encountered geometry for trivalent copper, in contrast to the distorted octahedral geometry that dominates the structural chemistry of divalent copper.

The anticipated square planar geometry is illustrated by the $[CuF_4]^-$ ion and oxide materials such as $MCuO_2$ (M = Li, Na, K, Rb, Cs). Much of the work on the previous trivalent copper oxides was done by Hoppe and co-workers [12]. $KCuO_2$, $RbCuO_2$ and $CsCuO_2$ [12,13] are all crystallised orthorhombic (*Cmcm*) whereas $LiCuO_2$ and $NaCuO_2$ [13,14] were found to adopt a monoclinic symmetry (C2/*m*). Differences also arise in their structure: while the chains in $KCuO_2$ are arranged in a corrugated manner, the chains in $LiCuO_2$ are closely placed (Figure 3.5). The Table 3.1 lists the cell parameters of the alkali metal trivalent copper oxides.

Table 3.1 Cell parameters of $MeCuO_2$ (Me = Li, Na, K, Rb, Cs) from references [12,14].

Me	*a*/Å	*b*/ Å	*c*/ Å	β/ °
Li [21]	5.733(1)	2.7176(3)	5.622(1)	120.68(2)
Na [20]	6.3512(2)	2.7474 (1)	6.1027(2)	120.767(2)
K [20]	4.3742(1)	11.6859(4)	5.4124(2)	
Rb [19]	4.78	12.02	5.43	
Cs [19]	5.22	12.19	5.43	

In these oxide materials the observed copper oxygen bond lengths are considerably shorter than the corresponding lengths for square planar oxides of divalent copper. They are typically 1.8 Å, this is 0.1 shorter than the corresponding length in square planar divalent copper compounds.

Although the predominant geometry observed for trivalent copper is the square planar one described above, trivalent copper is also found in octahedral geometry. The symmetrical occupancy of the d orbitals as a result of the d^8 electronic configuration means that the trivalent copper is not subject to Jahn-Teller effect and the octahedral symmetry around trivalent copper sites need not be distorted as is the case in the corresponding situation for divalent copper. The series of compounds M_3CuF_6 where M can be drawn from a number of group Ia and IIa metals, containing the octahedral $[CuF_6]^{3-}$ [16] ion are well known. Also, in $LaCuO_3$, the CuO_6 octahedra are essentially regular, that is not distorted [17]. In contrast, the $[CuO_6]$ octahedra in the perovskite based SrLaCuO4 [18] are reported as being tetragonally distorted in a manner similar to that regularly observed for divalent copper in octahedral geometry. Four of the bond lengths are reported as being 1.88 Å long with the remaining two reported as being greater than 2.2 Å.

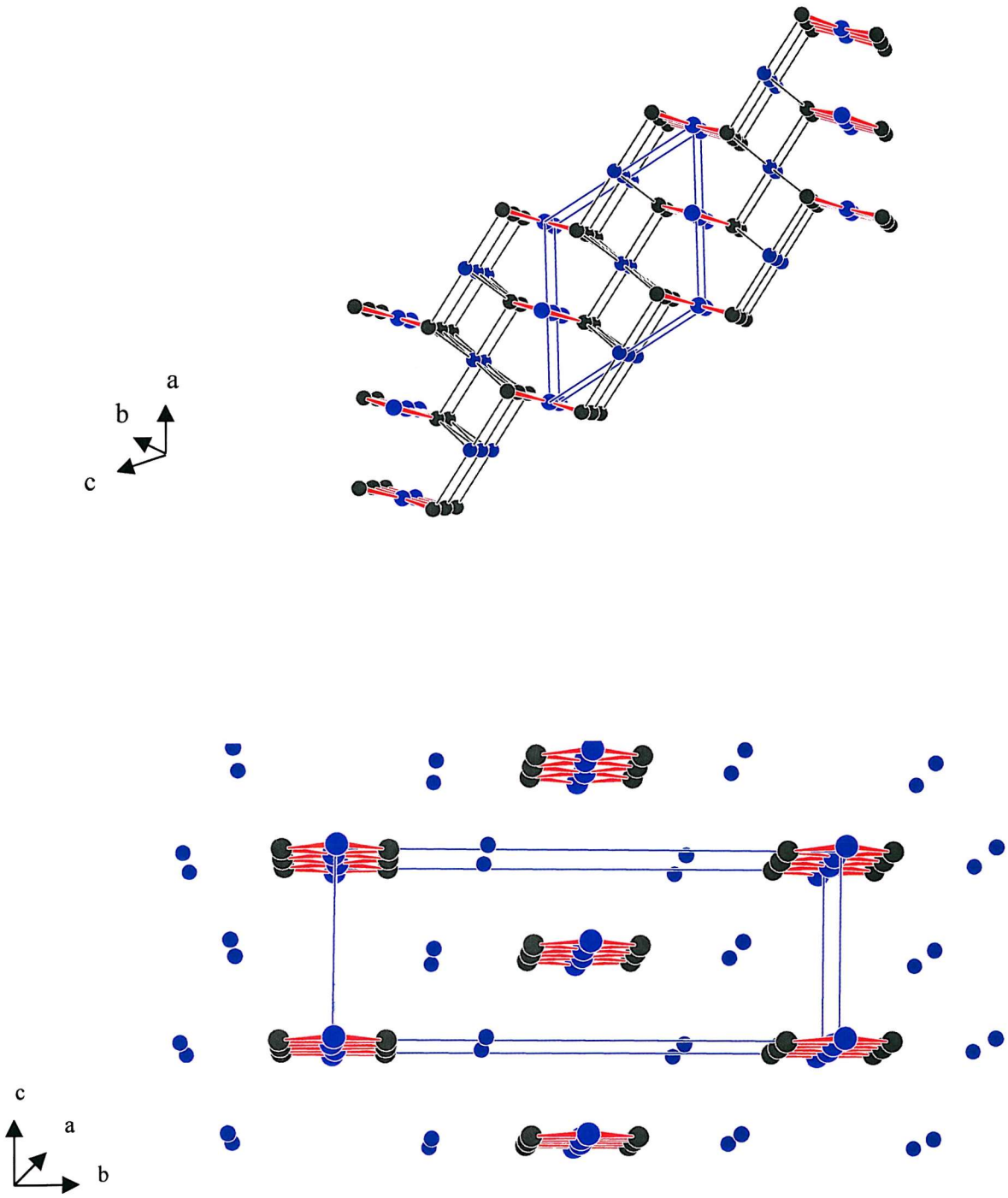

Figure 3.5 Crystal structures of $LiCuO_2$ and $KCuO_2$ showing the chains of square-planar $[CuO_4]$. Black and light blue circles indicate oxygen and copper respectively.

Top: lithium are shown as dark blue circles and occupy the centre of octahedral ion cavities in $LiCuO_2$.

Bottom: potassium are shown as dark blue circles and occupy the centre of prismatic ion cavities in $KCuO_2$.

3.2.3 Structural chemistry of tetravalent copper

There are very few compounds containing copper in this oxidation state. Consequently the structural chemistry of tetravalent copper is very limited. The fact that the electronic configuration of tetravalent copper is d^7 would suggest that the tetravalent ion should be subject to significant Jahn Teller distortion in low spin cubic symmetries. The compound most conclusively shown to contain copper in the tetravalent state is Cs_2CuF_6 [19]. This phase has been prepared by high pressure fluorination of a mixture of caesium and cupric chlorides. The material crystallises in a structure closely related to K_2PtCl_6 structure with a Jahn Teller distorted copper fluoride octahedron.

In conclusion, although little is known of the tetravalent copper ion it seems reasonable to expect that if any further compounds of tetravalent copper are to be observed, the copper site will be essentially octahedrally coordinated by electronegative anions such as fluoride and oxides.

3.2.4 Structural chemistry of mixed valence copper systems

There are a number of different compounds containing copper in mixed valences. The sulphide chemistry of copper is particularly complex with many sulphides containing copper in mixed valences between +I and +II known. Disregarding these complex materials there are still a large number of simpler mixed valence copper containing materials.

The most commonly observed mixed valence copper materials contain copper in its most stable oxidation states, that is, mono- and divalent oxidation states. $Cu_2SO_3.CuSO_3.2H_2O$ is an example of such a mixed valence salt. In this material the chemically different copper are accommodated on tetrahedral and distorted octehedral sites within the structure. These polyhedra are absolutely typical of geometries regularly seen for mono- and divalent copper. More specifically for oxide materials, there are only a few phases that contain mono- and divalent copper. The binary oxides, Cu_4O_3 [20] and Cu_3TuO_4 [21] have an average copper oxidation state of between I and II and again Cu^I is in linear coordination and Cu^{II} in a undistorted octahedral site. Also $TlCu_2O_2$ [22], $LiCu_2O_2$ [23] and $LiCu_3O_3$ [23] are all mixed valence materials. In the latter two materials, the individual valence coppers have been relatively easily differentiated, with the univalent copper forming

typical linear geometries in both materials and the divalent coppers forming equally typical "4+1" and "4+2" polyhedra.

There are a number of mixed di- and trivalent copper oxide materials. In fact trivalent copper is more regularly observed in materials in combination with divalent copper than in purely trivalent copper. $Li_3Cu_2O_4$ is a mixed valence compound of Cu^{II} and Cu^{III}, first synthesised by Klemm *et al.* [24]. The structure solved by powder X-ray and neutron data [25,27] contains infinite chains of edge sharing CuO_4 planes separated by lithium in octahedral and tetrahedral coordinations (Figure 3.6). A small distortion at 6% from a perfect square was found in the chains [27].

The mixed valence can also be considered to be the result of an oxygen excess non-stoichiometry in effectively divalent materials leading to copper oxidation. For example, phases such as $BaCuO_{2+x}$ and Ba_2CuO_{3+x} display such non-stoichiometry and as a result have small portions of trivalent copper present. Similarly some of the superconducting materials such as $YBa_2Cu_3O_{7-y}$ have oxygen non-stoichiometries and mixed di- and trivalent copper. The average copper oxidation state in many of these superconducting materials is approximately 2.33 highlighting the mixed valence. Structurally di- and trivalent copper are capable of assuming similar geometries and as a consequence the two valences cannot be as easily differentiated within a structure as is the case in the mixed mono- and divalent materials. Alternative methods of differentiating between the two different valence sites has been sought, *e.g.* bond valence calculations [28,29]. $Sr_2CuO_{3.9}$ [30] has shown the possibility of a mixed Cu^{III}/Cu^{IV} compound.

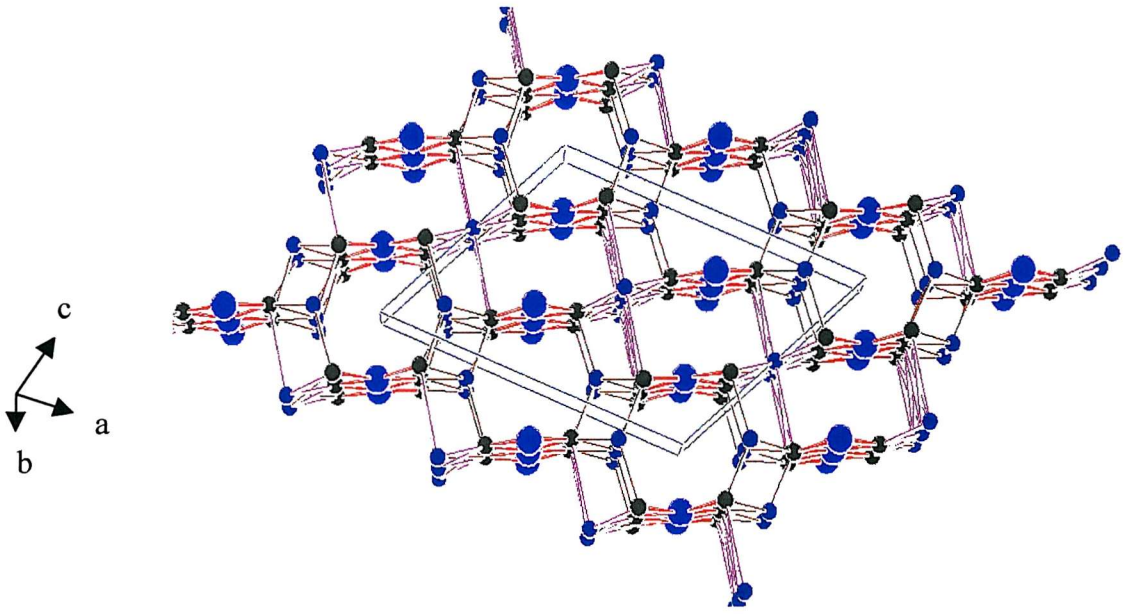

Figure 3.6 Corrugated chains of square-planar CuO_4 in the crystal structures of $Li_3Cu_2O_4$. Black and light blue circles indicate oxygen and copper respectively. Lithium are shown as dark blue circles occupying the centre of tetrahedral and elongated octahedral ion cavities.

3.3 Synthesis and characterisation of Li_xCuO_2 (x = 2, 1) and $LiACu_2O_4$ (A = Li, Na)

3.3.1 Introduction

As discussed previously, the copper, due to its unfilled d orbital exists under different oxidation states and thus, under different environments. With oxide ligands, the divalent and trivalent copper ions tend to contain CuO_4 square planes. In the Li-Cu-O system, several ternary lithium copper oxides have been prepared, containing Cu^{I}, Cu^{II} and Cu^{III}, such as $Li_3Cu_2O_4$ [24,27], Li_2CuO_2 [7], LiCuO, Li_3CuO_3 [31], $LiCu_2O_2$ [23] and $LiCuO_2$ [15]. The previous phases have all been structurally characterised and are shown on the following composition diagram (Figure 3.7). As part of our investigation of the electrochemical properties in the Li-Cu-O system, our work has focussed around the three phases (encircled on the graph) of and $LiCuO_2$, whose structures are presented in Figures 3.3, 3.6 and 3.5 respectively. They all consist of square-planar copper chains arranged in corrugated manner for Li_2CuO_2 and $Li_3Cu_2O_4$. The lithium occupy various environments; tetrahedral in Li_2CuO_2, octahedral in $LiCuO_2$ and both sites in $Li_3Cu_2O_4$.

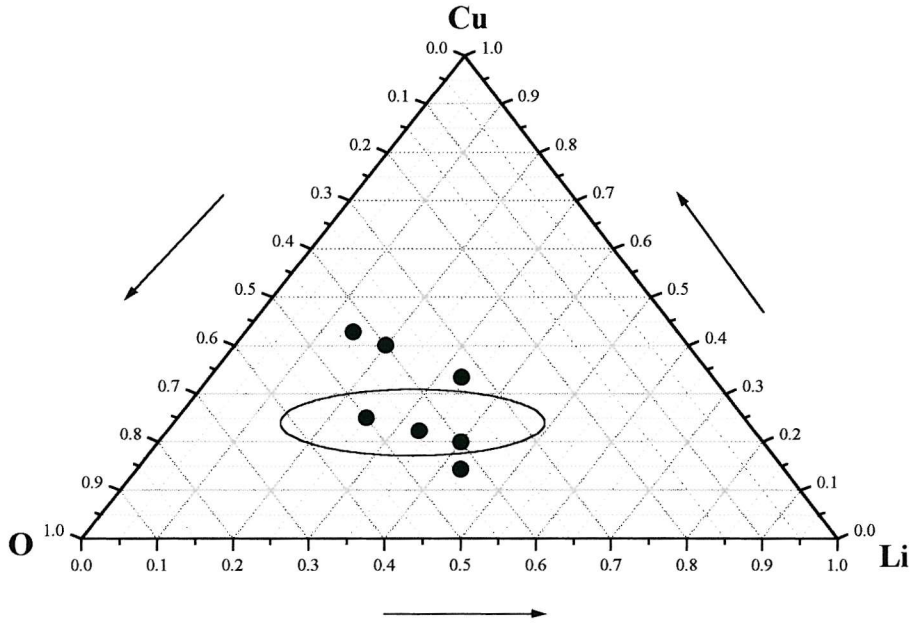

Figure 3.7 Composition diagram in the Li-Cu-O system showing from the top of the pyramid, $LiCu_3O_3$, $LiCu_2O_2$, LiCuO, $LiCuO_2$, $Li_3Cu_2O_4$, Li_2CuO_2, Li_3CuO_3. The phases circled are the ones synthesised in this work.

3.3.2 Li_2CuO_2

Li_2CuO_2 was obtained by a standard solid state reaction between $LiOH,H_2O$ (Aldrich, 98%) and CuO (Aldrich, 99%) at 800 °C for 12 hours in an alumina crucible. This phase has previously been synthesised by reaction of CuO with Li_2O [7] or Li_2CO_3 [8] at 600 °C and 720 °C respectively, for structural characterisation with single crystal, X-ray and neutron powder diffraction.

No structural refinement was undertaken since the angles and intensities of the present X-ray diffraction data agree with the previous structural studies of the compound. The purity was checked from the XRD pattern and less than 3% of CuO was found (Figure 3.8). The SEM picture at Figure 3.8 shows separate single crystallites of average size of 10 μm.

A sample was prepared at 400 °C in order to decrease the size of the crystallites but no change in the crystallite size was found.

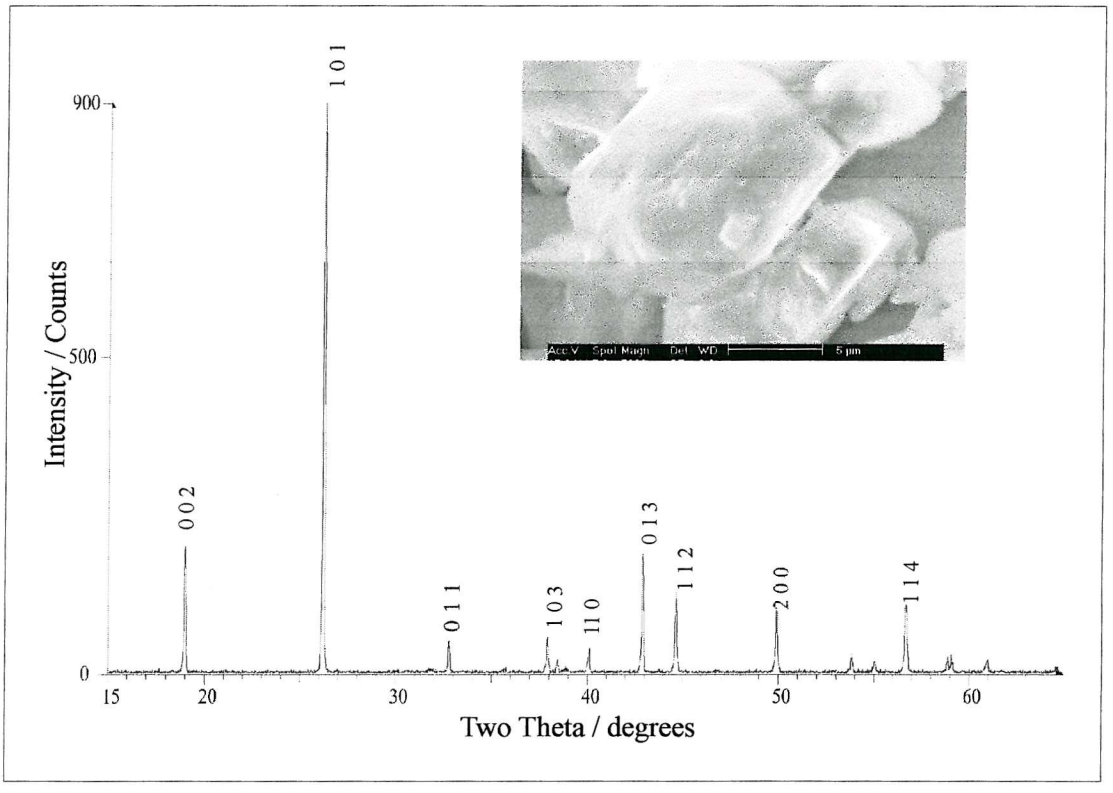

Figure 3.8 XRD pattern of the single phase Li_2CuO_2 indexed in an orthorhombic unit cell (*Immm*). The refined parameters are equal to a = 3.66 Å, b = 2.85 Å, c = 9.36 Å.

3.3.3 $LiACu_2O_4$ (A = Li, Na)

3.3.3.1 High-pressure synthesis and XRD identification of $Li_2ACu_2O_4$ (A=Li)

$Li_3Cu_2O_4$ was first synthesized by Klemm *et al.* [24] by the reaction of lithium and copper oxides at 300 °C over a period of several weeks and contains formally a mixed-valence compound of Cu^{2+} and Cu^{3+}. The structure has been solved from powder X-ray data following solid state synthesis in air [24,25] and from powder neutron diffraction after the synthesis under high oxygen pressure [26,27]. In this work, since the structure of $Li_3Cu_2O_4$ is known, the diffraction patterns of synthesised samples were compared with the calculated pattern (Figure 3.10). A different phase of stoichiometry $Li_{1.5}CuO_2$ was obtained by chemical deintercalation of lithium in Li_2CuO_2 using NO_2PF_6 in acetonitrile [32]. $Li_{1.5}CuO_2$ and $Li_3Cu_2O_4$ do not adopt the same symmetry.

Solid state synthesis of $Li_3Cu_2O_4$ was carried out in air and results in several parent phases. The high-pressure route allows a more facile and rapid synthesis of this phase in good purity and quantity. In fact, standard ceramic synthesis using Li_2O (Aldrich, 99%) and CuO (Aldrich, 99%) under flowing oxygen in air in the temperature range 400-500 °C gave, in addition to the desired compound, a large amount of Li_2CuO_2 and Li_2CO_3 and some residual CuO. The Figure 3.9 shows the X-ray patterns at 480 °C. At this last temperature, $Li_3Cu_2O_4$ began to form at the expense of the parent phases but still contains CuO after 6 weeks of heat treatment. At higher temperature Klemm *et al* [24] have shown more disproportionation and unreacted CuO. Therefore, a higher O_2 pressure is needed for a successful preparation of this phase for further characterisation.

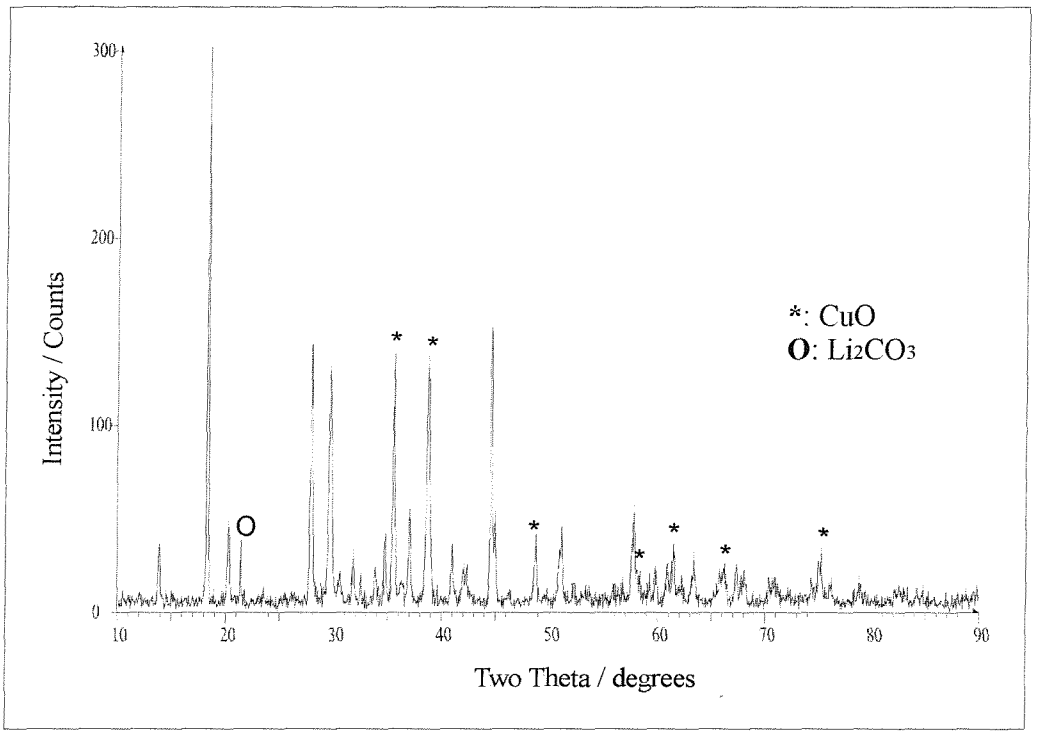

Figure 3.9 X-ray pattern of $Li_3Cu_2O_4$ at 480 °C containing residual CuO shown with asterisks. Li_2CO_3 is shown by **o.**

Pure phases of $Li_3Cu_2O_4$ could be obtained using high pressure flowing oxygen or hydrothermal synthesis.

A mixture of CuO (Aldrich, 99%) and Li_2O (Aldrich, 99%) was transferred into an open gold crucible and placed in the inner alumina tube of the high pressure oxygen apparatus. Excess of Li_2O (5%) was added to overcome losses through volatilisation. The synthesis was carried out in the flowing oxygen in the high pressure rig (250 atm) for several hours at 700 °C. The sample obtained will be called A sample.

In the hydrothermal synthesis, a stoichiometric mixture of Li_2O (Aldrich, 99%), Li_2O_2 (Aldrich, 99%) and CuO (Aldrich, 99%) was transferred in a gold tube that was sealed by arc-welding. The capsule was loaded into the high pressure vessel filled by water. A filler rod was added at the top to reduce the bomb volume. The temperature was allowed to rise with the bomb open to the outside reservoir . When the temperature of 600 °C was reached, the hydraulic pump was used to increase, step by step, the inner pressure to 1500 atm. The synthesis was carried out for 12 hours at 600 °C and at the pressure of 1500 atm. The sample obtained will be called B sample.

The A and B products, whose X-ray diffraction patterns and SEM pictures are shown at Figure 3.10, were well-sintered dark blue-black powders without traces of unreacted phases but only the formation of a slight amount of the parent phase Li_2CuO_2 in the compound prepared at pressure oxygen (sample A).

The refined parameters using the Cell program, for the B sample were found to be equal to a = 9.95 Å, b = 2.78 Å, c = 7.27 Å and β = 118.59 °. In both cases, rodlike crystallites of $Li_3Cu_2O_4$ were found to be of dimensions 2 x 2 x 10 μm (Figure 3.10).

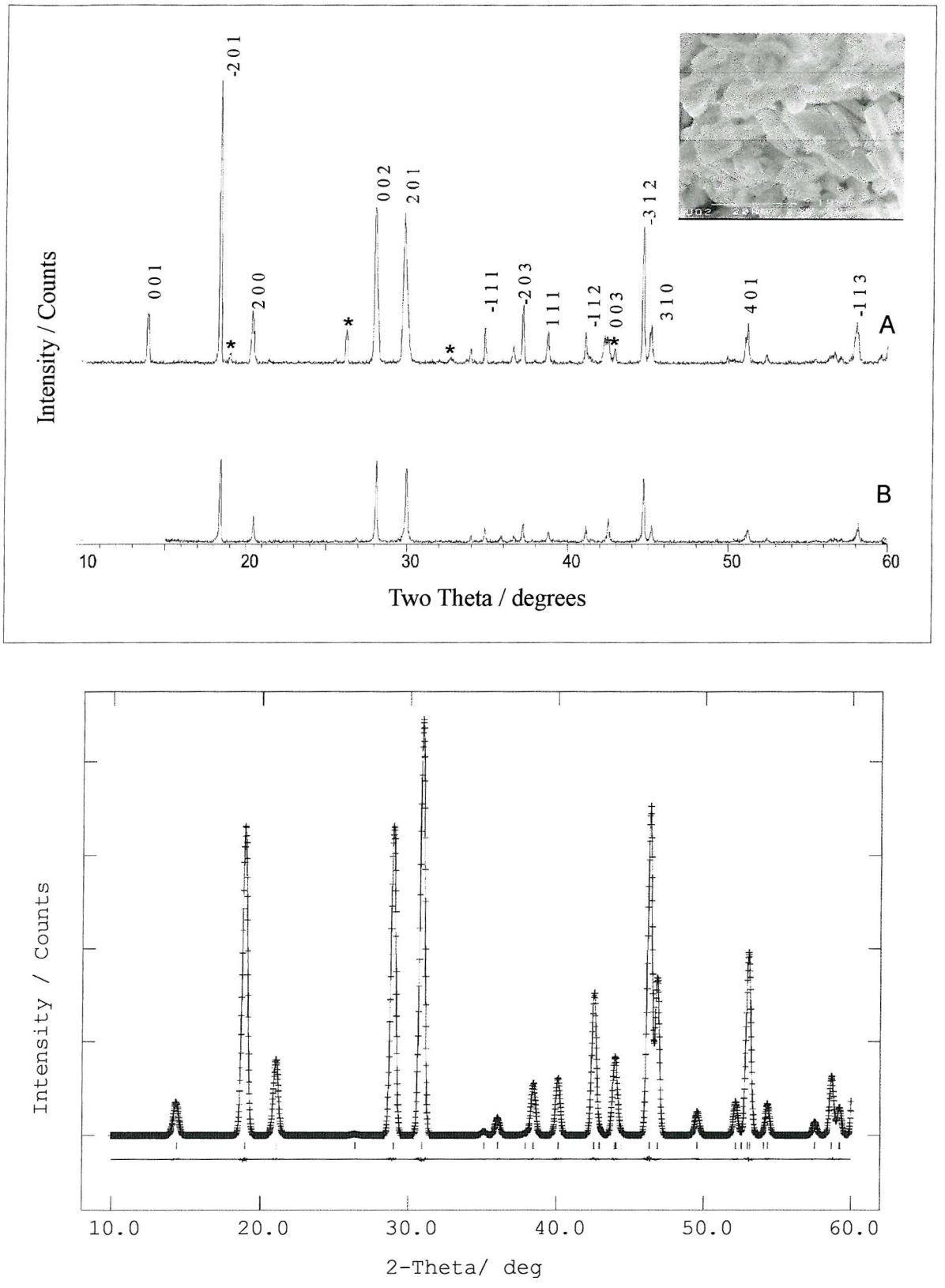

Figure 3.10 Top: X-ray patterns of $Li_3Cu_2O_4$ synthesised at A: high pressure under flowing oxygen (340 atm) and at B: hydrothermal (1500 atm). Asterisks * show the peaks of Li_2CuO_2. The peaks are indexed in a monoclinic unit cell.
Bottom: Calculated powder diffraction pattern of $Li_3Cu_2O_4$.

3.3.3.2 $Li_2ACu_2O_4$ (A=Na)

The first evidence of a new phase of stoichiometry $LiNaCuO_2$ in the system Li-Na-Cu-O was reported by Arai *et al* [3] in his study of the lithium insertion into $NaCuO_2$. New X-ray diffraction lines similar to Li_2CuO_2 were present after the lithium insertion into $NaCuO_2$ until the formula reached $Li_{0.2}NaCuO_2$ at 1.5 V. The cell parameters of the unit cell were determined by analogy with Li_2CuO_2 in the space group *Immm*, a = 4.01 Å, b = 2.81 Å, c = 9.80 Å [3]. The phase of $NaCuO_2$ showed low rechargeability with suggested sodium extraction, occurring during the first charge.

In this work, we investigate the synthesis and properties of a new sodium substituted $Li_3Cu_2O_4$ of stoichiometry $Li_2NaCu_2O_4$. Since two lithium sites are present in the structure of $Li_3Cu_2O_4$, the arrangement of the alkali cations over the tetrahedral and octahedral sites was studied by time-of-flight powder neutron diffraction on a sample made with ^7Li. A ^7Li MAS-NMR study of Li_2CuO_2, $Li_3Cu_2O_4$ and $Li_2NaCu_2O_4$ has been used to confirm the Li/Na ordering.

3.3.3.2.1 Synthesis

As a pure phase, $Li_2NaCu_2O_4$ could be obtained from a ground mixture of Li_2O (Aldrich, 99%), Na_2O (Aldrich, 98%) and CuO (Aldrich, 99%) in a gold crucible by heating at 700 °C under a high flow of oxygen at 250 atm for 4 hours.

Excess of Li_2O and Na_2O (10 %) were added to overcome losses through volatilisation. $^7Li_2O$ was made from $^7LiOH.H_2O$ (Aldrich, 99%) by dissolving in ethanol, adding hydrogen peroxide and firing the resultant precipitate at 700 °C.

^7Li was used instead of ^6Li to decrease the absorption of neutron by the lithium. This is possible due to a smaller absorption cross section of ^7Li (0.0454 barn) compare to Li (70.5 barn), the barn corresponding to the absorption cross section for 2200 m/s neutrons. The grey-black powder of $Li_2NaCu_2O_4$ contained traces of hygroscopic Li_2O and Na_2O and was kept in a dry atmosphere. Datas used for structure refinement were collected from a sample made with ^7Li for 2 hours on the Polaris medium resolution diffractometer at the Rutherford Appleton Laboratory. Data obtained from the backscattered detector, in a time-of-flight range of 3000-19580 μs were used for the refinement of $Li_2NaCu_2O_4$.

3.3.3.2.2 T. o. f. PND (powder neutron diffraction) of $Li_2NaCu_2O_4$

The similarity of the powder XRD pattern of $Li_2NaCu_2O_4$ shown in Figure 3.11, to that of $Li_3Cu_2O_4$ (Figure 3.10) was immediately apparent but with a significant shift in the reflection positions to the higher d-spacings. The lattice parameters were refined using the programme *Cell* and entered into GSAS programme [33] suite with the PND data, using the atoms positions and space group of $Li_3Cu_2O_4$. Neutron scattering lengths of –0.22, 0.771 and 0.5803, all 10^{-12} cm, were assigned to ^{7}Li, Cu and O respectively.

Initially the lattices parameters, profile coefficients and background were refined. The octahedral lithium site in $Li_3Cu_2O_4$ was found [27] to be split in disordered sites displaced from a mean octahedral position (½, ½, ½) to (0.579, 0.5, 0.561) with a site occupancy of 0.5. Sodium was initially placed on this mean position since it is considerably larger than lithium and could be expected to better fill the site. Refinement of all the positions and temperature factors led to a good fit, the introduction of anisotropic temperature further improved this fit.

The refinement of the sodium occupation, either by allowing vacancies or by substituting lithium, resulted in no change from full sodium occupation within 3 × e.s.d. In order to verify any possible lithium occupancy in disordered sites, the lithium was placed close to the mean position. The sodium and lithium occupancies in the octahedral site were then fixed to be equal to unity, by taking into account the different multiplicities of both sites. It was found to refine to a distant site with small fractional occupation and no improvement in fit statistics. The positive neutron scattering length of sodium and negative scattering length of lithium would make neutron diffraction sensitive to any disorder of this nature. The final fit statistics, obtained using the full neutron data set, are listed in Table 3.2
and the fit profile in Figure 3.12.

Table 3.2 Refined atomic co-ordinates for $Li_2NaCu_2O_4$ described on C2/*m*. Esds are given in parentheses

Atom	Site	Occupancy	x	y	z
Cu	4i	1	0.1617(2)	0	0.2530(2)
O1	4i	1	0.0680(2)	½	0.3127(2)
O2	4i	1	0.2528(2)	½	0.1809(3)
Li	4i	1	0.1357(4)	½	0.8774(6)
Na	2c	1	½	½	½

Atom	U11	U22	U33	U12	U13	U23
Cu	0.57(4)	0.30(3)	0.76(4)	0	0.52	0
O1	0.95(5)	0.64(4)	1.54(6)	0	1.04(4)	0
O2	0.93(6)	0.86(5)	1.03(6)	0	0.62(5)	0
Li	1.39(13)	1.79(13)	1.47(14)	0	0.62(11)	0
Na	1.59(10)	0.86(7)	1.39(9)	0	1.18(8)	0

Monoclinic, space group: C2/*m*, *a*=10.2733(2) Å, b = 2.80324(3) Å, c=7.58532(9) Å, β =119.6903(8)°

χ^2= 0.948 for 3661 observations and 44 variables, R_p= 3.78 %, R_{wp}= 1.56 % and R_{exp} = 1.28 %

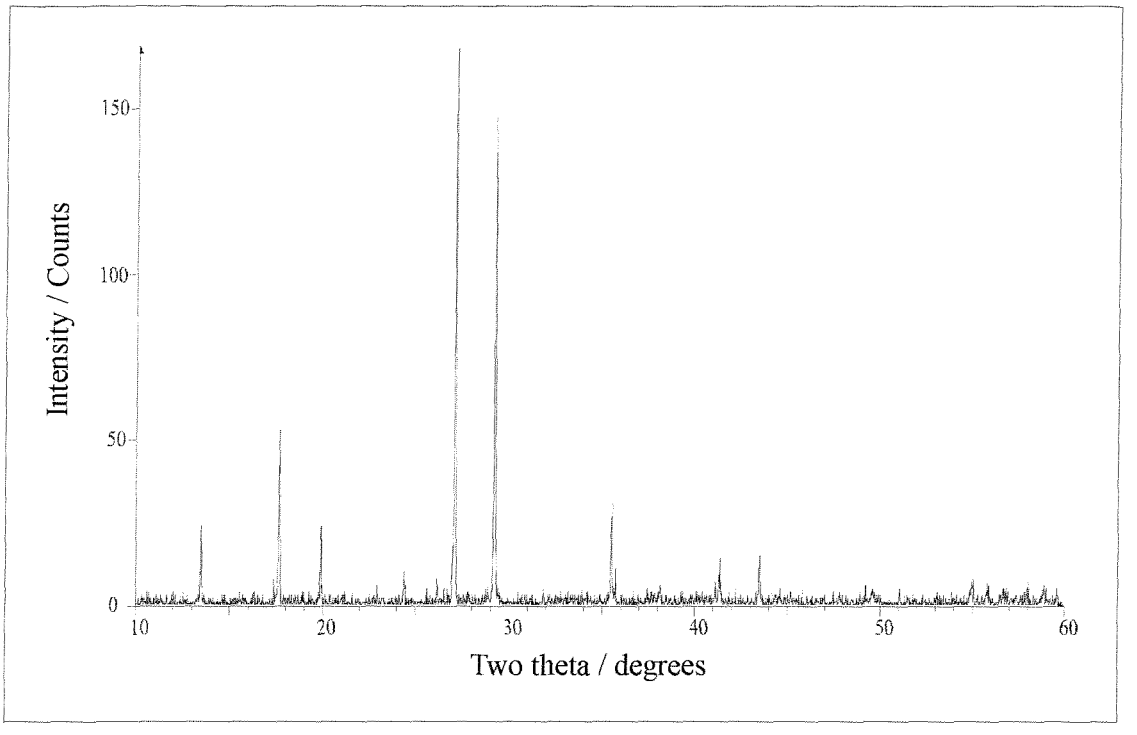

Figure 3.11 XRD pattern of $Li_2NaCu_2O_4$ showing similarity with $Li_3Cu_2O_4$ pattern at Figure 3.10.

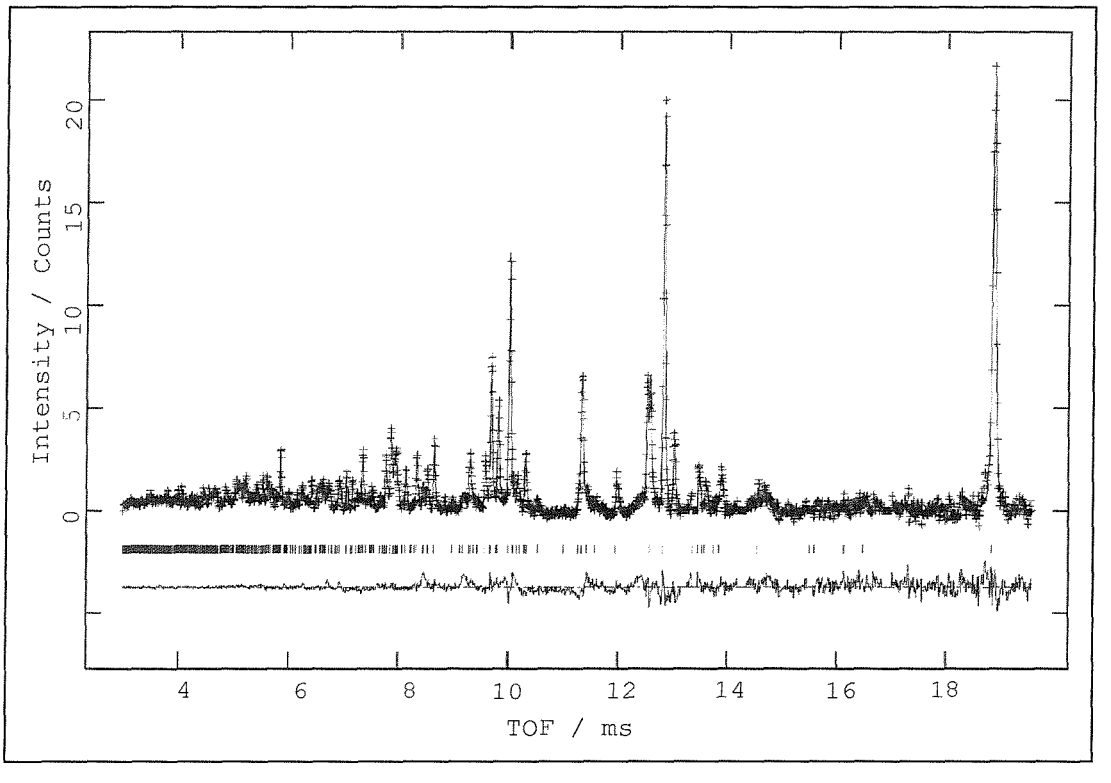

Figure 3.12 PND profile fit of $Li_2NaCu_2O_4$. The cross marks show experimental data, the upper continuous line calculated profile and the lower continuous line the difference. Tick marks show reflection positions. Time of flight (ms) can be converted to d-spacing (Å) by division by 6.17.

3.3.3.2.3 ^7Li MAS NMR

In order to investigate the lithium site populations of $Li_2NaCu_2O_4$, spectra were collected for the known Li_2CuO_2 (all tetrahedral sites for Li), $Li_3Cu_2O_4$ (1:2 for the octahedral:tetrahedral Li occupancy ratio) and $Li_2NaCu_2O_4$ (expected all tetrahedral sites for Li). Spectra are shown at Figure 3.13.

Li_2CuO_2 (spectrum A) has a single peak at around 340 ppm, with multiple spinning sidebands of lower intensities. This corresponds to the response of the tetrahedral lithium sites.

The spectrum of $Li_3Cu_2O_4$ (spectrum B) has two major features, a strong peak at close to 0 ppm and a smaller peak at around 400 ppm. The spinning sidebands do not allow accurate measurements of the relative intensity but these main features may be assigned as the octahedral lithium (O_h) and the tetrahedral lithium (T_d) respectively. In fact the tetrahedral site, closer to copper is more influenced by its electron and the chemical shift is positively shifted compared to the octahedral sites. The peak height ratio of about 5:1 (O_h:T_d) compares with a known compositional ratio of 1:2 in $Li_3Cu_2O_4$. This reflects the relative response of the two lithium sites.

The ^7Li NMR spectrum of the $Li_2NaCu_2O_4$ (spectrum c) shows a very different O_h:T_d (octahedral:tetrahedral) peak height ratio of approximately 3:4, *i.e.*, there is a marked reduction in the proportion of octahedral lithium ions. Combining the two data sets a ratio of octahedral:tetrahedral of about 1:7 is obtained. However there will be a large contribution to the tetrahedral peak in $Li_3Cu_3O_4$ from strong spinning sidebands of the octahedral peak so that the real ratio will be much higher. It is thus not possible to give accurate occupancy for octahedral and tetrahedral sites in $Li_2NaCu_2O_4$ from the present MAS NMR experiment. But the data confirm the expected coordinations found by neutron diffraction.

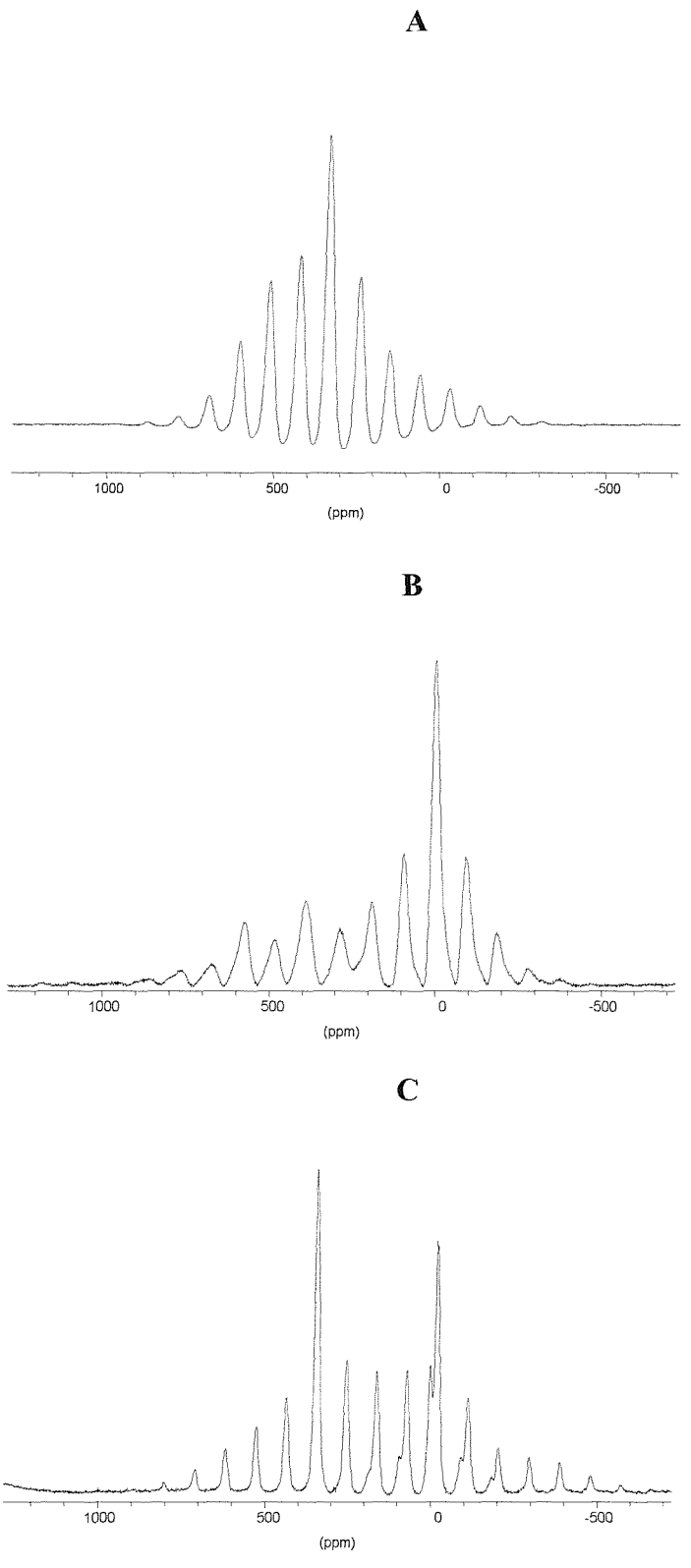

Figure 3.13 ^{7}Li MAS-NMR of Li_2CuO_2 (a), $Li_3Cu_2O_4$ (b) and $LiNaCu_2O_4$ (c)

3.3.3.2.4 Structure of $Li_2NaCu_2O_4$

The structure of $Li_2NaCu_2O_4$ (Figure 3.14) is found to be very similar to that of $Li_3Cu_3O_4$ with small increases in the lattice parameters as would be expected to result from the substitution of lithium with larger sodium ions. In $Li_2NaCu_2O_4$, the average Cu-O bond length of 1.895 Å is slightly shorter than the distance in $Li_3Cu_3O_4$ of 1.910 Å, possibly reflecting the underbonding of the octahedral lithium site in this material. The tetrahedral lithium site has an average Li-O distance of 1.964 Å, comparable with the 1.931 Å distance in the all-lithium material. The average Na-O distance in the octahedral site is 2.385 Å which agrees with the prediction from ionic radii of 2.40 Å [34].

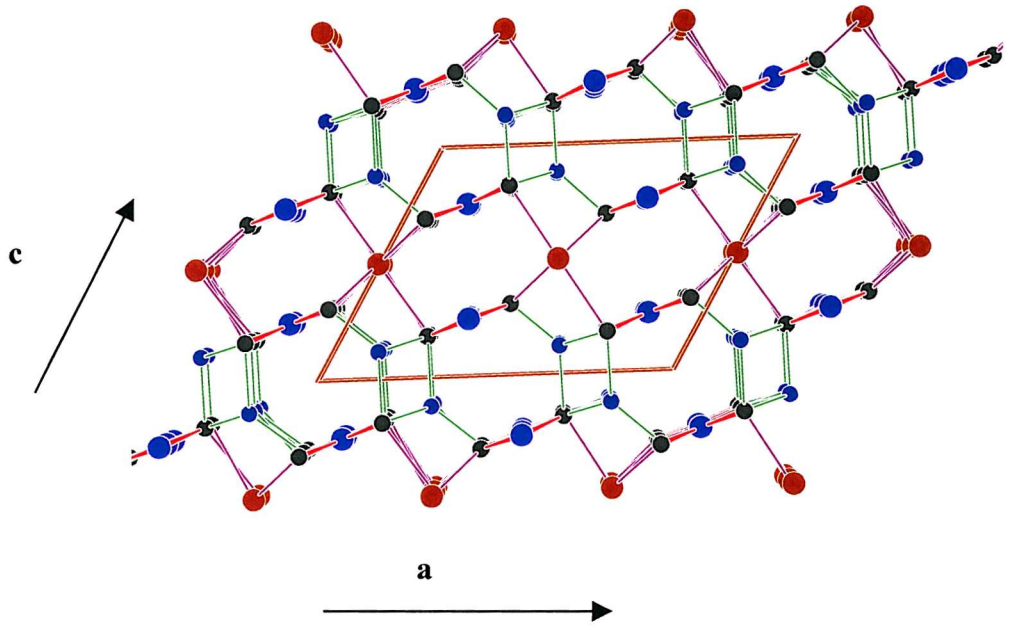

Figure 3.14 Crystal structures of Li_2NaCuO_2 showing the coordination geometries of Na and Li (red and dark blue spheres respectively). O and Cu are shown as black and light blue spheres respectively.

3.3.4 $LiCuO_2$

3.3.4.1 Room temperature synthesis of $LiCuO_2$

The previous synthesis of $LiCuO_2$ was described by Wizanski *et al* [32] and Imai e*t al* [35] through delithiation of Li_2CuO_2. In the first case, the chemical extraction using NO_2PF_6 in acetonitrile gave a mixture of two phases, Li_2CuO_2 and $Li_3Cu_2O_4$. Using iodine as an oxidising agent in acetonitrile, a single phase of $LiCuO_2$ was obtained. In the latter case, tetrabutylammonium iodide was added as a complexing agent to dissolve CuI, formed by a reaction of iodates ions with Li_2CuO_2 and $LiCuO_2$, as a complex such as CuI_2^-. Also tetrabutylammonium iodide produces I_3^-, which reacts faster with Li_2CuO_2 than I_2. In such reactions, CuO was formed in addition to the desired phase; a further disadvantage of this technique is the low yield.

A comparison of the redox potentials shows that the oxidation power of Br_2 (E^0 Br_2/Br^- = 1.065 V) is higher than I_2 (E^0 I_2/I_3^- = 0.536 V). The use of bromine by Berger *et al* [26] was found to accelerate the chemical delithiation of Li_2CuO_2 at room temperature. Therefore, bromine was tried in the present work of the delithiation of $Li_3Cu_2O_4$ obtained from the previous high pressure hydrothermal reaction (Figure 3.10). The delithiation was carried out using 70-fold excess of Br_2 in acetonitrile for five hours at room temperature. $Li_3Cu_2O_4$ (0.12 g, 0.56 mmole) and Br_2 (~1 ml, 20 mmole) were mixed and left under stirring The equation of the reaction with Br_2 is as follows:

$$2Li_3Cu_2O_4 + Br_2 \xrightarrow{CH_3CN} 4\ LiCuO_2 + 2Li^+ + 2Br^-$$

After several washes in the pure solvent of acetonitrile to remove LiBr and after being dried, the X-ray diffraction pattern of the product (Figure 3.16) has also shown in this case the presence of the parent phase CuO (marked by asterisks). A smaller soaking time could have reduced the formation of CuO. The crystallites have kept more or less their original shape with however the appearance of more asperities on the surface. The rods are now of average size of 5 μm (Figure 3.15).

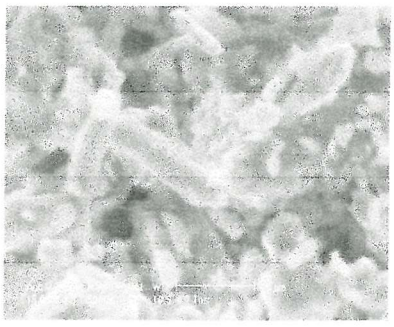

Figure 3.15 SEM picture of $LiCuO_2$ after the chemical extraction in Br_2/ CH_3CN.

3.3.4.2 Structure refinement

Data for $LiCuO_2$ were collected on a Siemens D5000 diffractometer operating with $CuK\alpha_1$ radiation over a period of 5 hrs. The data could be indexed in both monoclinic and orthorhombic unit cells. The models are very similar since the main structural difference between the orthorhombic and monoclinic models concerns the orientations of the oxygen atoms, while the heavy copper and lithium sites are practically identical. The scattering power by copper dominates in the X-ray case, which explains why the two different models may give identical results at first sight.

In fact a controversy exits between two models. Utsimu *et al* [36] have shown that $LiCuO_2$ transforms from an orthorhombic symmetry to a monoclinic one by applying pressure. However recent work [14] indicates however a preference for a monoclinic $NaCuO_2$-type structure at ambient pressure.

The refinement of X-ray diffraction data was undertaken using the GSAS Rietveld refinement programme [33] using both structures as starting models. The orthorhombic symmetry did not allow the refinement to converge and was rejected. The refinement using the monoclinic description was then carried out as follow.

Initially the background, profile coefficients, the lattice parameters and atomic positions were refined. The isotropic temperature factors were fixed equal to the value of 10 and 15 Å. Since their refinement led to very high values, they were not permitted to vary. The refined parameters for $LiCuO_2$ can be seen at Table 3.5.

3.3.4.3 Surface area and particle size

The surface area measurements were carried out using the BET method employing a Micromeritics Gemini 23670 instrument for the different lithium copper oxides. By substituting in the Sherrer formula $B(2\theta) = 0.9\ \lambda\ /L_m \cos\theta$, the widths of the Bragg peaks at half of their maximum intensity $B(2\theta)$ in radians, the average crystallite size L_m (Å) could be deduced.

Table 3.4 Surface area and crystallite size for the different lithium copper oxides synthesised.

Compounds	m^2/g	Average crystallite size by SEM (μm)	with Sherrer formula (Å)
Li_2CuO_2	1.05	10 (square shape)	680
$Li_3Cu_2O_4$	1.5	2 × 2 × 10 (rodlike shape)	700
$LiCuO_2$	15	5 (rodlike shape)	<600

Significant broadening of the peaks at high angles is noticed for $LiCuO_2$ due to possible strains or disorders in the structure. The surface area for this compound is much higher. The material seems to have decomposed during the BET heat treatment as the XRD pattern after the BET has confirmed. For the other oxides, the particle sizes are in accordance with the surface area found.

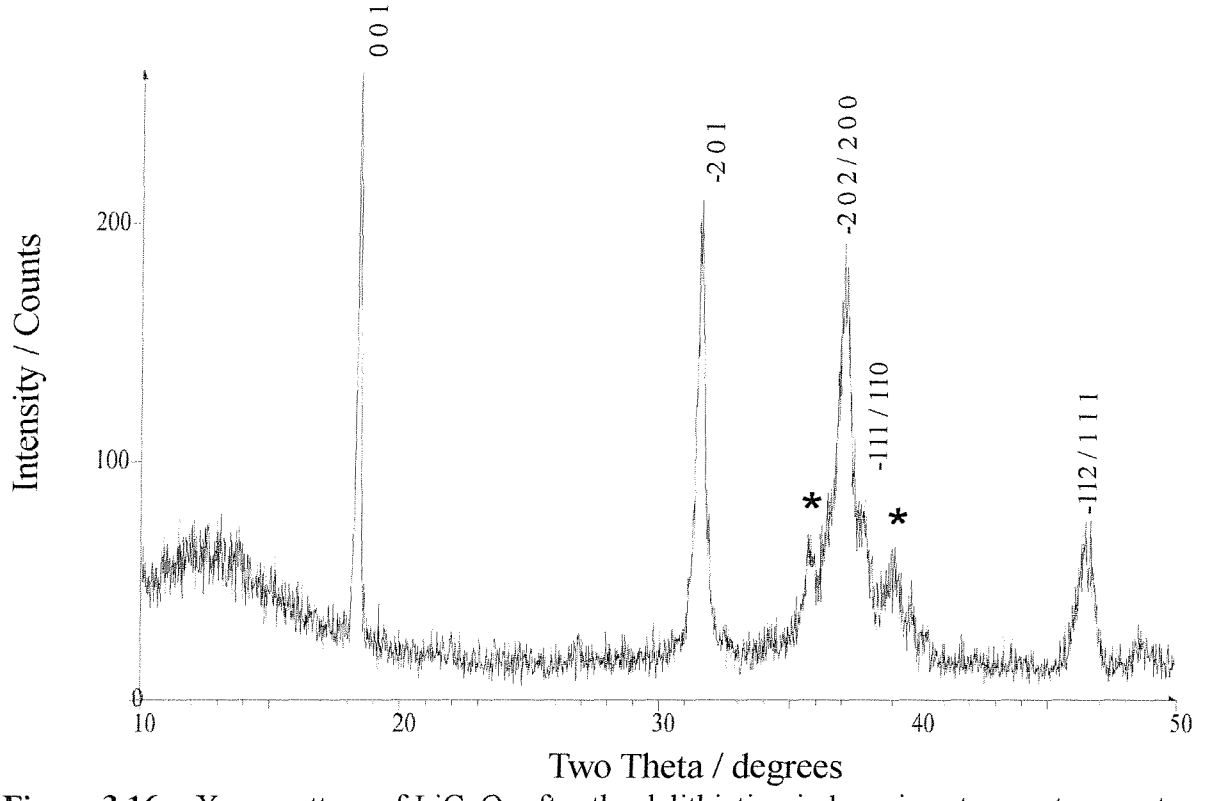

Figure 3.16 X-ray pattern of $LiCuO_2$ after the delithiation in bromine at room temperature. The peaks are indexed in the monoclinic *C*2/*m* unit cell. The asterisks indicate the presence of CuO.

Table 3.5 Refined atomic co-ordinates for $LiCuO_2$. Standard errors are given parentheses.

Atom	Site	Occupancy	x	y	z	$U_i/U_e/Å^2$ (×100)
Li	2b	1	0.5	0	0.5	10
Cu	2a	1	0	0	0	15
O	4i	1	0.32(1)	0	0.61(1)	15

Monoclinic, space group C2/*m*, a = 5.061 (3), b = 2.508(1), c = 4.931(4) Å, β = 119.95(3) °

χ^2 = 1.09 for 1999 observations and 45 basic variables, R_p= 16.7 %, R_{wp}= 22.3 %.

3.4 Conclusion

The existence of different oxidation states accessible by copper, suggests that the lithium copper oxides contain significant redox charge density and therefore justify its use for cathode material in lithium rechargeable batteries.

The relatively easy and fast synthesis of Li_2CuO_2, $Li_3Cu_2O_4$ and $LiCuO_2$ by a standard ceramic reaction in air, under high pressure and by "chimie douce" at room temperature respectively, is an advantage for battery application. The purity of the phases was found to be very good (less than 3% of CuO) for Li_2CuO_2 and $Li_3Cu_2O_4$. The phase obtained by delithiation of Li_2CuO_2 using a bromine treatment, contains CuO. The replacement of the lithium by the sodium ions in the octahedral sites in $Li_2NaCu_2O_4$ was shown to be successful and is aimed to investigate the effect it causes on the pathway of the lithium ions during the cycling.

The structures of the lithium copper oxides synthesised all consist of one-dimensional infinite chains of the stoichiometry CuO_2. Transitions between these oxides are expected to occur during the insertion and removal of Li ions. The similarity of their structure will contribute to the stability of the materials during the charging and discharging of the material.

Cu^{II} and Cu^{III} adopt respectively a d^9 and d^8 electronic configuration with fully occupied t_{2g} levels and two or one electrons in the e_g orbitals. The location of the Fermi level in the higher energy e_g orbitals, compared with the lower energy t_{2g} orbitals in the conventional Co^{III} used in $LiCoO_2$, is expected to result in an average voltage slightly lower for the oxidation of Cu^{2+} to Cu^{3+}.

The electrochemical properties will be developed in the following chapter together with the investigation of phase transitions followed by *in* and *ex-situ* X-ray diffraction in the electrode material. The results of the measurement of electronic transport and chemical diffusion coefficient for Li ions in $Li_2Cu_3O_4$ and Li_2CuO_2 will be discussed with reference of their electronic structure and electrochemical performances.

3.5 References

[1] L. Dechenaux, G. M. Gerbier, J. F. Laurent, *Revue Bimastriella Entropie*, **13** (1967) 15.

[2] J. P. Gabano, US Patent, **3** (1967) 542.

[3] H. Arai, S. Okada, Y. Sakurai, J. Yamaki, *Solid State Ionics*, **106** (1998) 45.

[4] J. P. Gabano in *Lithium Batteries*, Academic Press, (1983) 91.

[5] S. Grugeon, S. Laruelle, R. Herrera-Urbina, L. Dupont, P. Poizot, and J-M. Tarascon, *J. Electrochem. Soc.*, **148** (2001) A285.

[6] C. L. Teske, H. Müller-Buschbaum, *Z. Anorg. Allg. Chem.*, **371** (1969) 325.

[7] R. Hoppe and H. Rieck, *Z. Anorg. Allg. Chem.*, **379** (1970) 157.

[8] M. T. Weller, D. R. Lines, *J. Solid State Chem.*, **82** (1989) 21.

[9] J. C. Boivin, J. Thehoux, D. Thomas, *Bull Soc. Fr Minèr Crystallogr.*, **99** (1976) 193.

[10] B. J. Hathaway, *Structure and Bonding*, **57** (1984) 55.

[11] H. Effenberg, *J. Solid State Chem.*, **73** (1988) 118.

[12] K. Hestermann, R. Hoppe, *Z. Anorg. All. Chem.*, **367** (1969) 249.

[13] N.E. Brese, M. O'Keeffe, R.B. von Dreele, V.G. Young, Jr., *J. Solid State Chem.*, **83** (1989) 1.

[14] R. Berger, L Tergenius, *J. Alloys Comp.* **203** (1994) 203.

[16] W. Levason, M. D. Spicer, *Coord. Chem. Rev.*, **76** (1987) 45.

[17] D. B. Currie, M. T. Weller, *Acta Crystal.*, **C47** (1991) 696.

[18] J. B. Goodenough, G. Demazeau, M. Pouchard, P. Hagen-Muller, *J. Solid State Chem.*, **8** (1973) 325.

[19] W. Harnischmager, R. Hoppe, *Angew. Chem. Int. Ed.*, **12** (1973) 582.

[20] M. O'Keefe and J. O. Boivin, *Amer. Mineral*, **63** (1978) 180.

[21] K. J .Range and F. Ketterl, *Z. Naturforsch.*, **B32** (1977) 1356.

[22] A. Adam, C. Felser-Wenz, H. U. Schuster, R. Hope, *Z. Anorg. Allg. Chem.*, **597** (1991) 6.

[23] S. J. Hibble, J. Köhler, A. Simon , S. Paider, *J. Solid State Chem.*, **88** (1990) 534.

[24] W. Klemm, G. Wehrmeyer, H. Bade, *Z. Electrochem. Ber. Bunsenges. Phys. Chem.*, **63** (1959) 56.

[25] M. T. Weller, D. R. Lines, D. B. Currie, *J. Chem. Soc. Dalton Trans.*, **11** (1991) 3137.

[26] R Berger, *J. Less-Common Met.*, **169** (1991) 33.

[27] D. B. Currie, M. T. Weller, *J. Mat. Chem.*, **3** (1993) 229.

[28] W. H. Zachariasen, *Acta Crystallogr.*, **16** (1963) 385.

[29] I. D. Brown, *Acta Crystallogr.*, **33B** (1977) 1305.

[30] R. C. Lobo, F. J. Berry, C. Greaves, *J. Solid State Chem.*, **88** (1990) 513.

[31] H. N. Migeon, A. Courtois, M. Zanne, C. Gleitzer,, J. Aubry, *Rev. Chimie Miner.*, **12** (1975) 203

[32] A.R. Wizansky, P.E. Rauch, F.J. Disalvo, *J. Solid State Chem.* **81** (1991) 203.

[33] Generalised Structure Analysis System, (GSAS). A. C. Larsen, R. B. von Dreele, MS-H805 Los Alamos National Laboratory, MN 87545, (1990).

[34] R. D. Shannon, *Acta Cryst.*, **32 A**, (1976) 751.

[35] K. Imai., M. Koike, H. Takei, H. Sawa, D. Shiomi, K. Nozawa and M. Kinoshita, *J. Phys. Soc. Jpn.*, **61** (1992) 1819.

[36] W. Utsumi, K. Imai, M. Koike, H. Takei, T. Yagi, H. Takahashi, N. Mori, *J. Solid State Chem.*, **107** (193) 507.

Chapter 4

Electrochemical properties of Li_xCuO_2 (x = 2, 1) and $LiACu_2O_4$ (A = Li, Na) as insertion cathode materials

4.1 Introduction

The electrochemical properties of the lithium copper oxides prepared in the Chapter 3, *i.e.* Li_2CuO_2, $Li_3Cu_2O_4$ and $LiCuO_2$ were tested as positive insertion materials in rechargeable lithium batteries. The stability of the host structure is essential for the reversibility of the insertion reaction and *in-situ* experiments were carried out to check the integrity of the electrode during the cycles. The number of lithium ions participating to the insertion-extraction processes has been estimated from the charge through the systems and the slanted plateaux correspond to two-phase reactions. The structural changes accompanying the cycling of the materials have been confirmed by *ex-situ* and *in-situ* X-ray diffraction, as well as the formation of other phases.

The insertion of lithium in $Li_3Cu_2O_4$ was found to be more difficult than in the conventional $LiCoO_2$ or $LiNiO_2$, as shown by the measurement of the diffusion coefficient. However $Li_3Cu_2O_4$ and Li_2CuO_2 exhibit a relatively high conductivity with a small activation energy for $Li_3Cu_2O_4$ that could be associated with hopping electron conductivity in the mixed valence $Cu^{3+/2+}$ state.

4.2 Experimental

In this study, the composite electrodes were prepared using a dry method technique described in Chapter 2 (2.11.1). An attempt to use a slurry of the material, Kynar Flex 2801 and carbon in THF, using a Doctor Blade technique, was unsuccessful due to a decomposition of the active material. The fraction of the polymer binder used polytetrafluoroethylene (PTFE) was kept equal to 5 wt %. The active material and the carbon black represent 70 wt % and 25 wt % respectively.

When the carbon black Monarch 1400 was used, *e.g.* for $Li_3Cu_2O_4$, the amount of carbon black was increased in order to maintain the resistance of the film below 10 Ω. The effect of the composition on the performance of the materials was out of the scope of this work. The results of the recent works by Mandal *et al* [1] and in the laboratory by S. Spong *et al* [2] were used to determine the black carbon fraction of 25 wt %. It was shown that the effective conductivity of the film increases with the fraction of the black carbon. The relationship is not linear. The conductivity increases rapidly until a threshold of carbon black percolation is achieved. In the case of $LiMn_2O_4$ with the same dry technique, the percolation

threshold for a maximum of conductivity is of 7 wt % (resistance of the film of *c.a.* 16 Ω) and even lower for a maximum of capacity (5 wt %)[2].

Thin films of average thickness 0.15 mm were obtained. The positive electrodes were cut equal to 1.1 cm of diameter. The pellets were dried under vacuum for 10 h at 130 °C and the cells assembled under argon atmosphere in a glove box (Unilab, Mbraun, USA). The characteristics of the pellet and conditions of cycling are reported for each material.

The *in-situ* XRD was performed using the *in-situ* cell described at Chapter 2 Figure 2.9. As the reflection mode was used, low intensities at low angles are collected. The overlapping with the peaks of the beryllium window was not a problem for the *in-situ* experiment of the lithium copper oxides $Li_3Cu_2O_4$ since the peaks were all separate.

4.3 Insertion electrode properties of Li_xCuO_2 (x = 2, 1.5, 1) Comparison of the cycling for $Li_3Cu_2O_4$ and $Li_2NaCu_2O_4$

4.3.1 Lithium extraction from Li_2CuO_2 and following cycles

The Figure 4.1 shows the charge and discharge profile of the Li/Li_2CuO_2 cell between 1.8 V and 3.8 V at a constant current of 0.2 mA over the sample mass of 24.8 mg (surface of the pellet: 0.95 cm^2). The characteristics and conditions of cycling for Li_2CuO_2 are reported at Table 4.1.

An increase followed by a sudden decrease in the potential during the first charge is characteristic of a nucleation of a new phase.

The plateau at 3.4 V corresponds to the removal of ~1.2 Li ions in Li_2CuO_2 up to 3.8 V. During the following discharge, at 2.8 V, the capacity of 190 mAh/g corresponds to the insertion of ~0.8 Li ion in $Li_{0.8}CuO_2$ according to the process $0.8Li + Li_{0.8}CuO_2 \rightarrow Li_{1.6}CuO_2$. A loss of 100 mAh/g in the initial capacity indicates that irreversible changes take place.

The following charges show plateaux centered at 3.05, 3.2 and 3.3 V *vs* Li. A gradual loss in the discharge capacity causes discharge capacity fading of 8% after 4 cycles. The attribution of the two-phase reaction to the plateaux at Figure 4.1 is based on the present electrochemical process and the following X-ray diffraction study(see 4.4.1).

Table 4.1 Characteristics and conditions of cycling for Li_2CuO_2.

Preparation of Li_2CuO_2	High temperature solid state reaction in air of CuO and $LiOH,H_2O$ at 750 °C (see chapter 3 section 3.3.2)
Weight Ratio Active Material/Black Carbon/PTFE	75:20:5
Type of Black Carbon	Acetylene Black
Weight of active material / mg	18.6
OCV / V	2.87
Theoretical Specific Capacity $mAhg^{-1}$ (based on total Li extraction)	489.4
Cycling Rate/ mAg^{-1}	10.8
Initial Practical Discharge Rate	C/17.7

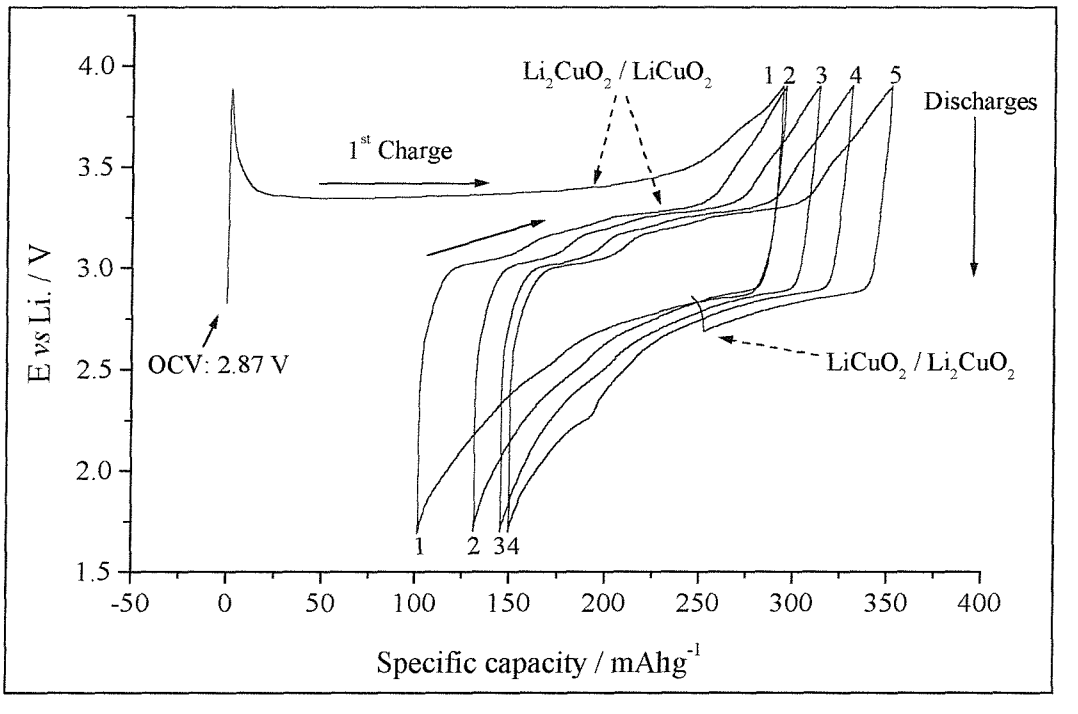

Figure 4.1 Charge and discharge profile of Li/Li_2CuO_2 between 1.7 and 3.8V at a constant current of 0.2 mA. Composition of electrode: 75% of the oxide, 20% of Acetylene Black and 5% of PTFE. Weight of the active material in the pellet : 18.6 mg.

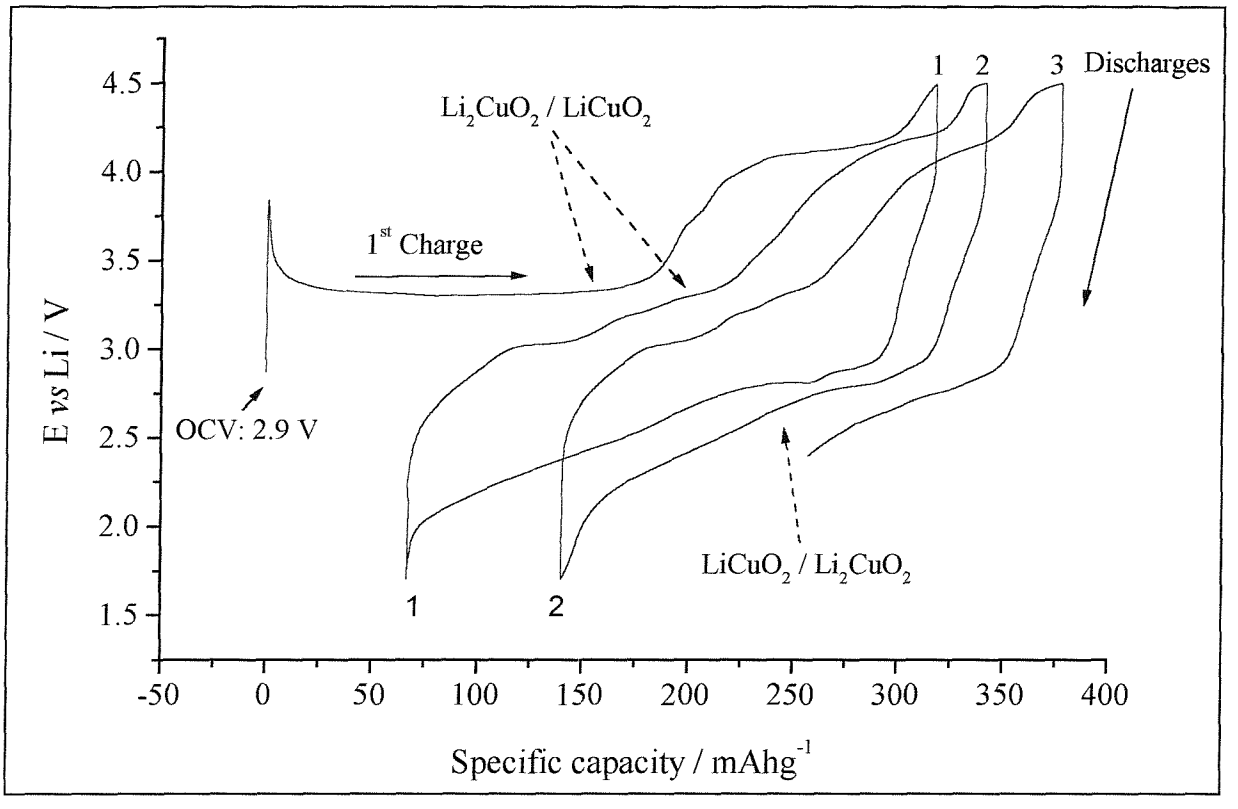

Figure 4.2 Charge and discharge profile of Li/Li_2CuO_2 between 1.7 and 4.5 V at a constant current of 0.2 mA. Composition of electrode: 75% of the oxide, 20% of Acetylene Black and 5% of PTFE. Weight of active material: 18.3 mg.

When charged up to 4.5 V *vs.* Li. at the same rate (Figure 4.2), an initial capacity of 320 $mAhg^{-1}$ (~1.35 Li ions), corresponding to the plateaux situated at 3.4 (200 $mAhg^{-1}$, 0.8 Li ions) and 4.2 V (120 $mAhg^{-1}$), is obtained for an electrode having the same characteristics than previously. The additional plateau at 4.2 V does not correspond to any electrolyte decomposition but to the irreversible decomposition according to $Li_xCuO_2 \rightarrow CuO + ½\ O_2 + xLi$. This is followed by an impressive discharge density of 250 $mAhg^{-1}$ (~1.2 Li ions) distributed mostly between 3 and 2 V. The discharge process proceeds according to $1.2Li + Li_{1.2-x}CuO_2 \rightarrow Li_2CuO_2$. The irreversible initial capacity is less than for the previous example (70 $mAhg^{-1}$) but the capacity faded more rapidly. The attribution of the two-phase reactions at the plateaux (Figure 4.2) is based on the present electrochemical process and the following X-ray diffraction study (see 4.4.1).

4.3.2 Application of Li_2CuO_2 as an additive in positive electrode with $LiMn_2O_4$.

The high initial charge density of Li_2CuO_2, 330 $mAhg^{-1}$ delivered at 3-4.5 V *vs.* Li. suggests a possible use as additive in positive electrode of $LiMn_2O_4$. Like the tetragonal LT-$LiMnO_2$, it could be well suited to compensate the irreversible loss of lithium in the passivation of the negative carbon electrode estimated to be of 10 % of the initial capacity [3].

Li_2CuO_2 shows little capacity above 3 V on the following discharge (Figures 4.1 and 4.2) and would not interfere with the discharge performances of $LiMn_2O_4$. It also possesses a relatively high electronic conductivity of 10^{-3} S cm^{-1} (section 4.5.2).

The Figure 4.3 shows the first cycles between 3.2 V and 4.5 V at a constant current of 0.2 mA over the sample mass of 22.4 mg (surface of the pellet: 0.95 cm^2) of a pellet having a nominal composition of 60 % of $LiMn_2O_4$ (Sedema), 15 % of Li_2CuO_2 (solid state reaction between LiOH and CuO at 750 °C), 20 % of Shawinigan carbon black and 5 % of PTFE (binder). On the first charge, the overvoltage noticed at 4.2.1 is present and corresponds to the nucleation of the particles in the beginning of the extraction.

The expected first charge capacity of 162 $mAhg^{-1}$ is based on the contribution of $LiMn_2O_4$ (115-120 $mAhg^{-1}$) and Li_2CuO_2 (330 $mAhg^{-1}$) for 80 % and 20 % of the total active material (16.8 mg), respectively. The results on the charge and discharge capacities are at Figure 4.3. The first charge was found to be equal exactly to the expected capacity of 162 $mAhg^{-1}$. The reversible discharge capacity becomes 92 $mAhg^{-1}$ corresponding to $LiMn_2O_4$ being the only material active in the range 3-4.5 V vs. Li.

Figure 4.4 shows the charge and discharge capacities after 15 cycles, calculated for the mixture Li_2CuO_2 + $LiMn_2O_4$ and for $LiMn_2O_4$ only. The first discharge of $LiMn_2O_4$ only is found to be equal to 115 $mAhg^{-1}$. Without any Li_2CuO_2, the spinel material itself covers the irreversible capacity loss. The first capacity on charge would have been of ~115-120 $mAhg^{-1}$ and the first discharge capacity of ~100 $mAhg^{-1}$ due to the loss of lithium on the layer. The effect of the Li_2CuO_2 additive was shown to increase the initial capacity and to compensate the irreversible capacity loss. The amount of additive was chosen in the present case, higher than the amount needed to balance this loss.

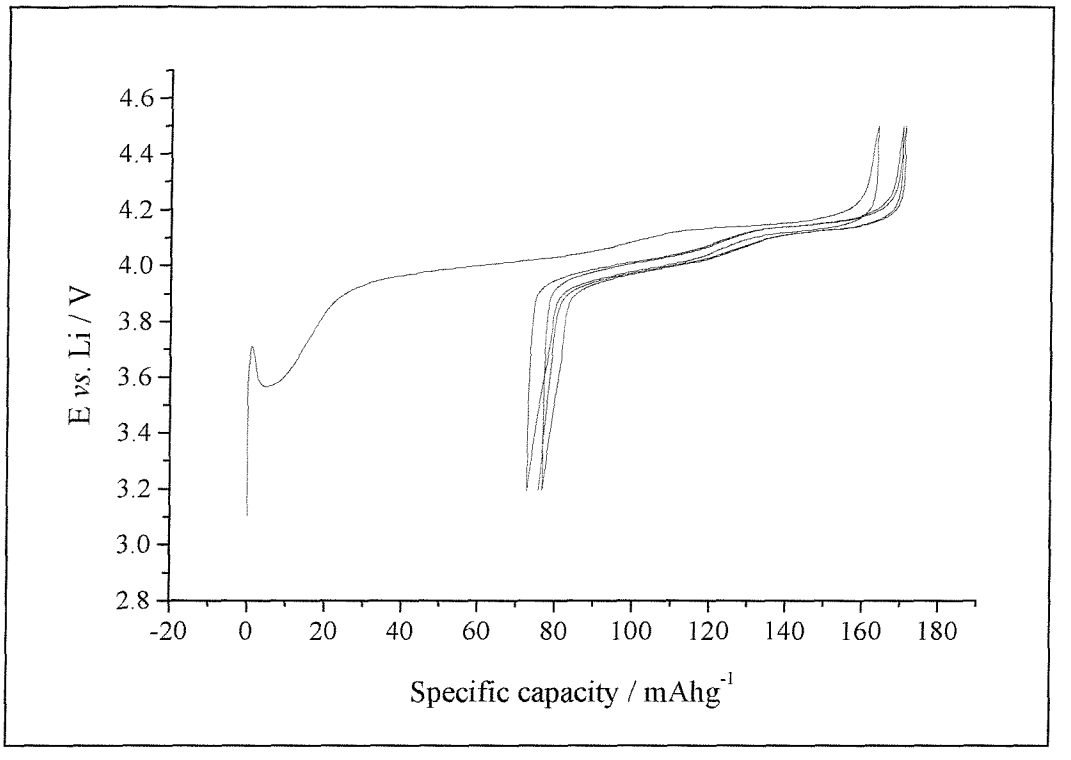

Figure 4.3 Charge and discharge profile of Li/Li_2CuO_2 (20 % of AM) + $LiMn_2O_4$ (80 % of AM) between 3.2 and 4.5 V at a constant current of 0.2 mA. Composition of electrode: 75% of the oxides, 20% of Acetylene Black and 5% of PTFE. Weight of active material: 16.8 mg.

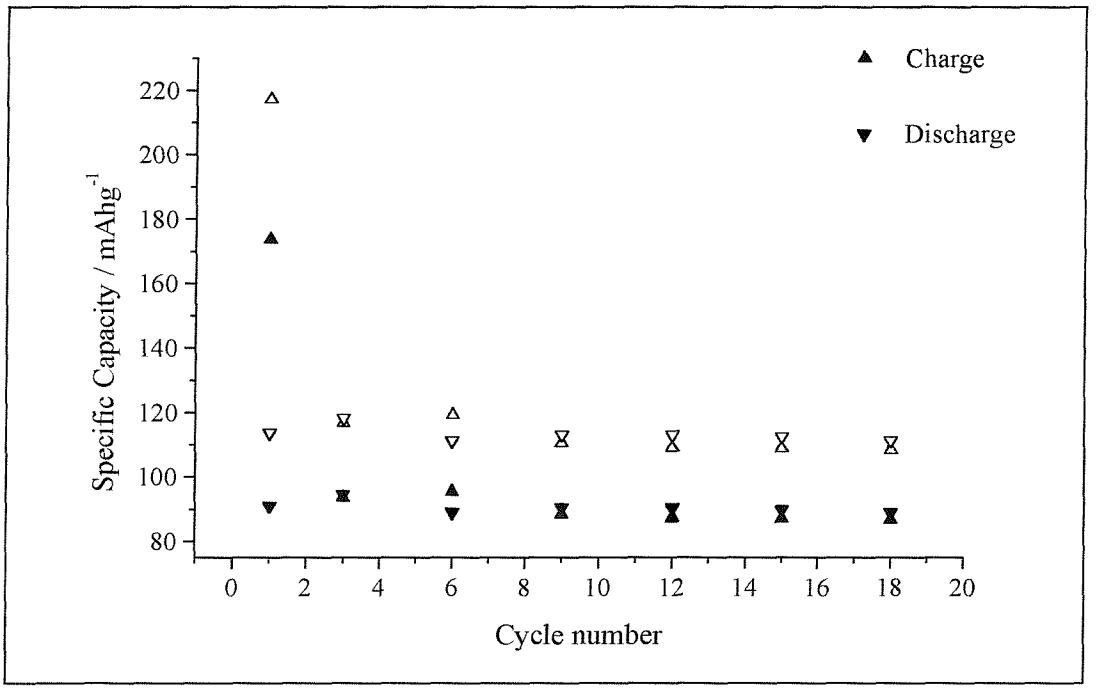

Figure 4.4 Capacity retention with the cycle number of both $Li/Li_2CuO_2 + LiMn_2O_4$ and of $Li/LiMn_2O_4$ cells. The open triangles show the calculated capacities for $LiMn_2O_4$ only, the plain ones with Li_2CuO_2 as additive. A capacity of 120 $mAhg^{-1}$ is recovered on the first discharge showing the role of Li_2CuO_2 to compensate the irreversible capacity for $LiMn_2O_4$.

4.3.3 Lithium extraction from $Li_2ACu_2O_4$ (A = Li, Na) and following cycles

4.3.3.1 Lithium extraction from $Li_3Cu_2O_4$ and following cycles

In the Figure 4.5, we report the cycling behaviour of the $Li/Li_3Cu_2O_4$ cell at a constant current of 0.15 mA (surface of the pellet: 0.95 cm^2) between 1.6 and 4.5 V over the sample mass of 27.2 mg. The characteristics and conditions of cycling for $Li_3Cu_2O_4$ are reported at Table 4.2.

Table 4.2 Characteristics and conditions of cycling for $Li_3Cu_2O_4$.

Preparation of $Li_3Cu_2O_4$	High pressure hydrothermal at 600 °C under 1500 atm (see chapter 3 section 3.3.3)
Weight Ratio Active Material/Black Carbon/PTFE	60:35:5
Type of Black Carbon	Carbon Black (Monarch 1400)
Weight of active material / mg	16.3
OCV / V	2.92
Theoretical Specific Capacity $mAhg^{-1}$ (based on total lithium extraction)	379.2
Cycling Rate/ mAg^{-1}	9.2
Initial Practical Discharge Rate	C/17.4

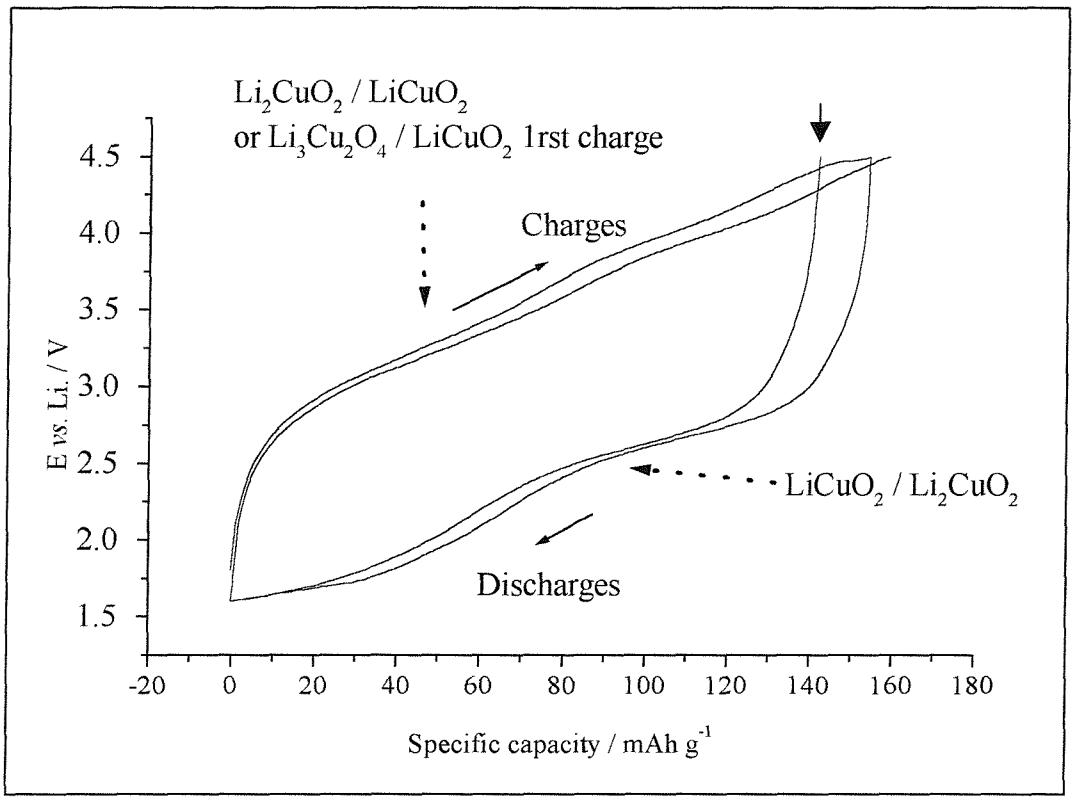

Figure 4.5 Charge and discharge profile of $Li/Li_3Cu_2O_4$ between 1.6 and 4.5 V at a constant current of 0.15 mA. Composition of electrode: 60% of the oxide, 35% of Carbon Black (Monarch 1400) and 5% of PTFE. Weight of active material: 16.3 mg.

The open-circuit voltage (OCV) of 2.92 V is found similar than for Li_2CuO_2. During the first charge, which is not shown on the graph, 0.35 lithium ion per $Li_3Cu_2O_4$ is first removed. The following discharge curve shows, a sloping voltage range between 3 to 2 V followed by another plateau starting at 1.8 V, corresponding to the total uptake of ~1.20 Li ions per unit formula of $Li_xCu_2O_4$, leading to reversible capacity of 160 $mAhg^{-1}$. Upon the following charge, a similar amount of Li ions is removed leading to the same capacity between 2.5 and 4 V. The overall electrochemical process for these reversible two-phase reactions proceeds according to $0.6Li + Li_{1.3}CuO_2 \rightarrow Li_{1.9}CuO_2$.

The attribution of the two-phase reactions to the plateaux at Figure 4.5 is based on the present electrochemical process and the following X-ray diffraction study (see 4.4.2). The reduction down to 1 V of the $Li_3Cu_2O_4$ electrode with the same characteristics and cycling conditions is shown at Figure 4.6. The maximum limit is now fixed to 3.5 V.

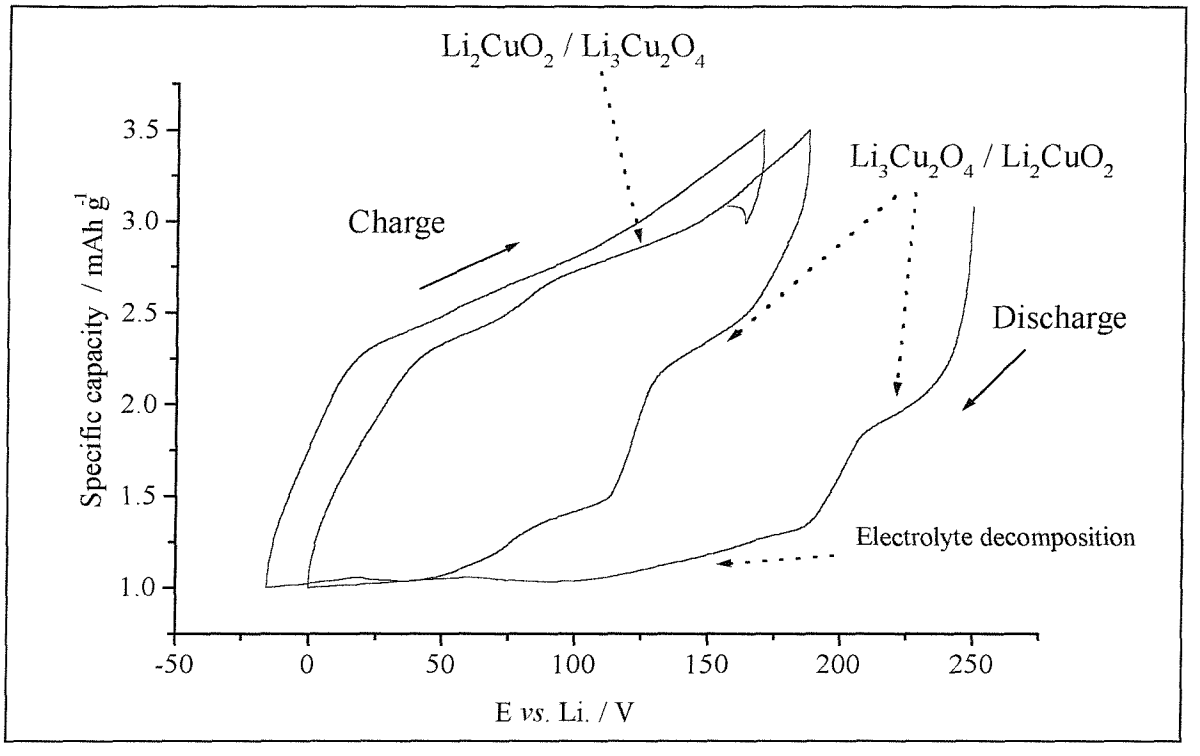

Figure 4.6 Charge and discharge profile of $Li/Li_3Cu_2O_4$ between 1 and 3.5 V at a constant current of 0.15 mA. Composition of electrode: 60% of the oxide, 35% of Carbon Black (Monarch 1400) and 5% of PTFE. Weight of active material: 17.6 mg.

The material was first discharged. During the first discharge, slanted plateaux at 1.8 and 1.2 V are shown. The plateau at 1.2 V is not terminated by the usual decline in potential and is therefore expected to involve electrolyte decomposition. The first discharge process proceeds according to $Li_{1.5}CuO_2 + 0.5\ Li \rightarrow Li_2CuO_2$.

The following charges show now two resolved plateaux between 2.3 and 3.5 V for which the following processes are proposed according to the lithium ions removed:

$Li_2CuO_2 \rightarrow 0.5\ Li + Li_{1.5}CuO_2$ in the range of 2.3-2.7 V

$Li_{1.5}CuO_2 \rightarrow 0.25\ Li + Li_{1.25}CuO_2$ in the range of 3-3.5 V

On the following discharge, the plateau at 2.3 V may be ascribed to the reaction $Li_{1.25}CuO_2 + 0.35\ Li \rightarrow Li_{1.6}CuO_2$.

Below 1.5 V, there may be formation of an organic layer associated with an electrolyte decomposition. The attribution of the phases to the plateaux at Figure 4.6 is based on the present electrochemical process and the following X-ray diffraction (see 4.4.2).

4.3.3.2 Lithium extraction from $Li_2NaCu_2O_4$

There is an absence of plateaux when the cycling of $Li_2NaCu_2O_4$ (Chapter 3, 3.3.3) is carried out in the voltage range 1.5 and 4 V at a constant current of 0.5 mA (diameter of the pellet 16 mm). The Figure 4.7 shows that the charge voltage rises steadily to 4.3 V from the open circuit potential of 2.4 V. The theoretical capacity of 235 $mAhg^{-1}$ was not reached in the voltage range 2.4-4 V. Initially the result was interpreted as electrolyte decomposition since no sign of an end-point is seen. It is thought now that some extraction is occurring. Unfortunately the experiment cannot be repeated within this work. During the following discharge, the capacity drops to 1.5 V showing a capacity of only 25 $mAhg^{-1}$.

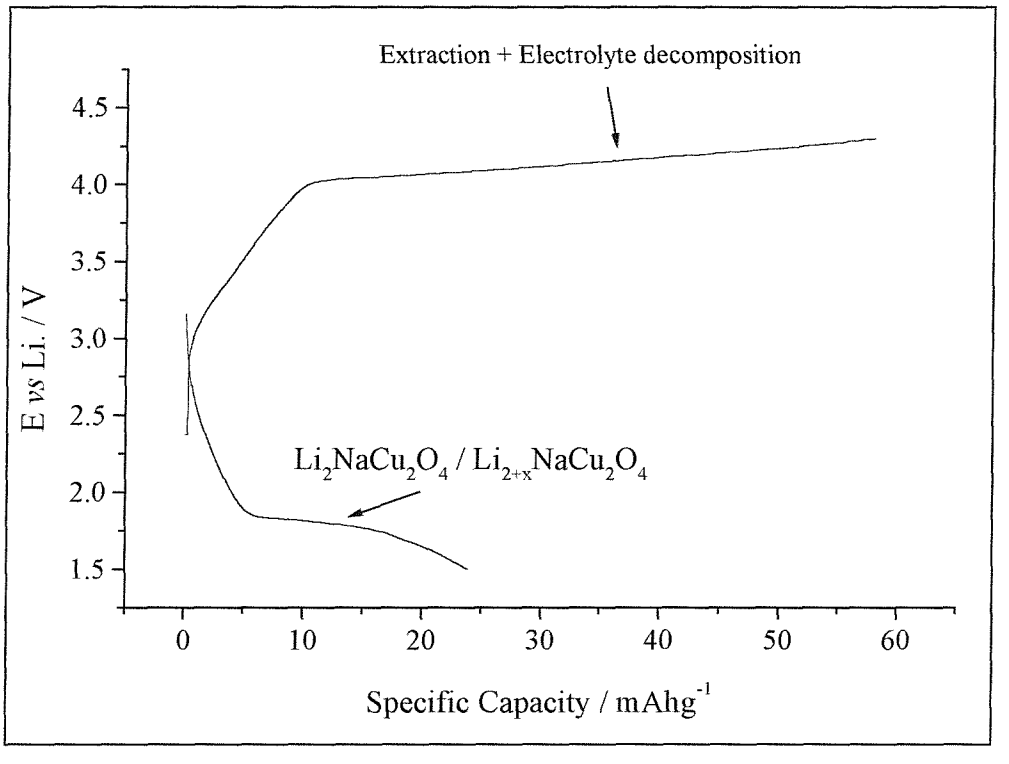

Figure 4.7 Charge and discharge profile of $Li/Li_2NaCu_2O_4$ between 1.5 and 4.3 V at a constant current of 0.5 mA at a cycling rate of 19.2 mAg^{-1}. Composition of electrode: 80% of the oxide, 10% of Carbon Black (Monarch 1400) and 10% of PTFE. Weight of active material: 26 mg.

4.3.4 Lithium extraction from $LiCuO_2$ and following cycles

The cycling behaviour of $LiCuO_2$ between 2 and 4.3 V at a constant current of 0.2 mA is reported at Figure 4.8 and the characteristics and cycling conditions at Table 4.3.

Table 4.3 Characteristics and conditions of cycling for $LiCuO_2$.

Preparation of $LiCuO_2$	Room temperature delithiation of $Li_3Cu_2O_4$ with Br_2 in AN (see chapter 3 section 3.3.4) Refined composition $LiCuO_2$
Weight Ratio Active Material/Black Carbon/PTFE	70:25:5
Type of Black Carbon	Carbon Black (Monarch 1400)
Weight of active material / mg	13.7
OCV / V	3.11
Theoretical Specific Capacity $mAhg^{-1}$ (based on total lithium extraction)	263
Cycling Rate/ mAg^{-1}	14.6
Initial Practical Discharge Rate	C/8.9

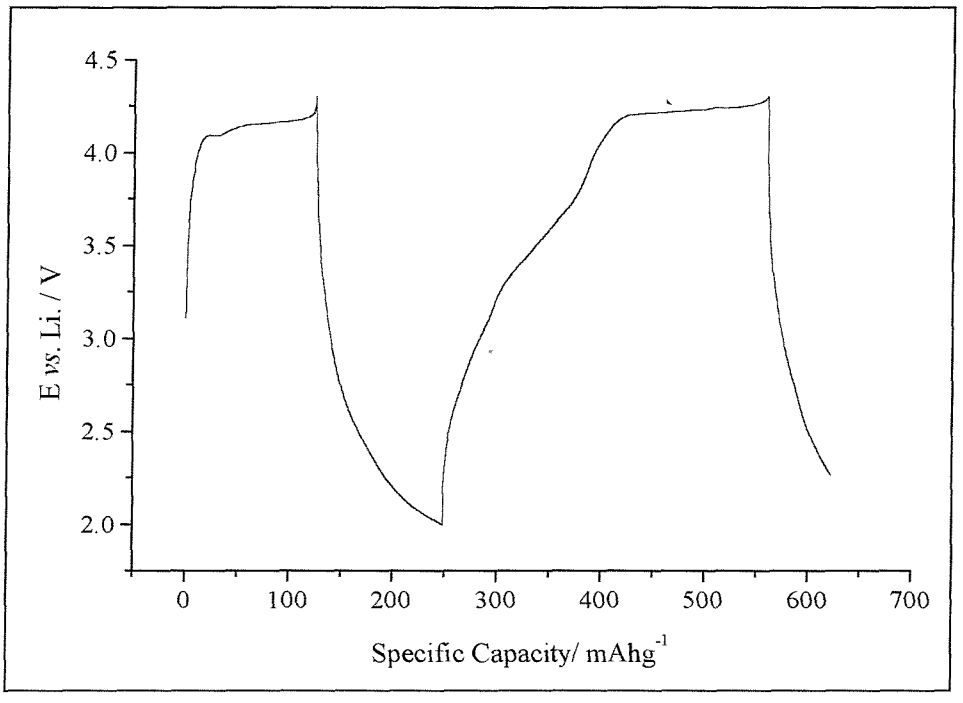

Figure 4.8 Charge and discharge profile of $Li/LiCuO_2$ between 2 and 4.3 V at a constant current of 0.2 mA . Composition of electrode: 70% of the oxide, 25% of Carbon Black (Monarch 1400) and 5% of PTFE. Weight of active material: 13.7 mg.

The open-circuit voltage of freshly assembled cells was 3.11 V, lower than expected for the oxidised compound $LiCuO_2$ due probably to the presence of CuO seen in the X-ray diffraction pattern (Chapter 3 Figure 3.16). During the first charge, the voltage rises from the OCV to 4.1 V, at which point a plateau starts to appear, offering a specific capacity of 100 $mAhg^{-1}$ up to 4.3 V. The process was not found reversible since the voltage drops on the discharge from 4.3 to 3 V without showing any capacity in this range (Figure 4.9). On the following charge, a total capacity of 300 $mAhg^{-1}$ was delivered on a short process at ~3.5 V and on a plateau at 4.1 V. Since no X-ray study was carried out on this material during the cycling, it is more difficult than in the previous curves to assign to the plateaux the presence of two-phase reactions.

The lower voltage limit was fixed to 1 V (Figure 4.9). The discharge capacity delivered at the average voltage of 1.5 V, was then equal to ~500 $mAhg^{-1}$. The discharge must involve the formation of substantial amount of Cu^I or Cu^0. A previous study on the electrochemical properties of CuO and Cu_2O by Tarascon *et al* [4] has shown that the reduction of Cu_2O by Li between 1.4 and 1 V leads to the formation of highly reactive metallic nanograins of Cu, which enables the formation-decomposition of Li_2O upon subsequent cycles. Although metallic copper has not been evidenced during the cell

discharge, the following charge curve could include below 3 V the re-oxidation of the metallic copper.

The cycle at Figure 4.10 shows the charge and discharge after the discharge down to 1 V. A capacity of 375 $mAhg^{-1}$ is delivered reversibly.

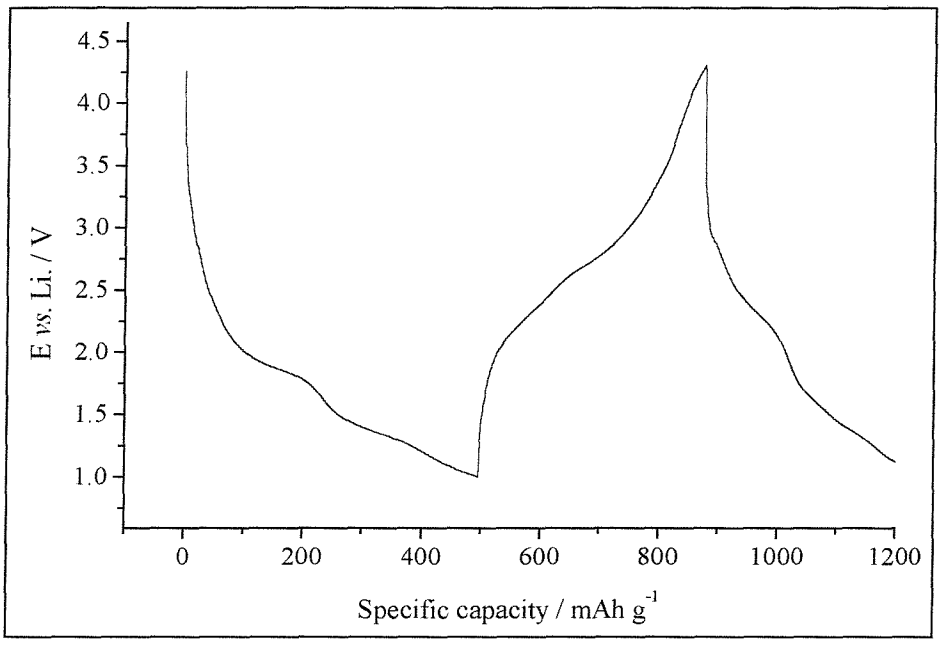

Figure 4.9 Charge and discharge profile of $Li/LiCuO_2$ between 1 and 4.3 V in same conditions as in Figure 5.22.

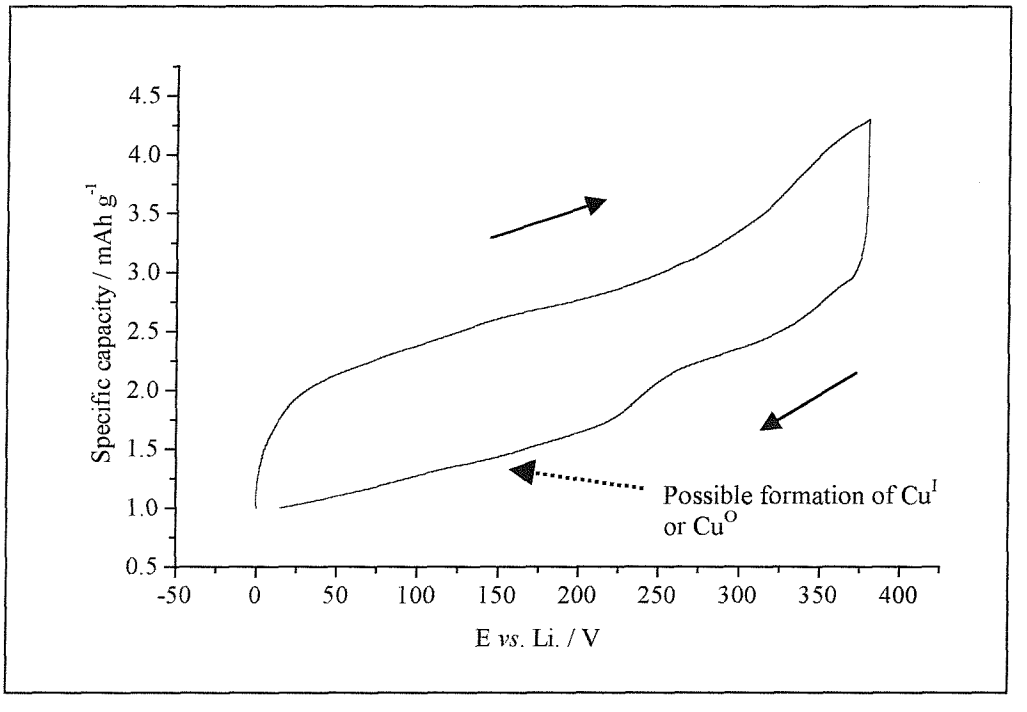

Figure 4.10 The voltage capacity curve of the previous $Li/LiCuO_2$ cell after a discharge down to 1 V.

4.4 *Ex-situ* and *in-situ* X-ray diffraction analysis

XRD analysis of composite electrodes of Li_2CuO_2 and $Li_3Cu_2O_4$ were performed using *ex-situ* and *in-situ* techniques. The electrochemical cycling of both materials are reported previously at paragraphs 4.2.1 and 4.2.3 respectively. The *in situ* technique has the advantage to probe the pellet in different states of the cycling where as in the ex-situ technique the pellet is removed and reassembled in different cells.

4.4.1 In the Li/$LiPF_6$ in EC-DMC/ cell

The Figure 4.12 presents XRD patterns of a composite pellet of Li_2CuO_2, prepared at Chapter 3 Figure 3.8, at different voltages denoted by the letters A, B, C. In this *ex-situ* experiment, the Li_2CuO_2 was cycled and stopped on charge (A, C) and discharge (B). At each voltage, after a relaxation time of 10 hours when the potential equilibrates, the pellet is removed from the cell and dried before the XRD. The cell is then reassembled in the glove-box and cycled to the next potential.

When charged up to 4 V (pattern A) a new phase of $LiCuO_2$ is present together with CuO marked with asterisks. During the following discharge (pattern B), Li_2CuO_2 is coexisting with $LiCuO_2$ at 2.7 V. The cell was discharged down to 1 V and at 3.7 V on the following charge (pattern C), Li_2CuO_2, present in small quantity, has mainly reacted back into $LiCuO_2$. The peaks that can be assigned to Li_2CO_3 by a + mark, are also present with more intense peaks of CuO.

We could unambiguously confirm, as suggested by the electrochemical process (see 4.3.1) on discharge, *i.e.* $0.8Li + Li_{0.8}CuO_2 \rightarrow Li_{1.6}CuO_2$, that the plateaux at 3.8 and 2.8 V on charge and discharge correspond to two-phase reaction between Li_2CuO_2 and $LiCuO_2$. The presence of CuO in the 4 V region is in accordance with the presence of a plateau at 4.2 V (Figure 4.2) which correspond in this case to two-phase reaction between $LiCuO_2$ and CuO. The formation of CuO from $LiCuO_2$ is attributed to the following reaction $LiCuO_2 \rightarrow Li + CuO + \frac{1}{2} O_2$.

The presence of Li_2CO_3 and lithium alkyl carbonates has been noticed in previous study of Li/CuO [4] when cycled at low voltage. This could correspond to an organic coating layer resulting from the reaction of the solvent electrolyte molecule at the surface.

It was not fully characterised in this study but an electrolyte decomposition has been mentioned already in the case of the discharge of $Li_3Cu_2O_4$ (Figure 4.6) below 1.5 V.

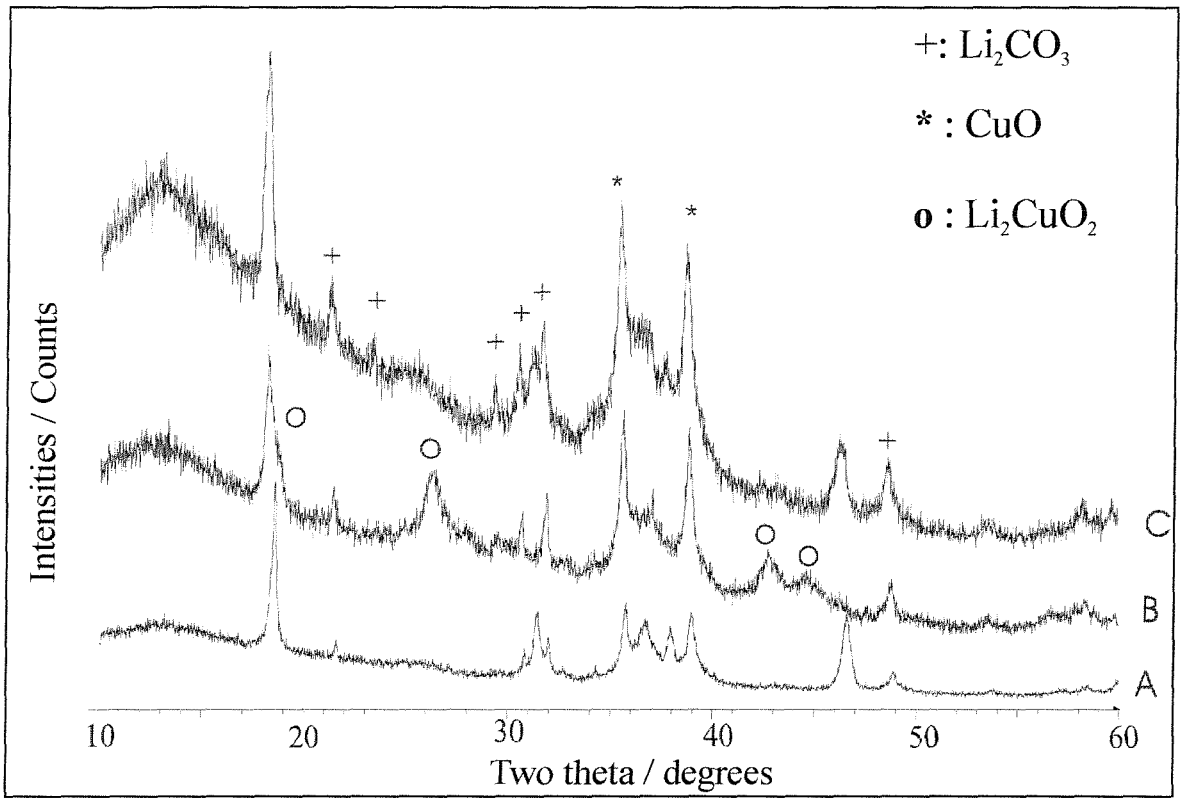

Figure 4.12 XRD patterns collected at various states of charge of a Li/Li_2CuO_2 electrochemical cell. A: 4 V (charge), B: 2.7 V (discharge) and C: 3.7 V (charge).

4.4.2 In the Li/$LiPF_6$ in EC-DMC/$Li_3Cu_2O_4$ cell

The Figures 4.13, 4.14 and 4.15 show the *in-situ* XRD patterns collected at various states of discharge and charge denoted by the letters A, B, C, D, E, F, G and H on the E = f(x) curve shown in the inset. The cell was stopped at higher potentials to allow it to reach its equilibrium potentials after 10 hours. At high voltages (C and D), the XRD patterns were obtained without any relaxation time. The slow variation of the potential limited the changes during the record of the XRD.

The first pattern (Figure 4.13, pattern A) shows the scan of the cell freshly assembled. The peaks seen show the presence of the initial phase of $Li_3Cu_2O_4$ together with the peaks at 38.5° and 44.5° in 2θ (denoted by + marks) corresponding respectively to metallic silver and beryllium, the silver paste being used to enhance electrical contact between the beryllium window and the cell holder. First we could notice that the peaks show lower intensities than expected at low angles because of the larger penetration of the beam though the beryllium window.

The pattern B, C and D show the appearance of broad peaks centred around 18.4°, 31.3° and 36.6° in 2θ corresponding respectively to the [001], [-201] and [-202] most intense Bragg reflections of the monoclinic $LiCuO_2$ (designed by ○ marks). On the D pattern, $Li_3Cu_2O_4$ and $LiCuO_2$ coexist and this confirms the two-phase reaction between $Li_3Cu_2O_4$ and $LiCuO_2$ for the sluggish plateau on the first charge between 3 and 4 V. At 4.5 V (pattern E), $Li_3Cu_2O_4$ has completely reacted into $LiCuO_2$ and the monoclinic CuO, whose peaks (denoted by *) are partially masked by the silver peaks.

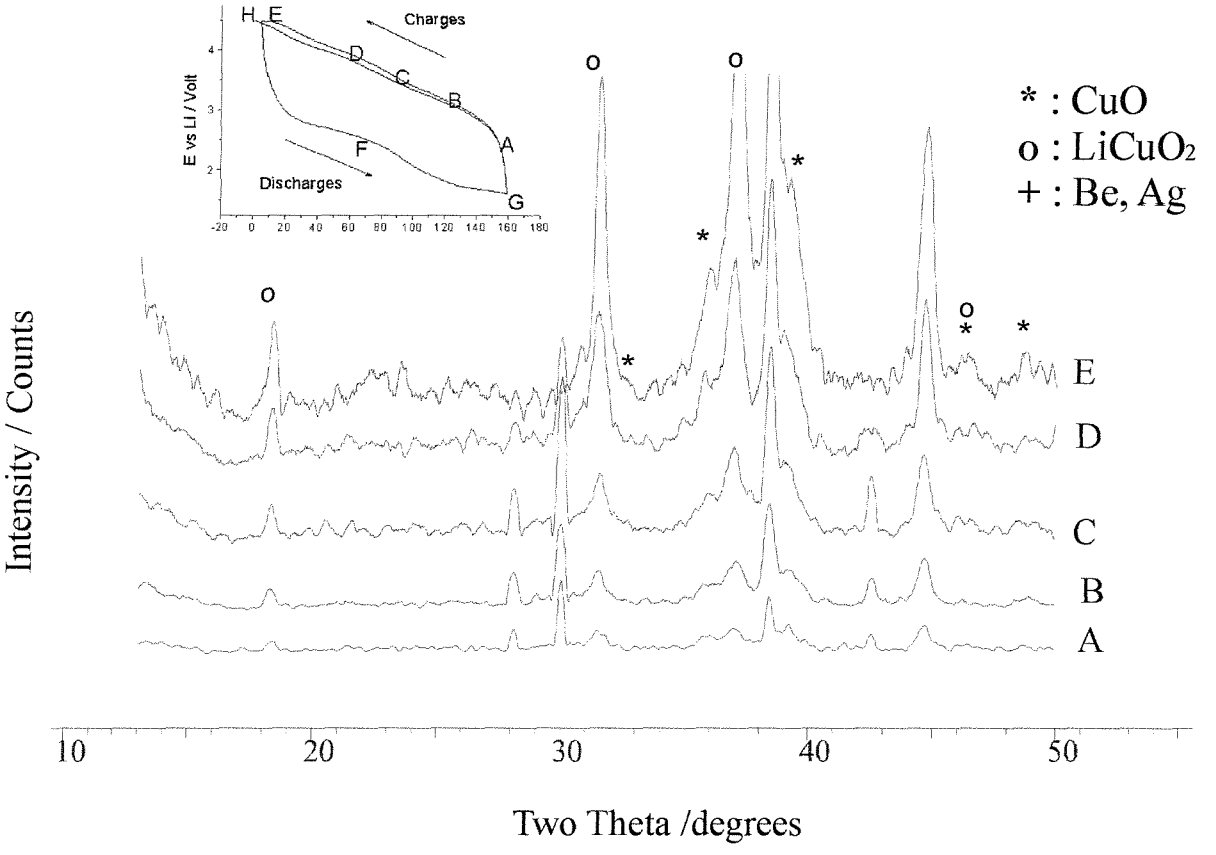

Figure 4.13 *In-situ* XRD patterns collected at various states of charge of a $Li/Li_3Cu_2O_4$ electrochemical cell. The inset shows the voltage-composition profile for such a cell with the letters denoting the stage at which the corresponding X-ray patterns were taken *i.e* A: OCV, B: 3 V, C: 3.5 V. D: 4 V and E: 4.3 V. The peaks designed by a cross + correspond to metallic silver and beryllium, by a **O** to $LiCuO_2$ and by * to CuO.

During the reduction down to 2.5 V and 1.5 V, the X-ray patterns F and G (Figure 4.11) display a decrease in amplitude of the peaks of $LiCuO_2$, CuO and a growth of a new broad peak centred at 26.3° in 2θ. This is ascribed to the intense [101] Bragg reflexion of the orthorhombic Li_2CuO_2. On the pattern F, coexist $LiCuO_2$, Li_2CuO_2 and CuO.

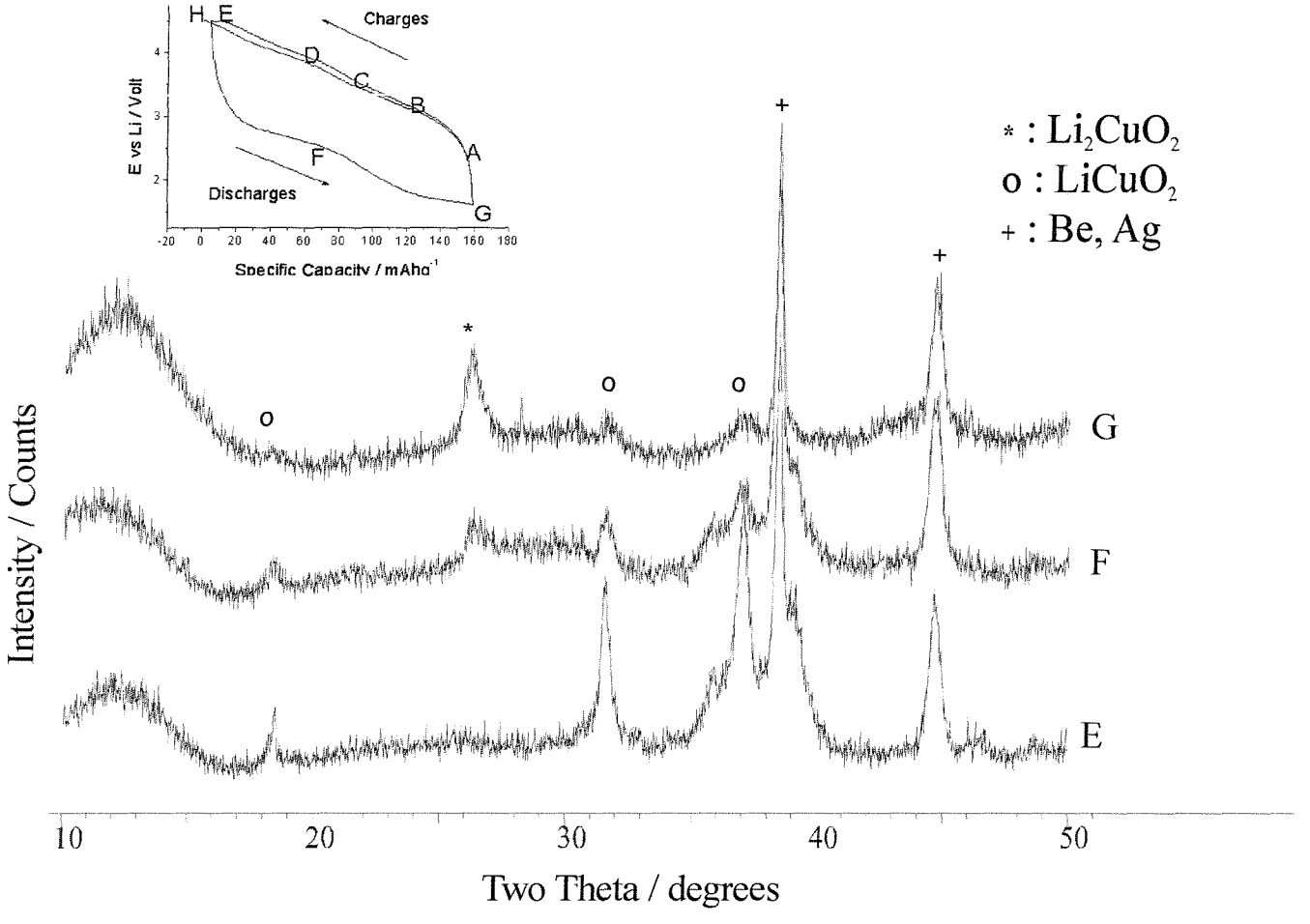

Figure 4.14 *In-situ* XRD patterns collected at various states of discharge of the $Li/Li_3Cu_2O_4$ electrochemical cell. The inset shows the voltage-composition profile for such a cell with the letters denoting the stage at which the corresponding X-ray patterns were taken *i.e.* E: 4.3 V, F: 2.5 V and G: 2 V. The peaks designed by a cross + correspond to metallic silver and beryllium, by a O to $LiCuO_2$ and by * to Li_2CuO_2.

After a new oxidation up to 4.4 V (Figure 4.15, pattern H), the curve shows the disappearance of the last Li_2CuO_2 peak together with the regrowth of a weak $LiCuO_2$ peak. The broadness of the XRD peaks of the phases indicates poor cristallinity of the electrochemically reduced-oxidised samples, at least with respect to X-rays. CuO is hardly distinguishable from the background.

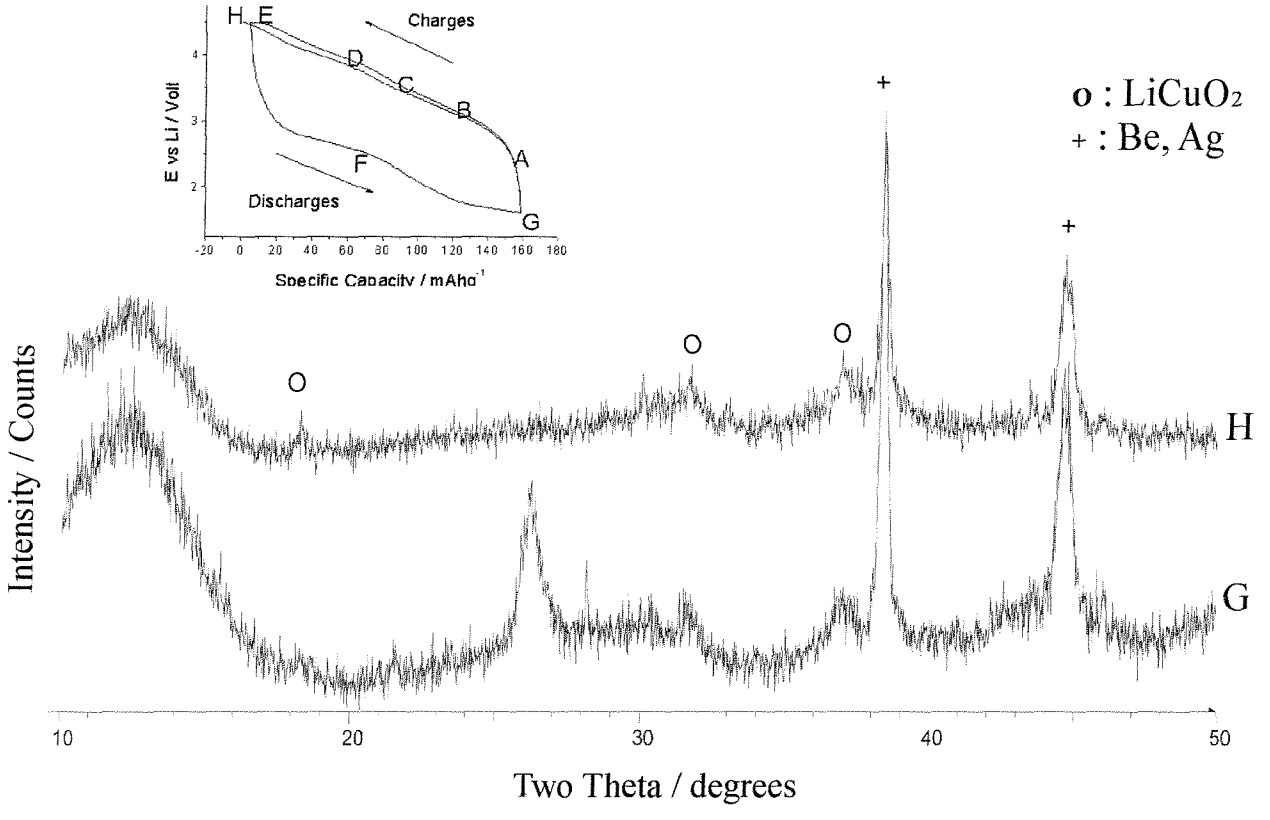

Figure 4.15 *In-situ* XRD patterns collected after the oxidation at 4.4 V of the $Li/Li_3Cu_2O_4$ electrochemical cell. G: 2 V and H: 4.4 V. The peaks hi-lighted by a cross + correspond to metallic silver and beryllium and by a O to $LiCuO_2$.

4.4.3 Discussion

The *in-situ* and *ex-situ* XRD study of Li_2CuO_2 and $Li_3Cu_2O_4$ shed further light on the structural changes during the cycling of the lithium copper oxides.

The phase transitions in the electrode involve the formation of the following phases: orthorhombic Li_2CuO_2, monoclinic $Li_3Cu_2O_4$, $LiCuO_2$ and the formation CuO above 4 V. These structural transformations contribute to the degradation of the electrode material as seen by the loss of cristallinity in the XRD (pattern G). Defects are also accumulating during the above reformations.

Although the one dimensional $[CuO_4]$ chains are maintained during the Li extraction/insertion processes in Li_2CuO_2, $Li_3Cu_2O_4$ and $LiCuO_2$, their different arrangement induces a displacement of copper chains during the cycling and is the cause of a low reversibility of the electrode.

The measurement of the lithium diffusion coefficient and conductivity in the next paragraph will allow to estimate the limiting factor in the (Li^+ + e^-) transports during the cycling.

4.5 Chemical diffusivity of lithium ions in $Li_3Cu_2O_4$

The chemical diffusivity of lithium ions in $Li_3Cu_2O_4$ was determined at room temperature by current-pulse techniques in an electrochemical cell Li/Li^+ ($LiPF_6$ in EC/DMC) /$Li_3Cu_2O_4$. This quantity can be much greater than the component diffusivity because of the enhancement factor W. This factor results from the influence of a concentration gradient during the transport process in the solid but is minimised in these experiments.

The responses of the electrode were determined using two electrochemical methods after and during the pulse, the FITT [6] and GITT [7] described in detail in Chapter 2 (2.11.3). The two time dependence of the potential are expressed as:

$$\frac{d(\Delta E)}{d(t^{-1/2})} = \frac{(dE/dx)V_M Q}{FA\sqrt{\pi D}}$$

$$\frac{d(\Delta E)}{d(t^{1/2})} = \frac{2(dE/dx)V_M i_0}{FA\sqrt{\pi D}}$$

In the formula,

$\frac{d(\Delta E)}{d(t^{-1/2})}$ is the slope of the voltage time relation ($Vs^{1/2}$ or $Vs^{-1/2}$),

dE/dx- the slope of the voltage versus composition curve ($Vmol^{-1}$) where dE represents the change in the equilibrium open circuit potential and dx the lithium ion removed calculated from Q,

V_M- the molar volume (cm^3),

Q- the charge sent through the cell equal to the time pulse by the current pulse (C),

A- the apparent surface of the active material (cm^2),

F- the Faraday constant 96 485 C mol^{-1},

D- the diffusivity of Li ions (cm^2 s^{-1}).

A ceramic disk of $Li_3Cu_2O_4$ with sputtered gold electrode on one side was used for this experiment. In the FITT method, a given amount lithium is removed from the surface of the electrode material after a positive pulse current i_0 equal to 0.05 mA. The current is turned off after a time τ of 120 s before the potential deviates more than about 300 mV . As lithium ions diffuse out of the bulk material under open circuit conditions, the surface composition will gradually approach the value characteristic of a uniform distribution. The time dependence of the potential is shown at Figure 4.17.

In the GITT method, D is evaluated from the change in the time dependent voltage during the pulse (Figure 4.18) and the equilibrium open circuit voltage after the pulse resulting from a positive current pulse (i_0= 0.05 mA with τ =420 s).

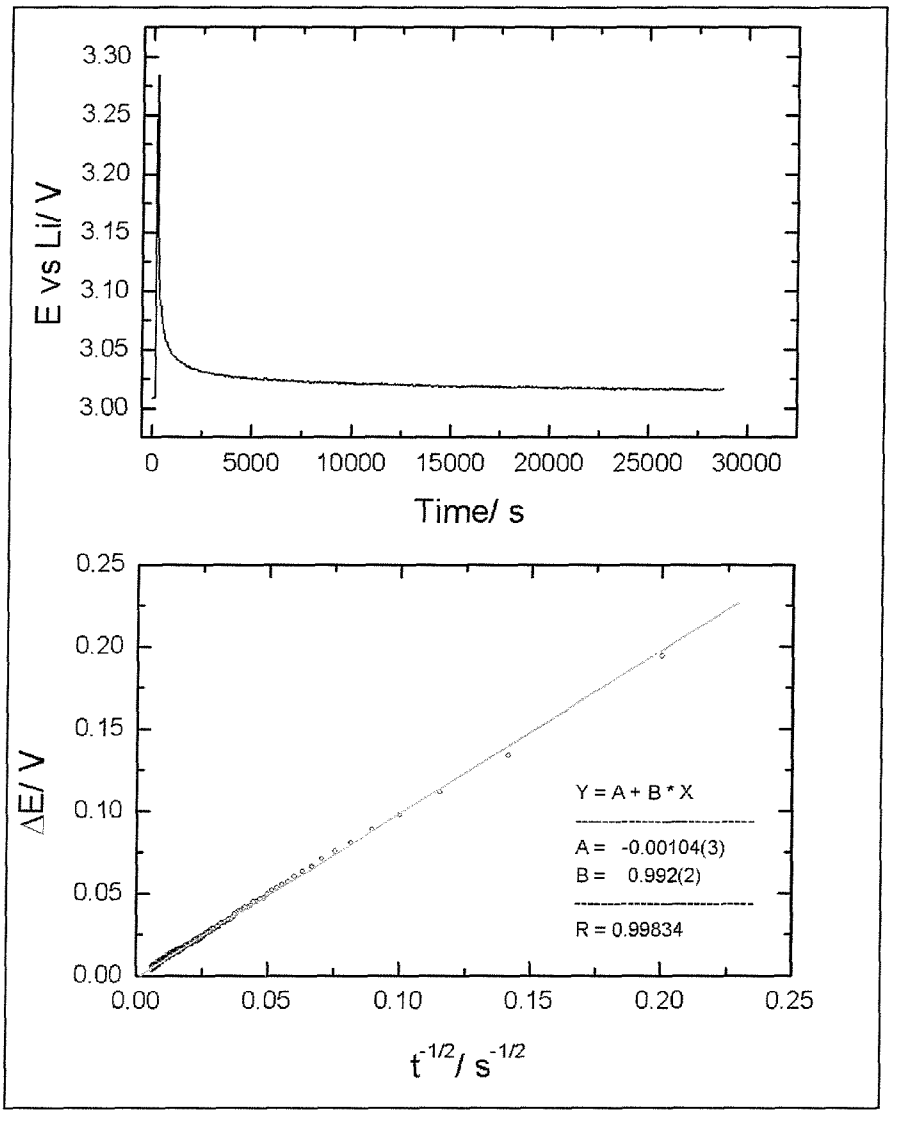

Figure 4.17 Voltage-time relation in the current pulse method FITT (after the pulse). i_0=0.05 mA and τ (duration of the pulse) = 120 s.

With Vm, the molar volume equal to 53 cm^3,

dE/dx (29.63 V/mol) calculated from the charge of 6 mC sent through the system, dE = 4 mV and $dx = 1.35\ 10^{-4}$.

the slope of the voltage-time relation (0.992 $Vs^{1/2}$),

the apparent surface area (A = 180 cm^2) of the material calculated using average crystal dimensions of 2×2×10 μm, assuming the electrolyte penetrates the porous electrode pellet (0.0434 g, 75% dense),

the chemical diffusivity of Li ions into $Li_3Cu_2O_4$ was calculated (Figure 4.17) and found equal to $9.70\ 10^{-14}$ cm^2/s.

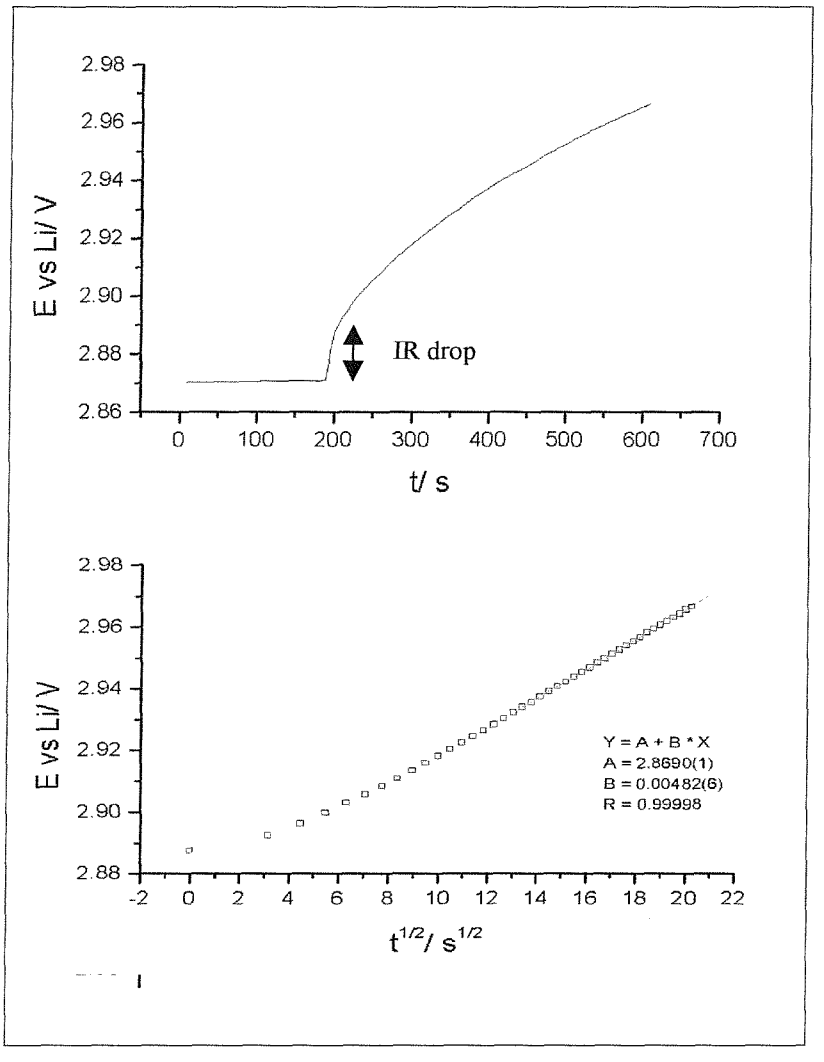

Figure 4.18 Voltage-time relation in current pulse method GITT i_0= 0.05 mA and τ =420 s.

The material is identical to the previous case so that the surface area A (180 cm^2) was kept the same. With a slope d*E*/d*x* equal to 15.6 (d*E* = 15 mV and dx = 9.6 10^{-4}), the slope of the voltage-time relation (0.00482V/$s^{1/2}$)), the chemical diffusivity of Li ions into $Li_3Cu_2O_4$ was calculated and found to be equal to 3.32 10^{-13} cm^2/s (Figure 4.18). Polarisation of the electrode is observed over a longer time.

The values determined by these two methods show discrepancies that could be due to the difference between the starting cell voltages. At higher and similar voltage of 3.10 V, both methods would show also differences (1.84 10^{-12} cm^2/s and 8.03 10^{-13} cm^2/s, the GITT giving lower D values.

In conclusion, the extraction of lithium from the oxides is not facile; the diffusion coefficient is of five order of magnitude lower than in $LiCoO_2$ and $LiNiO_2$ (10^{-7}-10^{-8} cm^2/s) [8,9]. The low value of D_{Li+} has a direct effect on extraction curve. The significant hysteresis

of 1 V occurring during the discharge of $Li_3Cu_2O_4$ cell is mainly due to the low lithium ion transport in the material. Such extraction in $Li_3Cu_2O_4$ is accompanied by oxidation of Cu^{2+} to Cu^{3+}. The following results on electronic conductivity measurements in the material will evidence that the lithium ion transport is the limiting factor.

4.6 Electronic transport properties in $Li_3Cu_2O_4$ and Li_2CuO_2

4.6.1 In $Li_3Cu_2O_4$

The conductivity measurements were carried out on Solartron 1296 on a sintered pellet at 400 °C (diameter: 7 mm, surface S: 0.3846 cm^2, height e: 0.385mm, e/S = 0.1 cm^{-1}). The frequency range was 5-13 10^6 Hz (a) and 10-5 10^5 Hz (b). The density of the sample was 75% of the theoretical one. Vacuum evaporated gold or silver paint was used for the electrode materials. The resistances were determined by the complex impedance method using a frequency response analyser as described in Chapter 2 (2.11.4).

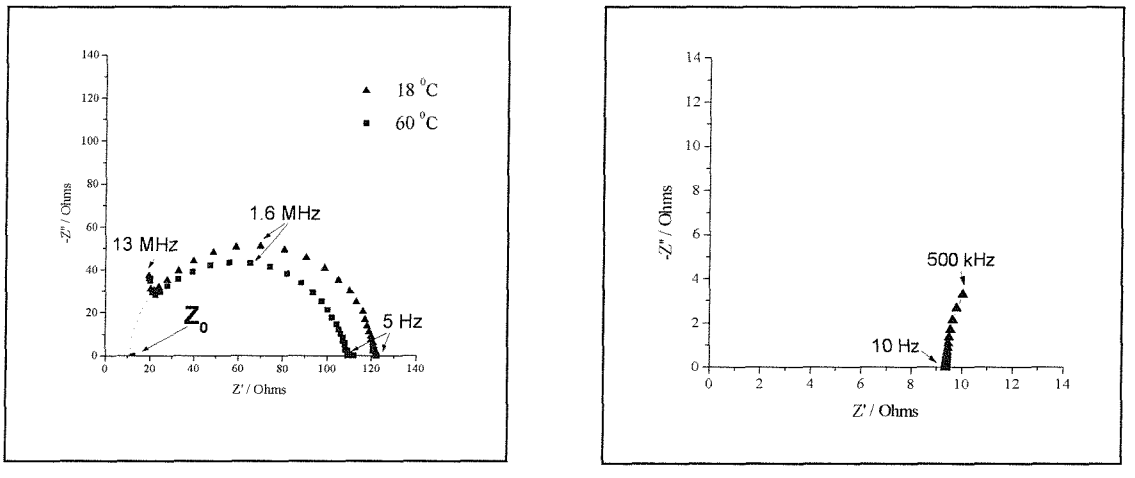

Figure 4.19 Left a: Impedance spectrum between 5 Hz and 13 MHz of the cell $Au/Li_3Cu_2O_4/Au$ at 18 °C and 60 °C showing a semi circle, contribution of Csl Rsl from the surface layer. The bulk resistance was estimated $Z_{o18} \approx 10\ \Omega$ and $Z_{o60} \approx 8\ \Omega$.
Right b: In the frequency range 10 Hz and 500 KHz, Ag/ $Li_3Cu_2O_4$/Ag at 22 °C after polishment of the surface to remove the layer formed during the heat treatment, $Z_{o22} = 9.4\ \Omega$.

The Figure 4.19 a shows the results of the gold evaporated electrode at 18 °C and 60 °C. The plots consist of one semi-circle due to the impedance from the surface layer. The total bulk resistance of the material is the intercept Z_0 on the real axis at the highest frequency.

The electronic conductivity calculated as the product of e/S with $1/Z_0$, was then found to be $\sigma_{18} = 10^{-2}$ S cm^{-1} and $\sigma_{60} = 1.25\ 10^{-2}$ S cm^{-1}.

The appearance of the electrode interface in the cell is unexpected for an interface of two electronic conductors: $Li_3Cu_2O_4$ and the metal. The surface layer on the pellet was thought to have formed during the heat treatment of the pellet. Thus, the electron charge transport between the gold electrode and $Li_3Cu_2O_4$ is blocked on the surface layer. In order to investigate the influence of the layer on the ac spectra, the pellet was polished, the electrode was removed and replaced by silver paint.

The Figure 4.19 b shows the spectra after polishing the surface (e/S = 0.09 cm^{-1}) between 10 Hz and 500 kHz. The polarisation on the electrode due to the layer has disappeared. There is no frequency dispersion over the temperature range of 22-100 °C. The conductivity increases from $\sigma_{22} = 9.6\ 10^{-3}$ S cm^{-1} to $\sigma_{100} = 1.17\ 10^{-2}$ S cm^{-1} with E_a = 0.097 eV in the $\ln\sigma T$-1/T coordinates while E_a = 0.073 eV in the $\ln\sigma$-1/T coordinates. The activation energy for electronic transport is found to be small and this can be associated with a small polaron hopping in the mixed- valence $Cu^{3+/2+}$ state [10]. Due to the superior electron conductivity, the lithium ion conductivity was not affected in the present impedance study.

4.6.2 In Li_2CuO_2

The electronic conductivity for Li_2CuO_2 was measured in the same conditions as previously. A pellet sintered at 400 °C (surface S: 1.05 cm^2, height e: 1.18 mm, e/S = 0.112 cm^{-1}) was placed after polishing on the conductivity cell linked to the Solartron 1296. The density of the sample was 75% of the theoretical one. Vacuum evaporated gold or silver paint was used for the electrode materials. The resistances were determined by the complex impedance in the frequency and temperature range 5-13 10^6 Hz and 20-105 °C, respectively. As previously, we did not observe any frequency dispersion. The conductivity increases from $\sigma_{20} = 1.6\ 10^{-3}$ S cm^{-1} to $\sigma_{105} = 4.9\ 10^{-3}$ S cm^{-1} with E_a = 0.125 eV in the $\ln\sigma$-1/T coordinates. The electron conductivity is found to be one order of magnitude lower than in the case of $Li_3Cu_2O_4$.

4.7 Conclusion

The electrochemical study of the performance of the lithium cupric and cuprate towards lithium insertion/deinsertion reveals higher specific capacities than in the conventional $LiCoO_2$ (practically 130 mAg^{-1}) or $LiNiO_2$ (150-160 $mAhg^{-1}$). The best discharge capacity delivered is by $LiCuO_2$ (350 $mAhg^{-1}$) with an average voltage of 2 V. As far as Li_2CuO_2 and $Li_3Cu_2O_4$, they deliver discharge capacities of 225 and 160 $mAhg^{-1}$ respectively distributed between 3 and 2 V, when cycled at a rate of ~10 mAg^{-1} between 4.5 and 1.7 V. Several points will limit their application in lithium ion batteries.

Structural changes occur during the cycling. The cycling of Li_2CuO_2 shows the presence of these two regions, Li_2CuO_2+$LiCuO_2$ and $LiCuO_2$+CuO at 3.2 and 4.1 V. In the case of $Li_3Cu_2O_4$, $LiCuO_2$ is present above 3.5 V on the charge and CuO at *c.a.* 4 V. The discharge of both materials is also similar with a plateau at 2.5 V corresponding to the coexisting region of $LiCuO_2$ and Li_2CuO_2.

In spite of their larger capacities, the lithium copper oxides suffer from low discharge potentials (2-2.5 V). In fact, the high number of lithium ion involved in the cycling of the material and the slow Li^+ transport (~$10^{-14}cm^2/s$ for $Li_3Cu_2O_4$) result in depletion and accumulation of lithium at the surface of the negative and positive electrode respectively. This is called concentration polarisation within the electrode materials and causes overvoltage, i.e. a drop in cell voltage during discharge and termination of the discharge before the maximum capacity of the electrode material is utilized.

The low voltage of Li_2CuO_2 is seen as an advantage when used as additive with $LiMn_2O_4$. Li_2CuO_2 was shown to be compatible with the manganese spinel and can be used to compensate the capacity loss during the initial cycle.

The phase of $Li_2NaCu_2O_4$ has shown poor performance in comparison with its parent phase of $Li_3Cu_2O_4$. The presence of sodium in the structure in octahedral sites may disrupt the lithium ion pathway leading to the marked change in cell behaviour.

The conductivity measurements in $Li_3Cu_2O_4$ and Li_2CuO_2 revealed in both cases, a semiconductor behaviour and a higher electronic conductivity of $\sigma_{22} \approx 10^{-2}$ S $cm^{-1}$for $Li_3Cu_2O_4$ compared to Li_2CuO_2 ($\sigma_{22} \approx 10^{-3}$ S cm^{-1}). The kinetics in $Li_3Cu_2O_4$ is thus limited by the confirmed slow ion transport in these materials.

4.8 References

[1] S. Mandal, J. M. Amarilla, J. Ibanez and J. M. Rojo, *J. Electrochem. Soc.*, **148** (2001) A24.

[2] A. Spong, 3rd Year Chemisty Report, University of Southampton, (2001).

[3] K. West, G. Vitins, R. Koksbang, *Electrochim. Acta*, **3** (2000) 3141.

[4] S. Grugeon, S. Laruelle, R. Herrera-Urbina, L. Dupont, P. Poizot, and J-M. Tarascon, *J. Electrochem Soc.*, **148** (2001) A285.

[5] H. Arai, S. Okada, Y. Sakurai, J. Yamaki, *Solid State Ionics*, **106** (1998) 45.

[6] W. Weppner, R. A. Huggins in *Electrochemical methods for determining kinetics properties of solids*, Annual Review of Materials Science, (1978) 269.

[7] W. Weppner, R. A. Huggins, *J. Electrochem. Soc.*, **124** (1977) 1569.

[8] M. G. S. R Thomas, P. G. Bruce, J. B. Goodenough, *Solid State Ionics*, **17** (1985) 13.

[9] P. G. Bruce, A. Lisowska-Oleksiak, M. Y. Saidi, C. A Vincent, *Solid State Ionics*, **57** (1992) 353.

[10] G. Dutta, A. Manthiram, J. B. Goodenough, J-C. Grenier, *J. Solid State Chem.*, **96** (1992) 123.

Chapter 5

Synthesis and structure of layered sodium and lithium Mn(IV) oxides, $A_2Mn_3O_7$

5.1 Introduction

In terms of battery applications the cobalt system $LiCoO_2$ has advantages associated with its sheet-like structure which allows lithium ions to be extracted from between the layers with little structural rearrangement. However, the cost and toxicity problems associated with cobalt has led to recent attention being directed at systems containing cheaper, low toxicity metals such as manganese and iron. Bruce *et al* [**1**] have managed to induce similar structural features to those of $Li_{1-x}CoO_2$ into manganese oxides with the formation of layered $LiMnO_2$ from α-$NaMnO_2$ through a low temperature ion exchange reaction. Lithium may be extracted from this system to produce $Li_{1-x}MnO_2$ ($0<x<1$). However, with manganese the formation of a Mn^{3+} d^4 system and cycling through this oxidation state during intercalation/deintercalation results in structural instabilities resulting from formation/destruction of the Jahn-Teller ion. These maybe overcome to some extent through partial replacement of manganese by cobalt in the same structure, $LiMn_{1-x}Co_xO_2$ [**2**]. However this defeats, to a large degree, the purpose of developing cobalt free batteries due to the perceived toxicity and costs associated with this element. Two further points are of concern regarding the performance of $LiMnO_2$ based systems. Firstly, the high oxidation states involved in the $Li_{1-x}CoO_2$, Co(III/IV) system produce more desirable, higher voltages than the Mn (III/IV) cycle. Secondly, the $LiMnO_2$ system is somewhat limited in terms of discharge range since only half the quantity of lithium can be reinserted from the first cycle.

A desirable goal is therefore a new lithium ion system based on Mn(IV) rather than Mn(III), as potential advantages associated with the low toxicity of manganese might be coupled with the avoidance of high levels of Mn(III) during cycling, a higher cell potential and a greater discharge range. Only a few pure Mn(IV) alkali metal oxides have been synthesised directly rather than through electrochemical oxidation/extraction methods. One of these $Na_2Mn_3O_7$ reported by Chang and Jansen [**3**] has a layered structure based on $Mn_3O_7^{2-}$ layers formed from linked MnO_6 octahedra separated by sodium ions.

In this work we report on the bulk synthesis of $Na_2Mn_3O_7$ and derivatives, $Li_2Mn_3O_7$, formed through a low temperature ion exchange route using LiBr in ethanol at 80 °C or in hexanol at 125 °C. The layered structures of both the precursor and products have been refined from powder neutron diffraction data. The influences of ion exchange conditions on the compositions and structures of the lithium manganese oxides were investigated and have

shown a different cation distribution within the α-$NaFeO_2$ type structure in hexanol. The properties of $Li_{2-x}Mn_{3-y}O_7$ as an intercalation positive electrode in rechargeable lithium battery will be presented in the following chapter.

5.2 Sodium Manganese (IV) Oxide $Na_2Mn_3O_7$

5.2.1 Synthesis

The previous synthesis and crystal structure of $Na_2Mn_3O_7$ was achieved by Chang and Jansen [3] hydrothermally under high oxygen pressure (p_{O2} = 2kbar). The structural study of a crystal obtained under such conditions showed that it crystallises triclinic in the space group $P\bar{1}$ with the following unit cell parameters a = 6.61909(14), b = 6.83962(10), c = 7.5282(4) Å, α = 105.7735(22), β = 106.8409(28), γ = 111.6316 °(13). The structure, shown at Figure 5.4, consists of $[Mn_2O_7]^{2-}$ layers held by Na^+ ions. A bulk powdered phase of $Na_2Mn_3O_7$ has never been prepared. Attempted syntheses in air yielded $NaMnO_2$ and other parent phases.

$Na_2Mn_3O_7$ was synthesised from the required stoichiometric mixture of oxides MnO_2 (Aldrich, 99%) and Na_2O (Aldrich, 97%). The mixture was packed tightly into a gold tube, which was closed by arc-welding. It was then placed in the hydrothermal bomb with a filler rod added at the top and water to fill the rest of the bomb volume. The bomb was lowered over the bomb, which remains opened to the line. In order to avoid pressurising the gold tube, the temperature was increased in small steps. With the bomb opened, the bomb was heated to about 500 °C at a pressure of 500-700 bars, then the bomb was sealed and in the temperature increased to 600 °C step by step. The pressure rose to approaching 1.4 kBar. The reaction was left for two days. The product was then ground and kept in the glove box (MBraun Labmaster130, <1ppm O_2 and H_2O). The dark grey powder obtained is found to be compact when ground in pestle and mortar.

Phase purity was verified by powder X-ray diffraction, the data are shown in Figure 5.1. The major peaks could be indexed using the triclinic cell given by Chang and Jansen [3] but the majority of the peaks intensity were weak.

The SEM picture of the product at Figure 5.2 shows the presence of platelets of average dimension of 1μm.

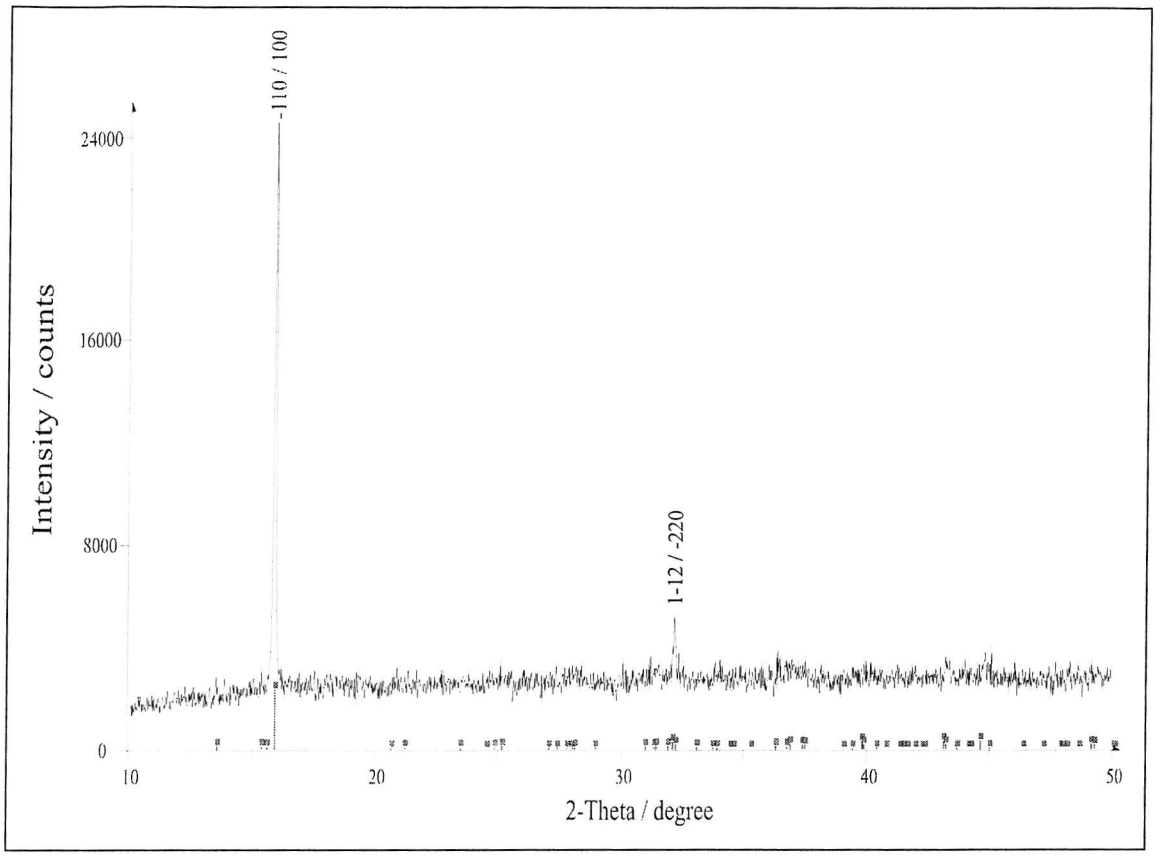

Figure 5.1 XRD pattern of $Na_2Mn_3O_7$. The most intense peaks are indexed in a triclinic unit cell.

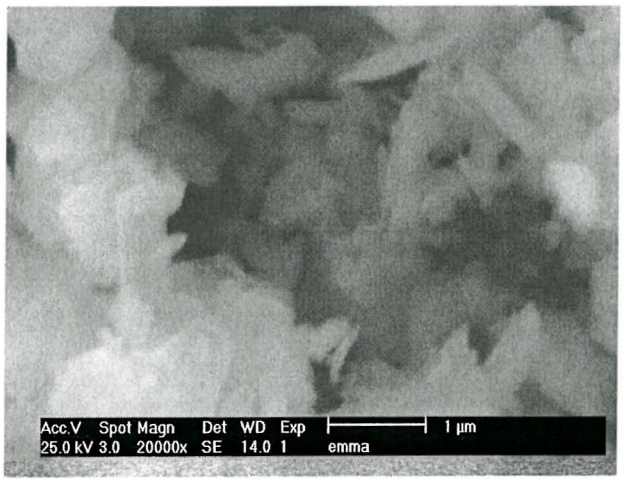

Figure 5.2 SEM picture of $Na_2Mn_3O_7$ prepared hydrothermally showing the presence of platelets of an average dimension 1µm. .

5.2.2 T.o.f. PND study

Powder neutron diffraction data were collected on the High Resolution Powder Diffractometer (HRPD) on ISIS at the Rutherford Appleton Laboratory. The sample was loaded into a vanadium can. Backscattered data were collected over a time-of-flight (T.O.F.) range 40 000 to 115 000 μs. The Rietveld refinement was carried out using the GSAS package [4]. Neutron scattering lengths of 0.363, -0.373, 0.5803 (all $\times$ 10^{-12} cm) were assigned to Na, Mn, O respectively [5].

The model used was based on the structural details obtained for $Na_2Mn_3O_7$ [3] such as the space group, lattice parameters and atomic coordinates. Attempts to re-index the data using a simpler or higher symmetry unit cell in the space groups C*mcm* and $R\bar{3}m$ were unsuccessful.

The initial stages of the refinement include the zero point, background, lattice parameters, peak shape parameters and isotropic thermal parameters. Identical refined temperature factors were used for each atom situated in different sites at the early stages of the refinement and were permitted to vary later. The refined occupancy values were very close to the initial occupancies and were therefore set equal to unity. Final stages involved parameters including scale factor, background, unit cell, peak shape, isotropic thermal factors and positional parameters.

The inspection of this profile fit and the values obtained for R_{wp} and R_p of 10.86 and 8.97 % respectively indicates that this structural model is not ideal. The main deficiencies in the profile fit were investigated and determined as deriving from a number of reflections whose Miller indices corresponded to the planes representing directions perpendicular to the manganese-oxygen layers e.g. (3,-3,0). Attempts to overcome these problems using a variety of preferred orientation parameters and anisotropic peak broadening terms were only partially successful.

In conclusion the basic structural model seems correct, producing a reasonable profile fit and full indexing of the data, but the true structure of this material in polycrystalline form is obviously more complex. One possibility for the obtained profile fit, is that in the bulk, powdered form $Na_2Mn_3O_7$ loses the perfect stacking sequence of the crystallographic description, that is the $Mn_3O_7^{2-}$ layers are no longer perfectly aligned throughout the crystal structure; such behaviour is common in materials with layered structures. This behaviour is

also clear in the powder X-ray diffraction patterns obtained from $Na_2Mn_3O_7$ (Figure 5.1) where the peak composed of the (-110) + (100) reflections is observed with any intensity. Results, final plot and refined atomic positions and temperature factors for the sample are summarised in Figure 5.3 and Table 5.1.

5.2.3 Structure

$Na_2Mn_3O_7$ has a layered structure based on $Mn_3O_7^{2-}$ layers formed from linked MnO_6 octahedra separated by sodium ions. The structure may be viewed as a layer of edge linked MnO_6 octahedra, as in the $NaFeO_2$ structure type, but with $1/7^{th}$ of the transition metal ions removed in a regular manner from the layer (Figure 5.4).

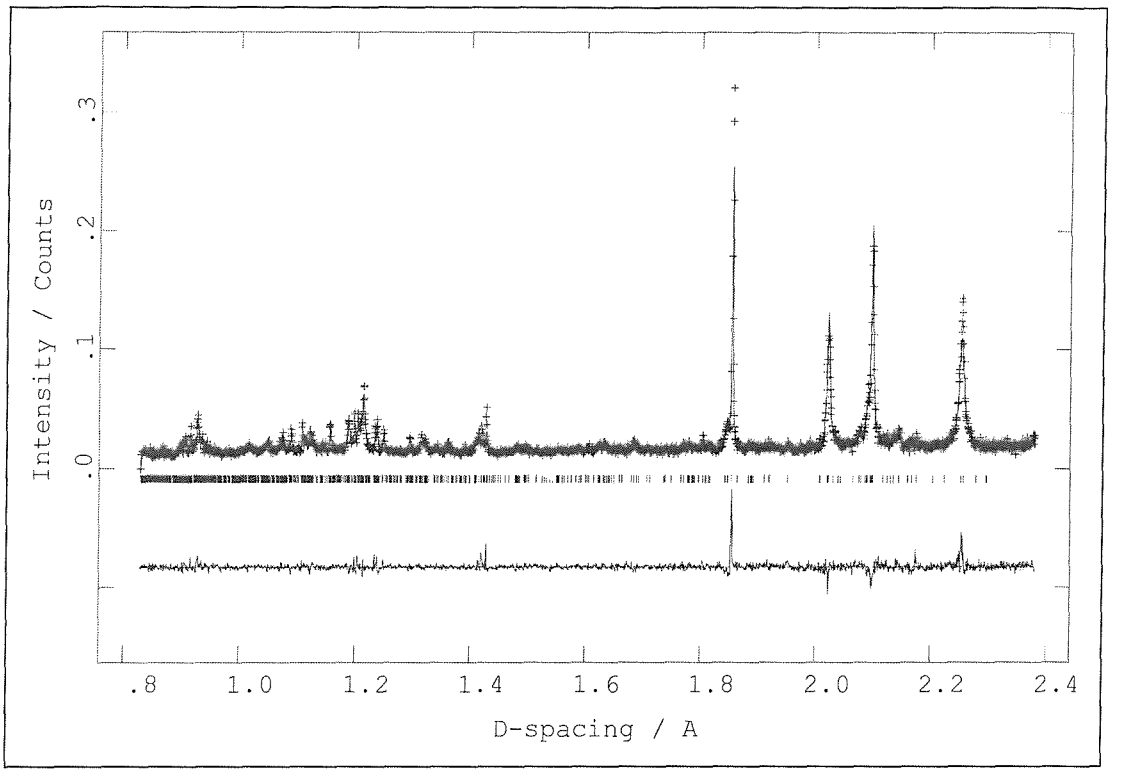

Figure 5.3 The final profile fit obtained of the powder neutron diffraction data obtained from $Na_2Mn_3O_7$. Cross marks show the experimental data, upper continuous line calculated profile and lower continuous line the difference. Tick marks show reflection positions.

Table 5.1 Refined atomic co-ordinates for $Na_2Mn_3O_7$. Esds are given in parentheses

Atom	x	y	z	U_i/U_e*100 /Å^2
Na1	.2351(20)	.6994(18)	.4863(22)	2.06(30)
Na2	.3236(19)	.8184(16)	.0528(16)	0.87(29)
Mn3	.0763(29)	.0867(25)	.2356(31)	2.86(43)
Mn4	.3499(34)	.3588(28)	.0677(34)	2.85(38)
Mn5	.2084(27)	.2196(25)	.6290(26)	1.58(30)
O6	.4115(17)	.2163(15)	.2551(15)	1.84(24)
O7	-.2629(29)	-.0683(26)	.1586(31)	7.58(52)
O8	.0396(12)	.2050(12)	.0213(20)	-0.07(19)
O9	.1468(17)	.3608(18)	.4452(18)	3.52(32)
O10	.6867(16)	.5256(18)	.1204(15)	1.48(23)
O11	.1187(34)	-.0663(29)	.4182(30)	8.78(60)
O12	.4401(13)	.6295(12)	.3018(14)	0.42(20)

Triclinic, space group P $\bar{1}$, a = 6.6191(2), b = 6.8393(2), c = 7.5300(3) Å,
α = 105.766(2), β = 106.848(2), γ = 111.632(1), Cell volume = 274.40(2) Å^3,
χ^2 = 1.892 for 10560 observations and 73 variables. R_p= 8.97 %, R_{wp}= 10.86 %,
R_{exp} = 7.89 %

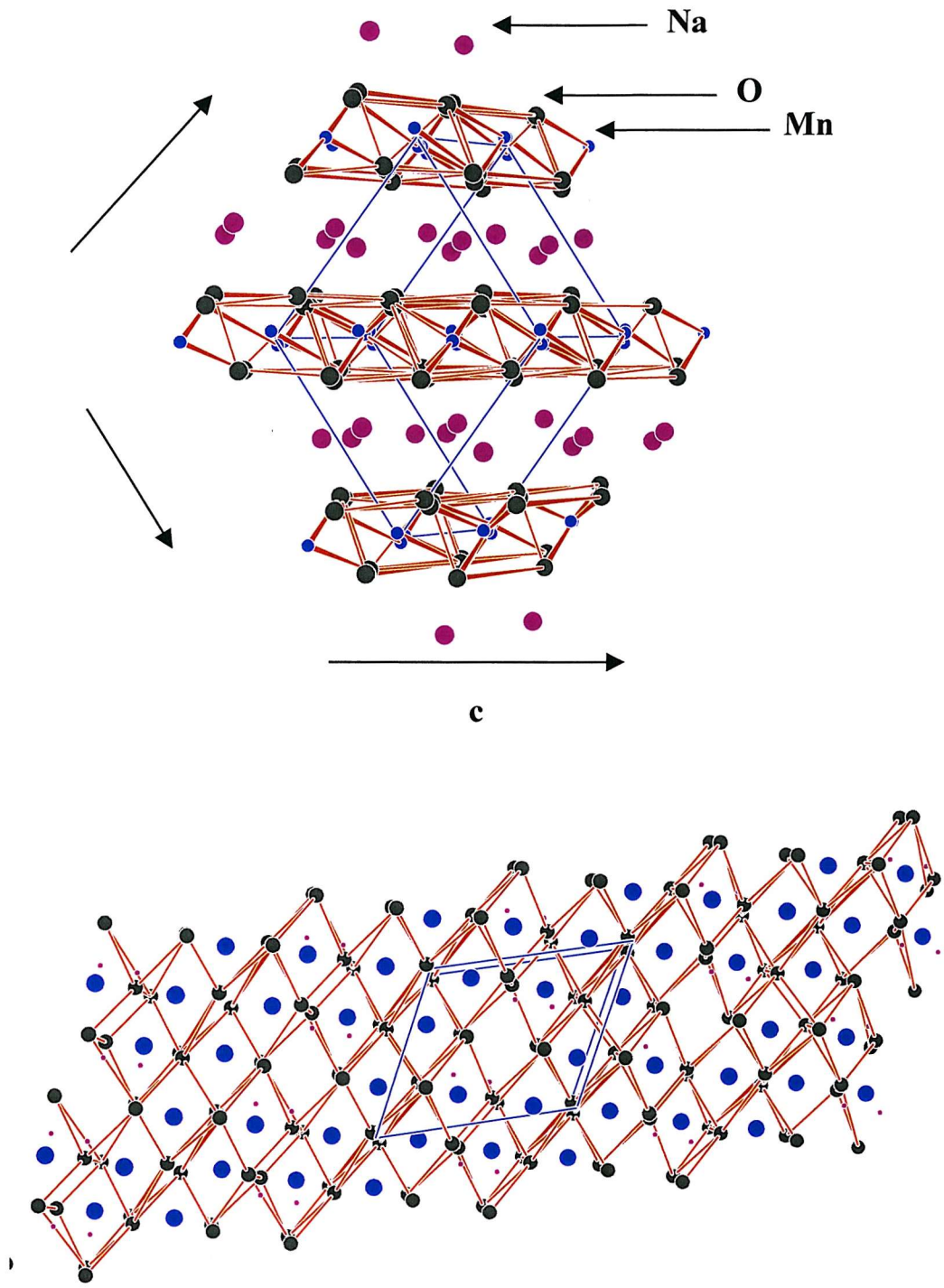

Figure 5.4 The structure of $Na_2Mn_3O_7$ viewed as follows. Oxygen and manganese are shown as black and blue circles and sodium as pink spheres. Top: close to parallel to the layers along [001]. Bottom: perpendicular to a single $Mn_3O_7^{2-}$ layer. MnO_6 octahedra are shown.

5.3 Lithium ion exchange reactions of $Na_2Mn_3O_7$. Conditions of synthesis and characterisation

5.3.1 Synthesis and preliminary inspection of the XRD patterns.

Lithium ion exchange reactions of sodium manganese oxide have been performed previously in the preparation of layered $LiMnO_2$ and $Li(Mn_{1-y}Co_y)O_2$ using hexanol at 150 °C with a 10-fold excess of LiBr for 6-8 h [1,2]. The ion exchange conditions such as the reflux solvent or temperature of the reaction, are found to affect the nature of product. For example, a study on the influence of ion exchange on the structure, composition and capacity of the resulting lithium compounds [6-8] in the layered $Li(Mn_{1-y}Co_y)O_2$, has shown that the use of ethanol instead of hexanol as a solvent, preserves the vacancies on the transitional metal sites of the sodium phase and enhances the cyclability of this electrode material in rechargeable lithium batteries.

In our study, the sodium manganese oxide possesses transition metal vacancies within the layers and the compounds resulting from the lithium exchange were expected to be affected by the conditions of the reaction. As a result, the lithium ion exchange of the sodium manganese oxide $Na_2Mn_3O_7$ was carried out using LiBr as the lithium source in either ethanol (*b.p.* 75°C) at 70 °C or hexanol (*b.p.* 135°C) at 125 °C.

The reaction involves refluxing under a nitrogen atmosphere in a Schlenk tube, the sodium phase $Na_2Mn_3O_7$ in dry distilled alcohol with a 20-fold excess of dry LiBr (Aldrich, 99%). In the case of the use of ethanol, a 6-fold excess 15-crown-5 ether (Aldrich, 99.9%), was used to facilitate the extraction of sodium bromide into the solution.

The mixture was heated in an oil bath with stirring to the desired temperature with the tube open to the nitrogen atmosphere to avoid any increase of the pressure. When the temperature has been stable, the nitrogen line was closed. The reaction was then left at this temperature for 12 hours under stirring. After cooling, the solid product was recovered under suction or decantation of the solvent, washed with dry ethanol or hexanol and dried in air at 220 °C.

The powder XRD patterns at Figure 5.6 and 5.7 were collected on a Siemens D5000 diffractometer operating with $CuK\alpha_1$ radiation over a period of 11 hours. The lithium exchanged samples, regardless of solvent or conditions of synthesis, could be indexed on a rhombohedral unit cell with systematic absences consistent with the space group $R\bar{3}m$,

similar to that adopted by layered oxides of the stoichiometry AMO_2. The XRD data show a marked shift in the position of the main reflection (from d = 5.57 Å to ~d = 4.8 Å), corresponding to the interlayer spacing, in agreement with the replacement of sodium by the smaller lithium ion between the layers. A reduction in average crystallite dimension is observed through the marked broadening of the reflections. The SEM images of the products (Figure 5.5) in both cases show the presence of thin plates with dimensions *c.a.* 0.2 × 1 × 1 μm.

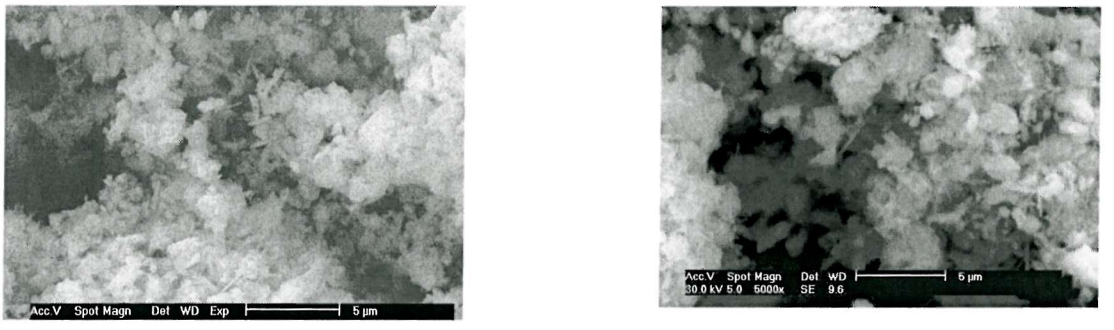

Figure 5.5 SEM images of the lithium ion exchanged products in ethanol (left) and in hexanol (right). Platelets of dimension up to 1μm are observed

Surface area measurement carried out using the BET method employing a Micromeritics Gemini 23670 instrument, yielded values of 1.9 and 3.3 m^2/g for the ethanol and hexanol compounds respectively. By substituting in the Sherrer formula $B(2\theta) = 0.9\ \lambda / L_m \cos\theta$, the widths of the (003) or (101) Bragg peaks at half of their maximum intensity $B(2\theta)$ obtained from the following XRD patter (Figure 5.7), the average crystallite size could be deduced.

Table 5.2 Surface area and crystallite size for the lithium manganese oxides synthesised.

Compounds	m^2/g	Average crystallite size by SEM (μm)	Sherrer formula (Å)
Ethanol 70 °C	1.9	1	210
Hexanol 125 °C	3.3	1	200

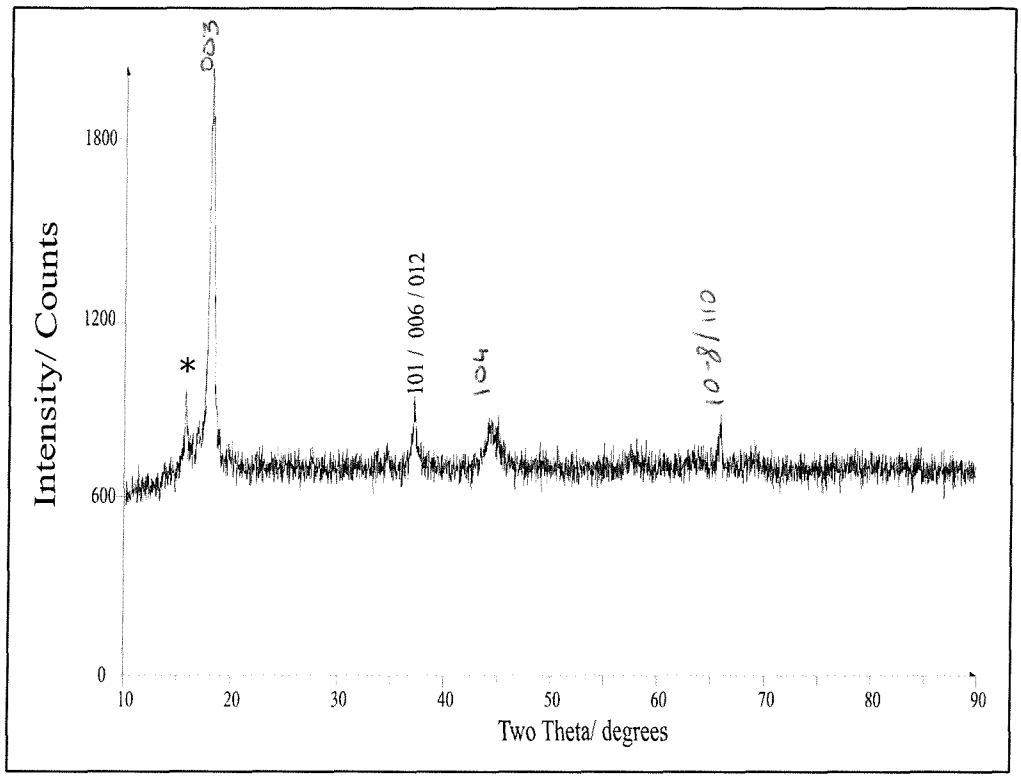

Figure 5.6 XRD pattern of the lithium ion exchanged compound after reaction in ethanol at 70 °C. The Miller indices of the Bragg peaks are indicated over each peak.

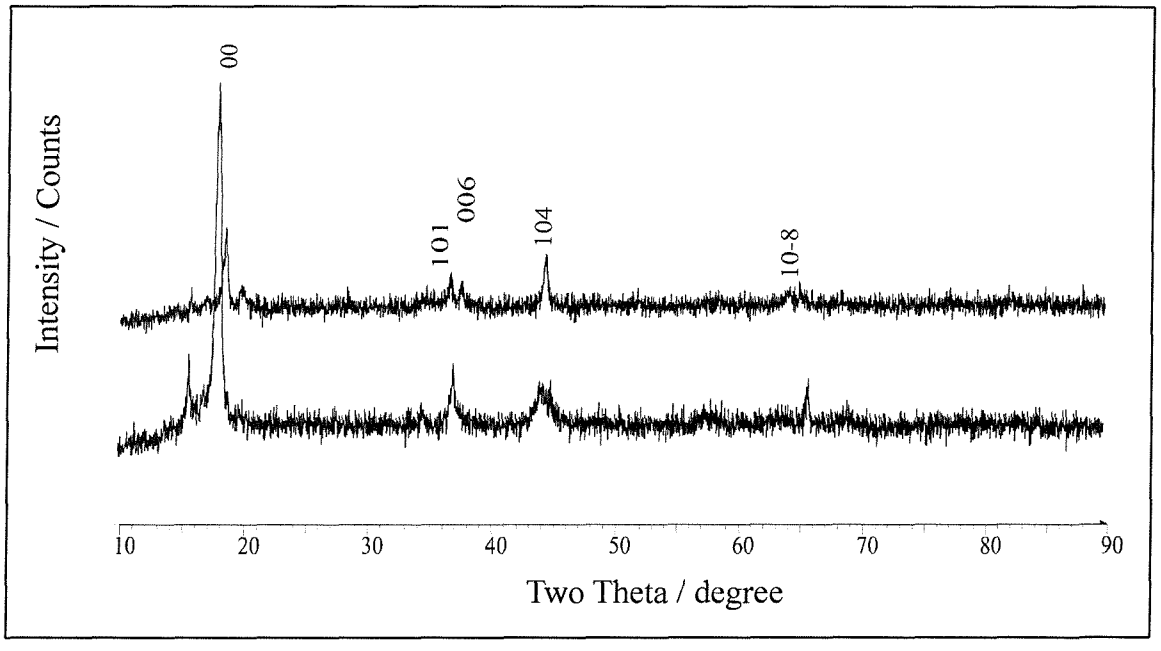

Figure 5.7 Upper pattern: XRD pattern of the lithium ion exchanged compound after reaction in hexanol at 125 °C.
Lower pattern : XRD pattern of the lithium ion exchanged compound after reaction in ethanol at 70 °C.

The products still contain some $Na_2Mn_3O_7$, but in different quantity, as evidenced by the peak at $2\theta = 15.7°$ seen in Figures 5.6 and 5 .7. The estimated amount was found to be of 20 %.

5.3.2 Elemental Analysis

Chemical analysis of the lithium ion exchanged compounds was carried out using the flame emission analysis and the UV-visible spectroscopy. The manganese oxidation state was determined by titration with a ferrous sulphate solution [9]. A description of the measurements is reported here. The results of the analysis figure in section 5.4.1.

5.3.2.1 Flame emission analysis

Lithium and sodium contents of the product were determined by flame emission analysis on a Corning 400 flame photometer.

For each content, the apparatus was calibrated using an appropriate standard solution of lithium (3.2 to 12.9 10^{-3} M) or sodium (1 to 5 10^{-3} M). The sample to be analysed was prepared as follows. The lithium ion exchanged compound (0.103 g) was dissolved in 100 ml of water with dilute hydrochloric acid (2 ml), followed by a reaction with hydrogen peroxide to reduce the manganese to Mn^{2+}. The solution was boiled to allow the formation of the LiCl and $MnCl_2$ precipitates. After drying at 190 °C, the precipitates were dissolved in water and the solution was used for the flame emission analysis.

5.3.2.2 UV-visible spectroscopy

Manganese content was determined photometrically by UV-visible spectroscopy (Perkin Elmer Lambda19). Standard solutions of known concentration of potassium permanganate (1 to 4 10^{-4} M) were prepared for calibration. In 5 ml of the solution prepared previously for the flame analysis, concentrated sulphuric acid (0.5 ml) and a saturated solution of potassium periodate (20 ml) were added until the purple coloration of the potassium permanganate appears.

In this analyse, the manganese is oxidised with potassium periodate to the strongly coloured permangate ion MnO_4^- according to:

$$8\ Mn^{2+} + 5\ IO_4^- + 12\ H_2O \leftrightarrow 8\ MnO_4^- + 5\ I^- + 32\ H^+$$

The absorbance of the solution is measured at 545 nm with the spectrometer. A calibration curve of absorbance against concentration of permanganate ion enables the unknown concentration to be determined.

5.3.2.3 The ferrous sulphate method

This method consists of a back-titration of ferrous ammonium sulphate by potassium permangante. In 100 ml of 10 % (by volume) of sulphuric acid is introduced 0.5 g of ferrous ammonium sulphate with 11 mg of the sample to analyse. The content is brought to boil until the entire sample is decomposed according to the reaction:

$$Mn^{n+} + (n-2)\ Fe^{2+} \leftrightarrow (n-2)\ Fe^{3+} + Mn^{2+}$$

A volume of 5 ml of phosphoric acid is added and the excess ferrous ammonium sulphate is titrated with potassium permanganate.

$$5\ Fe^{2+} + MnO_4^- + 8H^+ \leftrightarrow Mn^{2+} + 5\ Fe^{3+} + 4\ H_2O$$

At the same time a blank is run with 0.5 g of the ferrous ammonium sulphate under identical conditions. The lithium content is known by the previous analysis and the oxidation state x is given by the formula:

$$x = 2 + (5\ 10^{-3}\ C\ V / N)$$

where

C = concentration of $KMnO_4$ used (M), $1.2\ 10^{-2}$ M.

V = the difference in the volume (ml) of $KMnO_4$ between the sample and the blank.

N = mass of the sample / molar mass of the sample function of x.

5.3.3 T.o.f. PND

Powder neutron diffraction data were collected for the samples exchanged with LiBr in ethanol and hexanol at 70 °C and 125 °C respectively, on the Polaris medium resolution diffractometer at the Rutherford Appleton Laboratory. The samples were loaded on a vanadium can and a capillary respectively. Backscattered data were collected over a time-of-flight range 2986 to 17000 μs. The Rietveld refinements were carried out using the GSAS package [4]. Neutron scattering lengths of -0.19, 0.363, -0.373, 0.5803 (all $\times 10^{-12}$ cm) were assigned to Li, Na, Mn, O respectively [5].

Although a previous study (section 5.3.1) has shown that the reflections could be indexed on a simple hexagonal unit cell of dimensions a=2.8 Å by c=14.4 Å, parameters obtained using Cell [10] from a least-squares refinement of the peak positions in the X-ray diffraction pattern, the refinement of the structures was considered in the variety of structure models that have been used to represent AMO_2 layer structures such as the monoclinic layered C/2*m* and orthorhombic P*mmn*. In both case, the best fit was found for the $R\bar{3}m$ space group of α-$NaFeO_2$.

The atomic positions of α-$NaFeO_2$ were used to describe the structures with lithium and manganese ions located on the 3a and 3b sites respectively. In this structure the oxide ions adopt a cubic close packed arrangement. The sheets of octahedral sites between the layers of the oxide ions are solely and alternatively occupied by transition metal and lithium ions.

For both refinements, the initial stage included the zero point, background, lattice parameters, peak shape parameters and thermal parameters. The occupancy of all the sites was kept equal to 1. Differences arise between the samples prepared in ethanol and hexanol when the occupancies of the Li and Mn ions on the 3a and 3b sites respectively, were permitted to vary. Because of the neutron scattering amplitude of lithium (-0.19×10^{-12} cm) and manganese (-0.373×10^{-12} cm) are of different amplitudes, it was possible to establish a favoured arrangement of lithium and manganese ions in the octahedral sites of the structure. Final results of the refinements are listed separately for both samples in the section 5.4.2.

5.4 Results and discussion

5.4.1 Composition figures from chemical analysis

In the following Table 5.3, the results of the chemical analysis for the lithium, sodium and manganese on the ethanol and hexanol reflux samples are presented. Rewriting the expected lithium phase $Li_2Mn_3O_7$ in terms of the same oxygen sheet stoichiometry as $LiMO_2$ gives the formula $Li_{0.57}Mn_{0.85}O_2$. The values of these chemical analyses are in reasonable agreement with the ones obtained from the refinement at section 5.4.2.

Table 5.3 Chemical analysis of materials prepared under different conditions.

Conditions	Chemical Analysis	Oxidation State from the analysis
Hexanol (LiBr, 125 °C, 12h)	$Na_{0.230}Li_{0.558}Mn_{0.816}O_2$	3.60 ±0.1
Ethanol (LiBr, 70 °C, 12h)	$Na_{0.201}Li_{0.436}Mn_{0.854}O_2$	3.95 ±0.1

The compositions reveal the presence of some sodium. This could be from unreacted $Na_2Mn_3O_7$ as shown in the XRD pattern at section 5.3.1 and from the residual and reintercalated sodium occupying octahedral sites in the structure. Results on the structure refinements (see section 5.4.2) indicate that the sodium content exclusively comes from the residual of the starting sodium phase.

In fact a small amount of sodium has also been found on the octahedral sites in the crystal structures. This was noticed by P. Bruce *et al* [8] after the ion exchange reaction in the layered $NaMn_{1-y}Co_yO_2$ and it was proposed that the vacancies on the transition metal sites bear a negative charge in that region of the crystal structure. This in turn can trap Na^+ ions, resulting in a small amount of residual Na after exchange.

Differences arise in the lithium content that is found to be larger for the hexanol sample at 125 °C. The more vigorous nature of these conditions leads to a more complete exchange of Na^+ and vacancies in the alkali metal layers by Li^+.

The initial manganese deficiency of the sodium phase $Na_{0.57}Mn_{0.85}O_2$, is maintained in both ethanol and hexanol, with however, more vacancies in the transition metal sites for the sample in hexanol.

The results of the oxidation state by a titration method shows a lower valence for the manganese on the hexanol sample. This is due to the high alkali metal content. The sodium content appears in this case to be higher than the one obtained by refinement (5.4.2.2).

5.4.2 Rietveld refinement

5.4.2.1 Exchange in ethanol

In the paragraph 5.3.3, the initial stages of the refinement were described and it includes the zero point, background, lattice parameters, peak shape parameters and thermal parameters. In the final stage of the refinement, the occupancies of the various sites were permitted to vary without constraint. The refined lithium and manganese contents were found to be less than unity and equal to $Li_{0.48}Mn_{0.89}O_2$. It is in close agreement with the expected $Li_{0.57}Mn_{0.85}O_2$ stoichiometry from the synthesis. The attempt to mix the lithium sites with sodium or with manganese did not allow the refinement to converge.

The profile fit was good ($\chi^2 = 5.54$) and the factors R_{wp} and R_p equal to 2.98 and 4.69 respectively. The refined neutron diffraction profile of the product from Li ion exchange in ethanol is shown in Figure 5.8. Crystallographic data obtained are summarised in Table 5.4.

5.4.2.2 Exchange in hexanol

In contrast to the previous structure refinement, in which the octahedral sites 3a and 3b are solely occupied by lithium and manganese ions, the present refinement yielded a rocksalt structure in which the 3a and 3b octahedral sites are partially occupied by both lithium and manganese ions. Marked variation in the relative intensities of the (003) and (104) reflections (decrease of the ratio $I_{(003)}$ / $I_{(104)}$) at Figure 5.7 has already suggested that the manganese ions adopt a different arrangement in both structures.

In fact without the introduction of the disordering on the cations sites, the refinement of the lithium and manganese contents do not converge... Refinement of this structure gives a cation arrangement of $(Na_{0.05}Li_{0.50}Mn_{0.05})_{3a}[Mn_{0.74}Li_{0.07}]_{3b}O_2$ in which 5 % of the manganese reside in the lithium-rich layers and 7 % of the lithium in the manganese-rich layers. An attempt to refine the occupancy of sodium on the lithium site led to site occupancy of 5 %.

Given the disordered structure type and reflection widths, the profile fit was good ($\chi^2 = 3.35$) and the factors R_{wp} and R_p equal to 4.4 and 5.9 respectively. The refined neutron diffraction profile of the product from Li ion exchange in hexanol is shown in Figure 5.9. Crystallographic data obtained are summarised in Table 5.5.

Table 5.4 Refined atomic co-ordinates for $Li_{2-x}Mn_{3-y}O_7$ from the ion exchange reaction in ethanol with LiBr at 70 °C. Standard errors are given in parentheses.

Atom	Site	Occupancy	x	y	z	$U_i/U_e/Å^2$ (×100)
Li	3a	0.48(10)	0	0	0	9.00(23)
Mn	3b	0.890(23)	0	0	0.5	0.38(8)
O	6c	1	0	0	0.2646(2)	0.78(4)

Hexagonal, space group $R\bar{3}m$ (no.166), a = 2.83961(11) Å, c = 14.486(5) Å,

χ^2 = 5.541 for 3322 observations and 46 variables, R_p= 4.69 %, R_{wp}= 2.98 %, R_{exp} = 1.26 %

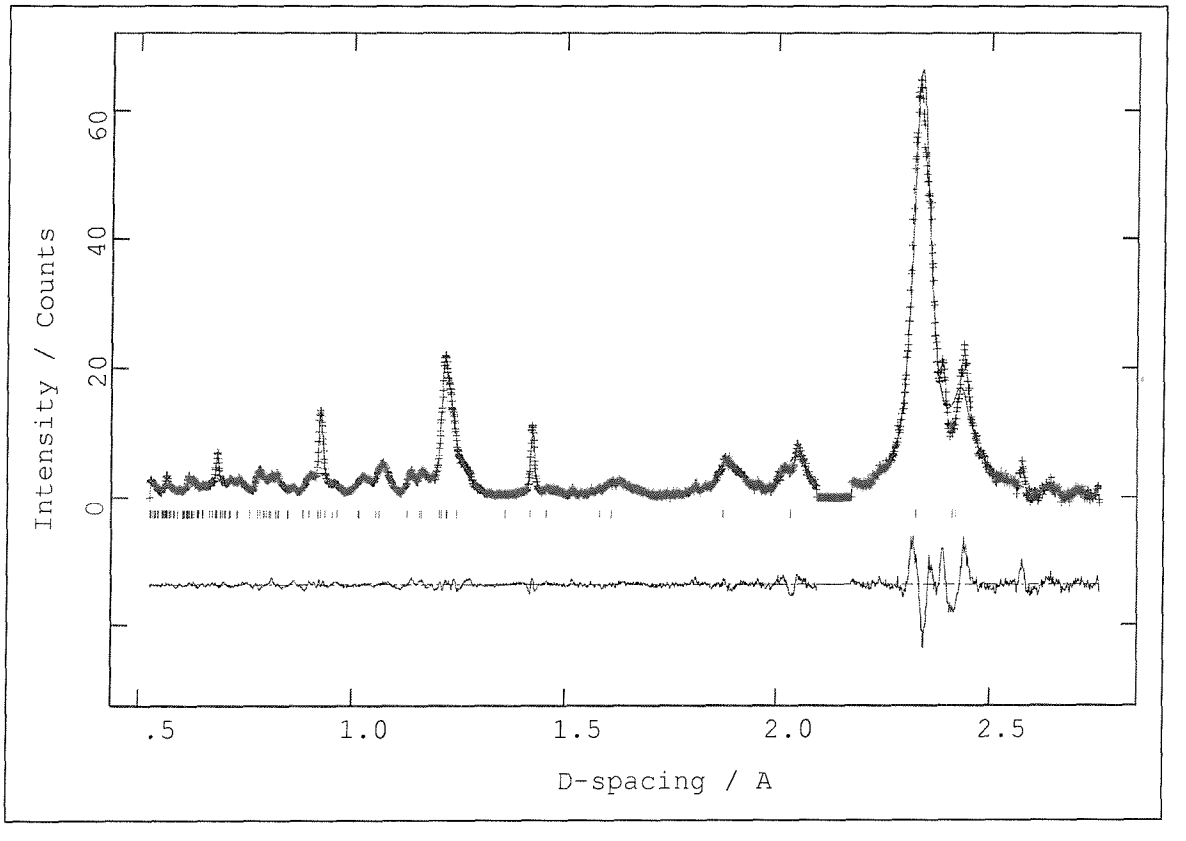

Figure 5.8 The final profile fit of the neutron diffraction data for $Li_{2-x}Mn_{3-y}O_7$ from the ion exchange reaction in ethanol with LiBr at 70 °C. Cross marks show experimental data, upper continuous line calculated profile and lower continuous line the difference. Tick marks show reflection positions.

Table 5.5 Refined atomic co-ordinates for $Li_{2-x}Mn_{3-y}O_7$ from the ion exchange reaction in hexanol with LiBr at 125 °C. Standard errors are given in parentheses.

Atom	Site	Occupancy	x	y	z	$U_i/U_e/Å^2$ (×100)
Li	3a	0.50(4)	0	0	0	2.14(41)
Na	3a	0.05(2)	0	0	0	2.14(41)
Mn	3a	0.05(1)	0	0	0	2.14(41)
Mn	3b	0.74(5)	0	0	0.5	0.21(9)
Li	3b	0.07(2)	0	0	0.5	0.21(9)
O	6c	1	0	0	0.2387(2)	0.88(4)

Hexagonal, space group $R\bar{3}m$ (no.166), a = 2.8703(3) Å, c = 14.3478(2) Å,

χ^2 = 3.35 for 5019 observations and 31 variables, R_p= 5.9 %, R_{wp}= 4.40 %,

R_{exp} = 2.4 %

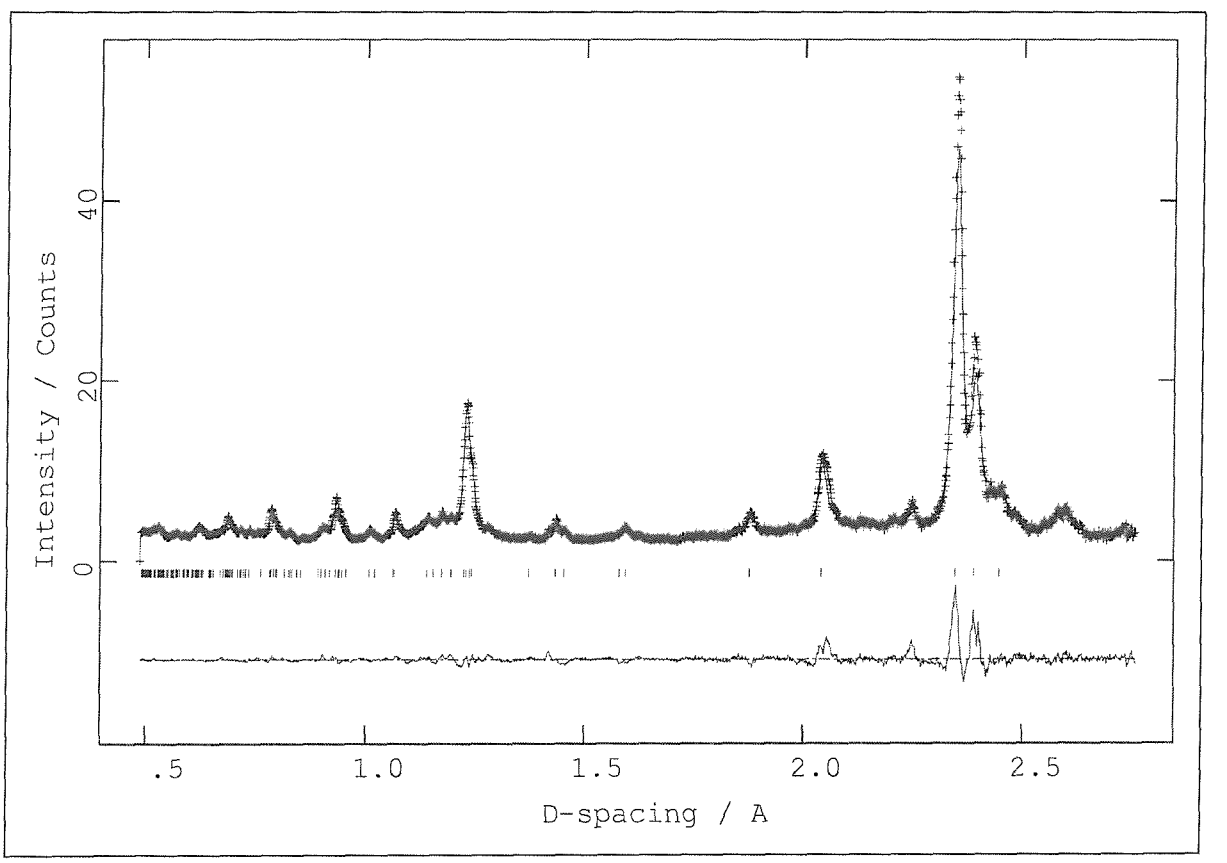

Figure 5.9 The final profile fit of the neutron diffraction data for $Li_{2-x}Mn_{3-y}O_7$ from the ion exchange reaction in hexanol with LiBr at 125 °C. Cross marks show experimental data, upper continuous line calculated profile and lower continuous line the difference. Tick marks show reflection positions.

5.4.3 Discussion

In the light of the compositions and crystal structures, we can interpret the change in the cell parameters (Table 5.6) obtained for the different oxides. The radii of the ions that figure in this discussion are taken from the data of Shannon [11].

Table 5.6 Lattice parameters and *c/a* ratio of materials prepared under different conditions.

Conditions	*a*/ Å	c/ Å	*c/a* / Å
Hexanol (LiBr, 125 °C, 12h)	2.8703(3)	14.3478(2)	4.998
Ethanol (LiBr, 70 °C, 12h)	2.8396(1)	14.486(5)	5.101

Table 5.5 shows that *a* and *c* parameters differ significantly in the two products. The value of the *a* parameter for the compound prepared in hexanol is larger than that for the ethanol product whereas the c parameter is smaller resulting in a smaller c/a ratio of 4.998. It has been shown previously that a *c/a* ratio of 4.90 in rhombohedral symmetry is equivalent to a cubic unit cell [12,13]. In the present case, the magnitude of the c/a ratios (> 4.90) shows that the layered rhombohedral compound is the dominant phase in the exchanged manganese oxides. This also manifests itself for instance in the XRD pattern of the hexanol sample (Figure 5.7) in which the (108) and (110) peaks at 63.8 ° and 65 ° respectively together with the (006) and (012) peaks at 36.70 ° and 37.55 °in 2θ, are now separated.

In the present case the presence of lithium ($r(Li^+)$ = 0.76 Å) in the manganese layer ($r(Mn^{4+})$ = 0.53 Å in the hexanol sample has an impact on the *a* parameter. In fact the lattice parameter *a* lies in the plane of the layered structure and is particularly sensitive to changes in the average transition metal to oxygen bond length. The replacement of manganese in the layer by a larger ion would result in a longer average transition metal to oxygen bond length (Table 5.6), the effect of which is to increase the *a* lattice parameter for the ethanol product.

The parameter *c* of the layered compounds is sensitive to the size and quantity of the alkali metal in the interlayers. Expansion may be due to weak van der Waal's bonding between oxides ion sheets when the alkali metal content decreases. In the samples prepared in ethanol the lithium content is lower (Table 5.2). This is consistent with the longer *c* axis.

5.4.4 Structure

The lithium manganese oxides $Li_{2-x}Mn_{3-y}O_7$, regardless of solvent or conditions of synthesis, adopt the highly symmetrical crystal structure of the layered α-$NaFeO_2$ ($R\bar{3}m$). In this O3 structure, the oxide ions adopt a cubic close packed arrangement (ABC stacking). The sheets of octahedral sites between layers of the oxides are occupied alternatively or conjointly by transition metal and lithium ions.

The samples do not exhibit a cooperative Jahn-Teller distortion due to the high oxidation state of manganese. The manganese deficiency in the octahedral layers is maintained at the level of the sodium parent phase. The alkali metal stoichiometry of the octahedral sites between the layers depends on the conditions and is found to be lower in ethanol. The main difference with the structures of the sodium phase is that there is an increased disorder of the cations between and within the layers. The positions of the manganese ion vacancies in neighbouring sheets also lose their fixed relative positions. That is the Mn_3O_7 layers remain in the ion exchanged compound, presumably with the same distribution of the $^1/_7$ Mn vacancies as exists in $Na_2Mn_3O_7$, Figure 5.4. The ion exchange reaction causes a disordering of these sheets along the *c* direction of $Li_{2-x}Mn_3O_7$, Figure 5.10

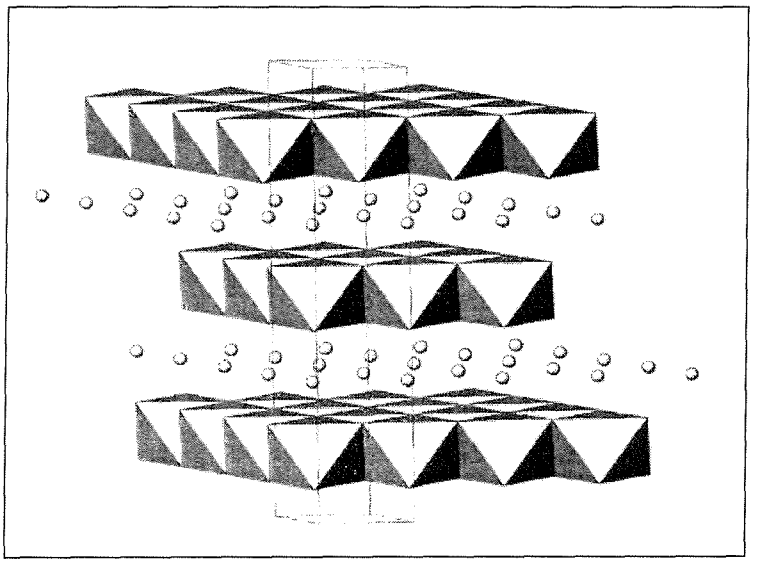

Figure 5.10 The structure of $Li_{2-x}Mn_3O_7$. Manganese deficient MnO_6 octahedra are shown as are the partially occupied lithium sites (shaded spheres).

Comparison of the alkali metal and transition metal to oxygen bond lengths obtained by refinement of the samples in ethanol and hexanol are indicated in Table 5.7. Consideration of the manganese environment in $Li_{2-x}Mn_2O_7$ shows this is to be a slightly trigonally distorted

octahedron in both cases, with angles O-Mn-O 84.6 ° (ethanol) and 85.5 ° (hexanol). This geometry is typical of Mn(IV) and quite different from that of the Jahn-Teller distorted Mn(III). In the case of $LiMnO_2$, the localized high spin $3d^4$ (t_{2g}^3 e_g^1) configuration of the Mn^{3+} ion induces a cooperative Jahn-Teller distortion of the octahedral sites, lowering the crystal symmetry from rhombohedral ($R\bar{3}m$) to monoclinic (C2/*m*) with Mn-O 1.92Å (x 4) and 2.27Å (x 2) [1,15].

The lithium ions also adopt distorted octahedral sites. The average alkali metal to oxygen bond length obtained by refinement, indicates a greater value in the case of the exchange in ethanol, consistent with the larger *c* parameter.

Table 5.7 Mn-O and Li-O bond lengths (Å) for $Li_{2-x}Mn_3O_7$.

Conditions	Mn-O (x 6)	Li-O (x 6)
Hexanol (LiBr, 125 °C, 12h)	1.954(1)	2.142(1)
Ethanol (LiBr, 70 °C, 12h)	1.918(1)	2.168(1)

5.5 Conclusion

The sodium ions in the layered manganate $Na_2Mn_3O_7$ can be ion exchanged in non-aqueous conditions to yield a new lithium manganese (IV) complex oxide. The basic layer structure with $Mn_3O_7^{2-}$ is maintained but increased disorder between the individual oxide layers is induced to give rise to the O3 structural type of the layered α-$NaFeO_2$ ($R\bar{3}m$). In $Li_{2-x}Mn_3O_7$, the high oxidation state of manganese of ~+3.95 and 3.60, prevents the Jahn-Teller distortion and an undistorted phase of rhombohedral symmetry is obtained.

The influence of the temperature of the Li-ion exchange reaction was investigated. Despite the fact that the differences in the synthesis conditions between reflux in ethanol and hexanol appear to be relatively small, it causes some changes in the compositions and structural parameters. The higher temperature used with the hexanol solvent, drives the reaction to completion. There is an overall trend towards larger c/a ratio value on changing the preparative conditions from hexanol to ethanol. Furthermore in hexanol, manganese and lithium ions were found to adopt a slightly more disordered arrangement of the layered structure.

These differences in the structural parameters and compositions of $Li_{2-x}Mn_{3-y}O_7$ are thought to be significant toward the electrochemical performances of these oxides as intercalation materials in rechargeable lithium batteries. In fact, many examples from previous studies have shown influences of the preparative conditions on the electrochemical properties. In the case of LT-$LiCoO_2$ [13] which presents cationic disorder within the layers, the electrochemical properties differ significantly from the HT-$LiCoO_2$ resulting in lower voltage. Also, at similar Co content, $Li_y(Mn_{1-x}Co_x)O_2$ [7] compounds obtained in ethanol exhibit higher capacity with a small fade rate on cycling.

The electrochemical properties will be developed in the following chapter 6.

5.6 References

[1] A. R. Armstrong, P. G. Bruce, *Nature*, **381** (1996) 499.

[2] A. R. Armstrong, A. D. Robertson, R. Gitzendanner.; P. G. Bruce, *J. Solid State Chem.*, **145** (1999) 549.

[3] F. Chang, M Jansen, *Z. Anorg. Allg. Chem.*, **531** (1985) 177.

[4] Generalised Structure Analysis System, (GSAS). A. C. Larsen, R. B. von Dreele, MS-H805 Los Alamos National Laboratory, MN 87545, (1990).

[5] Neutron News, **3(3)** (1992) 29.

[6] A. D. Robertson, A. R. Armstrong and P. G. Bruce, *J. C. S. Chem. Commun.*, **2000** (2000) 1997.

[7] A. D. Robertson, A. R. Armstrong , A.J. Fowkes, P. G. Bruce, *J. Mater. Chem.*, **11** (2001) 113.

[8] A. D. Robertson, A. R. Armstrong and P. G. Bruce, *Chem. Mater.*, 2380 (2001).

[9] M. J. Katz, R. C. Clarke, W.F. Nye, *Anal. Chem.*, **28** (1956) 507.

[10] CELL (Program to calculate cell parameters from indexed powder data), University of Oxford.

[11] R. D. Shannon, *Acta Cryst.*, **32 A** (1976) 751.

[12] J. N. Reimens, W. Li, E. Rossen, and J. R. Dahn, *Mat. Res. Soc. Symp. Proc*, **293** (1993) 3.

[13] R. J. Gummow, D. C. Liles, and M. .M. Thackeray, *Mat. Res. Bull.*, **28** (1993) 235.

[14] R. J. Gummow, M. M. Thackeray, W. I. F David, S. Hull, *Mat. Res. Bull.*, **27** (1992) 327.

[15] F Capitain, P. Gravereau, C. Delmas, *Solid State Ionics,* **89** (1996) 197.

Chapter 6

Electrochemical properties of the lithium Mn(IV) oxides, $Li_{2-x}Mn_3O_7$

6.1 Introduction

The purpose of investigating the electrochemical properties of the layered compounds $Li_{2-x}Mn_{3-y}O_7$ obtained by lithium ion exchanged from $Na_2Mn_3O_7$ (see Chapter 5), is to establish if such a process could enhance the ability of these compounds to sustain the removal and reinsertion of lithium. It has been shown in the previous chapter that the main difference between the synthesis in hexanol and ethanol at 125 and 70 °C respectively, lays with the cationic disorder in the layers of the structure, signature of a slight transformation to a spinel-type structure for the reflux in hexanol. It was then important to examine the influence of the synthesis on the electrochemical properties.

In this chapter, we explore the electrochemical properties of $Li_{2-x}Mn_{3-y}O_7$ and discuss their performances in the light of their compositions and structures. Like $LiMnO_2$ [1] and $Li_xMn_{1-y}Co_yO_2$ [2], they convert to a spinel-like phase upon cycling and the rate of conversion differs, depending on the ion exchange conditions. The structural changes on cycling will be followed by *in* and *ex-situ* XRD. Kinetic property of lithium transport in the oxide host will be investigated by an Intermittent Titration Technique (FITT) and ac impedance. The porous insertion electrode $Li_{2-x}Mn_{3-y}O_7$ will be modelled for purposes of ac impedance analysis carried out at during the intercalation of lithium ions.

6.2 Experimental

In this study, the composite electrodes were prepared using a dry method technique described in Chapter 2 (2.11.1). The fraction of the polymer binder using polytetrafluoroethylene (PTFE) was kept equal to 5wt %. The ratio of active material / carbon black varies depending of the type of carbon black (Monarch or Shawinigen) in order to maintain the resistance of the film below 10 Ω (see Chapter 3 section 3.1).

Thin films of average thickness 0.1 mm were obtained. The positive electrodes were cut with a diameter equal to 1.1 cm. The pellets were dried under vacuum in a Bücchi TO-50 for 10 h at 130 °C and the cells assembled under an argon atmosphere in a glove box (Unilab, Mbraun, USA). The characteristics of the pellet and conditions of cycling are reported in a table for each material.

For convenience, the voltage-composition curves correspond to the number of lithium ions per $Li_xMn_yO_2$ unit formula, x and y being different for both compounds.

6.3 Exchange in Ethanol *vs* Hexanol

The variation of the discharge capacity with the cycle number for the exchanged manganese oxides are presented in Figure 6.1, together with the cycling data of $LiMnO_2$ [2] and $Li_xMn_{1-y}Co_yO_2$ (y = 0.2, 0.025) [3]taken from the work of A. R. Armstrong *et al.* For the samples $Li_{2-x}Mn_{3-y}O_7$ refluxed in hexanol and in ethanol, the cycling was carried out at a current density of 0.2 and 0.5 $mAcm^{-2}$ respectively, between the potential limits of 2 and 4.5 V. This corresponds to a cycling rate of 17 and 37.7 mAg^{-1}.

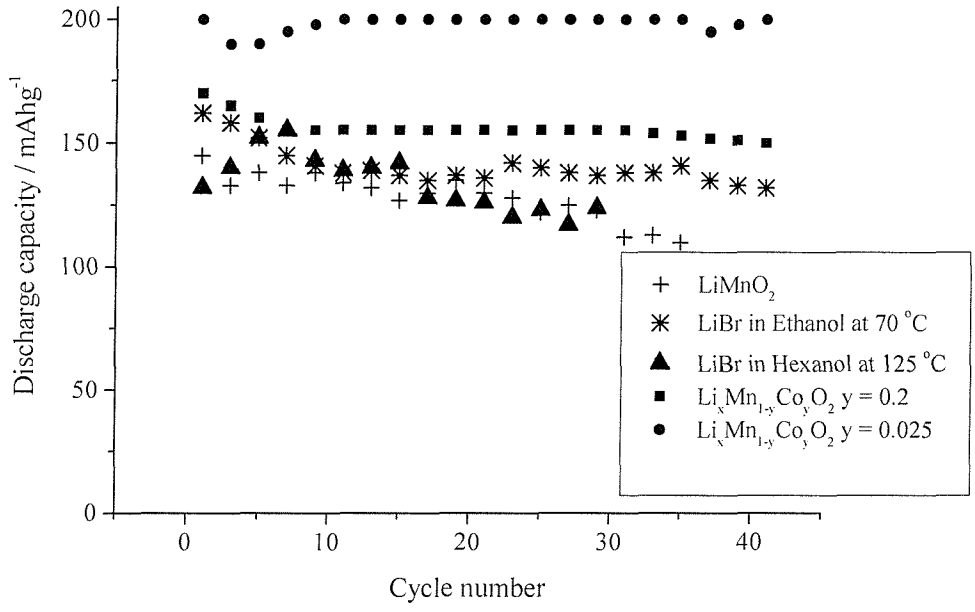

Figure 6.1 Discharge capacity as a function of the cycle number for the layered $Li_{2-x}Mn_3O_7$ prepared in hexanol and ethanol at a rate of 17 and 38 mAg^{-1} respectively, potential range 2-4.5 V. Capacity data of $LiMnO_2$ and $Li_xMn_{1-y}Co_yO_2$ (y = 0.2, 0.025) are also reported from Ref [2] and [3] (cycling at a rate of 25 mAg^{-1} and potential range 2.4-4.6 V).

$Li_{1.54}Mn_{3.01}O_7$ ($Li_{0.44}Mn_{0.86}O_2$ from chemical analysis in Chapter 5, section 5.4.1) prepared in ethanol shows, during the first 10 cycles an important drop in its initial discharge capacity of 162 $mAhg^{-1}$, falling to ~140 $mAhg^{-1}$. Then the capacities vary little with the cycle number with a fade rate of only 0.15 % per cycle. Its capacity retention is similar to that of $Li_xMn_{1-y}Co_yO_2$ (y = 0.2, 0.025) prepared in ethanol [3] for which the good performance could be explained by the *in-situ* formation of the nanostructured spinel-like phases.

After a rise within the first five cycles, the loss of discharge capacity increases on extended cycling for the sample in hexanol $Li_{1.96}Mn_{2.87}O_7$ ($Li_{0.56}Mn_{0.82}O_2$ from chemical

analysis in Chapter 5, section 5.4.1) to yield discharge capacities of ~125 $mAhg^{-1}$ after some 30 cycles.

6.4 Electrochemical properties of $Li_{0.44}Mn_{0.86}O_2$ prepared in ethanol at 70 °C

The characteristics and conditions of the cycling of the material are reported in Table 6.1. Figure 6.2 shows the voltage-composition curve for the sample obtained in ethanol. The sample was first discharged from its OCV to 2 V, showing a plateau in the 3 V region corresponding to the lithium ions uptake of ~0.48 per unit formula $Li_{0.44}Mn_{0.86}O_2$.

Well-defined plateaux at 3 V on charge and discharge develop together with ones on charge in the 4 V region after the first few cycles. During the following cycles, almost all of the lithium ions can be removed leading to an average reversible capacity of 140 $mAhg^{-1}$. Although the load curve for the material suggests significant structural change after the 10^{th} cycle, it is apparent that the capacity is insensitive to this structural transformation. The stability of the load curve from cycle 10 to 30 is in accordance with the stable discharge capacity observed in Figure 6.1.

The incremental capacity plot was derived from the previous curve. The electrochemistry shows that there is similarity with the spinel phase in the 4 V region. For a spinel compound, there are normally two pairs of redox peak at 4 and 4.1 V. These two oxidation peaks are here not well developed and only a hint of reduction process is seen.

Another feature appears after 20 cycles. An oxidation peak around 3.7 V indicates the formation of an intermediate layered-spinel phase. This peak was noticed before by Co. Gummow, Liles and Thackeray near 3.7 V in low temperature $LiCoO_2$ that has a structure intermediate, between normal spinel and high temperature layered $LiCoO_2$ [4]. This intermediate structure is the result of the displacement of manganese ions from the transition metal layers into the octahedral sites in the lithium layers, during the extraction of octahedral lithium ions. The single spinel phase is obtained when one quarter of manganese ions pass through a tetrahedral oxygen environment in order to migrate into the lithium layers.

It is of interest to note that this disordered structure is of the same kind as the one adopted by the compound resulting from the reflux in hexanol for which the electrochemical properties have been studied and are presented here.

Table 6.1 Characteristics and cycling conditions for the "ethanol compound".

Li source, solvent and temperature of the reflux of $Na_2Mn_3O_7$	LiBr in ethanol at 70 °C
Composition of the Materials from the Chemical Analysis	$Li_{0.44}Mn_{0.86}O_2$
Weight of active material in the composite pellet/ mg	13.3
Type of Carbon Black	Cabot Monarch 1400
Weight Ratio Active Material / Black Carbon / PTFE	65:30:5
OCP/ V	3.28
Theoretical Specific Capacity $mAhg^{-1}$	319
Cycling Rate mAg^{-1}	37.6 (I=0.5 mA)
Initial Practical Rate	C/3.9
Li^+ ion intercalated during the 1^{rst} discharge	0.48

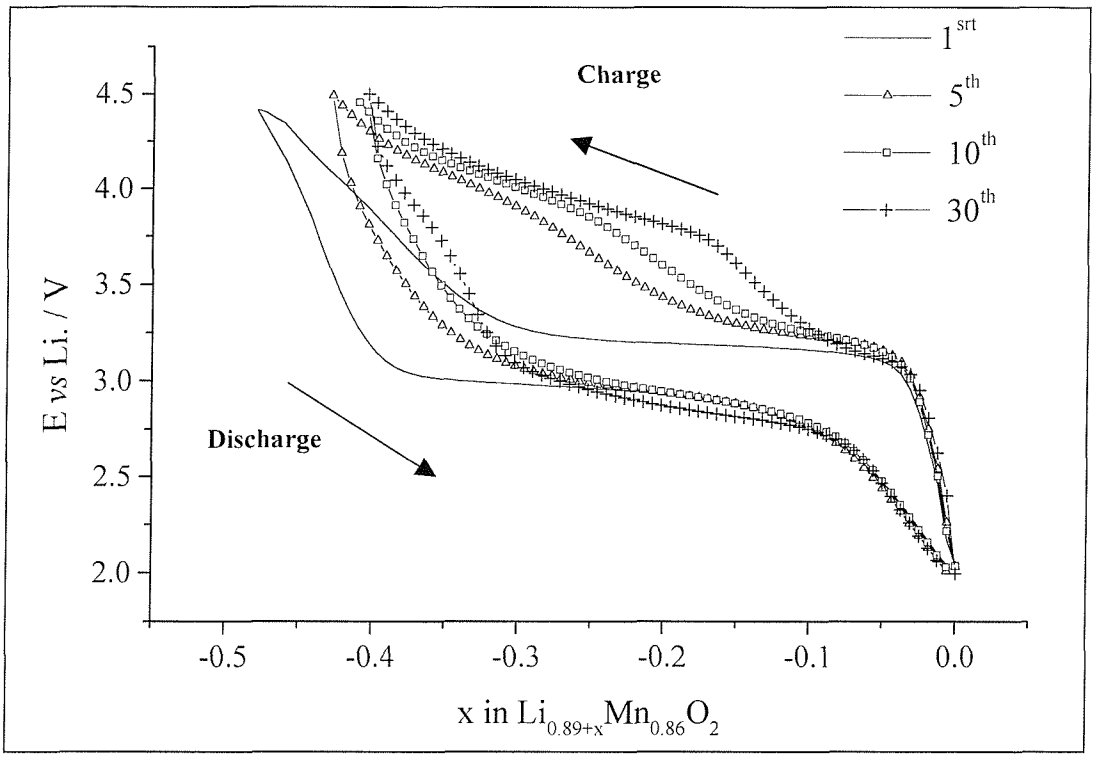

Figure 6.2 Voltage-composition curves for $Li_{0.44}Mn_{0.85}O_2$ obtained from ion exchange in the reflux of ethanol at 70 °C. The data were collected at a constant current of 0.5 $mAcm^{-2}$. The material was first discharged to 2 V changing the stoichiometry to $Li_{0.92}Mn_{0.85}O_2$.

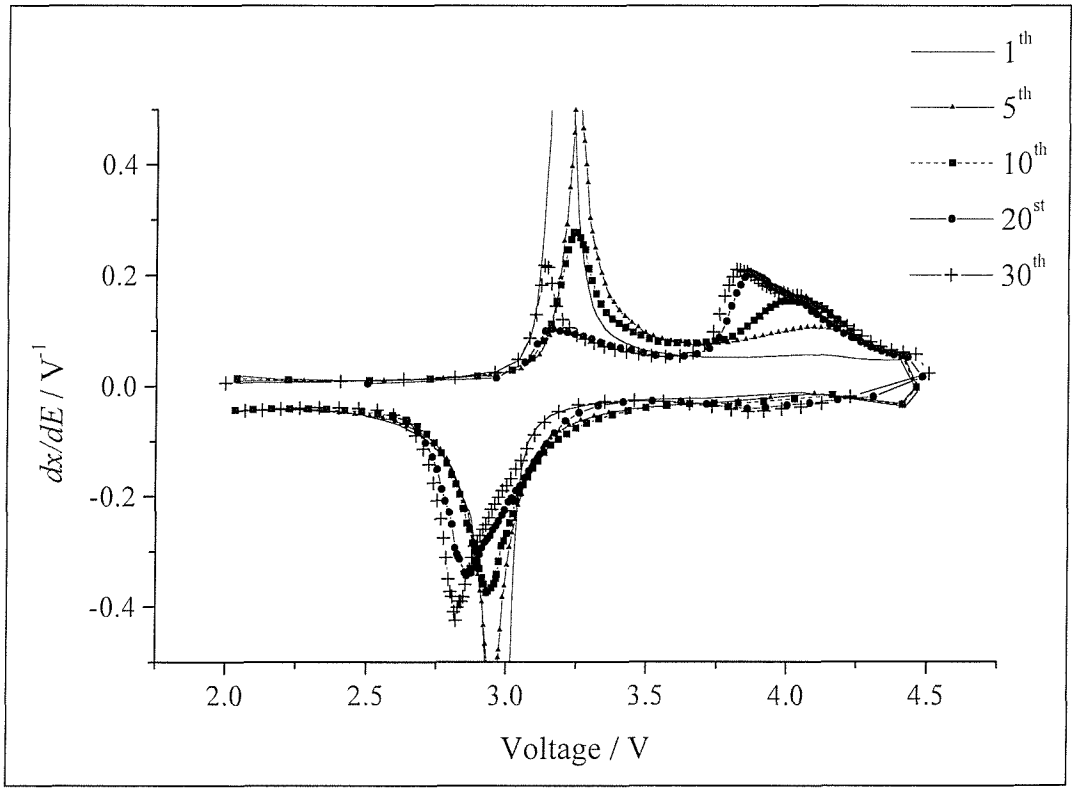

Figure 6.3 Incremental capacity plots for $Li_{0.44}Mn_{0.85}O_2$. Data collected at 0.5 $mAcm^{-2}$ (C/4).

6.5 Electrochemical properties of $Li_{0.56}Mn_{0.82}O_7$ prepared in hexanol at 125°C

The characteristics and conditions of the cycling of the material are reported at Table 6.2. Figures 6.4 and 6.5 show the voltage-composition curve and incremental capacity plot for the sample prepared in hexanol at 125 °C. The cycling was carried out at constant current densities of 0.2 $mAcm^{-2}$ between the potential limits of 2 and 4.5 V. Because of the high oxidation state of manganese, the material was first discharged from its OCV (3.04 V) to 2 V and 0.21 lithium ion per unit formula of $Li_{0.56}Mn_{0.82}O_2$ was inserted in the material. After several following cycles, ~0.37 lithium ion was cycled in the material, offering a capacity of 125 $mAhg^{-1}$

While on charge and discharge, the curves show plateaux in the 3 and 4 V regions from the early cycles due to the cationic disordered structure of the material. Two pairs of redox peaks are evident, coincident with the peaks from the spinel phase. This is the important insertion process at 4 V that leads to an increase of the discharge capacity during the first cycles (Figure 6.1) which is followed by a gradual loss in the capacity retention marked after 10 cycles. The oxidation peak at 3.7 V, mentioned in the previous study of the compound prepared in ethanol, is now present from the early cycles and its intensity decreases upon cycling. An additional reduction peak also appears in the 2 V region during the first cycles and seems to reach its maximum intensity after 5 cycles. This process also contributes to the increase during the early discharge capacity. This additional peak in the 2 V region was also noticed on discharge in the case of the orthorhombic phase of $LiMnO_2$ prepared at high temperature [5]. It was also coupled to an oxidation peak at 3.75 V.

In order to compare and discuss the differences arising between the two samples, their incremental capacity plots are shown together in Figures 6.6 and 6.7, for the first and the fifth cycle. The curves indicate that transformation to spinel is much slower for the sample prepared in ethanol. Even if the discharge capacity is higher for the sample prepared in hexanol at the 5^{th} cycle, the capacity fade, during the following cycles, is greater than for the material that had transformed slowly into spinel phase.

The oxidation and reduction peaks at 3 V for the material prepared in hexanol are shifted toward the lower potential. The shift (Figure 6.5) between them increases upon cycling and this has its origin in the structural change accompanying the transformation from

the disordered layer structure to the spinel. The intensity of the reduction peak at 2.8 V tends to increase upon cycling.

Table 6.2 Characteristics and cycling conditions for the "hexanol compound".

Li source, solvent and temperature of the reflux of $Na_2Mn_3O_7$	LiBr in hexanol at 125 °C
Composition of the Materials from the Chemical Analysis	$Na_{0.05}Li_{0.558}Mn_{0.816}O_2$
Weight of active material in the composite pellet/ mg	11.8
Type of Carbon Black	Shawinigen Acetylene Black
Weight Ratio Active Material / Black Carbon / PTFE	70:25:15
OCP/ V	3.04
Theoretical Specific Capacity $mAhg^{-1}$	325
Cycling Rate mAg^{-1}	17 (I=0.2 mA)
Initial Practical Rate	C/8.7
Li^+ ion intercalated during the 1^{rst} discharge	0.21

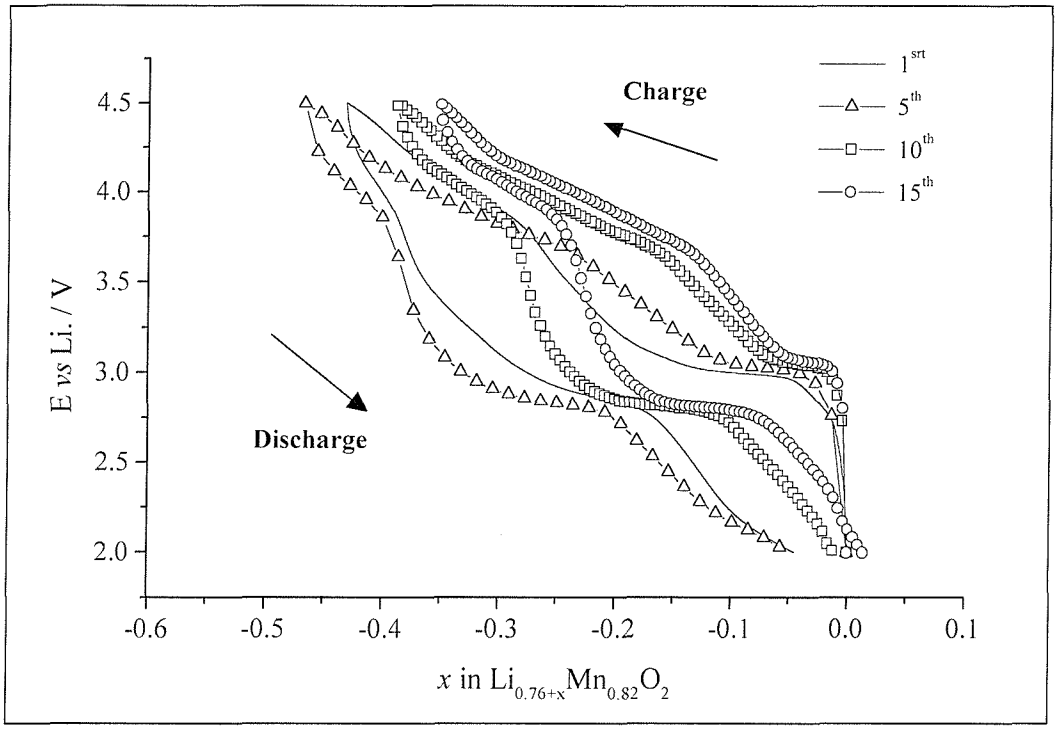

Figure 6.4 Voltage-composition curves for $Li_{0.56}Mn_{0.82}O_2$ obtained from ion exchange in reflux of hexanol at 125 °C. The data were collected at a constant current of 0.2 $mAcm^{-2}$. The material was first discharged to 2 V changing the stoichiometry to $Li_{0.76}Mn_{0.82}O_2$.

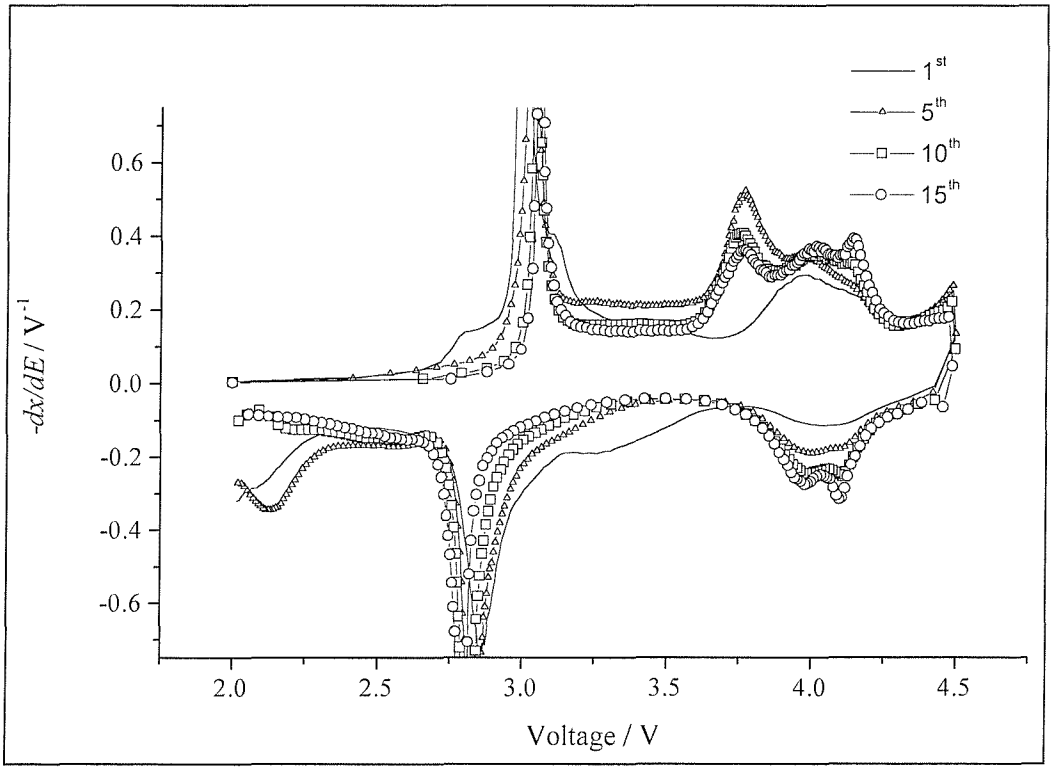

Figure 6.5 Incremental capacity plots for $Li_{0.56}Mn_{0.82}O_2$. Data collected at 0.2 $mAcm^{-2}$ (C/9).

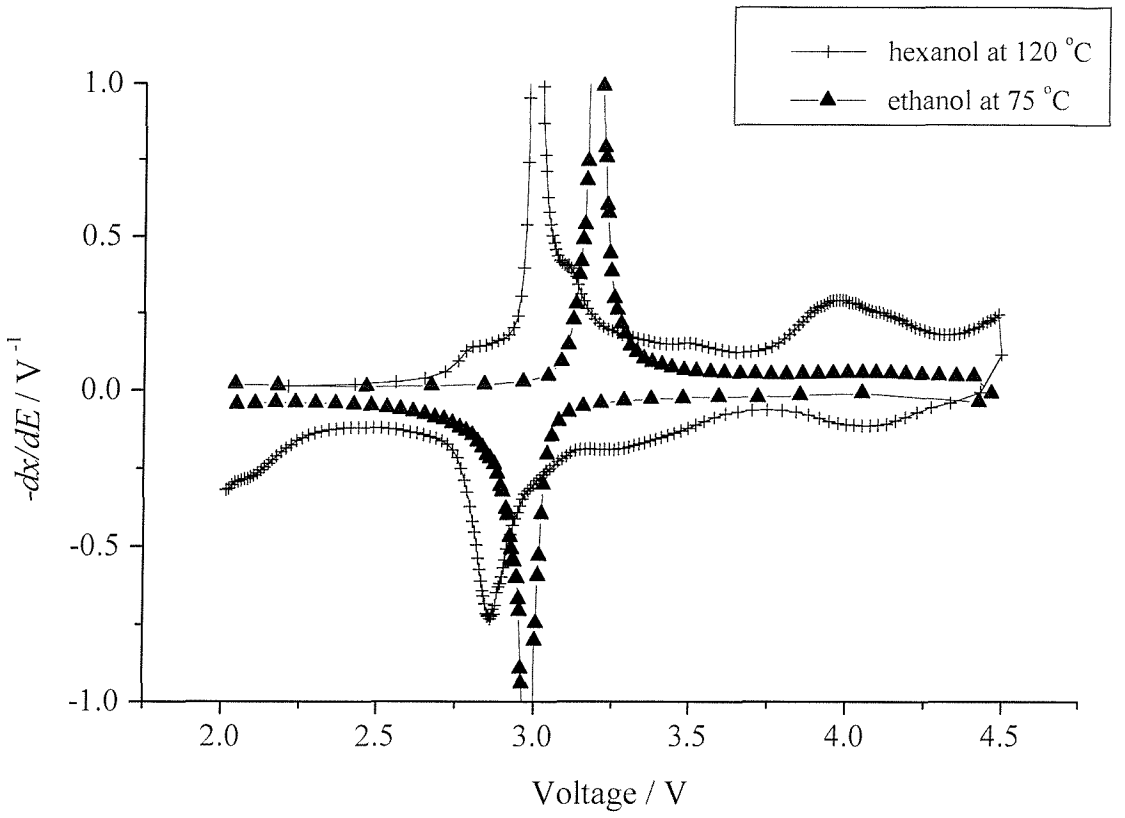

Figure 6.6 Incremental capacity plots of the 1[srt] cycle after a preliminary discharge to 2 V for $Li_{0.44}Mn_{0.85}O_2$ and $Li_{0.56}Mn_{0.82}O_2$.

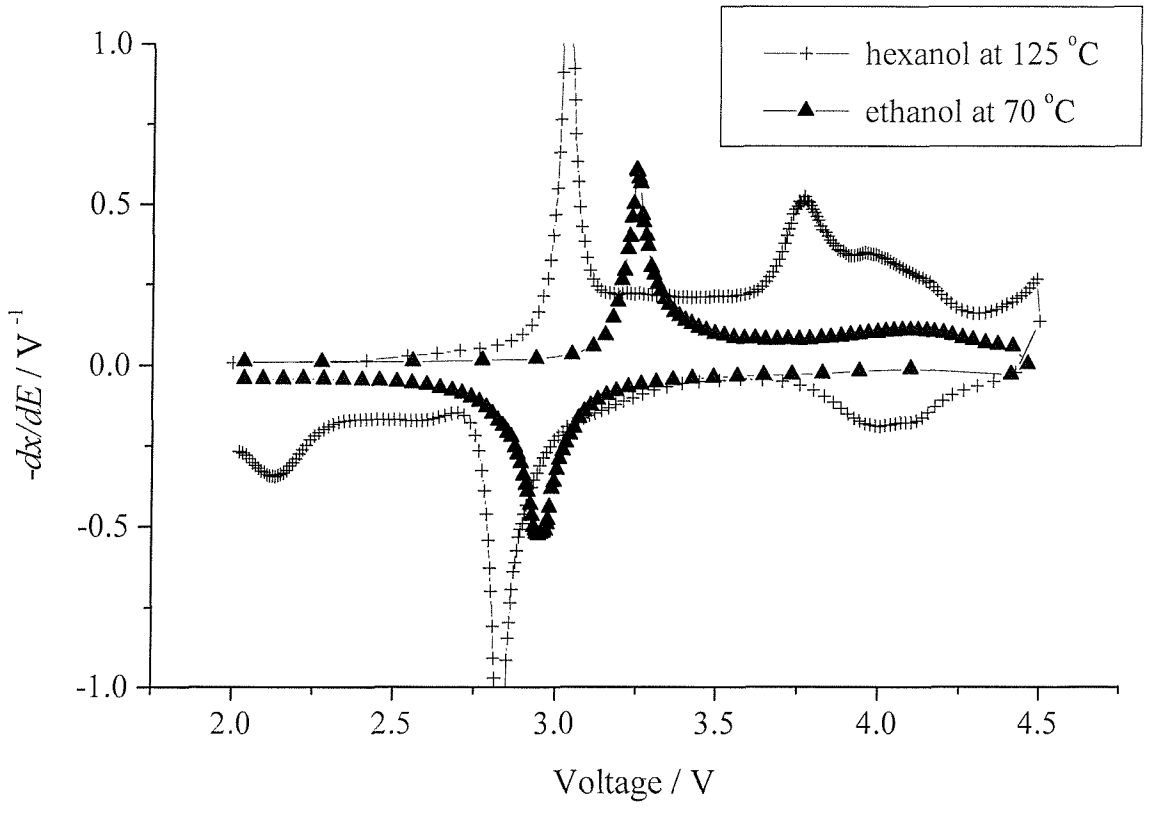

Figure 6.7 Incremental capacity plots of the 5[th] cycle for $Li_{2-x}Mn_3O_7$.

6.6 *Ex-situ* and *in-situ* X-ray diffraction analyses

In the *ex*-situ experiment, the electrochemical cells of lithium manganese oxides were stopped on charge at 3.7 V after the cycling. After an equilibrium time of one day, the cathodes were removed and dried before the X-ray analysis. The figures 6.8 and 6.9 show the XRD patterns of the samples obtained in ethanol and hexanol before the cycling and after 40 and 30 cycles respectively.

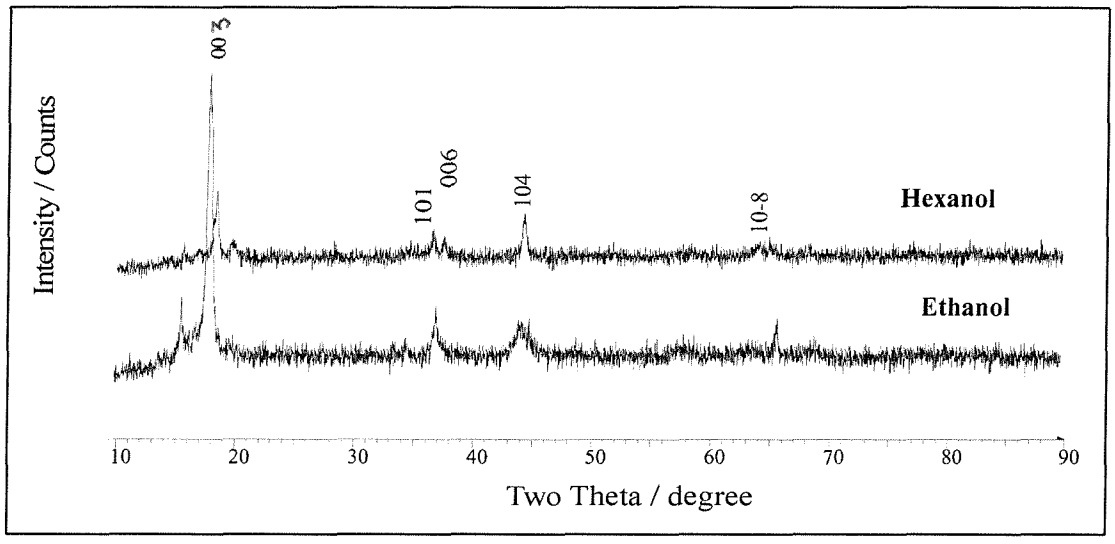

Figure 6.8 XRD patterns before the cycling of the lithium ion exchanged $Li_{2-x}Mn_{3-y}O_7$ after reaction in hexanol and ethanol.

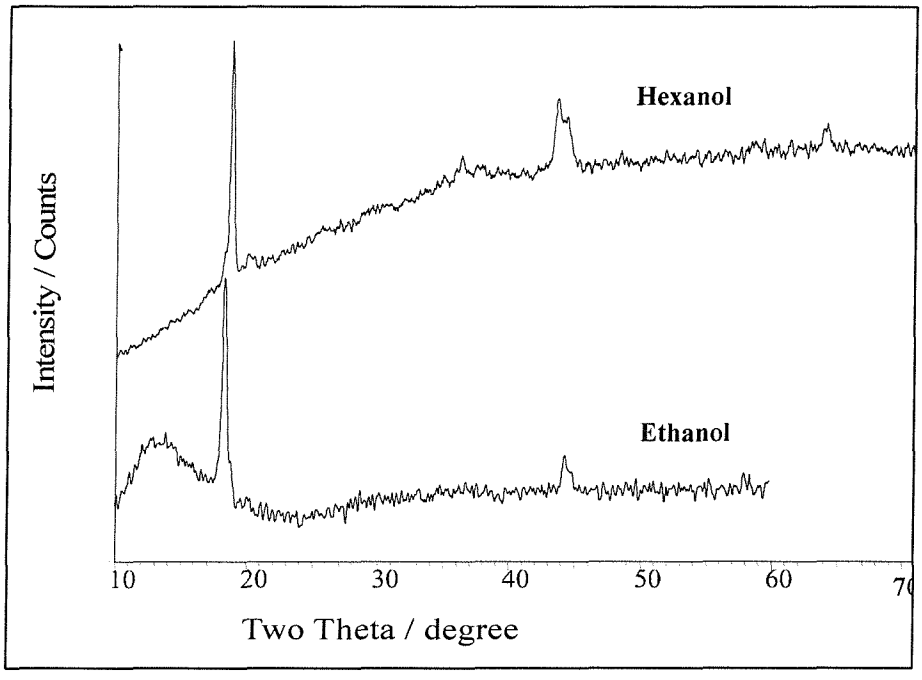

Figure 6.9 XRD patterns of the lithium ion exchanged $Li_{2-x}Mn_{3-y}O_7$ pellets after 30 (hexanol) and 40 cycles (ethanol).

The most intense peaks corresponding to the (003) and (104) reflections of the hexagonal $Li_{2-x}Mn_{3-y}O_7$ phases are still visible after the cycling, on Figure 6.9.. The contribution of the metallic support for the sample prepared in hexanol causes a more intense background. The phases have lost their crystallinity after cycling. The main peaks for the spinel, $LiMn_2O_4$ corresponding to the (111), (311), (400) reflections, are situated at ~19.1°, 31.4° and 45° respectively. There is no peak in the XRD patterns of the materials after cycling that could correspond to a spinel phase $LiMn_2O_4$.

The Figure 6.10 shows the *in-situ* XRD pattern collected during the first cycle of the sample prepared in ethanol at various states of discharge and charge denoted by the letters A, B, C and D. The cell was held at the given potential for 30 mins to allow the potential to equilibrate. Due to the intense peak of the beryllium, the scans were stopped at 50° to avoid a decrease in the intensity of the peaks in the area 10 to 50°.

The first pattern (pattern A) shows the scan of the cell freshly assembled, at a voltage of 3 V. The peaks seen are very weak, due to the reflection mode of this *in-situ* experiment. However the presence of the initial phase of $Li_{2-x}Mn_3O_7$ is seen together with the peaks at 38.5° and 44.5° in 2θ (denoted by + marks) corresponding respectively to metallic silver and beryllium, the silver paste being used to enhance electrical contact between the beryllium window and the cell holder.

No extra peaks were formed during the first cycle. The only change is a shift of the most intense peak at ~18.5 ° corresponding to the (003) reflection, towards the high angles on discharge (B pattern) and low angles on charge (C and D patterns). This is respectively characteristic of a decrease and increase of the *c* parameter on cycling when lithium ions are inserted and extracted between the layers.

The X-ray study confirms the formation of a phase having an intermediate structure between layer and spinel as seen previously in the incremental plot (Figure 6.3).

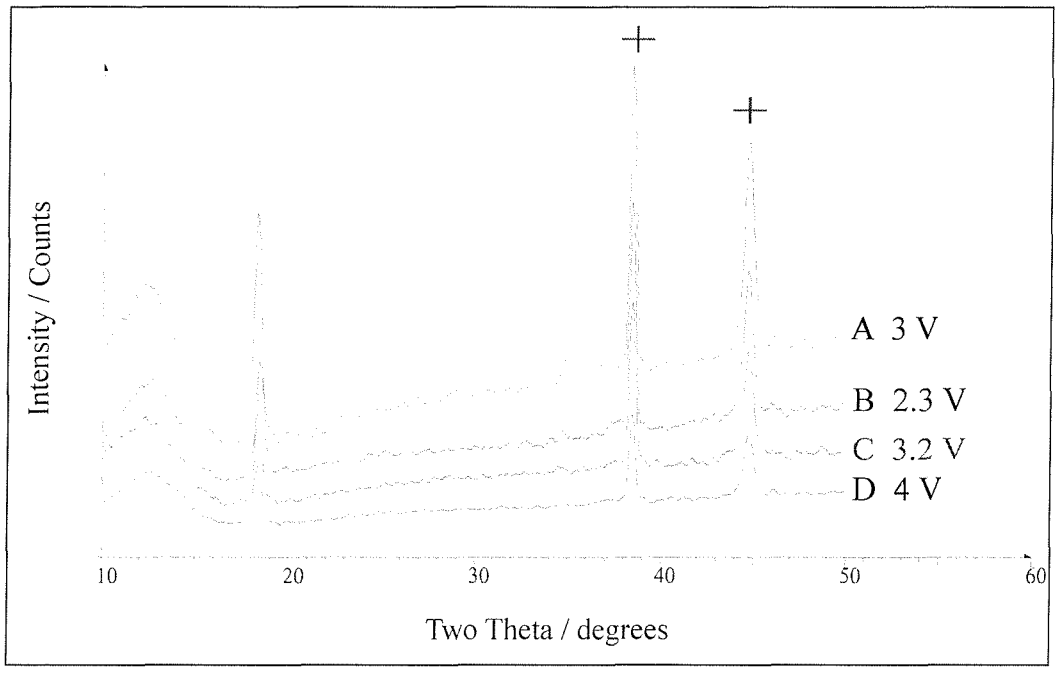

Figure 6.10 *In-situ* XRD patterns of $Li_{2-x}Mn_3O_7$ obtained in ethanol at different states of charge and discharge. The crosses indicate the peaks corresponding to the silver and beryllium reflections.

6.7 Chemical diffusivity of lithium in $Li_{0.44}Mn_{0.86}O_2$ in ethanol at 70 °C

The chemical diffusivity of lithium ions was determined at room temperature by current-pulse techniques in an electrochemical cell Li/($LiPF_6$ in EC/DMC)/$Li_{2-x}Mn_3O_7$ at a potential of 3.98 V. Lithium was introduced into the porous composite $Li_{2-x}Mn_3O_7$ electrode by a constant current-pulse (0.4 mA) for short times (~80s). The response of the electrode was determined by FITT [6] described in detailed in Chapter 2 (2.11.3). The time dependence of the potential with this method is expressed as:

$$\frac{d(\Delta E)}{d(t^{-1/2})} = \frac{(dE/dx)V_M Q}{FA\sqrt{\pi D}}$$

In the formula, the terms are equal to:

$\frac{d(\Delta E)}{d(t^{-1/2})}$,the slope of the voltage-time relation at Figure 6.11 ($Vs^{1/2}$ or $Vs^{-1/2}$), 1.44

dE/dx- the slope of the voltage versus composition curve ($Vmol^{-1}$), 8.2 calculated from dE =30 mV and $dx = 3.7\ 10^{-3}$

V_M- the molar volume (cm^3), 20 cm^3

Q- the charge sent through the cell equal to the time pulse by the current pulse (C), 0.032 C

A- the total apparent surface of the active material in the sample (cm^2), $1.86\ 10^2$ cm^2 calculated from the size of the particles by SEM or $1.5\ 10^2$ cm^2 calculated from the BET surface area.

F- the Faraday constant 96 485 C mol^{-1},

D, the diffusivity of Li ions was found equal to ~ $5\ 10^{-14}$ $cm^2\ s^{-1}$.

A value of $5\ 10^{-14}$ $cm^2\ s^{-1}$ seems too small, considering the electrochemical activity of the material during the cycling (Figure 6.3). The error could come from a wrong value of the total area A of contact between the electrode and electrolyte, estimated from the size of the particles in the material. The electrodes studied are in fact porous and we assume that the electrolyte penetrates fully in the electrode.

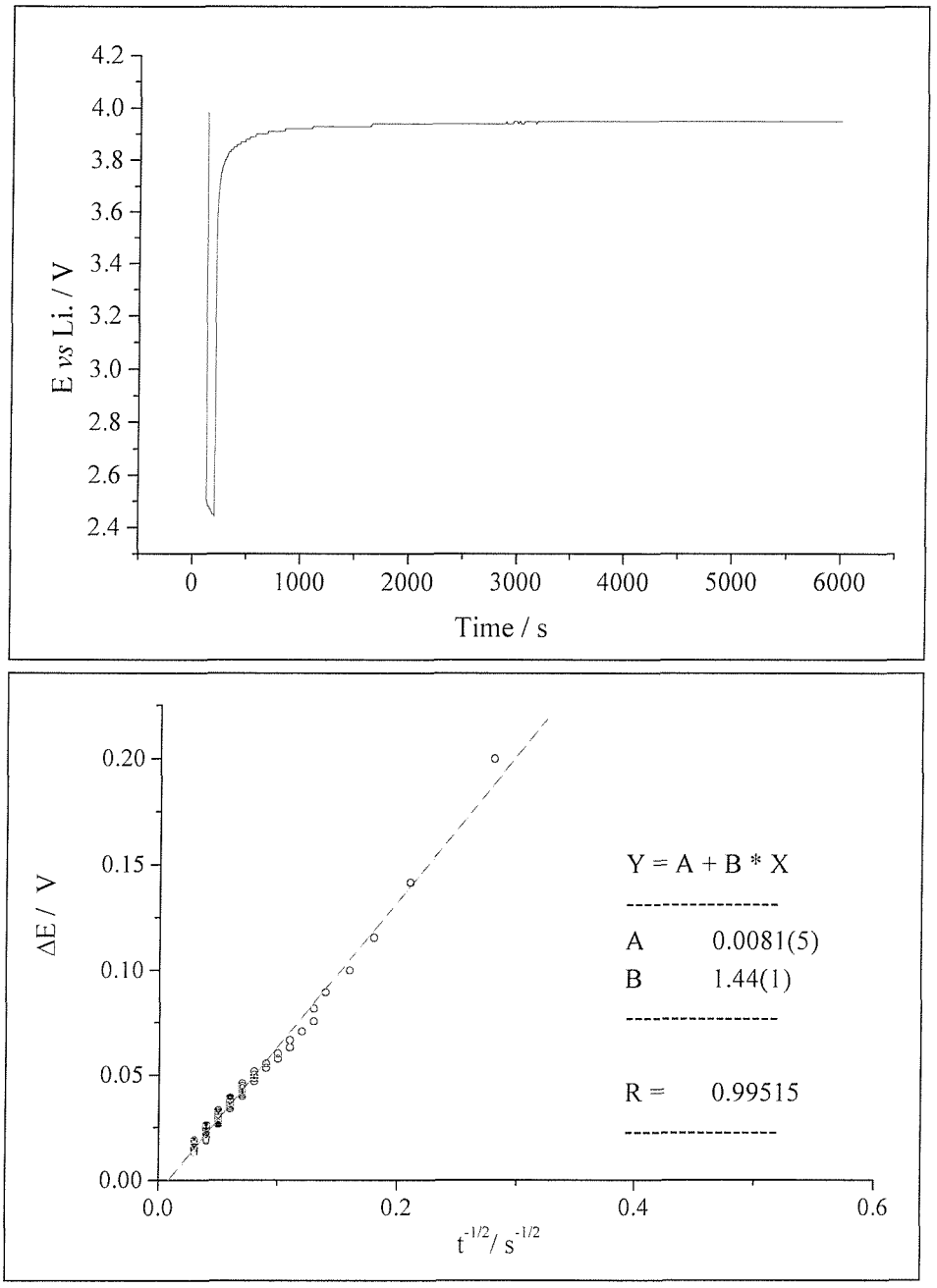

Figure 6.11 Voltage-time relation in the current pulse method (FITT) for $Li_{2-x}Mn_3O_7$ obtained in ethanol.

6.8 Study by ac impedance of the Li/($LiPF_6$ in EC/DMC)/ $Li_{0.44}Mn_{0.86}O_2$ cell

6.8.1 Experimental

The ac impedance measurements were carried out in the frequency range from 0.05 Hz to 100 kHz and at several potentials. The cell was first discharged to 2 V and then recharged to 3.15 V for 4 hours. The potential of the electrochemical cell Li/($LiPF_6$ in EC/DMC)/$Li_{2-x}Mn_3O_7$ (Figure 2.9 a) was then changed stepwise to the desired value and held at the given potentials for half an hour.

The ac impedance of the electrochemical cell is described by an equivalent circuit such as that shown in Figure 6.12. The model divides the problem into three segments: the bulk electrolyte, the interface and the bulk electrode, which correspond to separate regions on the plots (Figure 6.13): the resistance of the electrolyte R_e, a semicircle at high frequencies region, Warburg diffusion impedance Z_w at the low frequencies region and a capacitive behaviour at the very low frequencies region C_{dl}.

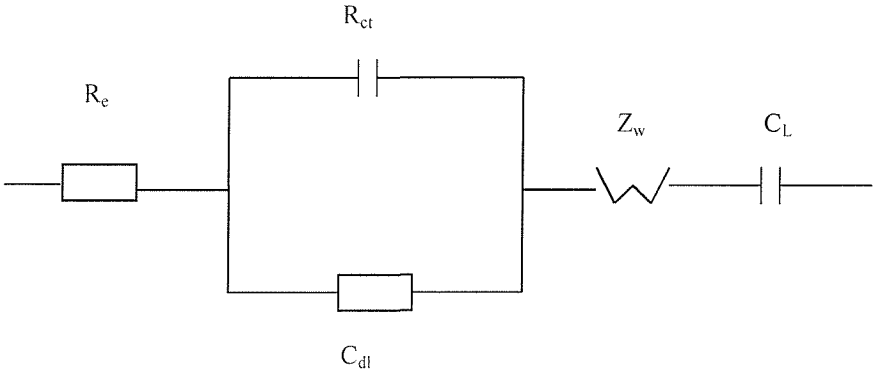

Figure 6.12 Equivalent circuit used to model the impedance spectra.

The different parameters were determined using the model described by a non-linear least square-fitting procedure with the Zview program.

6.8.2 Results and discussions

Between the open-circuit potential of 3.15 and 3.45 V (Figure 6.13), the size of the semicircle decreased which corresponds to a decrease of R_{ct} due to the variation of the conductivity of the materials during the extraction of lithium ions. This could also be ascribed to a decrease of the resistance of the passivation layer on lithium R_{pl}. In this two-electrode cell, the distinction of R_{ct} from the resistance due to the passivation layer on lithium

R_{pl} is not possible. C_{dl} increases with the voltage. (Figure 6.14). R_e was found to be constant and equal to ~5.6 Ω.

When the cell was held at 3.5 V and that the ac impedance measurements were carried out after several hours (Figure 6.15), R_{ct} and R_{pl} increase upon exposure while the C_{dl} decreases after 6 hours. This can be ascribed to the formation of a film at the surface of the electrode that could cause restricted electrode kinetics implying irreversible electrolyte decomposition. The formation of a surface layer was also observed by ac impedance analysis of a composite electrode [7] and pressed-powder electrodes of $LiCoO_2$ [8]. It was reported that, the semicircle in the high frequency region was due to film formation such as Li_2CO_3 at the surface of the oxide. The charge transfer becomes more difficult and the thickening of the surface film during the storage increases the R_{ct}.

The inclined spikes at 45 ° are present on all the Nyquist plots at Figure 6.13, 6.15, 6.17. The Warburg impedance is related to the diffusion coefficient of the insertion ion Li^+ in the electrode. At angular frequencies $\omega = D/l^2$, it becomes as a capacitor as finite conditions are reached.

In this case, l represents the radius of the particles (1 μm) and D the diffusion coefficient. With the value of D calculated by a pulse current technique, ω *is* estimated to be equal to $\sim 10^{-5}$ Hz. This value is related to the diffusion time of the mobile-ion inside the bulk of the active material and determined the limit below which the diffusion-control migration can be described by the Warburg impedance for $\omega >> D/l^2$.

$$A_w = \frac{V_M}{AnF(2D)^{1/2}} \frac{dE}{dx}$$

The A_w coefficient can be obtained from the slope of Z' or Z'' *vs.* $\omega^{-1/2}$ (Figure 6.18). In order to compare with the previous value from the Intermittent Titration Technique, the measurement was done at the same voltage of 4 V. The plot of Z' *vs.* $\omega^{-1/2}$ shows linear relation and A_w is found equal to 33 (Figure 6.18). From the previous equation,

A_w- the Warburg coefficient, 33

dE/dx- the slope of the voltage versus composition curve ($Vmol^{-1}$) at V = 4 V, 8.2

V_M- the molar volume (cm^3), 20 cm^3

A- the total surface of the active material (cm^2), 1.86 10^2 cm^2 calculated from the size of the particles by SEM or 1.5 10^2 cm^2 calculated from the BET surface area.

F- the Faraday constant 96 485 C mol^{-1},

D, the diffusivity of Li ions was found equal to ~ 6 10^{-14} cm^2 s^{-1}. By using the same value for the surface *A*, the coefficient is found to be similar to the one previously calculated.

The low frequency part of the plot at Figure 6.17 indicates a capacitive behaviour relative to the electrode and carbon black in the electrode (Figure 6.19). From the capacitance of the carbon used (~4 Fg^{-1}) we estimate the contribution of the carbon black, *i.e.* ~10^{-2} F, to the capacitance calculated from the plot at the lowest frequency (0.05 Hz), *i.e.* $C = 1/\omega Z''$ = 4.7 10^{-2} F. The capacity calculated from the derivation of the galvanostatic cycling (dQ/dE) gives for the active material $Li_{0.44}Mn_{0.86}O_2$ a capacity of ~250 F, which corresponds to Z'' = ~10^{-2} Ω at 0.05 Hz. The impedance Z'' is of 70 Ω at the lowest frequency of 0.05 Hz. This corresponds to a charge/discharge in 10 s in which case, the capacity delivered by $Li_{0.44}Mn_{0.86}O_2$ should be very low. The capacitive contribution of the active material is not seen in this frequency range.

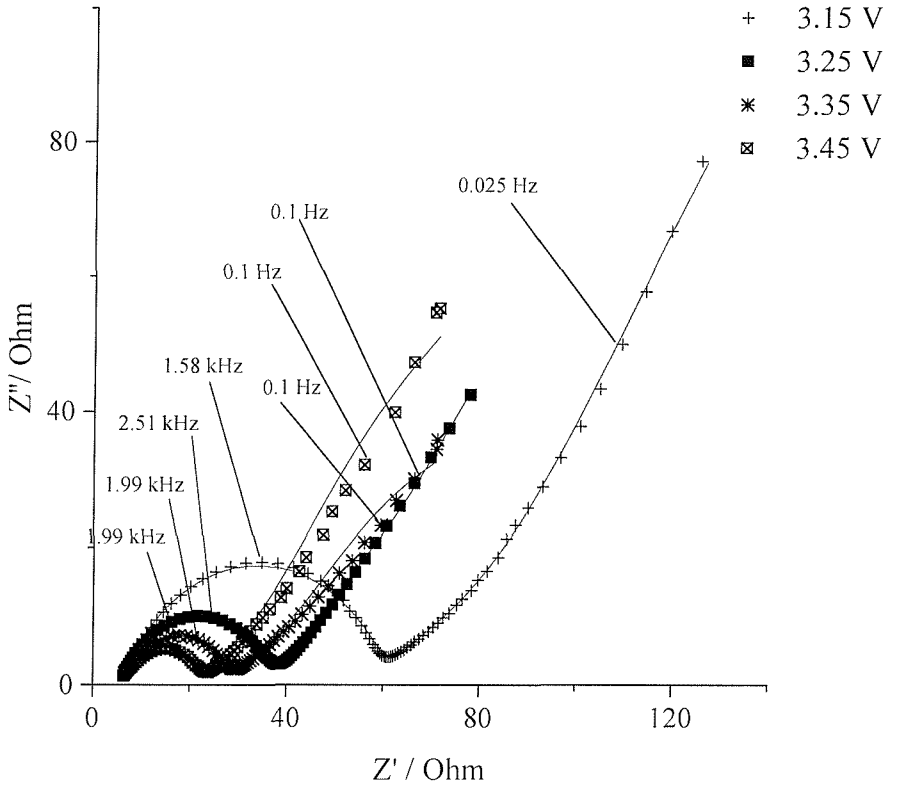

Figure 6.13 Nyquist plots for the Li/($LiPF_6$ in EC/DMC)/ $Li_{0.44}Mn_{0.86}O_2$ cell at various potentials.

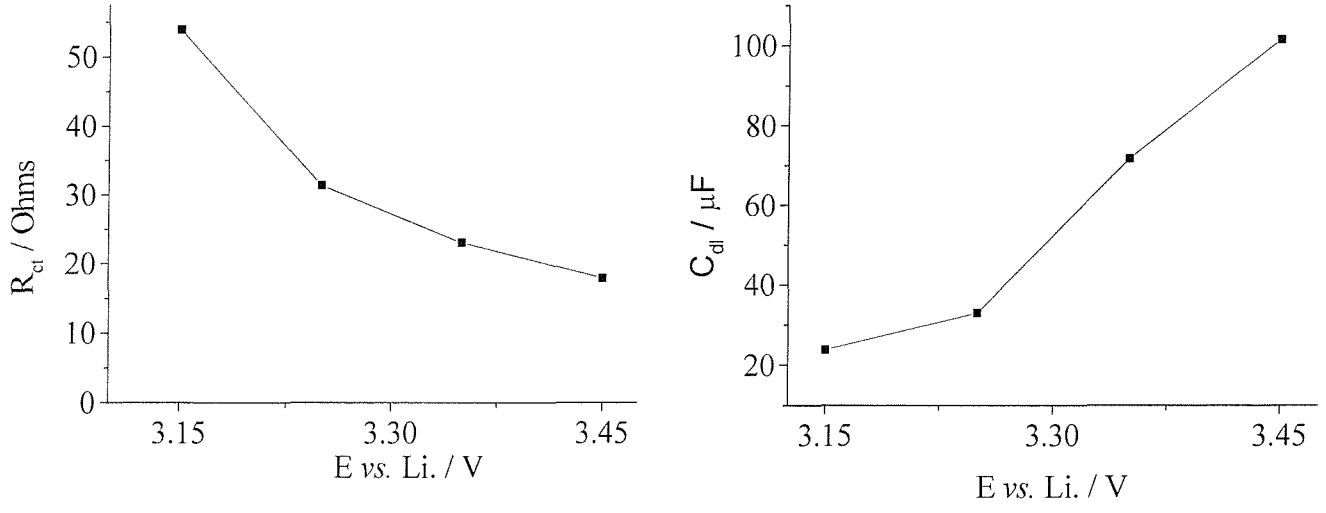

Figure 6.14 Variation of R_{ct} (left) and C_{dl} (right) with the potential of the cell

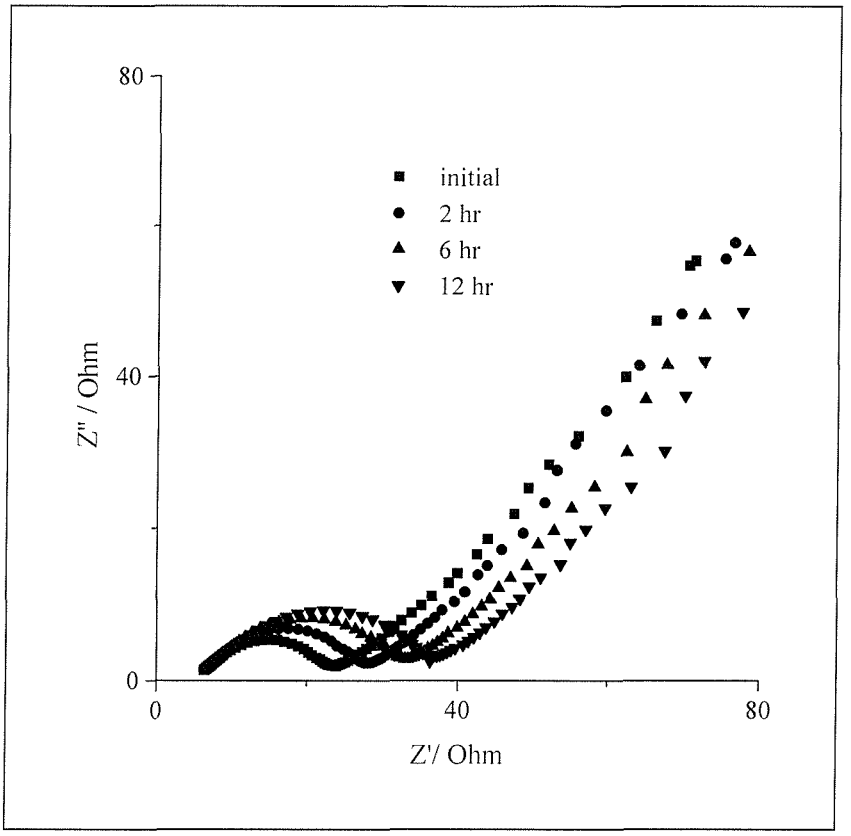

Figure 6.15 Variation of the Nyquist plots for the Li/($LiPF_6$ in EC/DMC)/ $Li_{0.44}Mn_{0.86}O_2$ cell upon storage. The electrode was held at 3.5 V and ac impedance was measured intermittently for up to 12 hours.

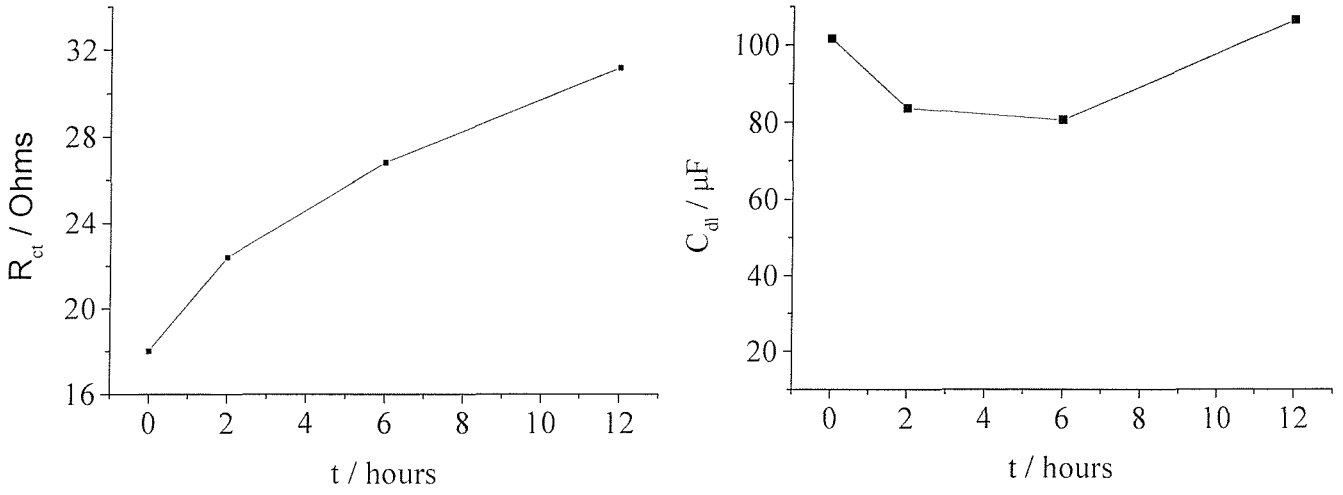

Figure 6.16 Variation of R_{ct} (left) and C_{dl} (right) when held at 3.5 V.

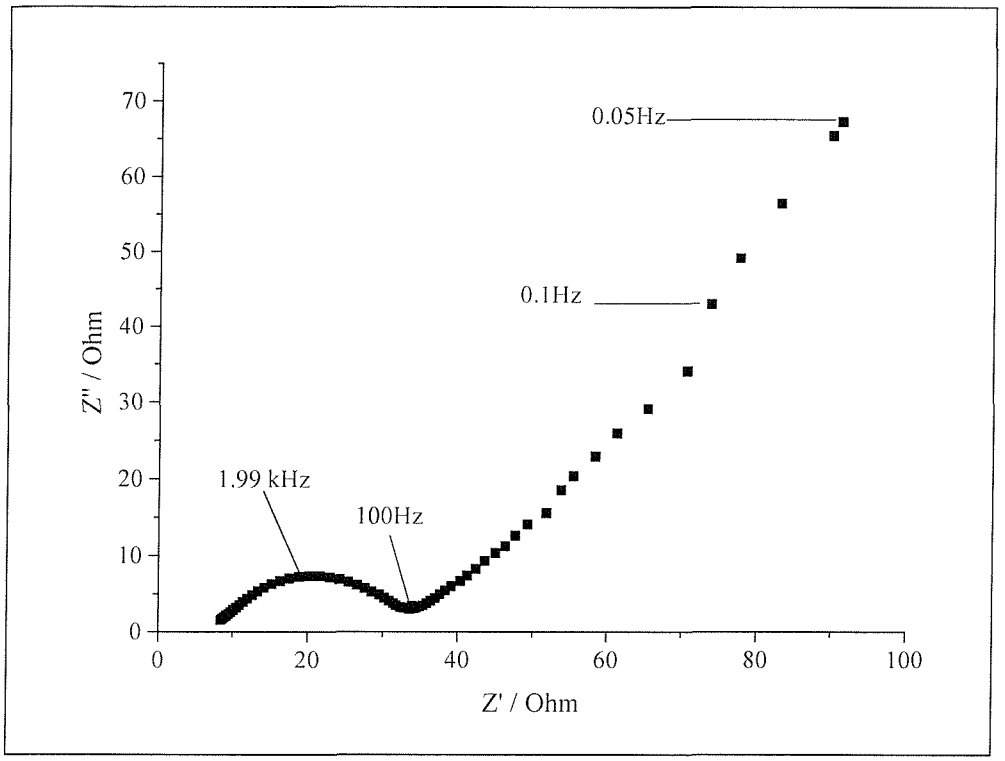

Figure 6.17 Nyquist plots for the Li/($LiPF_6$ in EC/DMC)/ $Li_{0.44}Mn_{0.86}O_2$ at 4 V.

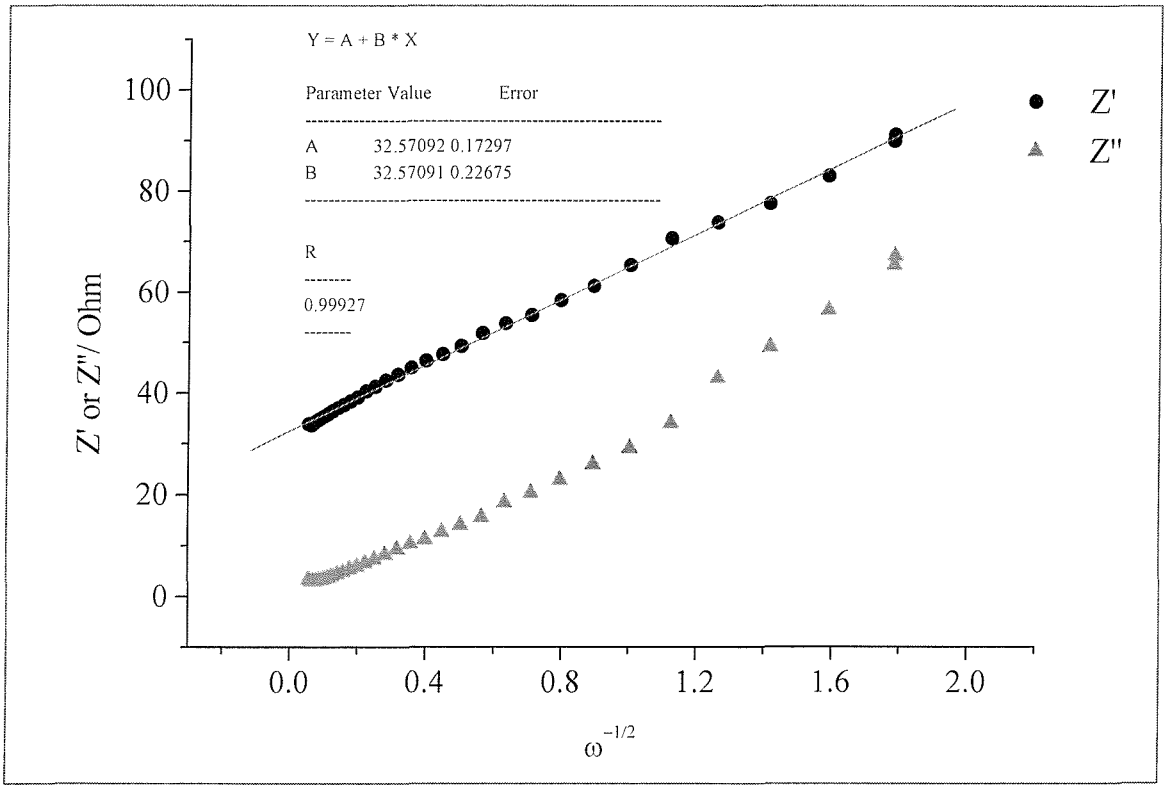

Figure 6.18 Plot of Z' and Z'' versus $\omega^{-1/2}$ showing the value of the Warburg coefficient calculated from the slope of the line.

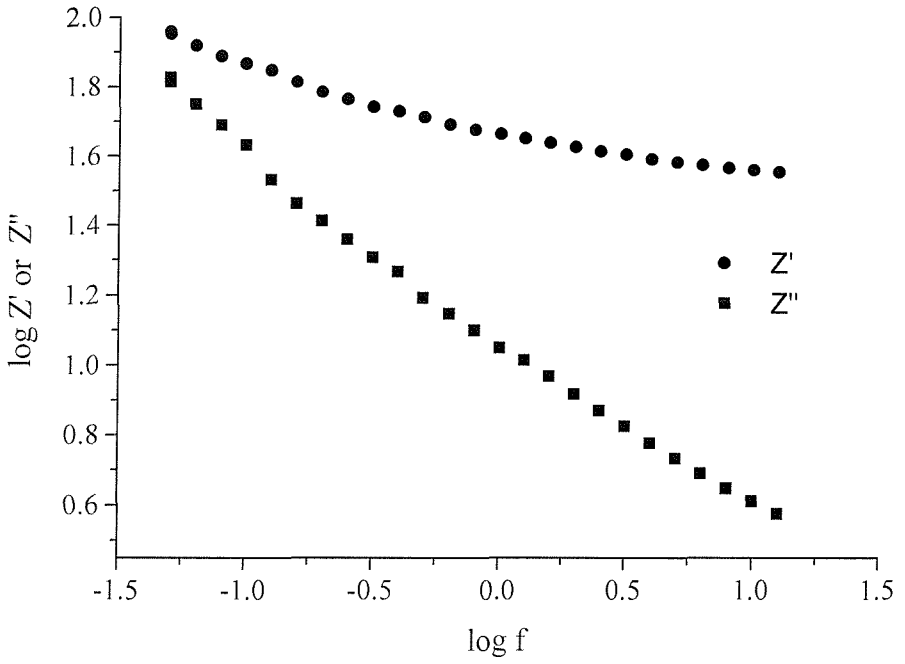

Figure 6.19 Bode plot showing a capacitive behaviour at low frequency.

6.9 Conclusion

The electrochemical properties of the lithium manganese oxides were found to depend on the ion exchange conditions. The compound obtained in ethanol exhibits a higher capacity to cycle lithium and a better specific capacity retention. The initial discharge capacity is of 162 $mAhg^{-1}$ with a fade rate of only 0.15 % per cycle on extended cycling.

Both layered compounds convert to a spinel-like phase on cycling, whether the ion exchange is carried out in hexanol or ethanol; however the rate of conversion depends on the ion exchange conditions. X-ray diffraction patterns collected after the cycling for both materials do not show clearly spinel-like characteristics, due to a loss of crystallinity of the phases. In the incremental capacity plots, the formation of a spinel-like phases for the reaction in hexanol is evidenced by the oxidation peaks at 3.7 and 4 V.

A nanostructured model was proposed by A. Robertson *et al* [3] to explain the origin of the difference of the cycling properties between materials prepared in hexanol and ethanol. In his model, the spinel phases are nanostructured with each crystallite composed of a mosaic of nanodomains that facilitate the Jahn-Teller transformation upon cycling. In this work, the formation of such structures has not been verified.

The chemical diffusion coefficient of $Li_{1.54}Mn_{3.01}O_7$, calculated by an Intermittent Titration Technique and the Warburg formula, is found to be very low, equal to $\sim 10^{-14}$ cm^2s^{-1}, $LiMn_2O_4$ having 10^{-9} cm^2s^{-1} [9]. The difficulty to estimate the right surface area A of the active material in contact with the electrolyte is thought to be at the origin of the error on the diffusion coefficient. The formation of the surface layer suggested by the ac impedance has not been fully evidenced in this work.

6.10 References

[1] A. R. Armstrong ; P. G. Bruce, *Nature*, **381** (1996) 499.

[2] A. R. Armstrong, A. D. Robertson, R. Gitzendanner, P. G. Bruce, *J. Solid State Chem.*, **145** (1999) 549.

[3] A. D. Robertson, A. R. Armstrong and P. G. Bruce, *Chem. Mater.*, 2380 (2001).

[4] R. J. Gummow, D. C. Liles, and M. M. Thackeray, *Mater. Res. Bull.* **28**, (1993) 235.

[5] G. Vitins, Thesis, University of Riga, Latvia (1999) 90.

[6] W. Weppner, R. A. Huggins, Electrochemical methods for determining kinetics properties of solids, Annual Review of Materials Science, (1978) 269.

[7] D. Aurbach, D. Levi, E. Levi, H. Teller, B. Markovsky, G. Salitra, U. Heider and L. Heider, *J. Electrochem. Soc.*, **145** (1998) 3024.

[8] M. G. R. S Thomas, P. G. Bruce, J. B. Goodenough, *J. Electrochem. Soc.*, **132** (1985) 1521.

[9] J. Barker, R. Pynenburg, R. Koksbang, *J. Power Sources*, **52** (1994) 185.

Chapter 7

Conclusion

The lithium copper oxides $Li_xCu_2O_4$ (x = 2,3,4) studied in this work can be seen as closely related to that of the α-$NaFeO_2$-type structure. Compounds of this type having as general formula $LiMO_2$ (M = Co, Ni, Mn), are widely studied for their applications in rechargeable lithium batteries. Extensive doping is possible by replacing, in part, cobalt, nickel or manganese by a variety of other ions. Recent work by C. Julien *et al* [1] on cobaltates, $Li(Co_{1-y}M_y)O_2$ with various M^{3+} cations, *e.g.* nickel, aluminium, or boron have shown good stability upon cycling.

$Li_xCu_2O_4$ (x = 2,3,4) are also built of MO_6 (M = Cu) and LiO_6 octahedra sharing edges. The octahedra formed by the next-nearest oxygen neighbours of copper in the lithium cuprates and cuprics are found however to be very distorted resulting in a square-planar environment around the copper. This results in the chain-like structure. The copper in this structure is more susceptible to be displaced during the insertion/extraction of lithium ions due to weaker Cu-O bond strength . The non-topotactic reaction due to the rearrangement of the host structure during the cycling causes irreversibility, slow lithium ion transport (D_{Li^+}= 10^{-13} cm^2s^{-1}) and low discharge potentials below 3 V in spite of the presence of the $Cu^{II/III}$ redox couple which was expected to give higher voltage.

Mediocre stability limits the application of the lithium copper oxides $Li_xCu_2O_4$ (x = 2, 3, 4) as cathode materials in lithium batteries since it is essential that the structural integrity of the electrode host structure is maintained throughout the discharge and charge processes for many hundreds of cycles. The properties of Li_2CuO_2, *i.e.* high initial charge density (320 $mAhg^{-1}$) and low discharge potentials, have shown an attractive application as additive in positive electrodes with $LiMn_2O_4$. Like the tetragonal LT-$LiMnO_2$ [2], it is well suited to compensate the irreversible loss of lithium in the passivation of the negative carbon electrode. The straightforward synthesis of Li_2CuO_2 (700 °C in air from CuO and Li_2O) could easily be scaled up to an industrial process.

The control of the intrinsic properties (symmetry, dimensionality of the structure) of the insertion compound itself is seen critically important as part of the ability to insert and subsequently remove guest species. Importance of other factors such as the conditions of synthesis and the effect on the size of the particles and surface areas should be taken into account in the strategy to design and optimise the electrode materials. The capacity delivered by a material at a given rate depends on the size and shape of the particles. Since the lithium ion diffusion within the material is slow, shorter diffusion distance is expected to have an important effect on their performances.

Recent studies of the particle size effect of micrometer-size copper oxides on their electrochemical performance clearly showed a better capacity retention for these compounds [3]. Such synthesis using precursors such as lithium and copper nitrates at low temperature in ethylene glycol can be a promising route to obtain micrometer-scale lithium copper oxide with narrow particle size distribution, higher surface area and high purity. At even smaller scale, works on nanostructured V_2O_5 [4] and layered metal chalcogenides (e.g. MoS_2, WS_2, $MoSe_2$, NbS_2) [5.6] have proved the possibility to synthesise new kinds of nanometer-scale materials with interesting but different properties than those of the bulk material.

The need for "greener" materials has resulted in an enormous effort to tame the manganese oxide systems with some success so far since it seems to represent the best compromise between cost, toxicity and electrochemical performance. In the work on the synthesis, structure and electrochemistry of new layered materials, $Li_{2-x}Mn_3O_7$ obtained by ion exchanging sodium by lithium in $Na_2Mn_3O_7$, interesting results were found concerning the influences of the synthesis and composition of the materials on their cycling performances. Variations in the temperature of the syntheses of $Li_{2-x}Mn_3O_7$ have introduced subtle but important differences in the composition and structure of the materials, *e.g.* (alkali metal composition, *c/a* ratio), which result in significant variations in their electrochemical properties. The conversion of $Li_{2-x}Mn_3O_7$ into spinel-like phase becomes less facile when the ion exchange temperature is lowered by reflux in ethanol at 70 °C.

The advantage of $Li_{2-x}Mn_3O_7$ is that it yields higher discharge capacities (~140 $mAhg^{-1}$ in the voltage range 2-4.5 V) than the useful capacity of $LiMn_2O_4$ (~10 $mAhg^{-1}$). It has still a lower discharge capacity than that of the doped layered lithium manganese cobalt oxide $Li(Mn_{1-y}M_y)O_2$ doped by Co or Ni, *e.g* $LiMn_{0.975}Co_{0.025}O_2$ which was found to offer a specific capacity of ~200 $mAhg^{-1}$ [7,8].

Further work in this field could consist of a study by electron microscopy of the spinel phase formed after several cycles. This is likely to bring evidence of the nanostructured character of this phase, mentioned already for other materials such as O-$LiMnO_2$ [9], Al-doped layered $LiMnO_2$ [10] and $Li(Mn_{1-y}Co_y)O_2$ [8].

Other systems worth citing in the conclusion are listed here. The new generation of iron or manganese oxyanions based on olivine (M_2SiO_4)-type structure, such as the mineral triphylite $LiFe_{1-x}Mn_xPO_4$, has quickly emerged as a high viable candidate cathode material [11]. $LiFePO_4$ has shown flat voltage curve at 3.5 V *vs.* Li., theoretical capacity of

c.a. 170 $mAhg^{-1}$ and good cyclability. Initial capacity loss delays however its commercial exploitation.

Finally it should be mentioned that the future of lithium batteries need not be restricted to inorganic compounds. New trends in intercalation compounds come from the organic-inorganic materials with, for instance, layered polyaniline-based (PAni) polymer PAni/HCF (hexacyanoferrate), which offers practical energy density up to 140 $mAhg^{-1}$ [12]. This is just an example of a going field of polymeric materials that will make the lithium battery not only more efficient but also more versatile in its application area.

References

[1] C. Julien, S. Gastro-Garcia, *J. Power Sources*, **97-8** (2001) 291.

[2] K. West, G. Vitins, R. Koksbang, *Electrochim. Acta*, **45** (2000) 3141.

[3] S. Grugeon, S. Laruelle, R. Herrera-Urbina, L. Dupont, P. Poizot, J-M. Tarascon, *J. Electrochem. Soc.*,**148** (2001) 285.

[4] C. Patrissi, C. Martin, ***J. Electrochem. Soc,***146 (1999) 3167.

[5] C. N. R Rao, B. C. Satishkumar, A. Govindaraj, M. Nath, *Chem. Phys. Chem.*, **2** (2001) 78.

[6] Y. Feldman, E. Wasserman, J. Srolovitch , R. Tenne, *Sciences*, **267** (1995) 222.

[7] D. Robertson, A. R. Armstrong , A.J. Fowkes, P. G. Bruce, *J. Mater. Chem.*, **11** (2001) 113.

[8] A. D. Robertson, A. R. Armstrong, P. G. Bruce, *Chem. Mater.*, **13** (2001) 2380.

[9] H. Wang, Y Jang, Y Chiang, *Electrochem. Solid. State Lett.*, **2** (1999) 490.

[10] H. Wang, Y Jang, Y Chiang, *Chem. Mater.*, **13** (2001)53.

[11] A. Anderson, B. Kalska, L. Haggstrom, J. Thomas, *Solid State Ionics*, **130** (2000) 41.

[12] G. Torres-Gomez, E. M Tejada-Rosales, P. Gomez-Romero, *Chem. Mat.*, **13** (2001) 3693.